

# Atomic Layer Deposition for CZTS Solar Cells

**Author:**

Cui, Xin

**Publication Date:**

2019

**DOI:**

<https://doi.org/10.26190/unsworks/2095>

**License:**

<https://creativecommons.org/licenses/by-nc-nd/3.0/au/>

Link to license to see what you are allowed to do with this resource.

Downloaded from <http://hdl.handle.net/1959.4/65558> in <https://unsworks.unsw.edu.au> on 2024-04-25

# **Atomic Layer Deposition for CZTS Solar Cells**

**Xin Cui**

A THESIS IN FULFILMENT OF THE REQUIREMENTS FOR THE  
DEGREE OF DOCTOR OF PHILOSOPHY



School of Photovoltaic and Renewable Energy Engineering  
Faculty of Engineering

December 2019

# Thesis/Dissertation Sheet

Surname/Family Name	: Cui
Given Name/s	: Xin
Abbreviation for degree as give in the University calendar	: PhD
Faculty	: Faculty of Engineering
School	: School of Photovoltaic and Renewable Energy Engineering
Thesis Title	: Atomic Layer Deposition for CZTS Solar Cells

## Abstract 350 words maximum: (PLEASE TYPE)

Kesterite  $\text{Cu}_2\text{ZnSnS}_4$  (CZTS) solar cells have recently emerged as a promising candidate for scalable thin-film solar cell development, mainly due to a generic similarity to commercialized  $\text{CuInGaSe}_2$  (CIGS) and  $\text{CdTe}$  solar cell technologies while consisting of only earth-abundant and non-toxic constituents. However, the photovoltaic performance of CZTS solar cells is still hampered by a relatively large open-circuit voltage ( $V_{oc}$ ) deficit which is correlated to bulk defects in CZTS absorber and recombination at the interfaces. To achieve high-performance CZTS solar cells, nanoscale layer coating and interface modification by atomic layer deposition (ALD) is an effective strategy to improve the device performance.

This thesis starts with the synthesis of ALD  $\text{Zn}_{1-x}\text{Sn}_x\text{O}$  films for application as a buffer layer in CZTS solar cells. A favorable band alignment is achieved using a 10 nm  $\text{Zn}_{0.77}\text{Sn}_{0.23}\text{O}$  buffer layer which enabled an impressive 10 % increase in  $V_{oc}$  and a 9.3% efficient CZTS solar cell, a world-record at the time of fabrication. The decreased interfacial defects stemming from the minor lattice mismatch at the CZTS/ $\text{Zn}(\text{S},\text{O})$ /ZTO hetero-interface in combination with the passivation provided by a higher sodium concentration throughout the CZTS/ZTO device explains the significant increase in  $V_{oc}$ .

Another strategy is the application of ALD  $\text{Zn}_{1-x}\text{Mg}_x\text{O}$  films as a window layer, which is essential to prevent shunt paths in CZTS thin-film solar cells. The wider bandgap of  $\text{Zn}_{0.8}\text{Mg}_{0.2}\text{O}$  layers minimizes the optical loss from the window layer and leads to an enhanced  $J_{sc}$ . A more favorable conduction band alignment is believed to contribute to the improvement in  $V_{oc}$ . A 9.2% efficient Cd-free CZTS device with a  $\text{Zn}_{1-x}\text{Mg}_x\text{O}$  window layer was fabricated without anti-reflection coating, thanks to the significantly enhanced  $J_{sc}$  and  $V_{oc}$ .

Lastly, I demonstrate the first Cd-free CZTS solar cell with an efficiency beyond 10 %, bringing this low-cost and green absorber one step closer to commercial practicality. This efficiency improvement is obtained by using an ALD  $\text{Al}_2\text{O}_3$  passivation layer to reduce interface recombination at the heterojunction, thus significantly reducing the  $V_{oc}$  deficit. It demonstrates the effective application of ALD  $\text{Al}_2\text{O}_3$  layers in Cd-free CZTS solar cells and provides fresh insights into the mechanism of  $\text{Al}_2\text{O}_3$  passivation on the nanoscale.

## Declaration relating to disposition of project thesis/dissertation

I hereby grant to the University of New South Wales or its agents a non-exclusive licence to archive and to make available (including to members of the public) my thesis or dissertation in whole or in part in the University libraries in all forms of media, now or here after known. I acknowledge that I retain all intellectual property rights which subsist in my thesis or dissertation, such as copyright and patent rights, subject to applicable law. I also retain the right to use all or part of my thesis or dissertation in future works (such as articles or books).

Signature

Date

The University recognises that there may be exceptional circumstances requiring restrictions on copying or conditions on use. Requests for restriction for a period of up to 2 years can be made when submitting the final copies of your thesis to the UNSW Library. Requests for a longer period of restriction may be considered in exceptional circumstances and require the approval of the Dean of Graduate Research.

#### **ORIGINALITY STATEMENT**

'I hereby declare that this submission is my own work and to the best of my knowledge it contains no materials previously published or written by another person, or substantial proportions of material which have been accepted for the award of any other degree or diploma at UNSW or any other educational institution, except where due acknowledgement is made in the thesis. Any contribution made to the research by others, with whom I have worked at UNSW or elsewhere, is explicitly acknowledged in the thesis. I also declare that the intellectual content of this thesis is the product of my own work, except to the extent that assistance from others in the project's design and conception or in style, presentation and linguistic expression is acknowledged.'

Signed .....

Date .....



## INCLUSION OF PUBLICATIONS STATEMENT

UNSW is supportive of candidates publishing their research results during their candidature as detailed in the UNSW Thesis Examination Procedure.

**Publications can be used in their thesis in lieu of a Chapter if:**

- The candidate contributed greater than 50% of the content in the publication and is the “primary author”, ie. the candidate was responsible primarily for the planning, execution and preparation of the work for publication
- The candidate has approval to include the publication in their thesis in lieu of a Chapter from their supervisor and Postgraduate Coordinator.
- The publication is not subject to any obligations or contractual agreements with a third party that would constrain its inclusion in the thesis

Please indicate whether this thesis contains published material or not:

☐

This thesis contains no publications, either published or submitted for publication

☒

Some of the work described in this thesis has been published and it has been documented in the relevant Chapters with acknowledgement

☐

This thesis has publications (either published or submitted for publication) incorporated into it in lieu of a chapter and the details are presented below

### CANDIDATE'S DECLARATION

I declare that:

- I have complied with the UNSW Thesis Examination Procedure
- where I have used a publication in lieu of a Chapter, the listed publication(s) below meet(s) the requirements to be included in the thesis.

**Candidate's Name**

**Signature**

**Date (dd/mm/yy)**

## **COPYRIGHT STATEMENT**

'I hereby grant the University of New South Wales or its agents a non-exclusive licence to archive and to make available (including to members of the public) my thesis or dissertation in whole or part in the University libraries in all forms of media, now or here after known. I acknowledge that I retain all intellectual property rights which subsist in my thesis or dissertation, such as copyright and patent rights, subject to applicable law. I also retain the right to use all or part of my thesis or dissertation in future works (such as articles or books).'

'For any substantial portions of copyright material used in this thesis, written permission for use has been obtained, or the copyright material is removed from the final public version of the thesis.'

Signed .....

Date .....

## **AUTHENTICITY STATEMENT**

'I certify that the Library deposit digital copy is a direct equivalent of the final officially approved version of my thesis.'

Signed .....

Date .....

# Acknowledgement

This thesis would not have been possible without a great deal of guidance and, both mental and practical, support. I would like to express my sincere thanks to those people who, during the past three and half years in which the thesis lasted, make this journey a gift to cherish.

First of all, I would like to thank Prof. Bram Hoex, my primary supervisor, for his expert guidance, sense of humor and constant encouragement throughout my studies. I am lucky to have had a chance to work with you as a friend rather than a student. The light in your office, whenever it is early morning or weekend, has always been the inspiration that guided my research and life. I am also deeply indebted to my joint-supervisor, A/ Prof. Xiaojing Hao, who has influenced this journey significantly. Your passion for research and tireless efforts towards works has really inspired each person around you. And thank you for taking the time during your holidays to read and comment on my papers, proposals, and thesis.

A special thanks to Prof. Martin Green, who has been the reason I chose UNSW as the destination of Ph.D. education. I cherish every moment that you spent with us in the group meeting, alumni party and international conference. Especially, your encouraging words after hearing my oral presentation in Melbourne and Xi'an have greatly enhanced my confidence in my academic career. Another early mentor who must be acknowledged is Prof. Allen Barnett, who brings me to the SPREE family. Although we do not share too much time after you left Australia to the U.S., I appreciate your attendance in every presentation I made during the IEEE conference,

both in Hawaii and Chicago.

My recognition also goes to the senior colleagues who paved the way for this journey. Great thanks to Kaiwen Sun, who teaches me how to make a CZTS solar cell with patience and carefulness. I could not have made the progress without your help and support at each stage of the journey. A special mention goes to Justin Lee, who is the kindest colleagues to work with and the warmest bother to talk to. You have set the bar high for the juniors and made the whole group united. I am also grateful to Dr. Jialiang Huang, whose scientific know-how skills have added pretty much value to this thesis. Thanks also to Alex To, one of the coolest guy I know, whose pursuits of advanced photovoltaic technology is a particular source of inspiration. Thank you to Li Wang and Alex Han, for your kind guidance and concern which have made life easier and comfortable during my first half-year oversea.

I would like to thank all the collaboration and technical support contributing to this project. Thanks to Dr. Md. Anower Hossain, for kindly offering help on the SIMS measurement in QEERI and discussion on a variety of topics; to Jae Sung Yun for doing the scanning probe microscope measurement and fruitful discussion on data analysis; A/ Prof. Lydia Helena Wong from NTU, for her contribution to the ALD processing and suggestion on my first journal paper; Katja Eder and Limei Yang from USyd, who performed the APT measurement and analyzed the data. I'm also very fortunate to have had the opportunity of meeting and working with Dr. Ivan Perez-Wurfl and A/ Prof. N. J. Ekins-Daukes. A great thank you to our admin team who have guaranteed the smooth running of the project: Craig Johnson, Rob Patterson, Alan Yee, Patrick Campbell, Tom Puzzer, Mark Griffin, Bernhard Vogl, Nicholas Shaw for the tool maintenance and lab induction. Thanks to Anne Rich, Yu Wang, Dorothy Yu, Bill Gong, Karen Privat, Yin Yao, Gordon Bates, Ute Schubert for the help on system training and sample characterization.

Words are not sufficient to thank my SPREE family, for the warm embrace, for the everyday laugh, and for sharing sweets and bitters together. First, a huge thanks to the

Carrier selective contact group who readily offers support whenever I needed any help; to Tian, for the shared experience we have had; to Atom, for the delicious pineapple cakes from Taiwan; to Kean, for the maintenance of our ALD buddy and instruction on the VR gaming; to Rong, for the free tickets of the Mid-Autumn Festival gala; to Yoyo, for preparing the yummy dishes for the whole group. Thanks also go to the Kesterite group who has been the best teammates to work with. Yuanfang, a warm-hearted partner who helps to fix any problems in the sputtering deposition; Chaowei, for the opinion within and outside of the academics; Chang, for sharing the secret of high-efficiency solar cell; Heng, for contribution to the CdS deposition and KPFM measurement; Aobo, for sharing his expertise on the device simulation. Thank you to all the former and current group members: Prof. Huang, Dr. Michael Pollard, Dr. Udo Romer, Taffy, Mengjie, Alessandro, Shuo, Sofia, UV, Borong, Shaozhou, Geedhika, Chuka; and Dr. Fangyang Liu, Dr. Jianjun Li, Jongsung, Yasaman, Mingrui, Chen, Fajun, Xueyun, Xiaojie.

I would also like to express my sincere thanks to the friends in Sydney: Felix and Sha, for driving me to the ANZ stadium, Jervis Bay and Mauna Kea; Ning and Yicong, for opening their home and hearts to me; Caixia, for sending me the shopping URL; Yan, for being the movers when I needed. Thank you to my friends: Jueming, Yong, Yijun, Shaoyang, Jessica and Dawei, Jonathon and Lucia, Yang and Liubing for the wonderful memories we share. In particular, thank you to the lovely Xiami, the best roommate and sister ever.

This thesis is dedicated to my family, whose value to me only grows with age. And finally, I would like to thank my Baymax, for his feeding and trusted advice over the past seven years. Our shared dream of creating a more sustainable world for every human being has motivated this journey, with peace and love.



# Abstract

Kesterite  $\text{Cu}_2\text{ZnSnS}_4$  (CZTS) solar cells have recently emerged as a promising candidate for scalable thin-film solar cell development, mainly due to a generic similarity to commercialized  $\text{CuInGaSe}_2$  (CIGS) and  $\text{CdTe}$  solar cell technologies while consisting of only earth-abundant and non-toxic constituents. However, the photovoltaic performance of CZTS solar cells is still hampered by a relatively large open-circuit voltage ( $V_{OC}$ ) deficit which is correlated to bulk defects in CZTS absorber and recombination at the interfaces. To achieve high-performance CZTS solar cells, nanoscale layer coating and interface modification by atomic layer deposition (ALD) is an effective strategy to improve the device performance.

This thesis starts with the synthesis of ALD  $\text{Zn}_{1-x}\text{Sn}_x\text{O}$  films for application as a buffer layer in CZTS solar cells. A favorable band alignment is achieved using a 10 nm  $\text{Zn}_{0.77}\text{Sn}_{0.23}\text{O}$  buffer layer which enabled an impressive 10 % increase in  $V_{OC}$  and a 9.3% efficient CZTS solar cell, a world-record at the time of fabrication. The decreased interfacial defects stemming from the minor lattice mismatch at the CZTS/ $\text{Zn}(\text{S},\text{O})$ /ZTO hetero-interface in combination with the passivation provided by a higher sodium concentration throughout the CZTS/ZTO device explains the significant increase in  $V_{OC}$ .

Another strategy is the application of ALD  $\text{Zn}_{1-x}\text{Mg}_x\text{O}$  films as a window layer, which is essential to prevent shunt paths in CZTS thin-film solar cells. The wider bandgap of  $\text{Zn}_{0.8}\text{Mg}_{0.2}\text{O}$  layers minimizes the optical loss from the window layer and leads to an enhanced  $J_{SC}$ . A more favorable conduction band alignment is believed to

contribute to the improvement in  $V_{OC}$ . A 9.2% efficient Cd-free CZTS device with a  $Zn_{1-x}Mg_xO$  window layer was fabricated without anti-reflection coating, thanks to the significantly enhanced  $J_{sc}$  and  $V_{OC}$ .

Lastly, I demonstrate the first Cd-free CZTS solar cell with an efficiency beyond 10 %, bringing this low-cost and green absorber one step closer to commercial practicality. This efficiency improvement is obtained by using an ALD  $Al_2O_3$  passivation layer to reduce interface recombination at the heterojunction, thus significantly reducing the  $V_{OC}$  deficit. It demonstrates the effective application of ALD  $Al_2O_3$  layers in Cd-free CZTS solar cells and provides fresh insights into the mechanism of  $Al_2O_3$  passivation on the nanoscale.



# Table of Contents

<b>Acknowledgement.....</b>	<b>i</b>
<b>Abstract .....</b>	<b>v</b>
<b>Table of Contents .....</b>	<b>vii</b>
<b>List of Figures .....</b>	<b>xi</b>
<b>List of Tables .....</b>	<b>xxiii</b>
<b>List of Abbreviations .....</b>	<b>xxv</b>
<b>Chapter 1 Introduction .....</b>	<b>1</b>
1.1 CZTS photovoltaics: a clean sustainable energy solution? .....	1
1.1.1 Thin film photovoltaics: current status and development.....	1
1.1.2 Why choose pure sulfide CZTS? .....	4
1.2 Opportunities for atomic layer deposition in photovoltaics .....	6
1.2.1 Fundamental limits of CZTS technology.....	6
1.2.2 How can ALD make a change? .....	10
1.2.3 Last step to fully environmental CZTS cell.....	12
1.3 Framework of this thesis .....	12
1.3.1 Objectives .....	12
1.3.2 Main structure of the thesis.....	14
<b>Chapter 2 Background .....</b>	<b>16</b>
2.1 Towards high efficient CZTS solar cells.....	16
2.1.1 Band alignment management.....	18

2.1.2	Alkaline doping.....	25
2.1.3	Interface defects passivation .....	29
2.1.4	Optical design .....	31
2.2	Atomic layer deposition.....	33
2.2.1	Precursors and co-reactants.....	35
2.2.2	Parameters for ALD development .....	36
2.2.3	Thermal and plasma-enhanced ALD .....	38
2.3	ALD application on chalcogenide solar cells .....	39
2.3.1	Absorber layer.....	39
2.3.2	Buffer layer .....	41
2.3.3	Window layer.....	47
2.3.4	Interface modification layer .....	49
<b>Chapter 3</b>	<b>Experiments.....</b>	<b>51</b>
3.1	Fabrication.....	51
3.1.1	Solar cell fabrication baseline .....	51
3.1.2	Atomic layer deposition process .....	53
3.2	Characterization.....	55
3.2.1	<i>In situ</i> measurement .....	55
3.2.2	Material characterization.....	58
3.2.3	Device characterization.....	70
<b>Chapter 4</b>	<b>ZnSnO as Cd-free CZTS buffer layer.....</b>	<b>74</b>
4.1	Introduction .....	74
4.2	Zn-based ternary oxides growth by thermal ALD .....	76
4.2.1	Growth of binary metal oxide .....	76
4.2.2	Deposition and properties of ZnSnO.....	82
4.2.3	Deposition and properties of ZnMgO .....	86
4.3	Application of ZnSnO as buffer layer on CZTS solar cell .....	90
4.3.1	Experiment.....	90
4.3.2	Influence of ZnSnO thickness on the device properties.....	91

4.3.3	Influence of ZnSnO composition on the device properties .....	94
4.3.4	Influence of heterojunction interface on the device properties.....	98
4.3.5	SCAPS simulation of CZTS/ZnSnO baseline model.....	113
4.4	General conclusions .....	118
<b>Chapter 5</b>	<b>ZnMgO as window layer for CZTS solar cell .....</b>	<b>120</b>
5.1	Introduction .....	120
5.2	ZnMgO growth by thermal and plasma-enhanced ALD.....	122
5.2.1	Comparison of ZnMgO growth property by in situ ellipsometry .....	124
5.2.2	Comparison of ZnMgO on morphology and structural property.....	128
5.2.3	Comparison of ZnMgO on optical and electrical property .....	132
5.3	Application of ZnMgO as window layer on CZTS solar cell .....	135
5.3.1	SCAPS simulation of ZnMgO as the window layer for CZTS solar cell .....	135
5.3.2	CZTS device made from ZnMgO window layer via thermal ALD and PE-ALD .....	139
5.3.3	Influence of ZnMgO composition on the device properties .....	140
5.3.1	Influence of ZnMgO deposition method on the device properties .....	143
5.4	General conclusions .....	148
<b>Chapter 6</b>	<b>Al<sub>2</sub>O<sub>3</sub> as interface passivation layer for CZTS.....</b>	<b>150</b>
6.1	Introduction .....	151
6.2	Passivation of CZTS/ZnSnO heterojunction interface by Al <sub>2</sub> O <sub>3</sub> .....	153
6.2.1	Experiment.....	153
6.2.2	Influence of Al <sub>2</sub> O <sub>3</sub> thickness on the device properties.....	155
6.2.3	Influence of ALD sub-steps on the device properties.....	156
6.3	Mechanism of heterojunction passivation by Al <sub>2</sub> O <sub>3</sub> .....	160
6.3.1	Interface properties of the device.....	160
6.3.2	Surface chemical analysis.....	162
6.3.3	Surface electronic analysis.....	169
6.3.4	Mechanism of Al <sub>2</sub> O <sub>3</sub> passivation on CZTS.....	174
6.4	General conclusions .....	178

<b>Chapter 7</b>	<b>Summary.....</b>	<b>179</b>
7.1	Conclusions .....	179
7.2	Original contributions.....	181
7.3	Perspectives .....	182
7.3.1	Alternative dopants for Zn-based buffer layers .....	183
7.3.2	Alternative oxides for interface layers .....	183
7.3.3	Alternative ALD process for window layers .....	184
<b>List of Publications</b>	<b>.....</b>	<b>185</b>
<b>Reference</b>	<b>.....</b>	<b>189</b>

# List of Figures

Figure 1. 1 Annual PV production by technology worldwide from the year 2000 to 2017.[6] .....	2
Figure 1. 2 Price learning curve by technology based on cumulative production up to Q4, 2017, expressed as module price per unit of generated power. The price of thin film modules has consistently been lower than the Crystalline Si modules. Reconstructed from Ref. [6]. .....	3
Figure 1. 3 Efficiency evolution of kesterite and chalcopyrite solar cells from the first year reported working solar cells. Adapted from [17]. .....	4
Figure 1. 4 Limiting processes in photovoltaic materials. Adapted from [1] .....	6
Figure 1. 5 Summary of the voltage deficit (with respect to the Shockley-Queisser limit) for kesterite and chalcopyrite solar cells. Adapted from Ref. [17]. .....	7
Figure 1. 6 Photocurrent efficiency in solar cells. Maximum possible short-circuit photocurrent density in the S-Q limit ( $J_{SCSQ}$ ) versus the photovoltaic gap ( $E_{gPV}$ ) compared with the experimental photocurrent density at short circuit ( $J_{sc}$ ) and maximum power ( $J_{MP}$ ) for the champion cells at AM 1.5 G illumination. Adapted from Ref. [30]. .....	8
Figure 1. 7 Diagram highlighting various roles ALD plays in the PV field. ....	10
Figure 1. 8 Different configurations of ALD thin film application for CZTS solar cells. ....	14
Figure 2. 1 $V_{OC}$ as a function of temperature data and its linear extrapolation to 0 K indicating the activation energy $EA$ of the recombination process. Adapted from Ref. [49] .....	17

Figure 2. 2 Schematic energy band diagram at the absorber/buffer interface: a) Spike-like type, b) Cliff-like type. ....	18
Figure 2. 3 The band alignment between CdS, $\text{Cu}_2\text{ZnSnS}_4$ , $\text{Cu}_2\text{ZnSnSe}_4$ , $\text{CuInSe}_2$ , and $\text{CuGaSe}_2$ (the effect of spin-orbit coupling is included). The red (dashed) line near the conduction band shows the pinning energy of the Fermi level for n-type doping. Adapted from Ref. [54]. ....	20
Figure 2. 4 Schematic bandgap diagram of CZTS solar cell under zero-bias voltage condition. ....	21
Figure 2. 5 Band alignments of ZnO, CdS, $\text{Cu}_2\text{ZnSnS}_4$ , $\text{Cu}_2\text{ZnSnSe}_4$ , $\text{CuInSe}_2$ , $\text{CuGaSe}_2$ , $\text{Cu}_2\text{O}$ , and SnS, where the conduction band minimum of ZnO is set to be 0.0 eV. Reconstructed from Ref. [63]. ....	24
Figure 2. 6 a) Formation energies of isolated intrinsic defects in $\text{Cu}_2\text{ZnSnS}_4$ as a function of chemical potential (Cu-rich and Cu-poor conditions) and b) transition-energy levels of the intrinsic defects in the electronic bandgap of $\text{Cu}_2\text{ZnSnS}_4$ . Reconstructed from Ref. [64]. ....	25
Figure 2. 7 a) Schematic of the total density of states (DOS) plot in conventional semiconductor materials such as Si/GaAs and modified DOS plot in disordered semiconductors (by heavy doping or introduction of a high density of lattice defects) and b) bandgap (left)/electrostatic potential (right) fluctuation in the electronic structures of CIGS and CZTS materials. Adapted from Ref. [65]. ....	27
Figure 2. 8 a) Optimal composition for the different alkali elements in terms of conversion efficiency reported by Haass <i>et al.</i> Adapt from [69] b) $V_{OC}$ gain for the most relevant extrinsic dopants published for kesterite. Adapted from Ref. [17]. ....	28
Figure 2. 9 Current loss in CZTSSe solar cells quantified by the analysis of wavelength-dependent EQE. The CZTSSe cell used for this analysis had a bandgap of 1.15 eV; losses are assigned by direct measurement of $J_{sc}$ and EQE, reflectance, TCO absorption (from both ITO and ZnO), and contact geometry. CdS absorption and IR “uncollected” losses are then separated at the location of the CdS bandgap as shown.	

Adapted from Ref. [97].	32
Figure 2. 10 Current loss in CZTS solar cells about analysis of EQE as a function of wavelength. The cell used for this analysis has a bandgap of 1.56 eV; losses are assigned by direct measurement of $J_{sc}$ and EQE, CdS absorption, ITO and ZnO absorption. The remaining is denoted as “uncollected” losses as shown.	33
Figure 2. 11 Schematic of the sequential atomic layer deposition process.	34
Figure 2. 12 Schematic illustration of the growth per cycle of ALD as a function of substrate temperature, purge time, and precursor dose.	36
Figure 2. 13 Supercycle and Co-injection method ALD used in ternary materials deposition with different composition.	37
Figure 2. 14 Band alignment for ZTO/CZTSSe heterojunction with different Sn/(Zn+Sn) ratio.	44
Figure 2. 15 Noticeable record efficiency for chalcogenide solar cells with different ALD materials.	47
Figure 3. 1. Schematic of the UNSW fabrication baseline of the CZTS/CdS thin film solar cell.	52
Figure 3. 2 Schematic representation of Fiji G2 ALD chamber equipped with a plasma source, <i>in situ</i> SE, OES and QCM, a turbopump and an automated load lock.	53
Figure 3. 3 Precursors used for ALD deposition. a) DEZ, b) TDMASn, c) Mg(CpEt) <sub>2</sub> , d) TMA	55
Figure 3. 4 Schematic setup of an ellipsometry measurement.	57
Figure 3. 5 a) Four-point probe configuration. b) Van der Pauw resistance measurement configurations (one of the eight possible configurations). c) Hall effect measurement configuration for thin films on an insulating substrate.	60
Figure 3. 6 Microanalysis techniques arranged according to their spatial resolutions and sensitivities. Adapted from Ref. [160].	62
Figure 3. 7 Data acquisition of different types of surface analysis in different materials. Adapted from Ref. [161].	63

Figure 3. 8 a) Difference in information depth for XPS and UPS. b) Work function measurement using the UPS spectra. Adapted from [161]. .....	64
Figure 3. 9 KPFM set up under illumination for CZTS/ZnSnO on Mo-coated glass substrate. ....	65
Figure 3. 10 Configuration of the electron microscopy compared with light microscopy. Adapted from Ref. [175]. ....	68
Figure 4. 1 a) <i>In situ</i> QCM and b) <i>in situ</i> SE measurements for ZnO deposition during thermal ALD cycles at 150 °C. ....	78
Figure 4. 2 Growth behavior of ZnO using thermal ALD, a self-limited reaction depending on a) DEZ pulse time, b) Ar purge time and c) temperature. ....	79
Figure 4. 3 Growth behavior of SnO <sub>x</sub> using thermal ALD, a self-limited reaction depending on a) TDMASn pulse time and b) Ar purge time. ....	80
Figure 4. 4 Growth behavior of MgO using thermal ALD, a self-limited reaction depending on a) (Mg(CpEt) <sub>2</sub> ) pulse time, b) Ar purge time and c) temperature. ....	82
Figure 4. 5 Schematic of super-cycle method used for ternary ZnSnO deposition by thermal ALD. ....	83
Figure 4. 6 a) Tauc plot and (b) refractive index and extinction coefficient as a function of the photon energy for the ZTO films grown using various Zn:Sn sub-cycle ratios. The absorption coefficient for the Tauc plot was determined from transmission-reflection while the optical properties were determined from spectroscopic ellipsometry measurements. The c) $E_g$ extracted from the Tauc plot analysis and spectroscopic ellipsometry as a function of the relative Sn ratio. d) GIXRD pattern of the ZTO films as a function of Zn:Sn sub-cycle ratio. ....	84
Figure 4. 7 Schematic of the super-cycle method used for ternary ZnMgO deposition by thermal ALD. ....	86
Figure 4. 8 a) Transmittance and (b) refractive index and extinction coefficient as a function of the wavelength for the ZMO films grown using various Zn:Mg sub-cycle ratios determined from spectroscopic ellipsometry measurements. The c) $E_g$ extracted	



from the Tauc plot analysis and spectroscopic ellipsometry as a function of the relative Mg ratio. d) GIXRD spectra of the ZMO films as a function of Zn:Mg sub-cycle ratio.	88
Figure 4. 9 Schematic of the fabrication of CZTS/ZnSnO thin film solar cell.	91
Figure 4. 10 a-d) Box-plots of performance parameters of CZTS cells for various ZTO buffer layer thickness. The Zn/Sn ratio was 3/1 during all ALD depositions. Box, horizontal bars, point symbols and indicate 25/75 percentile, min/max and mean values, respectively.	92
Figure 4. 11 $J$ - $V$ curves b) External quantum efficiency of the CZTS solar cells with different thickness of ZTO buffers.	93
Figure 4. 12 Box-plot of the one-sun solar cell performance parameters of CZTS cells made with the various compositions of the ZTO buffer layer. 10 CZTS solar cells were fabricated per experimental condition. Box, horizontal bars, point symbols and indicate 25/75 percentile, min/max and mean values, respectively. Results obtained for a CZTS device with a CdS buffer layer are included as a reference as well.	95
Figure 4. 13 a) $C$ - $V$ curves of the CZTS devices with different composition of ZTO buffer. b) Free carrier density and depletion width derived from the $C$ - $V$ curves.	96
Figure 4. 14 a) The current density-voltage, b) External quantum efficiency, and c) Room-temperature capacitance-frequency characteristics of the CZTS solar cells with different compositions of ZTO buffer layer compared to corresponding CdS control device, measured with 0 V (DC) and 0.01 V (AC) bias in the dark.	97
Figure 4. 15 a) The schematic of CZTS/CdS and CZTS/ZnSnO solar cell structures used in this work. b) $J$ - $V$ characteristics and c) EQE of the champion CZTS/ZnSnO solar cell with and without ARC compared with CZTS/CdS reference solar cell without ARC. d) High angle annular dark-field (HAADF) scanning TEM image of the enlarged CZTS/ZTO/i-ZnO/ITO stack (left) and corresponding estimated phase structure from the EDS mapping (right) of the best-performing CZTS/ZnSnO solar cell.	99
Figure 4. 16 a) $C$ - $V$ curves of the CZTS devices with ZTO and CdS buffer. b) Free carrier density and depletion width derived from the $C$ - $V$ curves. c) Room-temperature	

capacitance-frequency characteristics of the CZTS solar cells with ZTO and CdS buffer measured with 0V (DC) and 0.01 V (AC) bias under dark conditions. ....	101
Figure 4. 17 Surface XPS spectra of a) Zn 2p <sub>3/2</sub> , b) Sn 3d <sub>5/2</sub> , c) O 1s peak of Zn <sub>0.77</sub> Sn <sub>0.23</sub> O film on CZTS solar cells .....	102
Figure 4. 18 a) HAADF scanning TEM image and b) corresponding EDS element line scan of the CZTS/ZTO interface of the champion solar cell. c) Atomic-resolution HAADF image and the FFT pattern of the corresponding area of the CZTS/ZTO interface. d) A representative intensity profile for a cations column at the interface marked by the red rectangular in Fig. 6c. ....	103
Figure 4. 19 Estimated phase structure from the EDS mapping of the CZTS/ZTO interface.....	104
Figure 4. 20 High resolution transmission electron microscope (HRTEM) images of the CZTS/ZTO heterojunction region showing the microstructure for different ZTO buffers a) Zn <sub>0.77</sub> Sn <sub>0.23</sub> O b) Zn <sub>0.73</sub> Sn <sub>0.27</sub> O .....	105
Figure 4. 21 a) Atomic-resolution HAADF image of the CZTS/CdS interface. b) A representative intensity profile for a cations column at the interface marked by the red rectangular in Fig. S6a. c) Schematic of the band alignment at CZTS/CdS interface extracted from our previous report. ....	106
Figure 4. 22 a) Box-plots of performance parameters and b) <i>J-V</i> curves of the CZTS cells for ALD ZnSnO buffer layers with a different sequence of ZnO and SnO <sub>x</sub> sub-cycles.....	107
Figure 4. 23 a,b) TOF-SIMS elemental depth profiles from the TCO to the SLG substrate of CZTS solar cells with CdS and ZnSnO buffer. ....	108
Figure 4. 24 a) The XPS composition profile for CZTS absorber with a Zn <sub>0.77</sub> Sn <sub>0.23</sub> O buffer layer. The depth profile was divided into three regions, namely the ZTO region, CZTS/ZTO interface region, and CZTS bulk region as a function of sputtering time according to the composition transformation. b) Normalized VB data of CZTS/Zn <sub>0.77</sub> Sn <sub>0.23</sub> O heterojunction measured by XPS. Binding energies were measured	

with respect to the Fermi energy ( $E_F$ ). c) Band bending of the CZTS/  $\text{Zn}_{0.77}\text{Sn}_{0.23}\text{O}$  interface as a function of sputtering time. d) Schematic of the band alignment at CZTS/ $\text{Zn}_{0.77}\text{Sn}_{0.23}\text{O}$  interface with Zn(S, O) tunnel layer. .... 110

Figure 4. 25 a) Illustration of device structure used for CZTS/ZTO model. b) Schematic band diagrams under light at short circuit condition for CZTS/ZnSnO baseline model. .... 113

Figure 4. 26  $J$ - $V$  characteristics of measured data and simulation results for CZTS/ZTO baseline solar cell. .... 116

Figure 4. 27 Calculated contour plots of (a) open-circuit voltage, (b) short-circuit current, (c) fill-factor, and (d) efficiency for CZTS/ZnSnO devices with the variation of ZTO properties (left axis indicates bandgap  $E_{g,ZTO}$ , bottom axis indicates conduction band minimum offset at CZTS/ZTO  $\Delta E_c$ ). .... 117

Figure 5. 1 Schematic of the super-cycle method used for ternary ZnMgO deposition by T-ALD and PE-ALD. .... 123

Figure 5. 2 a) The initial stage of ZnMgO film growth during T-ALD and PE-ALD at 150 °C on Si (111). b) Experimental composition (solid line) from ICP-OES of the thin films closely follows the expected composition (dash line) from the weighted average of the growth rates (rule of mixtures, ROM). Growth per cycle of consecutive ZnO and MgO sub-cycles using c) T-ALD and d) PE-ALD as measured by *in situ* ellipsometry. The dashed lines indicate the growth per cycle for pure ZnO and MgO. .... 125

Figure 5. 3 GIXRD patterns for ZMO thin films deposited on SLG substrates through a) T-ALD and b) PE-ALD. .... 129

Figure 5. 4 Raman scattering spectra for ZMO thin films deposited through a) T-ALD and b) PE-ALD. An excitation wavelength of 325 nm was used for the measurements. .... 130

Figure 5. 5 AFM morphology of ZMO thin films deposited through a-c) T-ALD and d-f) PE-ALD. .... 131

Figure 5. 6 Transmittance as a function of the wavelength for the ZMO films grown using various Zn:Mg sub-cycle ratios through a) T-ALD and b) PE-ALD. .... 133

Figure 5. 7 Refractive index and extinction coefficient as a function of the wavelength for the ZMO films grown using various Zn: Mg sub-cycle ratios through a) T-ALD and b) PE-ALD determined from spectroscopic ellipsometry measurements.....	133
Figure 5. 8 a, b) Absorption coefficient as a function of the photon energy for the ZMO films grown using various Zn:Mg sub-cycle ratios through T-ALD and PE-ALD. c) $E_g$ extracted from spectroscopic ellipsometry as a function of the relative Mg ratio in ZMO.....	134
Figure 5. 9 a) Illustration of device structure used for CZTS/ZTO/ZMO model. b) Schematic band diagrams under light at short circuit conditions for CZTS/ZTO/ZMO baseline model. ....	136
Figure 5. 10 Calculated contour plots of a) open-circuit voltage, b) short-circuit current, c) fill-factor, and d) efficiency for CZTS/ZnSnO/ZnMgO devices with the variation of ZMO properties (left axis indicates doping density, bottom axis indicates electron affinity $\chi_{ZMO}$ ).....	138
Figure 5. 11 Schematic of the fabrication of CZTS/ZnSnO/ZnMgO thin-film solar cell.	140
Figure 5. 12 a-d) Box-plots of performance parameters of CZTS cells with a variable composition of ZMO window layer compared to the corresponding i-ZnO control device. 10 CZTS solar cells were fabricated per experimental condition. ....	141
Figure 5. 13 a) The current density-voltage curves b) External quantum efficiency of the CZTS solar cells with different compositions of ZMO buffer layer compared to a corresponding i-ZnO control device. ....	142
Figure 5. 14 a-d) Box-plots of performance parameters of CZTS cells with ZMO window layer deposited from T-ALD and PE-ALD compared to a corresponding i-ZnO control device.....	143
Figure 5. 15 a) The current density-voltage and b) external quantum efficiency of the CZTS solar cells with ZMO window layer deposited from T-ALD and PE-ALD compared to a corresponding i-ZnO control device. ....	144
Figure 5. 16 a-c) XPS peak of Zn 2p <sub>3/2</sub> , Mg 1s, O 1p, respectively, obtained from the	

surface of ZMO thin films deposited through T-ALD and PE-ALD.....	146
Figure 5. 17 a) Atomic composition, b) UPS spectra and c) band diagram of the CZTS solar cells with ZMO window layer deposited from T-ALD and PE-ALD. ....	147
Figure 5. 18 a) $J$ - $V$ characteristics and b) EQE of the champion CZTS/ZTO/PE-ZMO solar cell without anti-reflection coating.....	148
Figure 6. 1 Schematic of the fabrication of CZTS/ $\text{Al}_2\text{O}_3$ /ZnSnO thin-film solar cell.	153
Figure 6. 2. a-d) Box-plot diagram of the one-sun solar cell parameters of CZTS cells as a function of the number of ALD cycles used for the $\text{Al}_2\text{O}_3$ passivation layer. 10 CZTS solar cells were fabricated per experimental condition. The box, horizontal bars, and point symbols indicate the 25/75 percentile, min/max and mean values, respectively.....	155
Figure 6. 3 a) Schematic view of the processes investigated in this section to elucidate the impact of the various components of the $\text{Al}_2\text{O}_3$ ALD process. In addition to the full $\text{Al}_2\text{O}_3$ ALD process shown to the left, also the TMA and $\text{H}_2\text{O}$ half-reaction were investigated in isolation as well as exposing the sample solely to the process temperature used during the ALD process. b) Box-plot diagram of the one-sun $J$ - $V$ performance parameters of CZTS cells made with no treatment (Ref), $\text{Al}_2\text{O}_3$ treatment, TMA treatment, $\text{H}_2\text{O}$ treatment and heat treatment within the ALD chamber. 10 CZTS solar cells were fabricated per experimental condition. Box, horizontal bars, point symbols and indicate 25/75 percentile, min/max and mean values, respectively. ....	157
Figure 6. 4 a) $J$ - $V$ curves and b) EQE spectra and PL spectra of the CZTS devices with various treatment: no treatment (Ref), $\text{Al}_2\text{O}_3$ treatment, TMA treatment, $\text{H}_2\text{O}$ treatment and heat treatment within the ALD chamber.....	158
Figure 6. 5 a) Bandgap values extracted from the EQE measurements and PL peak position for devices with various ALD treatment. The inflection point of the EQE was used to determine the bandgap ( $E_g$ ), dash lines are plotted for guiding purpose. b) Time-resolved photoluminescence (TRPL) obtained at an excitation wavelength of 470 nm for the corresponding devices.....	159

Figure 6. 6 a) Saturation current density of different CZTS devices obtained by fitting their Suns- $V_{OC}$  curves using a two-diode model. b)  $C-V$  and DLCP profiling for the CZTS devices with no treatment (Ref) and  $Al_2O_3$  treatment. .... 161

Figure 6. 7 Defect density  $N_{DLCP}$  and  $N_{CV}$  at  $V_{dc} = 0$  derived from  $C-V$  and DLCP measurements of devices with different ALD treatment, respectively. .... 162

Figure 6. 8 Raman spectra for bare CZTS absorbers and CZTS/ZnSnO after different ALD treatment. An excitation wavelength of 514 nm was used for the measurements. 163

Figure 6. 9 a-c) XPS peak of Zn 2p3, Sn 3d, S 2p, respectively, obtained from the surface of CZTS absorbers with no treatment (Ref),  $Al_2O_3$ , TMA, and  $H_2O$  treatment. 164

Figure 6. 10 Surface chemical analysis. a-d) XPS peak of Al 2s, O 1s, Na 1s, Cu 2p3, respectively, obtained from the surface of CZTS absorbers with no treatment (Ref),  $Al_2O_3$  treatment, TMA treatment, and  $H_2O$  treatment. e-h) XPS peak of Al 2s, O 1s, Na 1s, Cu 2p3, respectively, at the surface of CZTS absorbers with no treatment (Ref) and  $Al_2O_3$  treatment after the sputtering with approximately 0.5 nm. i) Na and Cu atomic percentages measured at the surface of as-received absorbers with different treatments. j) Cu/(Zn+Sn) atomic percentage ratio of the surface of absorbers with different treatments before and after sputtering in a depth of 0.5 nm. Dash lines in i) and j) are plotted for guiding purposes. .... 165

Figure 6. 11 Atom Probe Tomography of the 10.2% efficient CZTS device. a) Atom probe reconstruction of the ZnSnO/ $Al_2O_3$ / CZTS interface area. Only the  $Na^{+1}$  ions are displayed in light green,  $Cu^{+1}$  ions in orange. A cylinder was positioned across the interface to determine concentration changes along the direction of the arrow, and the results are shown in the concentration profile b) A bin size of 1 nm was chosen and all species were decomposed into their constituent elements. c) Partial atom probe reconstructions of the CZTS absorber layer where Na segregation along a grain boundary.  $Na^{+1}$  ions are displayed in green. Na-rich areas are displayed by using an isoconcentration surface with a Na value of 0.9 at.%. A cylinder was positioned perpendicular across the grain boundary, to produce a one-dimensional cross-section

measure of the concentration changes. The results are shown in the concentration profile d) and e). A bin size of 1 nm was chosen and all species were decomposed into their constituent elements.....	168
Figure 6. 12 a) KPFM set up under illumination. b) Root-mean-square (RMS) roughness ( $R_q$ ) distribution profile across the captured images in Figure 5a,e. c) Average CPD values difference between dark and light at illumination intensities of 894 mW/cm <sup>2</sup> (400 nm) and 12000 mW/cm <sup>2</sup> (750 nm) for the reference and Al <sub>2</sub> O <sub>3</sub> treatment samples. Measurements were taken at a wavelength of 400 nm and 750 nm.	169
Figure 6. 13 Topography and light-induced surface potential measurements of the CZTS/ZnSnO heterojunction films with and without Al <sub>2</sub> O <sub>3</sub> treatment. KPFM measurements of the two samples showing a, e) Topography and b, f) simultaneously recorded CPD spatial maps in the dark c, g) CPD spatial maps under various laser illumination intensities at a wavelength of 400 nm d, h) CPD spatial maps under various laser illumination intensities at a wavelength of 750 nm of CZTS/ZnSnO and CZTS/Al <sub>2</sub> O <sub>3</sub> /ZnSnO, respectively. i) CPD distribution obtained in dark conditions for the two investigated samples. j) Average CPD values for the reference and Al <sub>2</sub> O <sub>3</sub> treatment samples as a function of illumination intensity at a wavelength of 400 nm and 750 nm. k) Average CPD values and CPD values difference between dark and light with illumination intensities of 894 mW/cm <sup>2</sup> (400 nm) and 12000 mW/cm <sup>2</sup> (750 nm) at GBs and GIs for corresponding samples. The scanning scales were 5 $\mu$ m $\times$ 5 $\mu$ m.....	171
Figure 6. 14 a) SEM cross-sectional image of Cd-free CZTS solar cell with an Al <sub>2</sub> O <sub>3</sub> passivation layer inserted between CZTS and ZnSnO. b) Current density-voltage ( $J-V$ ) characteristics and c) external quantum efficiency (EQE) of CZTS/ZnSnO record devices with Al <sub>2</sub> O <sub>3</sub> interlayer under 1 Sun illumination (AM 1.5G spectrum). The integrated photocurrent density is included on the right Y-axis. ....	174
Figure 6. 15 a, b) UPS spectra of the CZTS absorbers with different ALD treatment. c) Energy band positions for CZTS absorbers of valance band maximum with respect to Fermi level energy, $E_F$ . ....	176

Figure 6. 16 a) Schematic bandgap fluctuation in the electronic structures of CZTS with and without  $\text{Al}_2\text{O}_3$  treatment. Band diagrams illustrating the band alignment structure for b) CZTS/ZnSnO and c) CZTS/ $\text{Al}_2\text{O}_3$ /ZnSnO. d) Mechanism illustration of the CZTS absorber surface modification when exposed to ALD- $\text{Al}_2\text{O}_3$  treatment.. 177



# List of Tables

Table 2. 1 PV parameters of kesterite solar cells prepared with different buffer layers, with their conduction band offset (CBO), valence band offset (VBO), device parameters and deposition method, respectively. ....	22
Table 2. 2 Photovoltaic performance summary of best-performing thin-film cells with different ALD buffer layers, TCO layers, and interface layers. ....	41
Table 3. 1 List of dynamic measurements used in the ALD process. ....	56
Table 3. 2 List of material characterization methods used in this thesis. ....	59
Table 3. 3 List of device characterization methods used in this thesis. ....	70
Table 4. 1 Properties of ZnSnO thin films with different compositions compared to the pure ZnO and SnO <sub>x</sub> films. ....	85
Table 4. 2 Growth properties of ZnMgO thin films with different compositions. ....	87
Table 4. 3 Optical and electrical properties of ZnMgO thin films with different compositions. ....	90
Table 4. 4 Corresponding maximum values of device parameters of CZTS/CdS cells and CZTS/ZTO cells with ZTO buffer in different composition and thickness. ....	96
Table 4. 5 Corresponding values of photovoltaic parameters of the champion CZTS/ZTO solar cells compared to the champion CZTS/CdS reference. ....	100
Table 4. 6 Material parameters used for the simulation of CZTS/ZTO devices in SCAPS-1D. ....	115
Table 4. 7 Corresponding values of photovoltaic parameters of the experimental	

CZTS/ $\text{Zn}_{0.77}\text{Sn}_{0.23}\text{O}$ solar cells compared to the simulation results.....	116
Table 5. 1 Growth properties of ZnMgO thin films with different compositions synthesized by T-ALD and PE-ALD. ....	127
Table 5. 2 Optical and electrical properties of ZnMgO thin films changing along with Mg content synthesized from T-ALD and PE-ALD. ....	135
Table 5. 3 Material parameters used for the simulation of CZTS/ZTO/ZMO devices in SCAPS-1D. ....	137
Table 6. 1 List of key parameters used for different ALD processes.....	154
Table 6. 2 Corresponding values of photovoltaic parameters of the champion CZTS/ $\text{Al}_2\text{O}_3$ /ZnSnO solar cells compared to the previous champion CZTS/ZnSnO reference without $\text{Al}_2\text{O}_3$ passivation. Values based on the active area are reported in parentheses. ....	175

# List of Abbreviations

4PP	Four-point probe
AFM	Atomic force microscope
ALD	Atomic layer deposition
APT	Atom probe tomography
BIPV	Building integrated photovoltaic
BOS	Balance of system
CBD	Chemical bath deposition
CBO	Conduction band offset
CdTe	Cadmium telluride
$C-f$	Capacitance-frequency measurement
CIGS	Copper indium gallium diselenide
CPD	Contact potential difference
c-Si	Crystalline silicon
C-V	Capacitance-voltage measurement
CVD	Chemical vapor deposition
CZTS	$\text{Cu}_2\text{ZnSnS}_4$
CZTSe	$\text{Cu}_2\text{ZnSnSe}_4$
CZTSSe	$\text{Cu}_2\text{ZnSn}(\text{S},\text{Se})_4$
DEZ	Diethyl zinc
DFT	Density function theory
DLCP	Drive-level capacitance profiling measurement

DOS	Density of states
$E_C$	Conduction band minimum
EDS	Energy dispersive spectroscopy
$E_g$	Bandgap energy
EQE	External quantum efficiency
FF	Fill factor
FFT	Fast Fourier transform
GB	Grain boundary
GI	Grain interior
GIXRD	Grazing incidence X-ray diffraction
GPC	Growth per cycle
HAADF	High angle annular dark field
HRTEM	High resolution transmission electron microscope
HWF	High-work-function
ICP	Inductively coupled plasma
ICP-OES	Inductively coupled plasma optical emission spectrometry
i-ZnO	Intrinsic ZnO
$J_0$	Saturation current density
$J_{sc}$	Short circuit current
JV	Current density-voltage measurement
KPFM	Kelvin probe force microscopy
LCOE	Levelized costs of electricity
Mg(CpEt) <sub>2</sub>	Ethylcyclopentadienyl magnesium
PCE	Power conversion efficiency
PDT	Post-deposition treatment
PEALD	Plasma-enhanced ALD
PL	Photoluminescence
PV	Photovoltaic

QCM	Quartz crystal microbalance
Raman	Raman spectroscopy
rms	Root mean square
$R_s$	Series resistance
$R_{sh}$	Shunt resistance
SCR	Space charge region
SE	Spectroscopic ellipsometry
SEM	Scanning electron microscope
SLG	Soda-lime glass
SPV	Surface photovoltage
S-Q	Shockley-Queisser
Suns- $V_{oc}$	Suns- $V_{oc}$ measurements
TCO	Conductive oxide layer
TDMASn	Tetrakis (dimethylamino) tin
TEM	Transmission electron microscope
TMA	Trimethylaluminum
ToF-SIMS	Time of flight secondary ion mass spectroscopy
TRPL	Time-resolved photoluminescence
UPS	Ultraviolet photoelectron spectroscopy
UV	Ultra-violet
UV-Vis	UV/vis/NIR Spectrophotometer
VBO	Valence band offset
$V_{oc}$	Open circuit voltage
XPS	X-ray photoelectron spectroscopy
XRD	X-ray diffractometer
ZMO	$Zn_{1-x}Mg_xO$
ZTO	$Zn_{1-x}Sn_xO$



# Chapter 1 Introduction

## 1.1 CZTS photovoltaics: a clean sustainable energy solution?

### 1.1.1 Thin film photovoltaics: current status and development

The continuous development of human society requires escalating energy consumption. However, most of the global energy consumption in modern society comes from burning oil, gas, and coal, the so-called fossil fuels. Actually, all the energy in fossil fuels originates from the sun, namely captured through photosynthesis by plants. In this sense, we are withdrawing from our natural bank of stored solar power without making any significant deposits, which can be regarded as unsustainable. In order to maintain a sustainable utilization of the energy, renewable energy instead of exhaustible fossil fuels is required to tackle the escalating energy demand for human development. Photovoltaic (PV) technology, which converts the sunlight into electricity without releasing CO<sub>2</sub>, is among the most promising renewable energy technologies.[1-3] The photovoltaic industry has demonstrated rapid growth in the past decades reaching a global cumulative PV system installation of 500 gigawatts by the end of 2018.[4] Those installations bring us PV generated electricity, which represented 2.5% of global electricity demand at the end of 2018.[4] Crystalline silicon (c-Si) PV holds the majority share in the PV market mainly because of its rich material resources, non-toxic nature and proven long-term stable performance. It should be noted that the price of c-Si PV modules declined dramatically in the past years

whereby driving the levelized costs of electricity (LCOE) from PV down to 2 USD cents/kWh in some markets in 2019. Solar power is now close to or even (far) below “grid-parity” in many countries.[4] This impressive achievement can be attributed to PV technology research and development, economies of scales and the market-stimulating policies in the last forty years.[5]

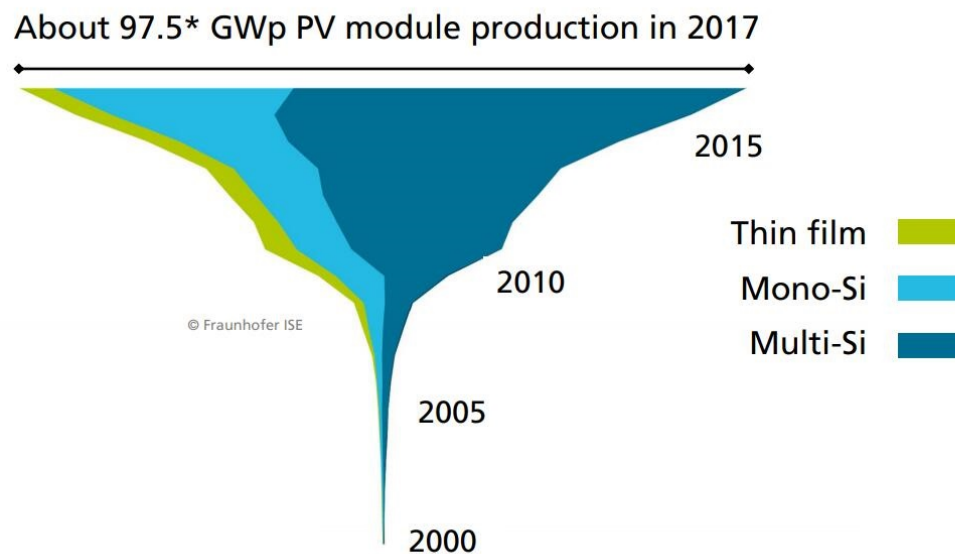


Figure 1. 1 Annual PV production by technology worldwide from the year 2000 to 2017.[6]

Silicon PV has a market share of more than 90% and the remainder is taken up by thin film PV technologies such as cadmium telluride (CdTe), copper indium gallium diselenide (CIGS) as shown in Figure 1. 1. Despite the fact that the market share of all thin film technologies combined was only ~5 %, the module prices of thin film PV still follow a similar declining trend at a comparable price level as c-Si PV as shown in Figure 1. 2.[6, 7] In some areas thin film PV is advantageous over c-Si PV as it utilizes less material.[8, 9] The active layer of thin film solar cells is usually only a few micrometers thick, much thinner than the conventional crystalline silicon cells which use wafers up to 200  $\mu\text{m}$ . Also, thin film solar cells can be fabricated onto both rigid and flexible substrate, which allows PV modules with much lower weight and higher



flexibility for wider applications. This is, in particular, relevant to markets such as building integrated photovoltaic (BIPV), portable electrical devices, electric vehicle integrated PV, and commercial unmanned aerial vehicles. [10] Another application scenario for thin film PV is the integration with c-Si to form cost-effective tandem solar cells with theoretical efficiency well beyond 40%. [11, 12] Stacking a high bandgap thin film solar cell on a c-Si bottom cell will produce high-efficiency solar cells without adding additional encapsulation or system cost. Efficiency improvement is regarded as the key to future PV development as the encapsulation and balance of system (BOS) costs are now dominating the cost of a PV system. [13] This approach will potentially lead to a huge reduction in the LCOE; simply because the same power can be generated from a smaller area.

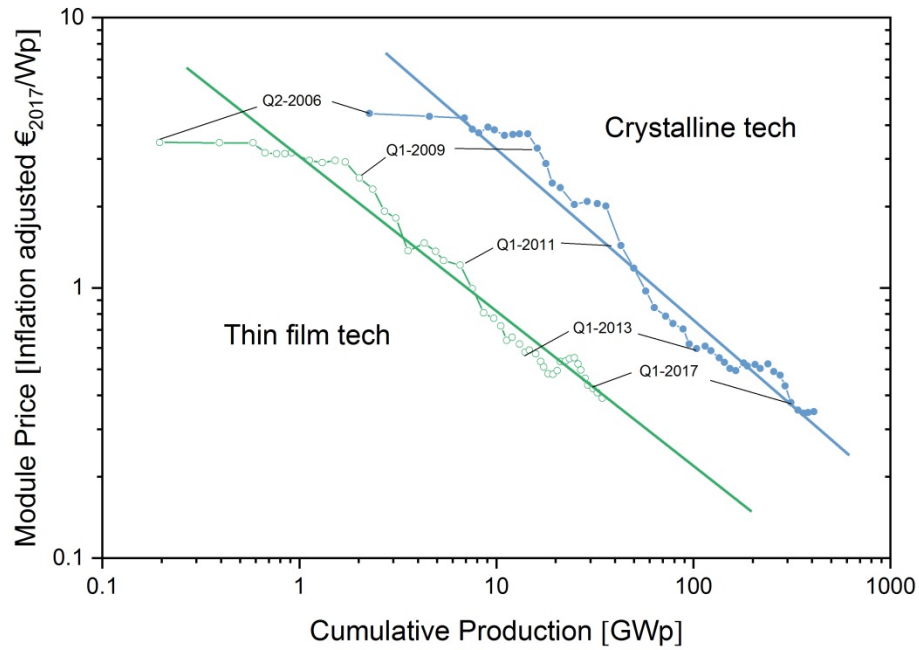


Figure 1. 2 Price learning curve by technology based on cumulative production up to Q4, 2017, expressed as module price per unit of generated power. The price of thin film modules has consistently been lower than the Crystalline Si modules. Reconstructed from Ref. [6].

On the lab scale, thin film solar cells have achieved a remarkable increase in

photovoltaic performance with efficiency beyond 22 % for CdTe[14] and 23 % for CIGS[15] solar cells. Metal halide perovskite-based solar cells even reached 25 % efficiency due to the significant strides made over the past several years.[16] However, these thin film technologies use either toxic elements such as cadmium and lead or scarce elements such as indium, gallium and tellurium which complicates scaling up these technologies to the terawatt level. Therefore, the development of thin film solar cells which only use earth-abundant non-toxic elements is desirable for terawatt -scale PV technology.

### 1.1.2 Why choose pure sulfide CZTS?

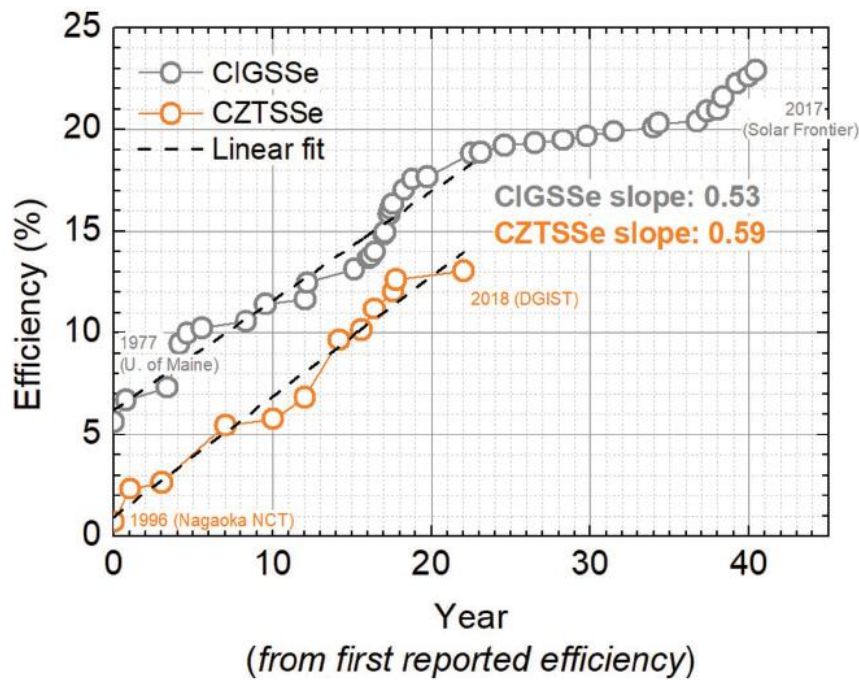


Figure 1. 3 Efficiency evolution of kesterite and chalcopyrite solar cells from the first year reported working solar cells. Adapted from [17]

Copper-based  $I_2-II-IV-VI_4$  quaternary kesterite compounds including  $Cu_2ZnSnS_4$  (CZTS),  $Cu_2ZnSnSe_4$  (CZTSe) and  $Cu_2ZnSn(S, Se)_4$  (CZTSSe) are promising candidates for thin film PV technology due to their outstanding performance, the usage

of only earth-abundant elements, and their potential for low-cost manufacturing.[18-20] Note that CZTS(e) will be used as a general acronym to represent those compounds in the remainder of the thesis. Kesterite-based solar cells have witnessed rapid development since the demonstration of the first working solar cell twenty years ago. Although the efficiency is not at the same level as CdTe and CIGS, kesterite-based solar cells still hold a slightly higher development speed than chalcopyrite solar cells during its first twenty-year development, as can be seen from Figure 1. 3.[17] If it can maintain this development speed, the efficiency of kesterite solar cells is expected to reach the 20 % threshold in the next decade.

Kesterite-based materials have a number of photoelectric properties which make it a promising light-harvesting material. In principle, CZTS(e) structure is quite comparable to CIGS where In and Ga are replaced by more earth-abundant Zn and Sn.[10, 21] The CZTS(e) system can crystallize to form three different structural phases including kesterite, stannite or primitive mixed Cu-Au, where kesterite is preferable to use for solar cells due to its most stable structural polytype[1]. Similar to chalcopyrite solar cells, the bandgap of CZTS(e) can be tuned over the range of 1.0 to 1.5 eV, which matches well with the optimum bandgap of 1.4 eV for AM1.5 solar spectrum[22]. Furthermore, the high absorption coefficient ( $>10^5 \text{ cm}^{-1}$ ) and natural *p*-type conductivity[23] make CZTS(e) an appealing choice for thin film PV applications. A 1~2  $\mu\text{m}$  thick absorber layer is enough to absorb most of the incident solar radiation[24]. Together with these properties, the substantial progress in kesterite solar cells has made it as the most promising candidate for sustainable large-scale PV deployment.

In this thesis, I will focus on pure sulfide CZTS instead of selenide compounds CZTSe or CZTSSe with the following reasons being identified.

- 1) Se is not earth-abundant[25] while S is very abundant.
- 2) Pure sulfide CZTS has a larger bandgap than e.g. CZTSSe cells which is desirable when applied in a tandem solar cell.[12]

- 3) Alternative buffer layers can be employed in CZTS solar cells while to date only toxic CdS buffer layers were successfully used in CZT(S, Se).[26, 27] As the previous research showed, the utilization of a Cd-free buffer layer enables higher efficiency in CZTS solar cells while not that successful in CZT(S,Se) cells.[26, 27]

In this way, CZTS solar cells provide a green plus pathway to a sustainable future using only earth-abundant and non-toxic elements.

## 1.2 Opportunities for atomic layer deposition in photovoltaics

### 1.2.1 Fundamental limits of CZTS technology

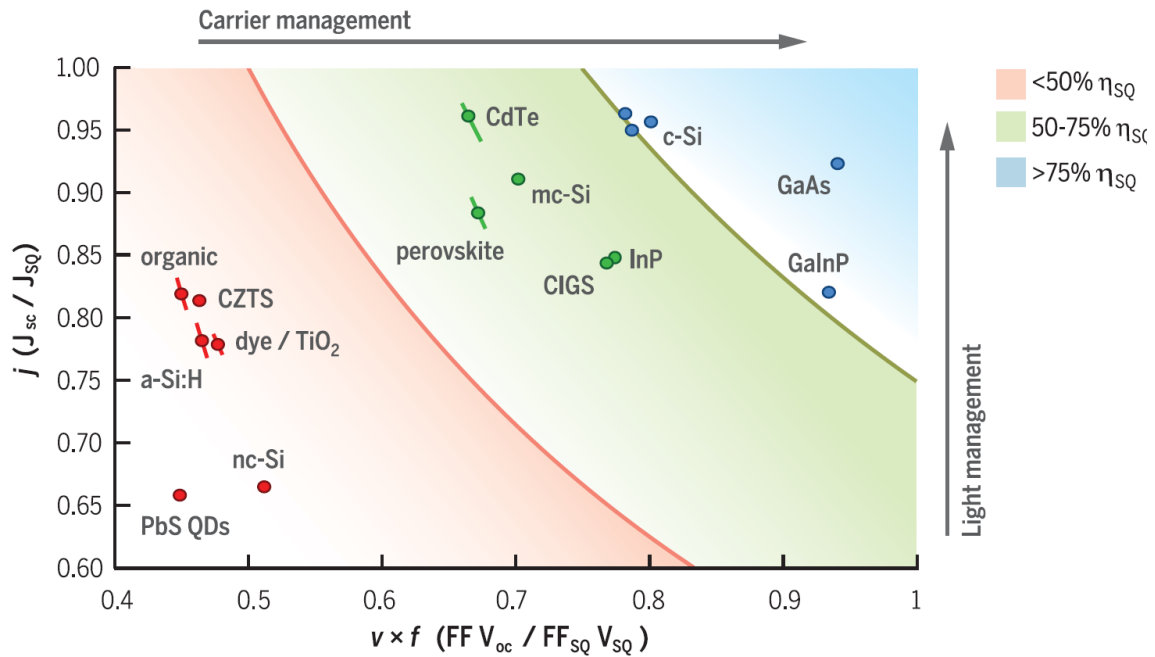


Figure 1. 4 Limiting processes in photovoltaic materials. Adapted from [1]

The main challenge for CZTS(e) solar cells at this moment is its relatively modest energy conversion efficiency. The record 12.6% efficient CZTSSe device is still significantly below its CIGS counterpart with a 23.35% record efficiency.[28, 29] Polman *et al.* compared the gap between the champion solar cell performance and the

fundamental Shockley-Queisser (S-Q) limit for a wide range of PV materials[1] as shown in Figure 1. 4. The experimental values for short-circuit current ( $J_{sc}$ ) and the product of open-circuit voltage ( $V_{oc}$ ) with fill factor ( $FF$ ) relative to their S-Q limiting values are shown for 16 record efficiency solar cells. From this figure, one can easily identify the dominant performance loss for each solar cell technology, e.g. a  $J_{sc}$  lower than the SQ limit indicates non-ideal light management and carrier collection, and a relatively low  $(V_{oc} \times FF)/(V_{sq} \times FF_{sq})$  identifies non-ideal carrier management, parasitic resistance or other electrical defects. In the case of the record CZTSSe solar cell, it can be observed that the  $V_{oc} \times FF$  lags with only 50% of its ideal value, which contributes to the main efficiency loss.

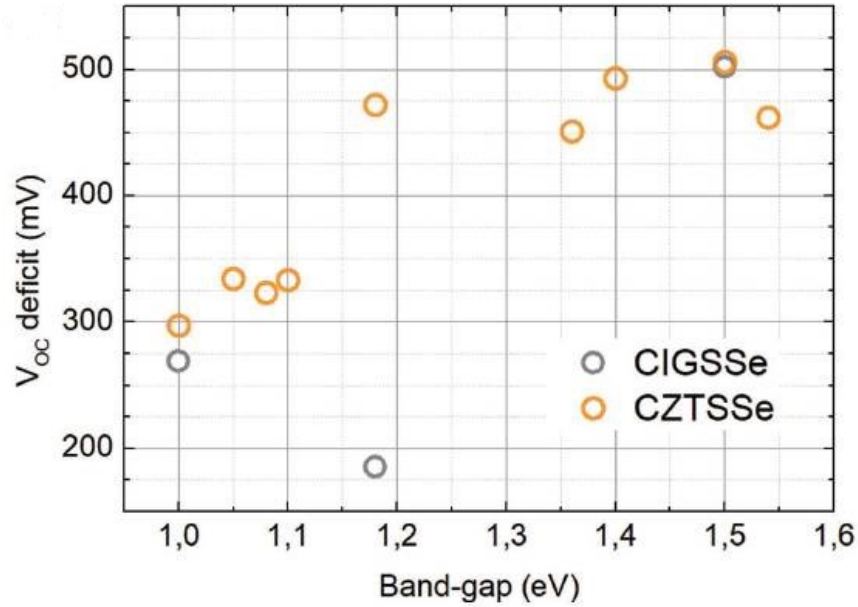


Figure 1. 5 Summary of the voltage deficit (with respect to the Shockley-Queisser limit) for kesterite and chalcopyrite solar cells. Adapted from Ref. [17].

This low  $V_{oc}$  value for CZTS(e) can be regarded as the main reason for the lower efficiency compared to that of chalcogenide CIGS solar cells. Most commonly,  $V_{oc}$  deficit is used to evaluate the gap between measured  $V_{oc}$  and the maximum thermodynamic  $V_{oc}$ . Therefore,  $V_{oc}$  deficit can be calculated using the following

equation,

$$V_{OC} \text{ deficit (mV)} = E_g/q - V_{OC} \quad \text{Equation 1. 1}$$

where  $E_g$  is the optical bandgap extracted from the onset of the external quantum efficiency (EQE),  $q$  is the electron charge,  $V_{OC}$  is obtained from the  $J$ - $V$  analysis under AM 1.5G conditions. Figure 1. 5 presents a comparison of the lowest  $V_{OC}$  deficit reported for kesterite and chalcopyrite as a function of the bandgap of the absorber. Notably, the  $V_{OC}$  deficit of kesterite and chalcopyrite is comparable for bandgaps of 1.0 and 1.5 eV, while the gap between them increases significantly in the intermediate bandgap region. Another phenomenon is that the  $V_{OC}$  deficit increases monotonically with the bandgap, indicating the performance of high bandgap CZTS is limited by the  $V_{OC}$  loss.

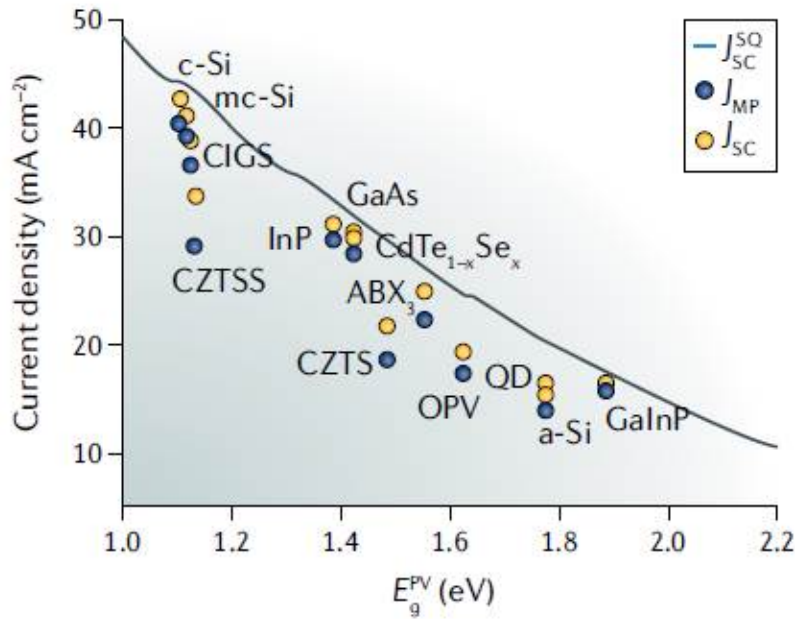


Figure 1. 6 Photocurrent efficiency in solar cells. Maximum possible short-circuit photocurrent density in the S-Q limit ( $J_{SC}^{SQ}$ ) versus the photovoltaic gap ( $E_g^{PV}$ ) compared with the experimental photocurrent density at short circuit ( $J_{sc}$ ) and maximum power ( $J_{MP}$ ) for the champion cells at AM 1.5 G illumination. Adapted from Ref. [30].

This large  $V_{oc}$  deficit is mainly attributed to a large number of defects in the lattice and more defect-induced energy levels in the electronic bandgap.[19, 21, 31] The presence of those defects leads to a large density of defect-induced energy levels within the bandgap, thus producing the band tailing in kesterite.[32] In addition, the stoichiometry range of single-phase kesterite CZTS(e) is much narrower than CIGS, normally with Cu-poor( $Cu/(Zn+Sn) = 0.8-0.9$ ) and Zn-rich ( $Zn/Sn = 1.1-1.4$ ) features[33]. Besides, the decomposition of CZTS at high temperatures and related binary phases (such as  $Cu_2S$ ,  $ZnS$ , and  $SnS$ ) further impedes attempts to create pure kesterite CZTS films[34, 35]. Apart from the discrepancies in absorber properties, the performance of CZTS(e) solar cells is also limited by the interface quality of the e.g. CZTS(e)/CdS and CZTS(e)/Mo interfaces.[36] Detailed investigation on bulk defects and secondary phase defects in CZTS(e) films and their influences on devices have been discussed in detail elsewhere [21, 31], and I will mainly focus on the interface management of CZTS solar cells in my thesis.

Another fundamental limit of the CZTS(e) cell performance is the low  $J_{sc}$ . Figure 1. 6 plot the current density versus bandgap energy for various types of solar cells, providing an overview of the photocurrent efficiency of the cells. The ratio of  $J_{sc}/J_{sc}^{SQ}$  can be used to evaluate the efficiency of photo capture and subsequent photo-generation and collection at the contact of a device.[30] The values of  $J_{sc}/J_{sc}^{SQ}$  are calculated to be 74% and 77% for CZTS and CZTSe cells, while the values for c-Si, GaAs and CIGS are 96%, 93% and 89%. Not surprisingly, the observed deviation of the experimental  $J_{sc}$  from the  $J_{sc}^{SQ}$  is much larger for CZTS(e) than c-Si, GaAs and CIGS solar cells. It indicates that CZTS(e) has poorer photocurrent efficiency than the other technology, which impedes performance improvement. A considerable photocurrent loss is believed to be related to the low EQE values in the short wavelength region in champion kesterite cells.[37, 38] The employment of a high bandgap window or thinner buffer layer could probably minimize the photon

absorption. It is also worth looking beyond the photon absorption to increase the photocurrent efficiency by reducing the non-radiative carrier recombination in the bulk and at the interface as well as shunt resistances which contribute to the loss in photogenerated carriers. The development and design of alternative buffer/window layer and interface layer will be the main strategy in this thesis to minimize optical loss and enhance the generation and collection of photogenerated carriers.

### 1.2.2 How can ALD make a change?

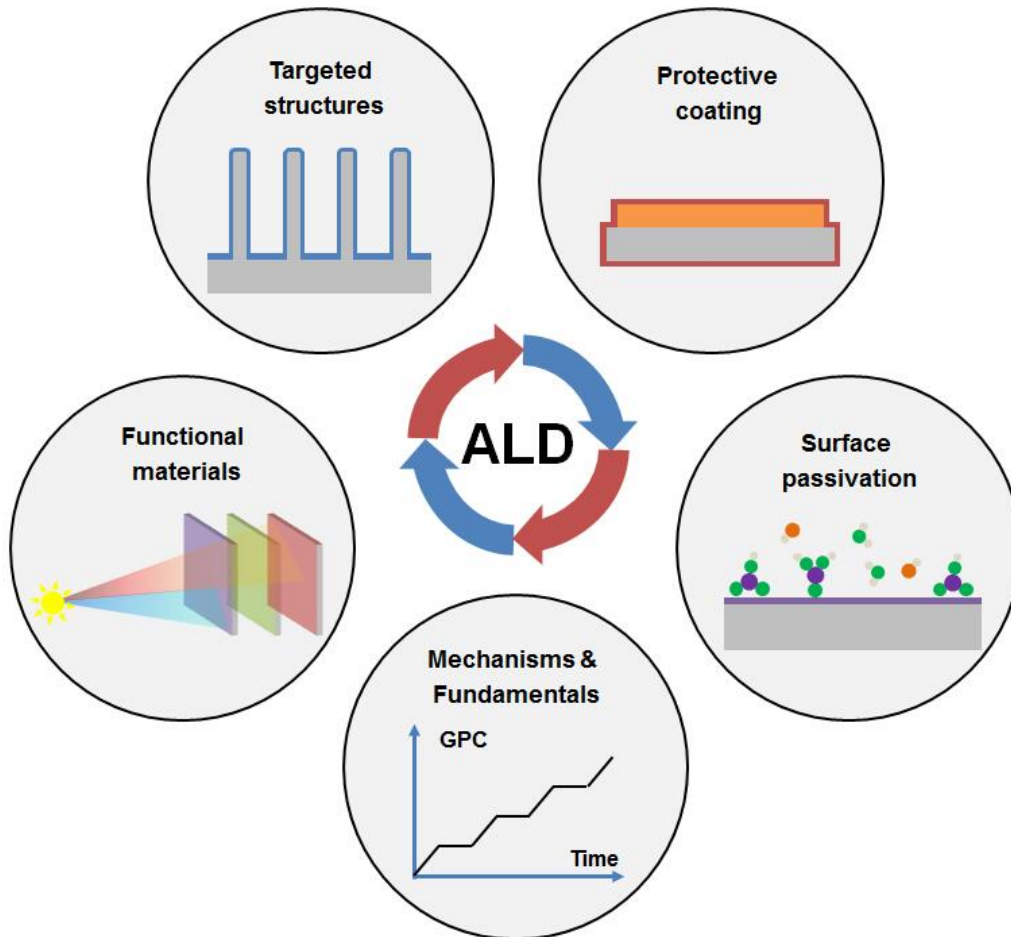


Figure 1. 7 Diagram highlighting various roles ALD plays in the PV field.

To solve the issues in CZTS solar cell's development, nanoscale layer coating and interface modification of CZTS is a critical approach to reduce the  $V_{OC}$  deficit and  $J_{sc}$



losses, leading to high-performance solar cells. Therefore, there is a number of opportunities for CZTS technology to benefit from the use of atomic layer deposition (ALD) processing, either from the view of environment protection or performance improvement. ALD is a technique enabling nanoscale engineering through self-limiting surface reactions and provides ultrathin, dense and continuous layers at the sub-nanometer scale. The self-limiting reactions also enable the excellent coverage and conformal coating on complex structures. In addition, the separation of sub-steps processing allows for the tuning of the structural, optical, electrical properties of materials such as gradient, stoichiometry and doping level at the monolayer scale. Especially for interface management purpose, ALD offers many advantages for precise, uniform and conformal film growth. Various functional layers such as absorber, buffer layers, passivation layers, and transparent conductive oxide layer can be deposited by ALD.

ALD has been used in many ways to enhance the device performance in the PV field, as categorized into five different areas presented in Figure 1. 7. These areas include the application on targeted structures, the construction of protective coating, the synthesis of functional materials, the employment of surface passivation and the study of mechanisms and fundamentals. Specifically, the various roles ALD played in the PV area are: (1) Targeted structures: the material coating on complex three-dimensional structures is the characteristic application of ALD due to its conformal, isotropic growth behavior. (2) Protective coating: the dense nature of ALD coatings can significantly improve the stability of the PV devices and extending their durability. (3) Functional materials: precise composition control on the functional materials deposited by ALD allows for performance to be well-tuned. (4) Surface passivation: ALD is extensively implemented to reduce interface recombination, in particular for c-Si solar cells. (5) Mechanisms and fundamentals: fundamental studies of the process mechanism can be performed in ALD through step by step characterization. In this thesis, the last three applications will be investigated in detail.

### **1.2.3 Last step to fully environmental CZTS cell**

Although kesterite solar cells have witnessed a rapid development in the past decades to the current power conversion efficiency (PCE) over 10%, [37-39] most of the high-performance kesterite devices have been fabricated using CdS as the buffer layer which is obviously not desirable when aiming for a fully environmentally-friendly process. Hence, the last step towards a fully environmental CZTS solar cell is to avoid the utilization of toxic Cd. The Cd-free buffer layer has shown great potential in chalcogenide solar cells as evidenced by the fact that Solar Frontier recently announced a record efficiency of 23.35% for Cd-free CIGS solar cell. [15] In contrast, the Cd-free CZTS solar cells only demonstrated a champion efficiency of 9.7 % [40] to date, posing significant constraints to compete with CIGS at a commercial level. As above mentioned, the interface recombination is mainly originating from non-ideal band-alignment and a high defect density at the CZTS/CdS heterojunction interface. Additionally, the relatively low bandgap of CdS ( $E_g = 2.4\sim 2.5\text{eV}$ ) results in significant optical absorption losses and thus reduces the short-circuit current density of the solar cell. Therefore, CdS buffer needs to be replaced by alternative buffer layers such as  $\text{In}_2\text{S}_3$ , [41]  $\text{Zn}(\text{O},\text{S})$ , [42] and  $\text{Zn}_{1-x}\text{Sn}_x\text{O}$  [43, 44], which have the potential to both improve the performance and achieve fully environmental device.

## **1.3 Framework of this thesis**

### **1.3.1 Objectives**

On the material level, the functional materials studied in this thesis will be deposited by using ALD, a moderate process based on self-limiting reactions on the surface. The key merit of ALD is the freedom to accurately control the properties of the film. I will investigate the growth, optical, electrical and structural properties of

ALD thin films for various materials. The implementation of ALD for functional layers benefits from the dynamic measurements during the process of deposition, which allows for evaluating the basic properties of the deposited films and precise control on the growth of desired materials. One functional material might exhibit different properties depending on its deposition condition, the precursors used and the ALD process employed. Hence, the effects of those factors will be discussed to find a suitable candidate for a certain purpose.

At the device level, as mentioned in Section 1.2.1, improvement in cell efficiency is the key point towards cost reduction in future PV development. Further improvements in efficiency have been mainly hampered by difficulties to tackle the large deficit in the  $V_{oc}$ , [1] which is correlated to deep defects and fluctuated composition in bulk, secondary phases, interface recombination, etc. [23, 32, 45] In this thesis, I will mainly focus on interface recombination. The interface recombination is mainly originating from a non-ideal band-alignment and a high defect density at the CZTS/CdS heterojunction interface. Thus, alternative Cd-free buffer materials will be employed to optimize the band alignment. Another origin of interface recombination can be attributed to the intrinsic point defects and local fluctuations of the bandgap and electrostatic potential in CZTS [1, 46, 47]. Heterojunction interface passivation will be required to effectively passivate interface defects. In addition to the  $V_{oc}$  deficit, the optical loss needs to be suppressed to increase the  $J_{sc}$  value. High bandgap materials will be utilized to replace the commonly used i-ZnO layer. As different function layer is to be used, an optimized combination of the buffer/window layer will be simulated as an approach to accelerate the experimental optimization works.

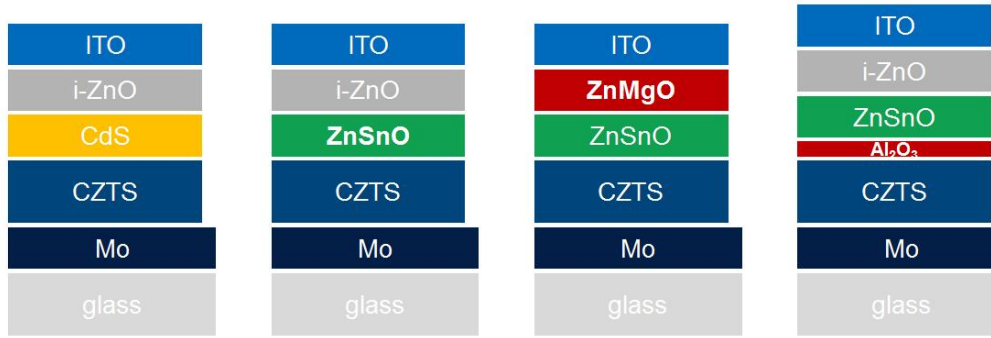


Figure 1. 8 Different configurations of ALD thin film application for CZTS solar cells.

ALD based buffer layers, passivation layers, and transparent conductive oxide can be explored in various configurations of CZTS solar cells. Previous studies indicate the great potential of ALD application on chalcogenide solar cell and therefore a number of exciting opportunities are there to boost the performance of CZTS solar cells. The proposed application of ALD thin film on CZTS devices is illustrated in Figure 1. 8. The main part of this thesis is categorized by the function of ALD materials applied in CZTS solar cells, namely the buffer layer, window layer, and interface passivation layer. Each part starts with the deposition and characterization of ALD thin films. The implementation of dynamic measurement accelerates the development of various functional materials. Subsequently, those thin films are applied in the CZTS device to look into its effects on the device performance. Together with the device simulation, the enhanced photovoltaic performance of the CZTS device is to be demonstrated and analyzed. Finally, the mechanism and fundamental basis of the improvement will be given based on advanced material and device characterization.

### 1.3.2 Main structure of the thesis

Chapter 2 begins with a theoretical background investigation on the possible approach towards a high efficient CZTS solar cell. It then summarizes the fundamental knowledge of understanding and developing a desirable atomic layer process. The last

part summarizes the current progress about the application of ALD on chalcogenide solar cells following the category of various functional materials.

Chapter 3 describes the experimental techniques used in this work to deposit various functional layers and characterization methods to measure thin films and photovoltaic devices. The characterization method was systematically described by dividing into three parts, namely, *in situ* diagnosis technique in ALD system, *ex situ* material characterization and device measurement.

Chapter 4 presents the study of Cd-free buffer layer deposited by thermal ALD and their application on CZTS devices. By carefully optimizing the thickness and composition of ZTO, a CZTS solar cell efficiency of 9.3 % is presented which can mainly be attributed to an enhanced  $V_{oc}$ . The microstructure, chemical nature and band structure of the CZTS/ZTO interface are carefully studied to explain the significant increase in  $V_{oc}$ .

Chapter 5 demonstrates the high bandgap window layer deposited by different ALD method and their application on CZTS devices. A 9.2% efficient Cd-free CZTS device with a structure of Mo/CZTS/ZTO/PE-ZMO/ITO was fabricated without anti-reflection coating, thanks to a significantly enhanced  $J_{sc}$  and  $V_{oc}$ .

Chapter 6 demonstrates  $Al_2O_3$  as an effective heterojunction passivation layer on CZTS devices. This part presents a champion efficiency of 10.2 % for Cd-free CZTS device resulting from the application of an  $Al_2O_3$  passivation layer prepared by ALD. A plausible mechanism for the passivation induced by ALD- $Al_2O_3$  was proposed on how to improve the  $V_{oc}$  and device performance.

Chapter 7 summarizes the major conclusions of this thesis and presents a road map towards high efficient Cd-free CZTS solar cells.

## Chapter 2 Background

To achieve the objectives of this thesis, the background of how ALD could improve the PV performance of Cd-free CZTS solar cells is systematically investigated in this chapter. Firstly, the possible approach towards high-efficiency CZTS solar cells is discussed, including the favorable band alignment, alkaline doping, interface passivation, band tailing suppression, and optical design. It is then followed by a fundamental background investigation of how to develop a desirable ALD process for PV application. The last part summarizes the current research progress on the application of ALD layers and processes in chalcogenide solar cells.

### 2.1 Towards high efficient CZTS solar cells

Based on the previous discussion, the main barrier for CZTS improvement comes from the  $V_{OC}$  deficit. To improve the  $V_{OC}$ , we need to understand the controlling of defect-mediated recombination mechanisms coming from bulk, grain boundaries and interface between device layers. [31, 35, 36, 48] The major recombination mechanism of low  $V_{OC}$  can be studied by analyzing the temperature ( $T$ ) dependent  $V_{OC}$ [49]:

$$V_{OC} = \frac{E_A}{q} - \frac{AkT}{q} \ln \frac{J_0}{J_L} \quad \text{Equation 2. 1}$$

where  $E_A$ ,  $A$ ,  $k$ ,  $q$ ,  $J_0$  and  $J_L$  are the activation energy for recombination, ideality factor, Boltzmann constant, electron charge, reverse saturation, and photocurrent current,

respectively. A straight line should be obtained by plotting the  $V_{OC}$  versus  $T$ , extrapolation to  $T=0$  K will give the activation energy  $E_A/q$ [49]. If the plotting intercept has a value less than the bandgap, it means that interface recombination is the dominating recombination mechanism. As shown in Figure 2. 1, the activation energy of CZTSSe solar cells is far below the bandgap, while the activation energy of CIGS is identical to the bandgap value. This large gap in CZTSSe solar cells is probably caused by the electrical defects or a negative bandgap offset at the CdS/CZTSSe interface[49]. Therefore, interface defects and band alignment offset at the CdS/CZTSSe interface impede the carrier collection efficiency, leading to decreased solar cell efficiency[37]. The large  $V_{OC}$  deficit gives us the motivation to further improve the CZTS solar cell performance. Having a better understanding and control of the functional layers and interface management will give us an opportunity towards high efficient CZTS solar cells.

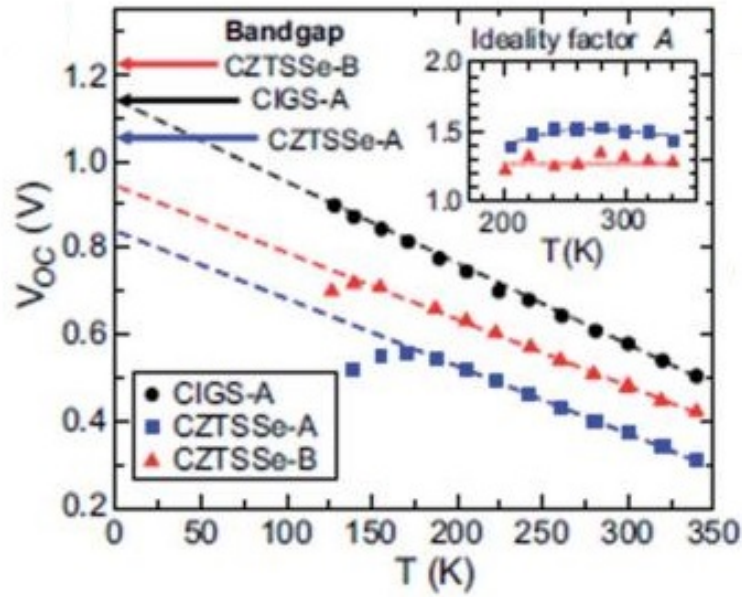


Figure 2. 1  $V_{OC}$  as a function of temperature data and its linear extrapolation to 0 K indicating the activation energy  $E_A$  of the recombination process. Adapted from Ref. [49]

### 2.1.1 Band alignment management

Band alignment is a critical research point as it helps to understand the carrier transportation and recombination mechanism at the interface. The band offset of conduction band minimum is defined as  $\Delta E_c$  while the band offset of valence band maximum is  $\Delta E_v$ . Also, the bandgap difference  $\Delta E_g$  at the interface is written to be  $\Delta E_g = E_g^l - E_g^s$ , where the superscripts denote large (l) and small (s) bandgaps. If the band offsets are defined to be  $\Delta E_v = E_v^l - E_v^s$  and  $\Delta E_c = E_c^l - E_c^s$ , then we can get the expression of  $\Delta E_g$  at each semiconductor/semiconductor interface as following:

$$\Delta E_g = \Delta E_v + \Delta E_c \quad \text{Equation 2. 2}$$

With these definitions, one can speak of positive and negative band offsets. If a band offset is positive, a charge carrier requires kinetic energy in order to overcome the energy barrier from the small gap to the large gap semiconductor. To give an example, let us discuss the heterojunction interface between the absorber and buffer layer.

#### 2.1.1.1 Absorber/buffer

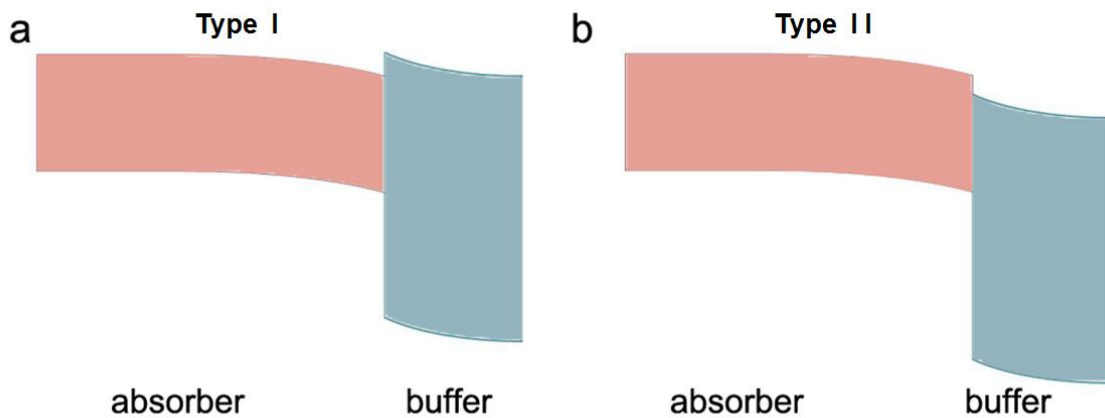


Figure 2. 2 Schematic energy band diagram at the absorber/buffer interface: a) Spike-like type, b) Cliff-like type.



Thin film solar cells featured by effective heterojunction to obtain high photovoltaic performance. Generally, a buffer layer is employed in combination with the absorber layer to create a  $p$ - $n$  junction. A buffer layer should benefit the device properties in terms of maximizing light transmission, effective carrier transportation as well as good mechanical compatibility. The buffer layer is typically an  $n$ -type material with large bandgap to minimize the absorption losses. Apart from this, the band offset at the heterojunction has been found to impact the extent of recombination at the interface.

In general, there are two types of conduction band offset (CBO) in a heterojunction interface as shown in Figure 2. 2. Type I is called ‘spike-like’ CBO with positive conduction band offset, or  $\Delta E_c > 0$ , where the conduction band of the buffer layer lies higher than the absorber layer. In this case, it is the electron concentration at the absorber surface which dominates the occupation of interface defects; therefore interface recombination is governed by the concentration of the free holes at the absorber surface. The hole concentration is small at zero bias and for forward bias which leads to decreased saturation current density  $J_0$ , thus high  $V_{OC}$ . By contrast, Type II is called ‘cliff-like’ CBO with a negative conduction band offset, or  $\Delta E_c < 0$ , which drives the electron transportation from the absorber to buffer. In this case, the  $V_{OC}$  declines proportionally to  $-\Delta E_c$  due to the large hole concentration at the absorber surface at forwarding bias. The smaller ‘spike-like’ conduction band offset (0–0.4 eV) is believed to be optimal for high-performance chalcogenide solar cells to facilitate electron-hole separation, according to device simulations [50, 51]. For  $\Delta E_c < 0.4$  eV, the influence of interface recombination on the  $J_{SC}$  is small. The reason is that the photogenerated electrons can pass the interface without significant recombination due to the fact that the hole concentration is much smaller than the electron concentration. However, for  $\Delta E_c > 0.4$  eV, the  $J_{SC}$  and  $FF$  decrease remarkably as the barrier for electrons becomes too high.

CdS is the most commonly used buffer layer in CZTS devices as well as in CIGS solar cells. The most efficient CZTS solar cells are fabricated using chemical bath deposition (CBD) of CdS buffer layers [37, 52, 53]. CdS as an  $n$ -type layer is deposited on  $p$ -type CZTS absorber to form the  $p$ - $n$  junction. The advantage of using CdS is to mostly satisfy the conduction band alignment to both absorber and the undoped ZnO layer. It is postulated that a ‘spike-like’ CBO is favorable for  $V_{OC}$  while ‘cliff-like’ CBO benefits a  $J_{SC}$ . Here then comes the question, what is the band offset between kesterite absorber and CdS buffer layer? The band alignment between kesterite absorber/CdS has been obtained from photoemission spectroscopy.

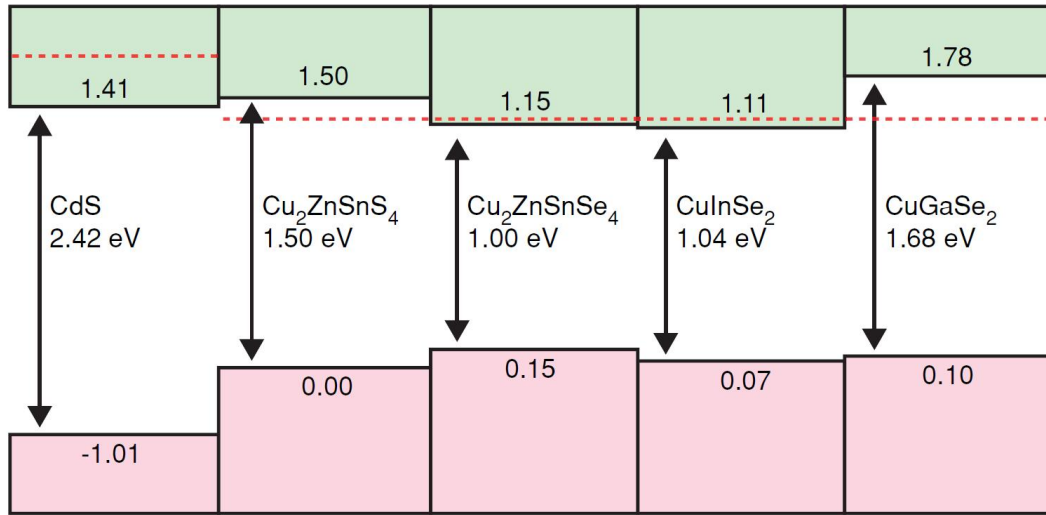


Figure 2. 3 The band alignment between CdS,  $\text{Cu}_2\text{ZnSnS}_4$ ,  $\text{Cu}_2\text{ZnSnSe}_4$ ,  $\text{CuInSe}_2$ , and  $\text{CuGaSe}_2$  (the effect of spin-orbit coupling is included). The red (dashed) line near the conduction band shows the pinning energy of the Fermi level for  $n$ -type doping. Adapted from Ref. [54].

There are some contradictory reported results by using different methods to determine the CBO at CZTS/CdS interface. Haight *et al.* used an indirect method to measure the valence band offset (VBO) under illumination by ultraviolet photoelectron spectroscopy (UPS) and obtaining the CBO determined from the VBO using bulk bandgap. [55] They found a ‘spike-like’ CBO for CZTSSe/CdS which is weakly

dependent on the S/Se ratio. The variation in the S/Se content mainly affected the VBO rather than CBO. A  $\Delta E_c$  of above 0.4 eV was found for all investigated CZTSSe compositions which were beyond the optimal value. In contrast, Bär *et al.* carried out a direct measurement of the actual surface bandgap using photoemission and inverse photoemission spectroscopy.[56] Their results presented a ‘cliff-like’ CBO of 0.33 eV for pure sulfide CZTS. Another study also indicated a ‘cliff-like’ CBO for CZTS/CdS investigated by X-ray photoelectron spectroscopy (XPS).[57] Both the indirect method by using core level together with XPS bulk valance band (VB) spectra and the direct method by analyzing XPS VB spectra at the interface gave a cliff-like behavior. In addition, first-principles calculations revealed that the band alignment changed from Type I for CZTSe to Type II for CZTS. The electron affinity of CdS is sitting right between CZTSe and CZTS.[54] Therefore, it is more reasonable to take CZTS/CdS as ‘cliff-like’ heterojunction based on most of the experimental and simulation results. The schematic bandgap diagram of conventional CZTS solar cells under zero-bias voltage condition is shown in Figure 2. 4. It can be deduced that the unperfected band alignment for CZTS might be one of the main reasons for the relatively larger  $V_{OC}$  deficit compared to CZTSSe.

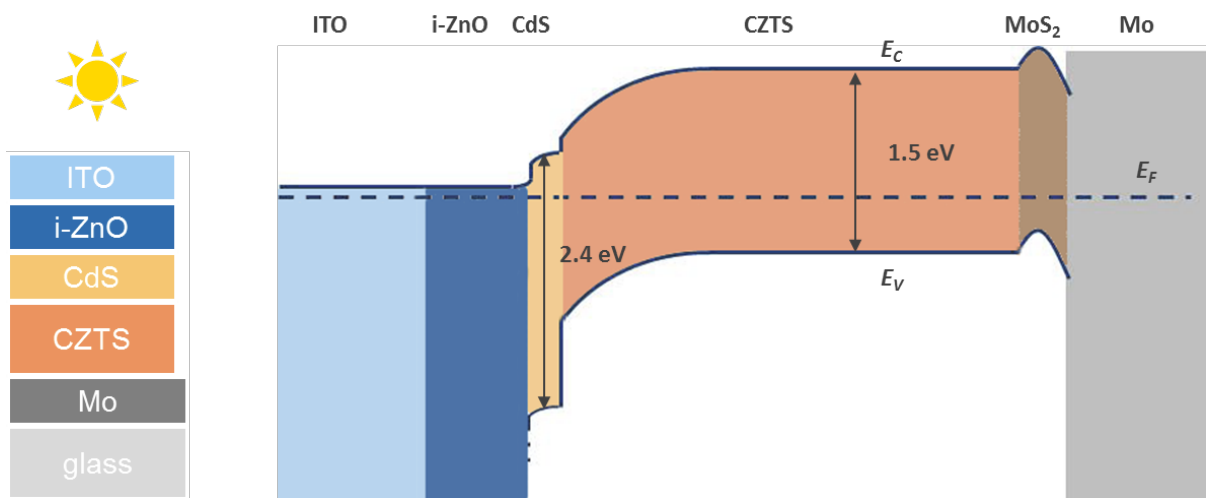


Figure 2. 4 Schematic bandgap diagram of CZTS solar cell under zero-bias voltage condition.

Table 2. 1 PV parameters of kesterite solar cells prepared with different buffer layers, with their conduction band offset (CBO), valence band offset (VBO), device parameters and deposition method, respectively.

Buffer layer	Dep. method	Absorber	CBO (eV)	VBO (eV)	$V_{oc}$ (V)	$J_{sc}$ (mA $\text{cm}^{-2}$ )	FF (%)	$\eta$ (%)	Ref
CdS	CBD	CZTSSe	–	–	0.513	35.2	69.8	12.6	[37]
ZnO	ALD	CZTSSe	$\pm 0.1$	-2.1	348	21	34	2.46	[41]
Zn(O,S)	CBD	CZTS	$0.92 \pm 0.1$	-0.98 $\pm 0.1$	76	0	0	0	[58]
Zn <sub>1-x</sub> Sn <sub>x</sub> O	ALD	CZTS	–	–	0.679	21.6	61.4	9	[43]
ZnS	CBD	CZTSSe	1.1	-1.3	690	0.1	0	0	[41]
Zn <sub>1-x</sub> Cd <sub>x</sub> S	SILAR	CZTS	$0.37 \pm 0.1$	-0.83 $\pm 0.1$	0.762	19.5	63	9.2	[59]
In <sub>2</sub> S <sub>3</sub>	CBD	CZTSSe	$0.15 \pm 0.1$	-0.75	0.424	32.3	0.55	7.6	[41]
In <sub>2</sub> S <sub>3</sub>	CBD	CZTS	0.11	-0.73	621	20	54.5	6.9	[60]
In <sub>2</sub> S <sub>3</sub> /CdS	CBD	CZTS	$0 - 0.1$	-1.0	0.708	21.6	60.1	9.2	[61]

Other factors might also affect the band alignment at the CZTS/CdS interface. The crystal structure and orientation at the CdS/CZTS interface were investigated and correlated to the resulting conduction band offset at the CZTS/CdS interface[62]. It was found that the CZTS/CdS showed a ‘cliff-like’ CBO in both cases of stannite and kesterite structure, independent of the heterojunction interface. There is another study on the influence of KCN etching before CdS deposition along with the interface band alignment investigation.[56] UPS and IPES measurements were performed at the KCN-etched CZTS/CdS interface. An enhanced surface bandgap was found for the

KCN-etched sample due to the modification of the surface composition. This provided a large barrier for the recombination, thus resulting in an improvement in  $V_{OC}$ .

The band alignment of alternative buffer layers such as  $\text{In}_2\text{S}_3$ [41],  $\text{Zn}(\text{O}, \text{S})$ [42],  $\text{Zn}_{1-x}\text{Cd}_x\text{S}$ [59],  $\text{Zn}_{1-x}\text{Sn}_x\text{O}$ [27, 43] has been reported on kesterite solar cells, with their measured CBO and VBO summarized in Table 2. 1. It shows that CZTSSe devices with binary compounds including  $\text{ZnO}$ ,  $\text{ZnS}$ , and  $\text{In}_2\text{S}_3$  as buffer layers do not yield as high efficiencies as compared to their  $\text{CdS}$  counterparts. For CZTSSe/ $\text{ZnS}$  interface, the ‘spike-like’ CBO of 1.1 eV was too large to allow the transportation of the photo generated current.[41] Although CZTSSe/ $\text{ZnO}$  had a proper CBO of 0.1 eV, its high series resistance and reduced band bending resulted in lower device performance.[41] A positive CBO has also been observed in CZTSSe/ $\text{In}_2\text{S}_3$  heterojunction, which resulted in an efficiency of 7.6 % for CZTSSe solar cells. [41] Similarly,  $\text{In}_2\text{S}_3$  was applied on CZTS absorber and lead to an efficiency of 6.9% due to a positive CBO of 0.11 eV at CZTS/ $\text{In}_2\text{S}_3$  interface. There are also good examples of ternary compound buffer layers being used in CZTS(e) solar cells. A remarkable improvement in open-circuit voltage has been shown in a 9.2% CZTS cell with  $\text{Zn}_{1-x}\text{Cd}_x\text{S}$  buffer layer. The CBO of the best performing CZTS/  $\text{Zn}_{1-x}\text{Cd}_x\text{S}$  device was estimated by XPS and proven to be ‘spike-like’, therefore mitigating the interface recombination in the heterojunction. A 9.0% efficient CZTS solar cell with an ALD  $\text{Zn}_{0.72}\text{Sn}_{0.28}\text{O}$  buffer layer was reported, where the optimal band alignment was adjusted by varying the substrate temperature.[43]

#### **2.1.1.2 Absorber/window**

Another band alignment management that should be taken into account is the conduction band offset between the absorber and window layer. The most commonly used window layer in chalcogenide solar cells is intrinsic  $\text{ZnO}$  (i- $\text{ZnO}$ ). The main function of i- $\text{ZnO}$  is to prevent the shunting path by blocking shunt pathways such as pinholes, cracks, and voids. The management of the absorber/window band alignment

is essential as it has been reported that the CBO of the window layer/absorber layer plays a key role in reducing the carrier recombination at the interface, thereby essentially reducing the  $V_{OC}$  deficit in chalcogenide solar cells.

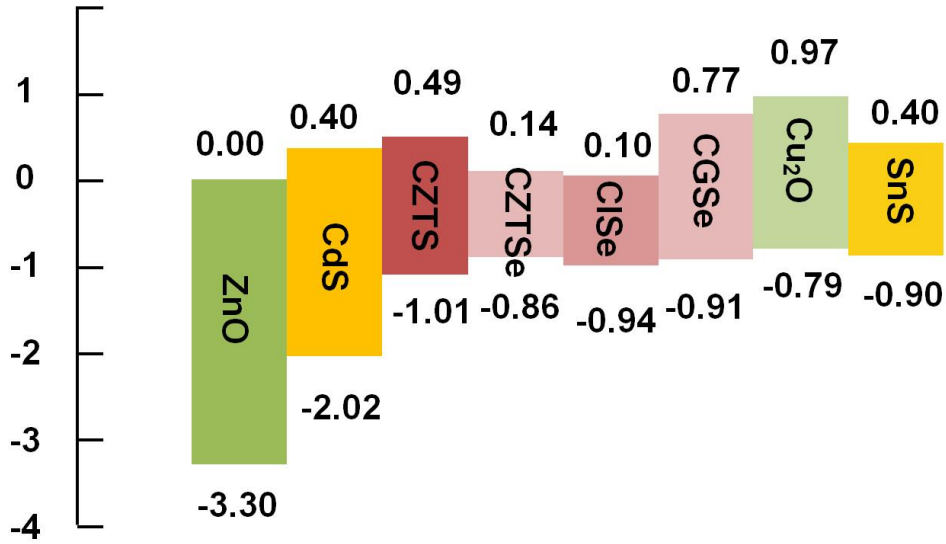


Figure 2. 5 Band alignments of ZnO, CdS, Cu<sub>2</sub>ZnSnS<sub>4</sub>, Cu<sub>2</sub>ZnSnSe<sub>4</sub>, CuInSe<sub>2</sub>, CuGaSe<sub>2</sub>, Cu<sub>2</sub>O, and SnS, where the conduction band minimum of ZnO is set to be 0.0 eV. Reconstructed from Ref. [63].

Murata *et al.* investigated the influence of the CBO between the absorber and transparent conductive oxide layer (TCO) on the thin film device performance by means of device simulation.[63] The optimized  $\Delta E_C$  at the buffer/TCO interface for high device performance was proposed to range from -0.2 to 0.6 eV and -0.4 to 0.6 eV for buffer carrier densities of  $1 \times 10^{13}$  and  $1 \times 10^{18} \text{ cm}^{-3}$ , respectively. Therefore, a too-large positive CBO would decrease the device performance due to the blocking of the photo-generated carriers at the buffer/TCO interface. In contrast, a too-small negative CBO would also deteriorate the cell efficiency as a result of decreased  $FF$  owing to the two diode characteristics. Experimental results in high-performance CIGS solar cells also demonstrated the importance of window layer combinations to reduce the open-circuit voltage deficit. Chantana *et al.* investigated the influence of different structures of CIGSSe solar cells with similar absorber quality on the interface

recombination. It showed that optimal  $\Delta E_C$  at both absorber/buffer and absorber/TCO interfaces contributed to the decreased interface recombination and led to an improved  $V_{OC}$ . An efficiency of 20.4 % was achieved by using an optimized CIGSSe solar cell with a top layers structure of  $\text{Cd}_{0.75}\text{Zn}_{0.25}\text{S}/\text{Zn}_{0.8}\text{Mg}_{0.2}/\text{Zn}_{0.9}\text{Mg}_{0.1}\text{O}:\text{Al}$ .

However, reports on the band alignment between the CZTS absorber and window layer have rarely been reported. The band alignments between ZnO and some of the materials reported in chalcogenide technology are depicted in Figure 2. 5. Note that the conduction band minimum ( $E_C$ ) of ZnO was set to be 0 eV and the numbers represented the energy difference of the  $E_C$  for other materials with respect to ZnO. It can be seen that both CZTS/CdS and CdS/ZnO interfaces exhibit cliff CBO behavior, which induces the recombination in both interfaces. Therefore, it is essential to explore the proper combination of buffer/window layers and investigate its influence on CZTS device performance.

### 2.1.2 Alkaline doping

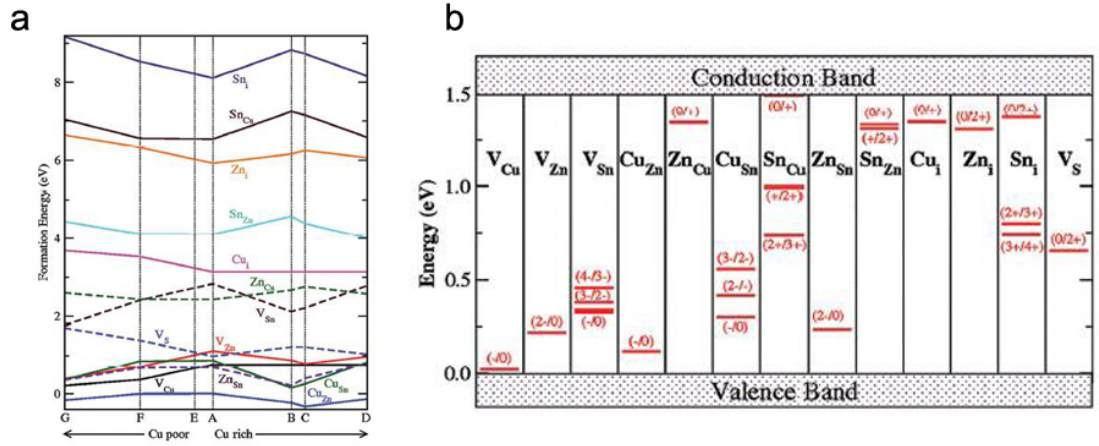


Figure 2. 6 a) Formation energies of isolated intrinsic defects in  $\text{Cu}_2\text{ZnSnS}_4$  as a function of chemical potential (Cu-rich and Cu-poor conditions) and b) transition-energy levels of the intrinsic defects in the electronic bandgap of  $\text{Cu}_2\text{ZnSnS}_4$ . Reconstructed from Ref. [64].

Another strategy to deal with the relative low  $V_{OC}$  is defect engineering in the bulk absorber and at the surface. Kesterite-based chalcogenide solar cell suffers from a large  $V_{OC}$  deficit mainly because of a large number of defects in the lattice and more defect-induced energy levels in the electronic bandgap. Theoretical calculations of defect formation energies predicted the feasible formation of different types of defects in the CZTS lattice.[64] Defects such as  $V_{Cu}$ ,  $V_{Zn}$ ,  $Cu_{Zn}$ ,  $Zn_{Cu}$ ,  $Cu_{Sn}$ , have relatively low formation energy and thus are likely to form in the CZTS lattice, as shown in Figure 2. 6a. Due to the similar ionic radii of  $Cu^+$  and  $Zn^+$ , the  $[Cu_{Zn}^+, Zn_{Cu}]$  defect complex may form spontaneously and remains the dominant defects in CZTS. The presence of those defects leads to a large density of defect-induced energy levels within the bandgap, thus producing the band tailing in kesterite. Additionally, a random distribution of those charged defects might trigger local potential fluctuations, resulting in a spatial fluctuation in the bandgap as shown in Figure 2. 7b. Such band tailing and bandgap fluctuation limit the possible light-induced separation between quasi-Fermi levels, thus substantially limit the  $V_{OC}$  as well as the current density due to the increased probability of carrier recombination.[65] The defects mentioned above can be compensated through well-designed extrinsic doping. One of the most effective extrinsic doping is to introduce isoelectronic elements from the same family as Cu, Zn and Sn, which including Ag, Cd as well as Ge. However, this kind of doping is not within the scope of this thesis. Another extrinsic doping approach is by alkaline doping such as Li, Na, K, Rb, and Cs. The effects of alkaline doping on the absorber and surface of chalcogenide solar cells will be discussed in the following part.



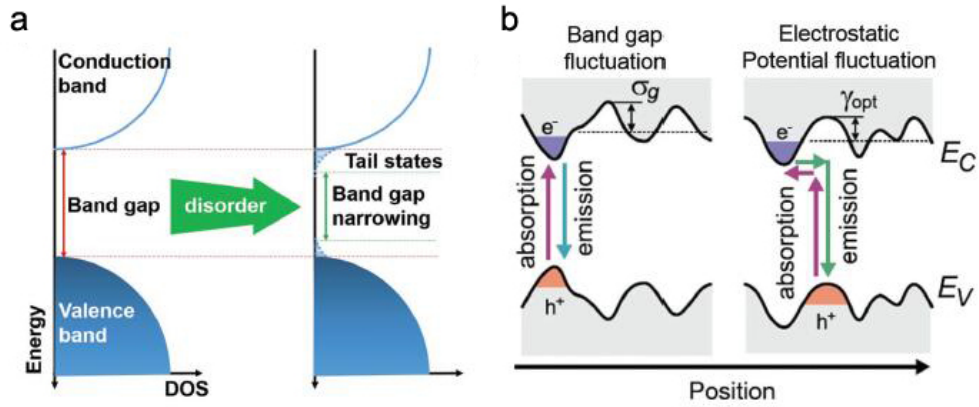


Figure 2. 7 a) Schematic of the total density of states (DOS) plot in conventional semiconductor materials such as Si/GaAs and modified DOS plot in disordered semiconductors (by heavy doping or introduction of a high density of lattice defects) and b) bandgap (left)/electrostatic potential (right) fluctuation in the electronic structures of CIGS and CZTS materials. Adapted from Ref. [65].

#### 2.1.2.1 Alkaline doping of the absorber

The effects of alkaline doping in kesterite absorber have been shown to improve the crystalline quality, increase the grain size, enhance the carrier concentration, etc. Na has been employed in kesterite and was believed to benefit for the grain growth as well as carrier concentration improvement, although the mechanism behind the observed improvements it is still unclear. There are two possible explanations for the impact of Na on the carrier concentration in CZTS. The first one proposes that Na is positioned in Cu-sites by replacing Zn in the  $Zn_{Cu}$  defects, thus resulting in a decreased concentration of shallow donors and consequently the *p*-type conductivity. Another mechanism is Na diffusing towards grain boundaries during the cooling process (sulfurization or selenization process), leaving behind an increased concentration of Cu vacancies, and thereby boosting the carrier concentration. Although remarkable results were reported by several research groups employing alkaline doping to improve the performance of CZTS solar cells, no consensus has been reached within the kesterite

community on which alkaline dopant is the best for optimal device performance.[66-68]

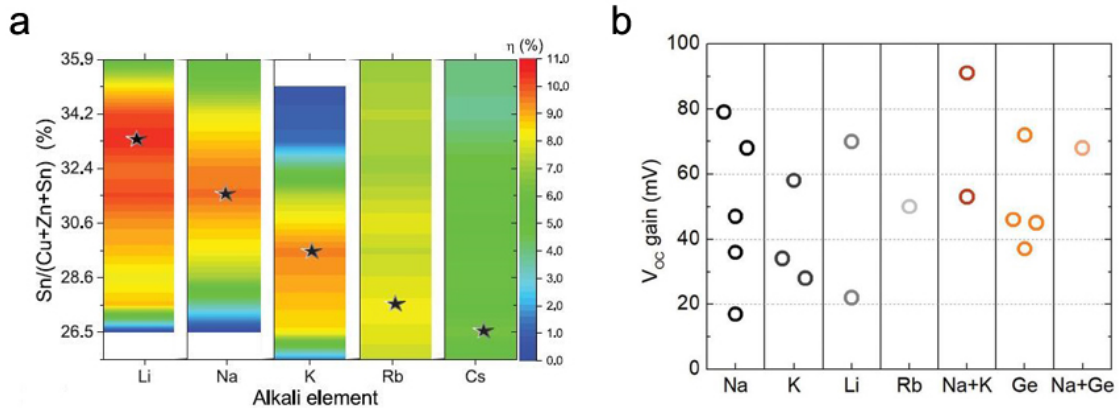


Figure 2. 8 a) Optimal composition for the different alkali elements in terms of conversion efficiency reported by Haass *et al.* Adapt from [69] b)  $V_{OC}$  gain for the most relevant extrinsic dopants published for kesterite. Adapted from Ref. [17].

Recently, Haass *et al.* performed a systematic investigation on the effects of alkaline doping in kesterite solar cells and revealed a complex interplay between different alkaline and Sn.[68] As shown in Figure 2. 8a, the optimized efficiency with different alkaline doping was dependent on the Sn content in the layer, indicating a strong correlation between Sn and alkali elements. It can be seen from Figure 2. 8a that lighter alkaline elements require a higher Sn content in order to achieve the highest conversion efficiency. Overall, devices doped with lighter alkaline elements such as Li and Na got very high efficiencies. With regards to the device performance, the main improvements could be attributed to an enhanced  $V_{OC}$ . The  $V_{OC}$  gain for the most relevant extrinsic dopants published for kesterite solar cells is summarized in Figure 2. 8b. The explanation of those beneficial effects differs among the research community. Besides the reason mentioned such as improved crystalline quality, improved grain size, modified carrier concentration, the effects of interfaces and grain boundaries passivation should also be considered.

### **2.1.2.2 Alkaline doping at the surface**

Alkaline doping (e.g. Na, K, and Rb) can suppress interface recombination by modifying the surface and grain boundary chemistry in chalcogenide and kesterite solar cells.[70-73] Specifically, an alkaline post-deposition treatment (PDT) in CIGS solar cells is shown to affect the electronic structure of the heterojunction interface via an enlarged surface bandgap or downshift of the band edges. For example, a NaF PDT induces a widening bandgap at the surface of CIGSe in high performing CIGSe solar cells. This surface bandgap becomes even larger if the NaF PDT is replaced by a NaF/KF PDT, which could be attributed to the formation of Cu- and Ga-depleted layers near the CIGSe surface.[74] In addition, a RbF post-deposition treatment on CIGSe/CdS heterojunction is found to cause an additional downward band bending which reduced interface recombination, leading to a pronounced improvement in the device performance.[75] An improved absorber/buffer interface of CZTS solar cells has also been reported through alkali metal doping such as Na, Li, and K.[67, 76] A recent study shows that lithium doping in CZTSSe solar cells enhances the  $V_{OC}$  and efficiency, with LiOH added to the CZTS precursor solution[77]. In this case, the bandgap of CZTSSe is tunable and band alignment at the CdS/CZTS interface behaves ‘spike-like’ with Li incorporation.

### **2.1.3 Interface defects passivation**

#### **2.1.3.1 Front interface**

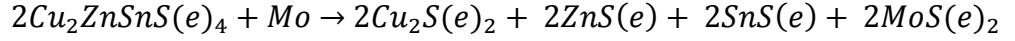
Defect passivation is another key point to improve the interface properties. In the silicon-dielectric interface, a large number of surface states exist due to the termination of periodic crystallographic structure, acting as effective recombination traps for minority carriers. Atomic layer deposition of  $Al_2O_3$  is now routinely applied as surface passivation film in high-performance silicon solar cells.[78] Similarly, passivation of

the CdS/CZTS(e) heterojunction has also been studied to reduce defect densities at the interface.[47, 79] CZTSe solar cell coated with ALD TiO<sub>2</sub> has been reported to improve the CdS/CZTSe interface quality[80]. TiO<sub>2</sub> films with a thickness in the 1–5 nm range are sufficient to reduce the interface recombination and support tunneling of charge carriers as well. With the introduction of ALD-Al<sub>2</sub>O<sub>3</sub> before the CdS buffer, Lee *et al.* demonstrated effective surface passivation as well as improved short-circuit current density  $J_{SC}$  and  $FF$ , leading to an enhancement of 15% relative in the efficiency for CZTSSe devices.[81] The applicability of ALD-Al<sub>2</sub>O<sub>3</sub> was also extended to CZTS solar cells with CdS buffer in the work of Park *et al.*, where hydrogen was proposed to account for the passivation effect at the surface.[82]

Annealing in air, air exposure, or an oxygen plasma treatment also works as an effective approach to reduce the defect density at the surface of CZTS(Se).[83-85] The introduction of oxygen (O) from the ambient atmosphere into Cu<sub>2</sub>ZnSnSe<sub>4</sub> is believed to form Cu<sub>2</sub>ZnSn(Se,O)<sub>4</sub>, which both lowers the valance band maximum as well as widening the bandgap, leading to effective minority carrier suppression at the grain boundary and surface.[84] It is interesting to note that surface sodium is usually correlated with the presence of oxygen in CZTS which combined play a key role in the suppression of the  $V_{OC}$  deficit. [86, 87]

### 2.1.3.2 Back interface

The molybdenum (Mo) back contact is deposited on the substrate as the back electrode in CZTS solar cells. A Mo rear provides a good ohmic contact, good adhesion and the formation of appropriate MoS<sub>2</sub> (MoSe<sub>2</sub>) which acts as a diffusion barrier layer [88, 89]. However, a thermodynamic analysis suggests that the Mo/CZTS(e) interface may not be as chemically stable as the Mo/CIGS interface[88]. The formation of MoS(e)<sub>2</sub> combined with the decomposition of CZTS are both present at the back contact during the annealing process, which can be presented by the following reaction.[88]



Equation 2. 3

The formation of MoS<sub>2</sub> (MoSe<sub>2</sub>) during sulfurization or selenization has a detrimental effect on CZTS solar cells if the thickness is not optimized, thereby affecting the  $V_{OC}$  and band alignment at the Mo/CZTS interface [90, 91]. There have been reports on the control of MoS<sub>2</sub> (MoSe<sub>2</sub>) formation by changing annealing time [88]. Another challenge at the Mo/CZTS interface is the formation of secondary phases such as Cu<sub>2</sub>S, ZnS, SnS which have deleterious effects on carrier transport to the electrode. To improve the back contact interface, several intermediate layers such as MoO<sub>x</sub>, ZnO, TiB<sub>2</sub>, TiN, Ag, carbon, have been investigated to optimize the device performance.[92-95] Another back contact interface management to reduce  $V_{OC}$  deficit is by applying high-work-function (HWF) back contact and imposing an internal electrical field to separate electrons and holes. Electrons then flow from the lower work function CZTSSe (5.2 eV) to higher work function MoO<sub>3</sub> (6.5 eV) or WO<sub>3</sub> (6.5 eV) to equilibrate the Fermi level. In this condition, holes are attracted to the back Mo contact and electrons are driven to the front CdS/CZTS junction.[96]

#### 2.1.4 Optical design

Although the  $V_{OC}$  deficit accounts for most of the gap between kesterite solar cells and the S-Q limit, it is obvious that photocurrent losses also need to be avoided for high-efficiency devices. The current loss can be attributed to several causes, generally categorized by whether the photons succeed or fail to reach the absorber layer. Photons that fail to reach the absorber layer are not able to produce photo-generated carriers that contribute to the  $J_{SC}$ . This includes the photons being reflected by the metal grids and absorption in the layers above the absorber layer, i.e. buffer/window/ TCO layers. For those photons reach the absorber, partly of them may be uncollected if they are not

absorbed within the drift/depletion region or penetrate the absorber without absorption. In the conventional structure of kesterite solar cells, CdS/ZnO/AZO(ITO) layers are usually applied as the top layers. For CZTSSe solar cells, Winkler *et. al.* performed optical modeling to demonstrate the current loss by analyzing the EQE as a function of wavelength as shown in Figure 2. 9. It is clear that there is a considerable photocurrent loss due to the toper layer absorption at the low wavelength range.

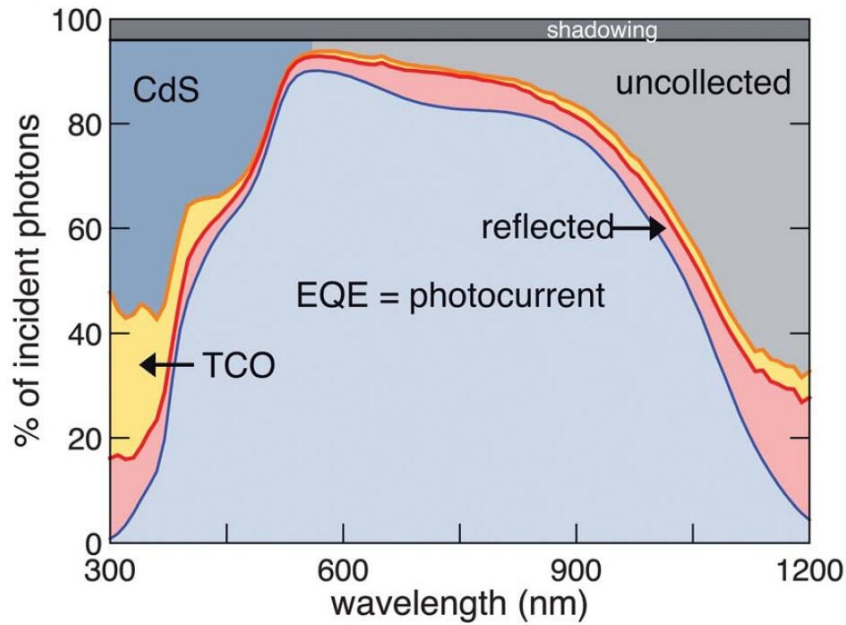


Figure 2. 9 Current loss in CZTSSe solar cells quantified by the analysis of wavelength-dependent EQE. The CZTSSe cell used for this analysis had a bandgap of 1.15 eV; losses are assigned by direct measurement of  $J_{sc}$  and EQE, reflectance, TCO absorption (from both ITO and ZnO), and contact geometry. CdS absorption and IR “uncollected” losses are then separated at the location of the CdS bandgap as shown. Adapted from Ref. [97].

A similar phenomenon can be observed on the current loss in CZTS solar cells from the EQE spectra in Figure 2. 10. A large optical loss can be attributed to the photon absorption in the CdS/ZnO/ITO stack. Optical design by choosing alternative buffer/window layer combinations could minimize the photoabsorption before

reaching the absorber layer. Previous research on CZTSSe solar cells suggests that the CdS buffer layer should be kept as thin as possible, while the total TCO layer-thickness should be in the range of about 50 nm in order to maximize the optical transmission.[97] Thickness tuning of the top layer stack will be a critical point in the optical design. Besides, alternative combinations of buffer/window layers with less absorption will be studied. Specifically, employing materials with a larger bandgap as the top layer is an effective strategy to enhance the spectral response in the UV range.

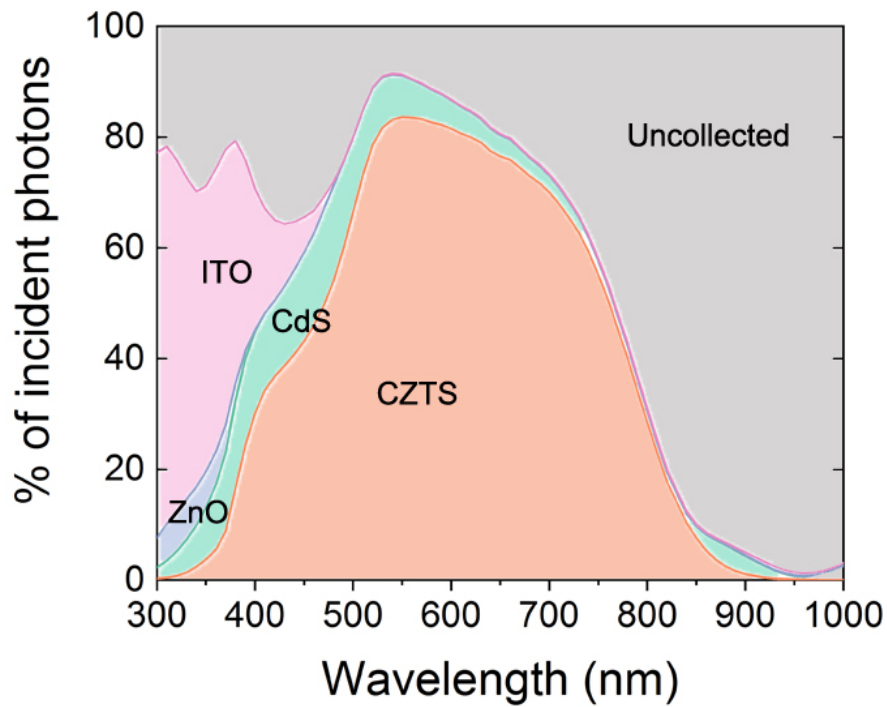


Figure 2. 10 Current loss in CZTS solar cells about analysis of EQE as a function of wavelength. The cell used for this analysis has a bandgap of 1.56 eV; losses are assigned by direct measurement of  $J_{sc}$  and EQE, CdS absorption, ITO and ZnO absorption. The remaining is denoted as “uncollected” losses as shown.

## 2.2 Atomic layer deposition

ALD originates from the 1970s which was referred to as “atomic layer epitaxy” at

first, the first deposited film was ZnS by Suntola and Antson for application in display devices.[98] After decades of development, ALD has become an important thin film deposition technique for a variety of applications. ALD is a vapor-phase deposition method to generate high-quality thin films such as metal oxides, sulfides, nitrides, and metals. ALD process is operated by self-limiting half-reactions, leading to atomic level control of thin-film growth. Benefiting from the sub-nanometer growth, ALD enables the fabrication of continuous, dense thin film without pinholes and defects.[99-102] This self-limiting virtue leads to conformal coatings on a variety of substrates with excellent surface coverage.

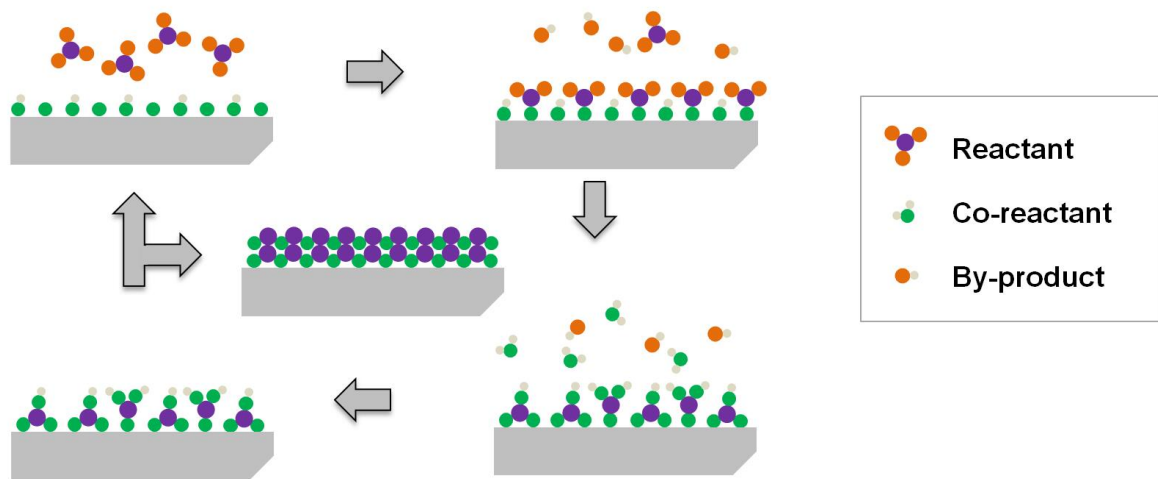


Figure 2. 11 Schematic of the sequential atomic layer deposition process.

A typical process of one cycle of ALD is illustrated in Figure 2. 11. The substrate is exposed to reactants and then purged with inert gas ( $N_2$  or Ar gas) to remove any excess reactants. Then the counter-reactants are introduced sequentially, followed by an inert gas purge to avoid chemical vapor deposition (CVD)-like reactions. This ALD cycle is repeated until reaching the desired thickness of the film. ALD typically only requires relatively low-temperature processes (100–350 °C), enabling the application on temperature-sensitive samples. Moreover, the sub-nanometer-scale control enables precise tuning of stoichiometry, density, and doping level; therefore regulate the



chemical, optical and electronic properties of film easily.

### **2.2.1 Precursors and co-reactants**

In an ALD process, there are reactants for the surface reaction which are called precursors. A key requirement is that an ALD precursor cannot react with itself to maintain a self-limiting surface reaction. Another point is it should be easily delivered into the ALD reactor. Therefore, the vapor pressure of the precursor must be higher than the reactor to be transferred to the ALD reactor. Moreover, precursors should be reactive enough to quickly react with the co-reactant in a certain temperature window without thermally decomposing. At the same time, the precursor must be stable at temperatures for as long as it will be on the substrate before the co-reactant is introduced into the reactor. If the precursor thermally decomposes at the process temperature, the film thickness will be non-uniform and greater than expected as the process becomes more CVD-like than purely ALD.

When the metal oxide is deposited by ALD, various materials can be used as the oxygen source. The most popular oxidizing co-reactant is water because it is cheap and easy to handle. But there will be times when water will not be the appropriate co-reactant. Some ALD oxide processes will require a stronger oxidizer. One of the options is ozone which can oxidize some ALD precursors inert to water. Another advanced option is using plasma  $O_2$  as an oxidizer, which contains high density of oxygen radicals or plasma species. These oxygen radicals are considerably more reactive than ozone and can broaden the process window significantly by enabling film depositions at much lower temperatures compared to  $H_2O$  and ozone.

Precursor choice is a critical consideration especially when ALD is used in solar cells. Most of the solar cells are sensitive to temperature thus the temperature window needs to be considered to enable positive effects. Other concerns include diffusion properties through narrow pores, and the compatibility of not only the reactants and co-reactants (such as ozone or an oxygen plasma) but also reaction by-products, such

as HCl formed from chloride precursors. Thermal ALD is mostly used when depositing thin film in solar cells due to its moderate reaction nature which leaves less damage to the surface. Although  $\text{H}_2\text{O}$ ,  $\text{H}_2\text{O}_2$ ,  $\text{O}_3$  as oxygen sources have been reported for thermal ALD,  $\text{H}_2\text{O}$  will be mainly adopted as co-reactant to avoid over oxidation of the surface.

### 2.2.2 Parameters for ALD development

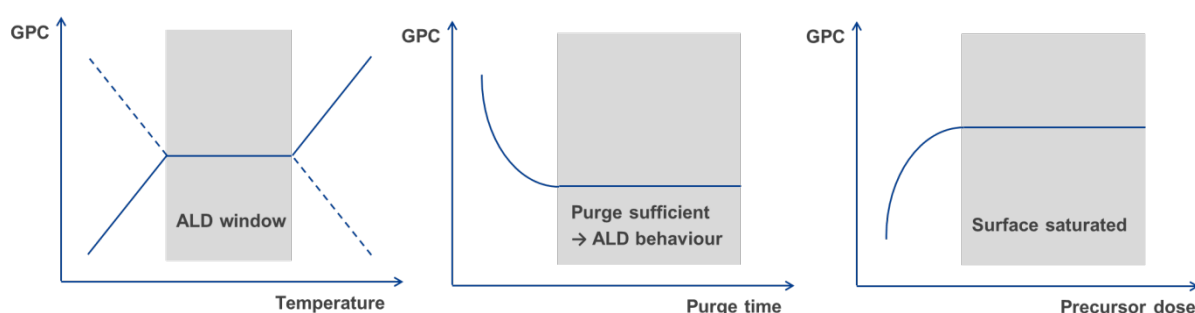


Figure 2. 12 Schematic illustration of the growth per cycle of ALD as a function of substrate temperature, purge time, and precursor dose.

In an ALD development process, there are several important parameters that need to be considered, including temperature, purge time, precursor dose. For thermal atomic layer deposition, the substrate temperature plays a critical role in the ALD process. There is a range referred to as the “ALD window” as depicted in Figure 2. 12, which graphically indicates the ALD process will be well-behaved with a well-defined deposition rate. The surface chemistry is significantly different above or below the ALD window, depending on the particular materials being investigated.

At temperatures below the ALD window, the observed deposition rates may be higher or lower than the anticipated ALD deposition rate. This phenomenon can be accounted to the fact that insufficient thermal energy is available to drive the precursor reaction at a lower temperature, leading to a slower growth rate. Another possibility is that rather than the monolayer of chemisorbed precursor, a thicker layer of precursor

chemical condenses on the substrate surface leading to a higher than expected observed deposition rate. At temperatures above the ALD window, the deposition rates observed can also be higher or lower than expected. In this case, the higher growth rate could be due to the thermal decomposition of the precursors on the substrate at high temperatures. Alternatively, thinner or no films could be deposited on the substrate resulting from precursor desorption from the substrate at higher temperatures.

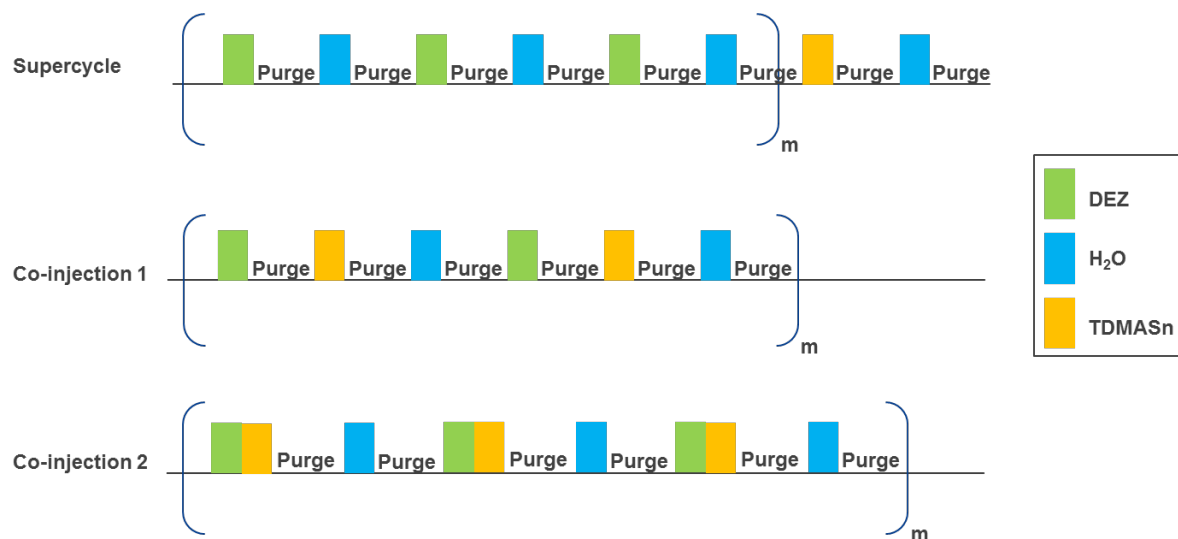


Figure 2. 13 Supercycle and Co-injection method ALD used in ternary materials deposition with different compositions.

The purge process is established to remove excess reactants or products by introducing inert gas into a reaction chamber. The time duration of purge needs to be optimized neither too short nor too long. Sufficient purge time is required to avoid CVD-like deposition, while purge time should be as short as possible to save time. Another key factor in ALD development is the precursor and reactant doses. Precursor and reactant doses ought to be kept as low as possible to save time and money, but as high as required for a saturated deposition.

ALD has the benefits to tailor the composition of thin-film when incorporating dopant sources into binary metal oxides. There are several methods to make doping efficient. The most applied process is called the supercycle method, which illustrated

in Figure 2. 13, using ZnSnO as an example. The supercycle method combining two normal ALD process in one supercycle, where  $m$  cycles represent the base material (ZnO in this case) followed by one cycle of X ( $X = \text{Sn, Mg, Al, B, etc.}$ ) doping material. The number of super cycles can be changed to tune the composition of thin-film and repeated until reaching the desired thickness. This approach is easy to implement, but it may produce a microstructure that may compromise the optical and electrical properties of thin film.

The co-injection method has also been used to adjust composition by changing the dose ratio of different precursors in one cycle rather than pulse ratio in the supercycle. One typical co-injection method is performed to change the dose volume of the precursors in each cycle, leading to different doping concentrations, illustrated as Co-injection 1 in Figure 2. 13. Another co-injection method is to co-dose both precursors into the reactor, and the dose time of the precursors is used to control the relative thin-film concentrations, as shown in Co-injection 2 in Figure 2. 13. Previous researches on ZnSnO[103-105] or ZnMgO[106-108] are usually based on supercycle method, while there are still many opportunities if using co-injection method as ternary oxide deposition technique.

### **2.2.3 Thermal and plasma-enhanced ALD**

A common scenario of ALD observed is nucleation which happens during the initial part of an ALD process that may last several cycles. The thin film during nucleation usually behaves a lower growth rate and density than expected. Nucleation happens due to the interaction between precursors with the substrate and is dependent upon the type of surface sites for self-limiting reactions. Nevertheless, nucleation can be controlled by surface treatment processes such as ultra-violet (UV) ozone. UV ozone treatment could clean the surface by removing organics and leave behind a hydroxyl-terminated surface that reacts more readily with many ALD precursors. Subsequent film growth after nucleation, however, is dependent upon processing

conditions such as precursor choice, temperature, substrate, etc.

Thermal ALD driven by thermal energy is the most commonly used ALD technique. However, high temperatures process in thermal ALD may be incompatible with certain substrates or specific applications such as solar cells. In these cases, plasma-assisted or plasma-enhanced ALD (PEALD) can be used. PEALD processes are driven by highly reactive plasma species with reduced thermal energy required for a surface reaction than thermal ALD. So that many reactions can happen under low temperatures and use less time for reactions. These properties could benefit large scale production with a lot economic advantages.

ALD is a vacuum-based process, which can also be extendible to large scale deposition as the reactant precursors are gas-phase molecules, independent of substrate geometry. While the issues of ALD used in large scale production are low deposition rate, precursor handling and uniformity control over large areas. By using recently advanced technology including spatial in-line ALD, high growth rates can be achieved by separating the gas precursors in space rather than in time, resulting in a high-throughput process for large-scale applications.[109-111] And by implementing batch ALD, large-area ALD, roll-to-roll ALD processes, much more potential of ALD could be discovered to solve the above issues.

## **2.3 ALD application on chalcogenide solar cells**

The application of ALD on thin-film solar cells has been primarily driven by the requirements for nanolayer deposition and interface modification. Here I categorize these applications into four areas, namely absorber layer, buffer layers, interface passivation layers, and transparent conductive oxide layer.[100-102]

### **2.3.1 Absorber layer**

The synthesis of absorber layers via ALD was mainly reported on chalcogenide

materials such as  $\text{Cu}_x\text{S}$ ,  $\text{Sb}_2\text{S}_3$ ,  $\text{CuSbS}_2$ ,  $\text{CuInS}_2$ , and  $\text{Cu}_2\text{ZnSnS}_4$ . [112-115] Thin films of  $p$ -type  $\text{Cu}_x\text{S}$  have been deposited by ALD on  $n$ -type  $\text{TiO}_2$  to form a good  $p$ - $n$  junction, exhibiting a  $J_{SC}$  of  $30 \mu\text{A}/\text{cm}^2$  and a  $V_{OC}$  of 200 mV under irradiation of  $2.8 \text{ kW}/\text{m}^2$ . The stoichiometry, crystalline phase and growth rate can be controlled through the process conditions, where  $\text{Cu}_{1.8}\text{S}$  formed with a bandgap of 1.75 eV and an absorption coefficient of  $2.3 \times 10^4 \text{ cm}^{-1}$  above a temperature of  $175^\circ\text{C}$ . [115, 116] Another binary  $\text{Sb}_2\text{S}_3$  absorber could be deposited by ALD with uniform thickness and low oxygen impurity. This high-quality absorber was implemented in a planar ALD- $\text{Sb}_2\text{S}_3$  solar cell with a structure of  $\text{Au}/\text{Poly-3-hexylthiophene}/\text{ALD-}\text{Sb}_2\text{S}_3/\text{bl-TiO}_2/\text{FTO}$  and demonstrated an impressive power conversion efficiency of 5.77%. [112] Compared to the  $\text{Sb}_2\text{S}_3$  deposited with conventional chemical bath deposition (CBD), ALD  $\text{Sb}_2\text{S}_3$  benefited from low oxygen impurities and uniform thickness control, which leads to less defect recombination and improved photovoltaic property.

ALD can also be applied for the growth of ternary chalcogenide copper antimony sulfide, an earth-abundant absorber for thin-film photovoltaics because of its suitable bandgap for solar energy conversion ( $\sim 1.5 \text{ eV}$ ) as well as large absorption coefficient ( $>10^4 \text{ cm}^{-1}$ ). [113] A low-temperature ALD route was proposed to deposit  $\text{CuSbS}_2$  thin films by carefully tuning the deposition parameter and taking advantage of the cation interdiffusion. Thin films with pure  $\text{CuSbS}_2$  phase may be fabricated through process control to acquire the suitable optoelectronic properties for photovoltaics.  $\text{CuInS}_2$  is another material studied that can be deposited by ALD and applied in a photovoltaic device. Nanu *et al.* reported a series of investigations on ALD  $\text{CuInS}_2$  deposition inside nanoporous  $\text{TiO}_2$  to form three dimensional solar cells. [117-119] By tuning the deposition temperature and copper to indium ratio in the ALD process as well as post-deposition annealing, optimized  $\text{CuInS}_2$  films with low defect density can be fabricated. [119] Together with ALD  $\text{In}_2\text{S}_3$  buffer and  $\text{Al}_2\text{O}_3$  passivation layer, an efficiency of 4% was achieved for a three-dimensional solar cell with a maximum

monochromatic incident photon-to-current conversion efficiency of 80%.[117] Besides the above-mentioned materials, quaternary chalcogenide  $\text{Cu}_2\text{ZnSnS}_4$  material can also be deposited by ALD through a trilayer strategy to achieve desired element ratios and chemical states.[114] A trilayer strategy was implemented by firstly depositing layers of binary sulfides and then mixing them by thermal annealing. However, the successful application of ALD CZTS absorber in the device still has not been reported until now.

### 2.3.2 Buffer layer

Table 2. 2 Photovoltaic performance summary of best-performing thin-film cells with different ALD buffer layers, TCO layers, and interface layers.

	Absorber	Eff (%)	$V_{OC}$ (V)	$J_{sc}$ (mA $\text{cm}^{-2}$ )	FF (%)	Area ( $\text{cm}^2$ )	Ref
<b>Buffer layer</b>							
ZnO	CIGSe	13.9	0.736	36.9	73.6	0.51	[120]
$\text{Zn}_{1-x}\text{Sn}_x\text{O}$	CIGSe	18.2	0.689	35.1	75.3	0.49	[121]
	CZTS	9.3	0.679	21.6	61.4	0.5	[122]
	CZTSSe	8.6	0.414	34.1	60.8	-	[27]
	$\text{Cu}_2\text{O}$	2.85	0.622	7.25	63.1	0.15	[123]
$\text{Zn}_{1-x}\text{Mg}_x\text{O}$	CIGSe	18.1	0.668	35.7	75.7	0.5	[124]
Zn(O,S)	CIGSe	19.8	0.715	36.5	75.8	0.522	[125]
	CdTe	8.0	0.593	21.0	64.2	-	[120]
	CZTS	4.6	0.482	17.2	55.5	-	[42]
<b>TCO layer</b>							
(Zn,Mg)O	CIGSSe	22.8	0.711	41.4	77.5	0.51	[126]
ZnTiO	CIGSe	20.8	0.726	37.7	76.2	0.23	[127]
<b>Interface layer</b>							
$\text{CdS}/\text{Al}_2\text{O}_3$	CZTS	11.5	0.515	32.1	69.2	-	[81]

CIGS and CZTS solar cells are the most successful cases by using different kinds of ALD materials as buffer layers. In the traditional structure of CIGS and CZTS solar cells, the CdS buffer layer deposited by chemical bath deposition is the commonly used material as its stable property and simple processing, which has enabled many high-performed CIGS and CZTS solar cells. However, the lower bandgap of CdS ( $E_g = 2.4\sim 2.5\text{eV}$ ) prevents the absorption of incident sunlight in the 350~550 nm part, which means more optical losses and lowers the current generation. Especially when using on CZTS absorber, the ‘cliff-like’ band offset forms at the heterojunction where the conduction band minimum of the CdS is lower than that of CZTS, therefore enhances interface recombination at heterojunction which reduces the  $V_{OC}$ . Alongside the environmental concern related to the presence of toxic Cd, there is the necessity to develop alternative buffer layers with environmentally friendly material. From the manufacturing perspective, it is preferable to develop a vacuum-based process to replace the current wet process to match with other vacuum processes. Therefore, the vacuum-based technique including ALD is compatible to deposit a variety of buffer layers on different thin-film absorbers.

ALD, in particular, is beneficial to deposit buffer layer accounting for the ability to control the thickness and composition of the thin film due to its layer-by-layer growth kinetics. Precise control of the composition of the buffer enables the deposition of different materials with tunable structure, optical and electrical properties. Therefore, ALD studies are capable of providing fundamental insight into how alternative buffer materials affect device performance. There has been a variety of research on ALD buffer layers such as  $\text{In}_2\text{S}_3$ [41],  $\text{Zn}(\text{O},\text{S})$ [42],  $\text{Zn}_{1-x}\text{Cd}_x\text{S}$ [59],  $\text{Zn}_{1-x}\text{Sn}_x\text{O}$ [27, 43],  $\text{Zn}_{1-x}\text{Mg}_x\text{O}$  which have been investigated on thin-film solar cells. A photovoltaic performance summary of best-performing thin-film cells with different ALD buffer layers is shown in Table 2. 2. Zinc containing buffer layers deposited by ALD is the most widely investigated buffer utilized in thin-film devices, with the first pure ZnO applied in CIGS by Chaisitsak *et. al.*[128] They found that the temperature of ALD



deposition and pre-treatments was critical to achieving high performing cells, demonstrating the highest efficiency of 13.9%.[120] However, further performance improvement of CIGS cells with ZnO buffer was hampered by the poor band alignment of the heterojunction and interface recombination, yet need to be replaced by other suitable buffers.[129, 130]

### 2.3.2.1 ZnSnO

Ternary zinc-containing oxides could benefit due to its tunable optical and electrical properties, among which  $\text{Zn}_{1-x}\text{Sn}_x\text{O}$  is one of the most investigated buffers in thin-film solar cells. The key feature of the ALD  $\text{Zn}_{1-x}\text{Sn}_x\text{O}$  buffer layer was that the composition tuning of  $\text{Zn}_{1-x}\text{Sn}_x\text{O}$  can be easily achieved to find the suitable band alignment with the absorber as well as enlarged bandgap to minimize the optical loss. Depending on the variation of the absorber layer, the optimized composition of  $\text{Zn}_{1-x}\text{Sn}_x\text{O}$  changes slightly to give the best performing devices.

Previous work on ALD  $\text{Zn}_{1-x}\text{Sn}_x\text{O}$  as a buffer layer in CIGS solar cells has been done systematically by J. Lindahl and co-workers.[103, 104, 121, 131] A record efficiency of 18.2% was achieved in ALD- $\text{Zn}_{1-x}\text{Sn}_x\text{O}$  /CIGS solar cell with CIGS deposited by an inline single-stage process, which is comparable to that with CdS buffer layer.[121] Generally, diethylzinc (DEZ) and tetrakis (dimethylamino) tin (TDMASn) are manipulated as ZnO and SnO precursors and  $\text{H}_2\text{O}$  as co-reactant in the deposition of ternary  $\text{Zn}_{1-x}\text{Sn}_x\text{O}$ . The bandgap and CBO can be tailored by different compositions of  $\text{Zn}_{1-x}\text{Sn}_x\text{O}$  which is controlled by tuning the relative amount of tin or zinc precursor pulses. It shows that the as-deposited ALD  $\text{Zn}_{1-x}\text{Sn}_x\text{O}$  is amorphous, therefore it benefits the buffer/CIGS interface by reducing the number of recombination centers at the grain boundaries. The optimized Sn/(Sn + Zn) ratio was 0.40 at a deposition temperature of 120 °C, with thickness maintained at  $13 \pm 5$  nm. A higher  $J_{sc}$  was obtained for the  $\text{Zn}_{1-x}\text{Sn}_x\text{O}$ /CIGS solar cell due to the higher mobility gap of  $\text{Zn}_{1-x}\text{Sn}_x\text{O}$  compared with CdS, resulting in a higher EQE response in the

UV-blue region.

The application of ZnSnO (ZTO) buffer layers has also been extended to kesterite CZTS solar cells by Platzer-Björkman *et al.*[43, 132] Pulse ratio changes enable tuning of the conduction band position at different temperatures. The best performance device with the highest  $V_{OC}$  was obtained by ZTO deposited at the temperature of 145°C, while the best  $FF$  was found at 165°C. It is noticeable that part of the performance improvement comes from the thermal experience during the ALD process. They fabricated a 9.0% efficient CZTS solar cell with an ALD  $Zn_{0.72}Sn_{0.28}O$  buffer layer at 145 °C, where the optimized band alignment was adjusted by varying substrate temperature. Another noticeable research result is the CZTSSe/ZnSnO solar cell study by Li and co-workers, getting an 8.6% efficiency on CZTSSe solar cells with improved band alignment at CZTSSe/ZTO heterojunction by optimizing Sn-content of ZTO to be 0.167.[27] A thickness of around 50 nm was used for the best performance solar cell. A different optimal Sn-content of ZnSnO was found compared with the application on pure sulfide CZTS solar cells to obtain a favorable band alignment at the heterojunction since CZTS has a higher conduction band minimum than CZTSSe.

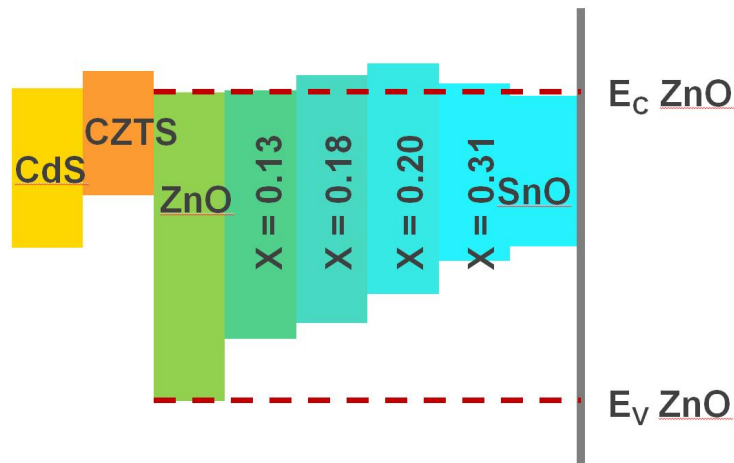


Figure 2. 14 Band alignment for ZTO/CZTSSe heterojunction with different Sn/(Zn+Sn) ratio.

Note that ultra-thin ZnSnO has also been implemented on  $Cu_2O$  to form  $p-n$

junction and resulted in a 2.85% solar cell. This efficiency was achieved due to the improved interface quality by controlling the chemical state of Cu at the Cu<sub>2</sub>O surface through changing the deposition temperature of ALD ZTO.[123] The band alignment for CZTS/ZnSnO junction and  $E_g$  extracted from the Tauc plot analysis and spectroscopic ellipsometry with different Sn/(Sn+Zn) ratios are shown in Figure 2. 14.[54, 105]

### 2.3.2.2 ZnMgO

Edoff and co-workers also introduced Mg into ternary zinc-containing oxides, making a Zn<sub>1-x</sub>Mg<sub>x</sub>O buffer layer as another good alternative for CdS in CIGS solar cells.[124, 133-136] By controlling the magnesium content in Zn<sub>1-x</sub>Mg<sub>x</sub>O, the bandgap of Zn<sub>1-x</sub>Mg<sub>x</sub>O buffer layers can be changed from 3.3 eV to 3.8 eV with increased magnesium added into ZnO. The increased bandgap was due to the increase in the conduction band level. The optimal Mg/(Zn+Mg) ratio was found to be 0.1-0.2 with bandgap values of 3.5-3.7 eV, while temperature needs to be controlled in the range of 105-135 °C. A champion efficiency of 18.1 % was obtained in CIGS solar cells by using an above 100 nm ALD Zn<sub>0.8</sub>Mg<sub>0.2</sub>O buffer layer deposited at 120 °C.[124] Another interesting phenomenon was the light soaking effect of ZnMgO buffer in CIGS solar cells.[107, 135] It was found that the efficiency accompanied by fill factor and open circuit voltage increased with light soaking. This increase in  $V_{OC}$  is attributed to hydrogen decomposed from the hydroxyl bond of ZnMgO induced by photoirradiation. It should contribute as a donor and defect passivation surfactant, thus enabling increased fill factor and  $V_{OC}$  in a device.

### 2.3.2.3 Zn(O, S)

Another notable achievement of ALD buffer in a thin-film solar cell is the use of ZnO<sub>1-x</sub>S<sub>x</sub>[120, 124, 125]. DEZ, hydrogen sulfide (H<sub>2</sub>S) and water vapor (H<sub>2</sub>O) were

usually used as ALD precursors to deposit  $\text{ZnO}_{1-x}\text{S}_x$  and the composition was tuned by changing the  $\text{H}_2\text{S}/(\text{H}_2\text{O}+\text{H}_2\text{S})$  pulse ratio. Platzer-Björkman *et al.* have demonstrated that the valance band edge increased strongly when small S content added into pure ZnO thereby led to narrowed bandgap for  $x < 0.5$ . [137] Whereas the conduction band edge increased strongly when  $x > 0.5$ , which caused larger CBO for CIGS/Zn(O,S) interface and blocking the photocurrent transportation. [138] Different from ternary ZnSnO and ZnMgO compounds, Zn(O,S) deposited by ALD have a sulfur gradient in the films which could be attributed to the longer incubation time for ZnO growth compared to ZnS growth. [138] It is interesting to note that CIGS/Zn(O,S) devices also have a light soaking effects similar to CIGS/ZnMgO cells. With a heat-light soaking post-treatment, Taizo Kobayashi and his co-workers demonstrated an ALD-Zn(O,S)/CIGSSe solar cell with a champion efficiency of 19.78%, which is comparable to those with a CdS buffer layer. The higher device performance for ALD-Zn(O,S)/CIGSSe cell mostly came from the higher  $V_{OC}$  of 0.718 V due to the shallower defect position after treatment, therefore less interface recombination as compared to CBD ZnS(O,OH) buffer layers.

Platzer-Björkman and co-workers also extend the application of Zn(O,S) buffer layer on CZTS to investigate its effect on the device performance. [42] They studied the conduction band alignment at the heterojunction interface by evaluating several Zn(O,S) buffer layers with different S/(O+S) ratios. The best performing CZTS devices had an efficiency of 4.6 % with a Zn(O,S) buffer layer, although lower than its CdS reference of 7.3 %. The main loss of the CZTS/Zn(O,S) device came from the defect recombination which deterred the improvement of device performance. There are also other studies working on the Zn(O,S) buffer layer in CZTSSe solar cells, while lower efficiency compared to the reference still happened in those cases. [139, 140]

Unlike the plenty of studies on the utilization of ALD-Zn(O,S) in CIGS devices, only a few studies of its application in CdTe solar cells have been reported. Perrenoud *et al.* have reported a Zn(O,S)/CdTe device with an 8% efficiency by optimizing the

$\text{ZnO}_{1-x}\text{S}_x$  composition.[120] They showed that the optimized performance of the device was achieved for  $\text{ZnO}_{0.48}\text{S}_{0.52}$ . The relatively favorable CBO at the interface could explain the better performance obtained in the CdTe device. However, the motivation for investigation of Cd-free buffer for CdTe cells was not urgent if considering the limited performance improvement and the cost decrease by using the ALD technique, thus limited studies have been done in this area.

### 2.3.3 Window layer

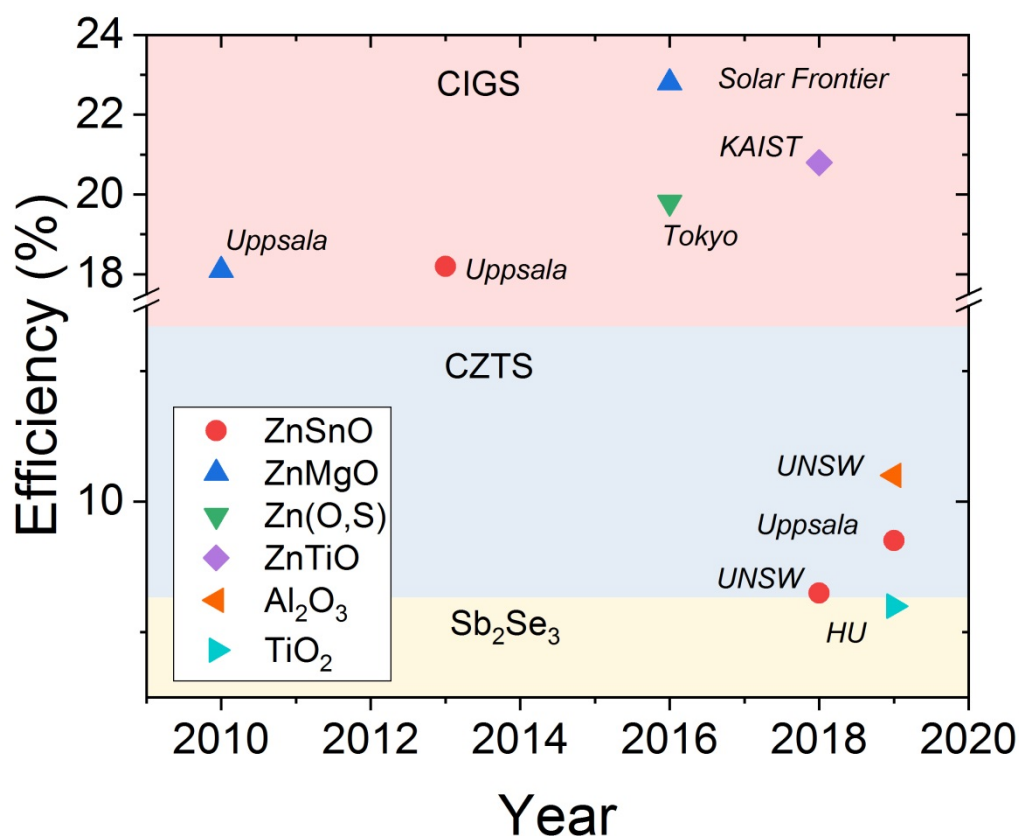


Figure 2. 15 Noticeable record efficiency for chalcogenide solar cells with different ALD materials.

Sputtered intrinsic ZnO layer is commonly used in CZTS/CIGS solar cells as a window layer to increase the shunt resistance by blocking shunt pathways such as

pinholes, cracks, and voids. As mentioned above, Mg-doped ZnO has a wider bandgap than intrinsic ZnO (i-ZnO), which gives us the chance to replace the window layer i-ZnO by ZnMgO. Chantana and his group recently demonstrated a 19.6 % efficient CIGSSe solar cell with  $\text{Zn}_{1-x}\text{Mg}_x\text{O}$  window layer together with (Cd,Zn)S buffer layer.[141] They deposited  $\text{Zn}_{1-x}\text{Mg}_x\text{O}$  by co-sputtering, where the optimal  $x$  value was found to be 0.211. Therefore, the gain in  $J_{sc}$  up to about 5.7% was obtained and efficiency of up to around 5.4% relatively comparing with the traditional CdS/ZnO counterpart. However, sputtering of the window layer might cause damage to the interface; therefore it could be replaced by moderate methods such as ALD or MOCVD.

Solar Frontier used ALD ZnMgO to replace i-ZnO as a second buffer layer in their high-efficient CIGS solar cells.[142] The device with the highest efficiency was achieved by using ZnMgO as a second buffer layer (or window layer) on top of the Zn(O,S,OH) buffer layer, yielding an efficiency of 22.8 %, even higher than the devices with a Cd containing buffer layer.[126] These achievements show the great potential of the ALD buffer layer to enhance the CIGS solar cell's performance.

Recently, ALD-ZnTiO was also prepared as a window layer for the application in CIGS solar cells.[143] A series of  $\text{Zn}_x\text{Ti}_y\text{O}$  layers with different Ti content was deposited by tuning the pulse ratio of Ti and Zn. The ZnTiO films were featured by amorphous when deposited at a low temperature of 100°C. The addition of Ti into ZnO makes the conduction band shift to a higher level, thus expand the bandgap of the material. By optimizing the composition of ZnTiO layer together with thinner CdS buffer layer, a champion efficiency of 20.8% was achieved. This enhancement of the PV performance mainly originated from the gain in  $J_{sc}$  due to the lower parasitic absorption of thinner CdS as well as the wider bandgap of ZnTiO. ALD processed layers have been used for various functional layers in chalcogenide solar cells and noticeable record efficiency for chalcogenide solar cells with different ALD materials has been achieved as shown in Figure 2. 15.

### 2.3.4 Interface modification layer

ALD  $\text{Al}_2\text{O}_3$  has emerged in the PV field for application as a surface passivation layer in silicon solar cells. Borrowing from the success in silicon solar cell, ALD  $\text{Al}_2\text{O}_3$  has been also implemented in thin-film devices including CdTe, CIGS and CZTS. For the application on CdTe cells, ALD  $\text{Al}_2\text{O}_3$  was incorporated into the device either between  $\text{Cu}_x\text{Te}$  and Au contact or between CdS buffer and TCO contact.[144, 145]  $\text{Al}_2\text{O}_3$  was applied as a surface modification layer on  $\text{Cu}_x\text{Te}$  by its rectification and tunneling function, thus improving the  $FF$  of the device.[144] The same function of  $\text{Al}_2\text{O}_3$  was also found when deposited on the TCO contact. ALD  $\text{Al}_2\text{O}_3$  formed a uniform and conformal coverage over the substrate, thereby reducing the leakage current and enhancing the  $FF$  effectively.

Yun Seog Lee and his group have published their study on atomic layer deposition  $\text{Al}_2\text{O}_3$  by protecting two interfaces in solution-processed CZTS devices.[81] In terms of heterojunction interface passivation,  $\text{Al}_2\text{O}_3$  could be deposited sequentially after the CZTS absorber layer to passivate the bulk grain boundary and surface defects. [81] [79] Benefitting from the reduced recombination in the interface, the CZTSe/CdS junction quality was improved by preventing inter-diffusion of Cd and Cu at the top interface. Substantial improvement in  $V_{oc}$  and  $FF$  was observed by the application of the dielectric  $\text{Al}_2\text{O}_3$  layer at CZTSe/CdS interface. In this case, the deposited  $\text{Al}_2\text{O}_3$  may be partly etched by the  $\text{NH}_4\text{OH}$ -containing solutions in CBD process, leaving behind passivated near-surface, grain boundary and pinholes.[81]

$\text{Al}_2\text{O}_3$  layer deposited by ALD can also be applied after the CBD CdS to get sufficient coverage on CZTS or CIGS solar cells.[81, 146] Yun Seog Lee *et. al.* inserted a thin  $\text{Al}_2\text{O}_3$  layer between CdS and TCO to improve the efficiency of up to 5% by preventing damage to CdS during TCO sputtering process. Extremely thin  $\text{Al}_2\text{O}_3$  films of around 1 nm are sufficient to passivate the CdS defects while allowing current transport via tunneling at the same time.[81] The intrinsic ZnO also can be replaced by

$\text{Al}_2\text{O}_3$  as a window layer, working as a protection layer before sputtered TCO to reduce ion damage.

For interface modification of thin-film cells by ALD, current research can still be further pushed by additional treatment of surface before deposition or by using different precursors to investigate different interdiffusion properties to bulk materials. Even more stable or common benefits of  $\text{Al}_2\text{O}_3$  passivation layer need to be confirmed to expand for wider-scale applications. Also, the theory behind experimental results should be studied towards an easily controlled passivation process.



## Chapter 3 Experiments

In this chapter, I describe the experimental techniques used in this work to deposit various functional layers and methods used to characterize the thin films and photovoltaic devices. The chapter starts with a detailed description of the standard process of CZTS solar cells. Subsequently, the ALD technique is described in detail as this is the main technique used in this thesis to grow the functional thin films. The characterization section is divided into three parts: *in situ* diagnosis techniques in the ALD system, *ex situ* material characterization and device measurement. The *in situ* measurements allow for evaluating the basic properties of the deposited films, thus providing precise control of the growth of desired materials. Detailed *ex situ* material characterization of thin films and interfaces is essential to understand the correlation between material/interface properties and device performance.

### 3.1 Fabrication

#### 3.1.1 Solar cell fabrication baseline

The UNSW baseline CZTS solar cells were fabricated following the process represented in Figure 3. 1. The substrates used in the UNSW baseline were commercially sourced Mo-coated soda-lime glass (SLG). They were usually in 10 cm  $\times$  10 cm (2~3 mm thick) when received and were then cut into 5 cm  $\times$  5 cm pieces for cleaning. The cleaning was performed in the sequence of detergent, de-ionized water, acetone, and isopropanol by sonicating for 15 minutes for each step. The nitrogen dried

substrates were then transferred into a magnetron sputtering system (AJA International, Inc., Model ATC-2200) where the CZTS was grown using co-sputtering Cu/ZnS/SnS targets. All targets used are 3 inch in diameter and the purities of the targets are all 4 N. Cu was deposited using direct current (DC) power supply at a power density of 0.37 w/cm<sup>2</sup> with a deposition rate of 1.80 nm/min. ZnS and SnS were deposited with radio-frequency (RF) power supply at a power density of 1.54 w/cm<sup>2</sup> and 0.83 w/cm<sup>2</sup> with a deposition rate of 3.53 nm/min and 3.74 nm/min respectively. The composition of the CZTS absorber was controlled to be Cu-poor ( $\text{Cu}/(\text{Zn}+\text{Sn}) = 0.88$ ) and Zn-rich ( $\text{Zn}/\text{Sn} = 1.18$ ). The CZTS absorber was then fabricated to be 700–800 nm in thickness.

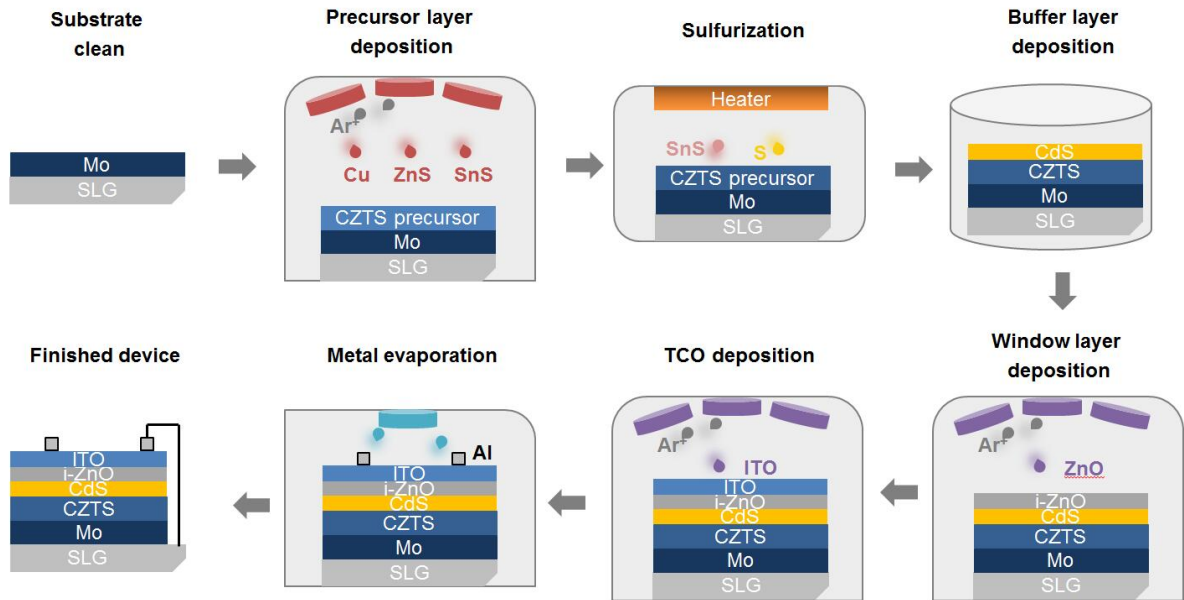


Figure 3. 1. Schematic of the UNSW fabrication baseline of the CZTS/CdS thin film solar cell.

Subsequently, the films were subjected to the sulfurization process using a rapid thermal processor (AS-One 100) in a combined sulfur and SnS atmosphere at 560 °C with a heating rate of 15 °C min<sup>-1</sup> for 3 min and then cooling down to room temperature naturally. Reference devices with 50 nm CdS buffers were fabricated using chemical bath deposition, where CdS was grown from cadmium sulfate

( $3\text{CdSO}_4 \cdot 8\text{H}_2\text{O}$ ), excess thiourea ( $\text{H}_2\text{NCSNH}_2$ ), and ammonium hydroxide at a bath temperature of  $80^\circ\text{C}$ . An i-ZnO/ITO (50 nm/210 nm) top contact was then deposited by radio frequency sputtering, followed by Al grids using thermal evaporation. An antireflection coating of 110 nm  $\text{MgF}_2$  was deposited on the champion devices by thermal evaporation and  $0.224\text{ cm}^2$  solar cells were finally defined by mechanical scribing.

### 3.1.2 Atomic layer deposition process

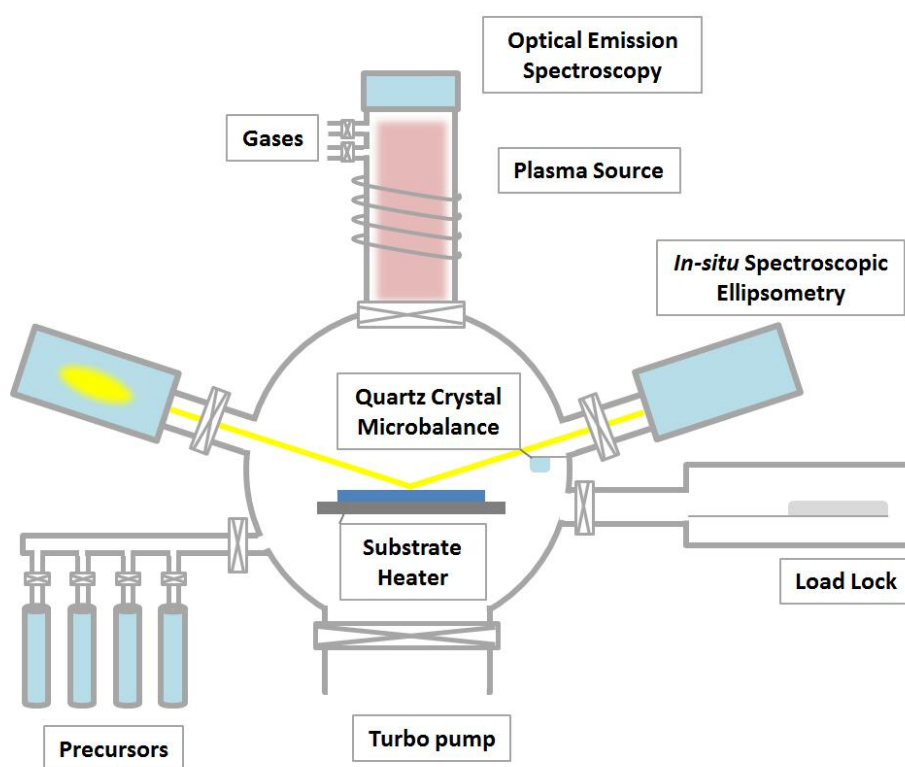


Figure 3. 2 Schematic representation of Fiji G2 ALD chamber equipped with a plasma source, *in situ* SE, OES and QCM, a turbopump and an automated load lock.

All the ALD deposition processes reported in this thesis were performed in the Fiji G2 ALD system developed by Ultratech/Cambridge Company unless otherwise specified. The Ultratech Fiji G2 Plasma Enhanced Atomic Layer Deposition (PEALD) system is a high-vacuum atomic layer deposition system with both plasma-enhanced

and thermal deposition modes while using a flexible system architecture that permits multiple configurations of precursors and plasma gases. A schematic representation of Fiji G2 ALD chamber is shown in Figure 3. 2. The system was equipped with a heated process chamber, remote Inductively Coupled Plasma (ICP) source, a turbomolecular pump, and an automated load lock for transferring substrates. The Fiji G2 ALD is intended for the deposition of a variety of thin films, including metals, oxides, and nitrides. It has the capacity to deposit thin films to atomically specified thickness with large area conformity. The substrate and the reactor wall can be heated up to 500 °C and 300 °C, respectively. In particular, there are chamber ports available for *in situ* process monitoring e.g. spectroscopic ellipsometry (SE), optical emission spectroscopy (OES) and quartz crystal microbalance (QCM). A Woollam M-2000U ellipsometer (245–1000 nm) was mounted directly onto the ALD chamber using two optical viewports. An Ocean Optics Jaz spectrometer was positioned on the top of the plasma source through a quartz window. An INFICON ALD Sensor is operated in the ALD chamber for QCM measurement which can withstand operational temperature up to 450 °C. Noticeably, a gas tube is used to purge SE and QCM port with nitrogen gas to keep the reactive chamber gases from entering the sensor head and keep quartz windows free of deposition materials.

The chemical structures of the precursors implemented in this thesis are illustrated in Figure 3. 3. As mentioned in section 2.1.1, the temperature of the ALD process should be moderate since long-time heating effects usually deteriorate the PV performance of chalcogenide devices.[43, 104, 121] The most commonly used Zn precursor for PV application is diethyl zinc (DEZ)[147, 148]. DEZ is a highly volatile precursor and is reactive towards H<sub>2</sub>O, thus zinc oxide (ZnO) can be easily deposited in under 200 °C. A non-halogenated Sn precursor tetrakis (dimethylamino) tin (TDMASn) was chosen as the Sn precursor for low-temperature tin oxide (SnO<sub>x</sub>) deposition. The deposition can be performed at deposition temperatures of 50-300 °C.[149] Higher volatility of ethylcyclopentadienyl magnesium [Mg(CpEt)<sub>2</sub>]

was used as Mg precursor to deposit binary magnesium oxide (MgO) [150]. The process window is in the temperature range of 125-400 °C. For Al<sub>2</sub>O<sub>3</sub> deposition, trimethylaluminum (TMA) was chosen as the Al precursor mainly because of its high reactivity and successful application on PV devices.[47, 78, 151] The experimental details for those oxides deposition will be given in the corresponding chapters.

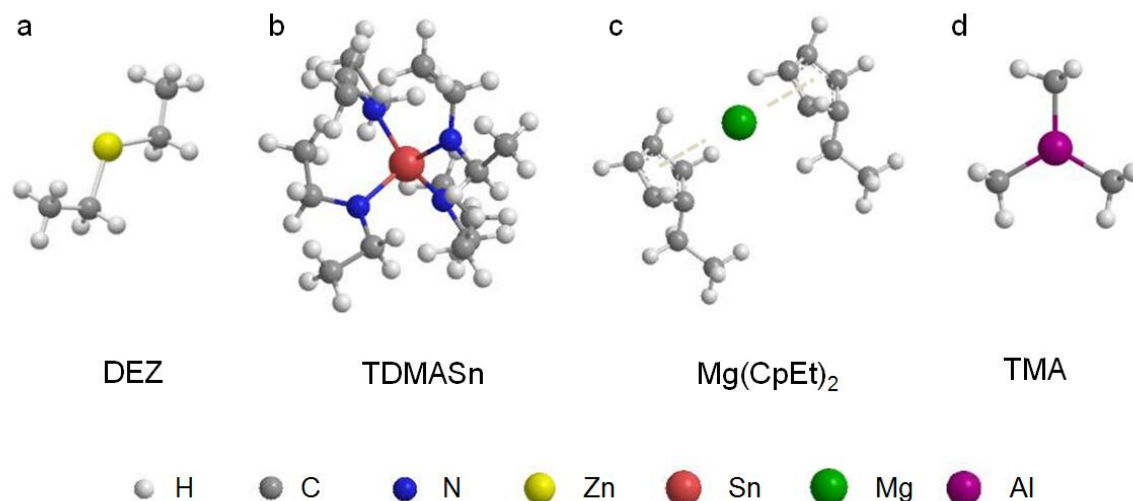


Figure 3. 3 Precursors used for ALD deposition. a) DEZ, b) TDMASn, c) Mg(CpEt)<sub>2</sub>, d) TMA

## 3.2 Characterization

### 3.2.1 *In situ* measurement

*In situ* measurement was implemented in the development of the ALD process to minimize the optimization time and material consumption. The dynamic measurements allow for evaluating the basic properties of the deposited films, thus providing precise control of the growth of desired materials. In the Fiji G2 ALD system, *in situ* quartz crystal microbalance and spectroscopic ellipsometry were utilized as the dynamic measurements as shown in Figure 3. 2.

Table 3. 1 List of dynamic measurements used in the ALD process.

Characterization method	Abbreviation	Purpose
Quartz crystal microbalance	QCM	Thickness, mass change
Spectroscopic ellipsometry	SE	Thickness, optical constant, bandgap, absorption, crystalline nature

Quartz crystal microbalance measurements can monitor the mass change during the ALD process. It measures the mass per unit area from the change in the resonance frequency of a quartz crystal. The resonance is disturbed by the addition or removal of mass due to oxide growth/decay or film deposition onto the surface of the acoustic resonator.[152] The QCM used in the Fiji G2 ALD system was the INFICON ALD Sensor which is designed to operate in the harsh environment of an ALD application. The QCM sensors were polished gold crystals with an oscillation frequency at 6 MHz. A gas tube was used to purge the back of the crystal and sensor cavity with inert nitrogen gas. This kept the reactive chamber gases from entering the sensor head and keeps the back of the crystal and electrical contacts free of deposition material. The signals from the crystal sensor were received by a thickness monitor every 0.1 s. The thickness change of the deposition can be calculated if the mass density of the deposited films is known.

Ellipsometry is a nondestructive technique that can be used to determine the dielectric properties, roughness, thickness, crystalline nature, composition, electrical conductivity and other material properties of thin films.[153, 154] Ellipsometry measures the change in polarization of light upon reflection from a sample. This polarization change is described as an amplitude component psi ( $\Psi$ ) and a phase difference delta ( $\Delta$ ). These values are related to the ratio of Fresnel reflection coefficients  $\widetilde{R}_p$  and  $\widetilde{R}_s$  for *p*- and *s*-polarized light, respectively.[155]

$$\rho = \frac{R_p}{R_s} = \tan(\psi)e^{i\Delta} \quad \text{Equation 3. 1}$$

Since ellipsometry measures the ratio of two values (rather than the absolute value of either), it is highly accurate and reproducible.

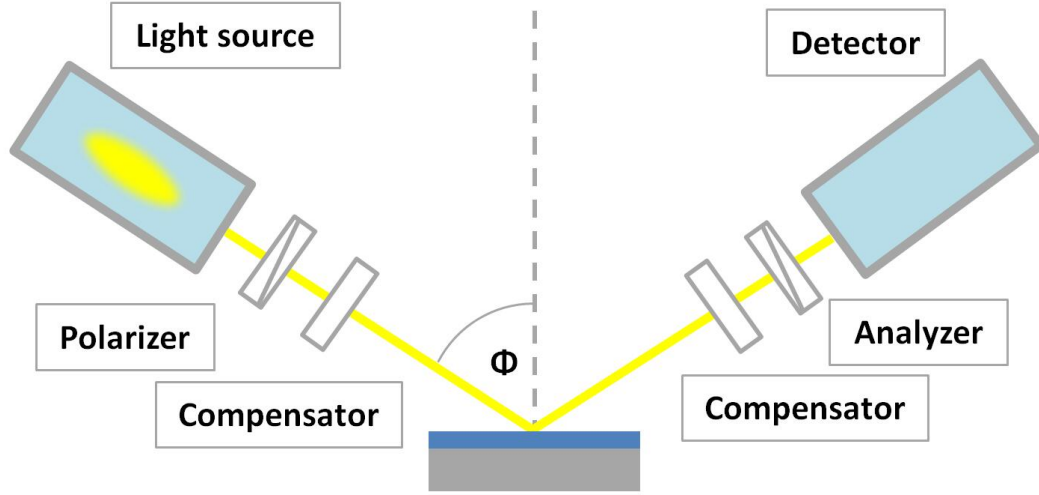


Figure 3. 4 Schematic setup of an ellipsometry measurement.

SE combined with variable angle of incidence allows for acquiring large amounts of data from a given sample, thus could be an extremely powerful measurement. Besides, the spectral acquisition range and angles of incidence may be optimized for the determination of certain sample parameters. Therefore, it has the flexibility to handle a wide range of materials and structures. A variable angle spectroscopic ellipsometer (JA Woollam M-2000VI) was implemented for *ex-situ* measurements of the samples in this thesis to determine the properties of the deposited thin film. Another ellipsometry method used in this thesis is the dynamic spectroscopic ellipsometry. The dynamic SE data can be acquired by using *in situ* spectroscopic ellipsometry (M-2000U Spectroscopic Ellipsometer, J.A. Woollam Co.). The spectral acquisition was performed over the 246-1000 nm wavelength range with a fixed angle of incidence of  $70^\circ$ . The SE measurements as a function of time were acquired at 0.5 s

intervals. The advantage of *in situ* monitoring can be illustrated by determining fundamental process parameters, such as the film thickness, the growth rate per cycle and the variation of optical properties with time. Furthermore, the samples can be measured at elevated temperatures during the ALD process, which implies different optical properties compared to samples at room temperature.

Modeling was carried out using the CompleteEASE software package.[156] The data from deposited film samples were modeled using a three-layer model, comprising Si, native SiO<sub>2</sub> and metal oxides. A temperature-dependent Si layer model from CompleteEASE software library was used to fit the parameter of Si depending on the process temperature. The ZnO film was modeled through an oscillator model, which including a polynomial spline function (the psemi-m0 oscillator) and a Tauc-Lorentz oscillator. The SnO<sub>x</sub> and MgO layers were modeled using a Lorentz oscillator and Sellmeier oscillator, respectively. The optical constants of the films were fitted in a Kramers–Kronig consistent manner.

### **3.2.2 Material characterization**

Material characterization of layers and interfaces is essential to develop high-performance solar cells and to investigate/understand its relationship with the device performance. In Table 3. 2, all the material characterization methods used in this thesis are listed which were used to determine the optical, structural, electrical, elemental, and surface properties of the thin film and interfaces.



Table 3. 2 List of material characterization methods used in this thesis.

Characterization method	Abbreviation	Purpose
UV/vis/NIR Spectrophotometer	UV-Vis	Light reflectance, transmittance, absorption and optical bandgap
Four-point probe	4PP	Sheet resistance, resistivity
Hall Measurement	Hall	Resistivity, Mobility, carrier density
X-ray photoelectron spectroscopy	XPS	Chemical state, valence band maximum
Ultraviolet photoelectron spectroscopy	UPS	Chemical state, CBO
Atomic force microscope	AFM	Morphology, uniformity
Kelvin probe force microscopy	KPFM	Surface potential, CBO
X-ray diffractometer	XRD	Crystalline phases
Raman spectroscopy	Raman	Structural analysis
Inductively coupled plasma optical emission spectrometry	ICP-OES	Elemental analysis
Time of flight secondary ion mass spectroscopy	ToF-SIMS	Element profile, including hydrogen
Scanning electron microscope	SEM	Surface topography and composition
Transmission electron microscope	TEM	Thickness, structure, depth profile
Atom probe tomography	APT	3D imaging and chemical composition

### 3.2.2.1 Optical and electrical properties

An UV/vis/NIR Spectrophotometer is a tool to quantitatively measure the reflection or transmission properties of a sample as a function of wavelength. The transmittance is measured by comparing the intensity of light after passing through a sample to the intensity of light before it passed through the sample. In the case of reflectance, it measures the intensity of light reflected from a sample and compares it

to the intensity of light reflected from reference material. A LAMBDA 1050 UV/vis/NIR Spectrophotometer (Perkin-Elmer) with an integrating sphere was used to measure the optical properties of the thin films. A deuterium lamp and a tungsten halogen lamp provided excitation wavelengths between 190 nm and 3300 nm. An integration sphere of 150 mm was available for diffuse reflectance measurements. It had the capability to collect light from a wide range of input angles and correct for inaccuracies due to refraction or light scattering effects, thus providing more accurate and reproducible measurements.[157]

A four-point probe can be used to measure the resistivity of semiconductor samples. When the probes are aligned, the resistivity measurement is taken by passing a current through two outer probes and measuring the voltage through the inner probes, as shown in Figure 3. 5a. However, it only allows for the measurement of the product of mobility and carrier concentration other than each parameter directly.[158] Thus, Hall effect measurement should be performed in addition if one requires information about the individual components.

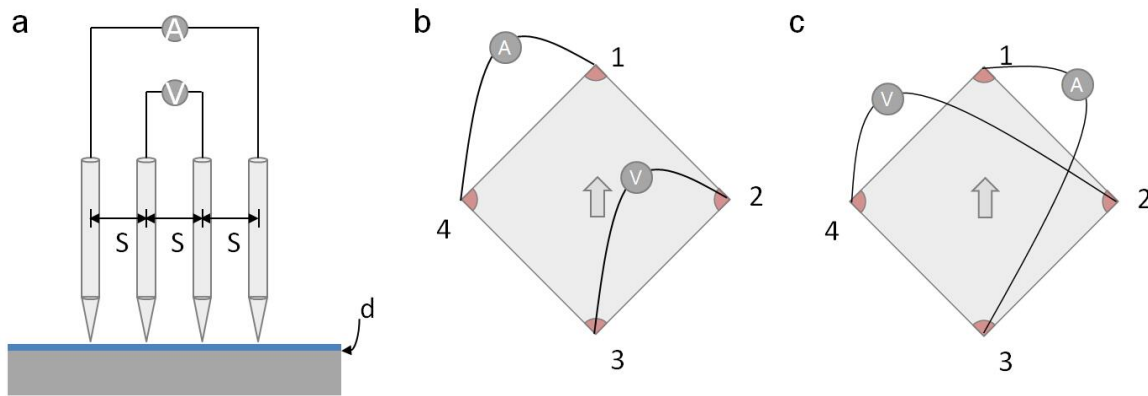


Figure 3. 5 a) Four-point probe configuration. b) Van der Pauw resistance measurement configurations (one of the eight possible configurations). c) Hall effect measurement configuration for thin films on an insulating substrate.

In order to determine both the mobility  $\mu$  and the bulk carrier density, a combination of a resistivity measurement and a Hall measurement is needed, together

with an accurate measurement of the sample thickness  $d$ . The Van der Pauw method was employed in the Hall measurement where a four-point probe placed around the perimeter of the sample to provide an average resistivity of the sample as in Figure 3. 5b. As originally devised by Van der Pauw, samples must be homogeneous and isotropic with uniform thickness and without isolated holes. Sample contact must be located at the edge of the sample which at least an order of magnitude smaller than the area of the entire sample.[159] The current was applied to two adjacent contacts and the voltages were detected between the other two. In the Hall measurement, however, a current is applied between opposite contacts (Figure 3. 5c) and the voltage is detected between the other two opposite contacts. Since Hall voltages and van der Pauw voltages can be as low as millivolts, the recommended test technique involves a combination of reversing source current polarity, sourcing on additional terminals, and reversing the direction of the magnetic field. These measurements were carried out by HMS-5000 Hall effect measurement system (Ecopia) at room temperature under a magnetic field of 0.5 T.

### **3.2.2.2 Surface properties**

Microanalysis is the qualitative or quantitative identification of the chemical elements and how the atoms of the elements are arranged with respect to each other. Figure 3. 6 shows some of the most commonly used microanalytical techniques arranged according to their spatial resolutions and sensitivities. The techniques are divided into different categories based on their capability (e.g. elemental composition, structural information, surface analysis) and those used in this thesis will be discussed in the following.

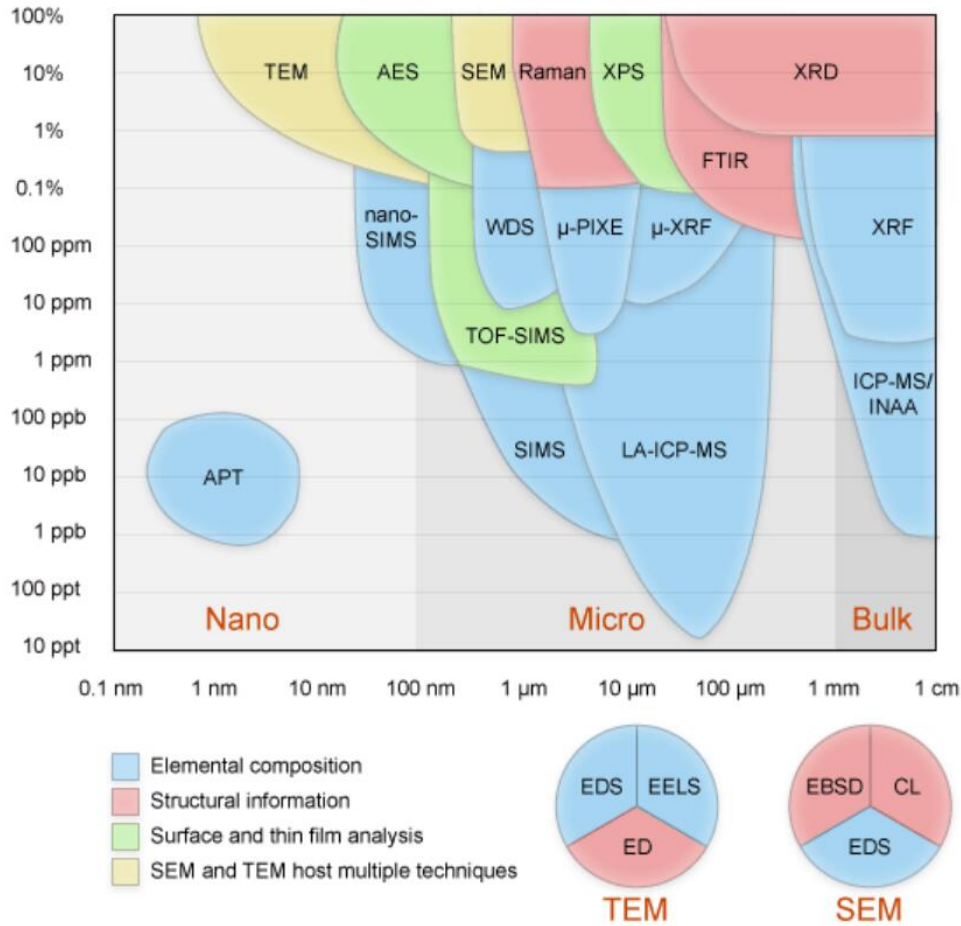


Figure 3. 6 Microanalysis techniques arranged according to their spatial resolutions and sensitivities. Adapted from Ref. [160].

XPS stands for X-ray photoelectron spectroscopy, it is a surface-sensitive technique to determine the elemental composition quantitatively and examine whether any contamination exists at the surface of a sample. It can also identify the chemical states, the depth of the surface layer, the binding energy of electronic states and the density of electronic states in material, etc. The XPS measurements were conducted using an ESCALAB250Xi (Thermo Scientific, UK) under ultra-high vacuum (better than  $2 \times 10^{-9}$  mbar). The X-ray source was monochromated Al Ka ( $h\nu \times 1486.68$  eV) with binding energy scale calibrated using carbon reference. Depth profiling data were achieved by mildly sputtering the samples with 1 keV  $\text{Ar}^+$  ions over an etching area of  $2.5 \times 2.5$  mm.

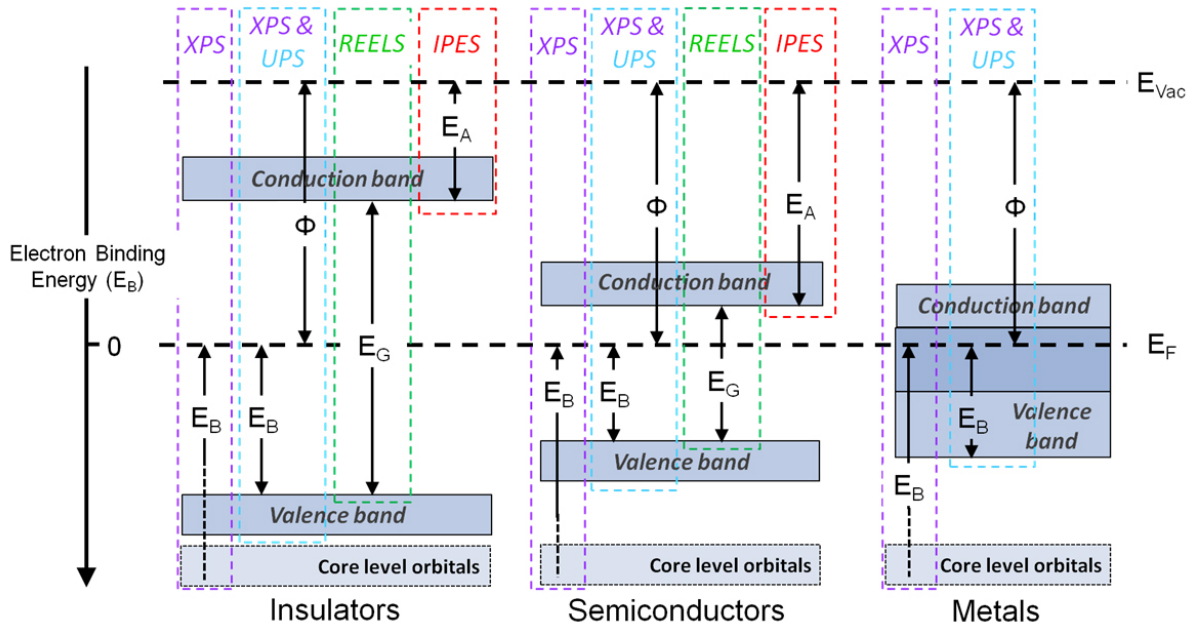


Figure 3. 7 Data acquisition of different types of surface analysis in different materials. Adapted from Ref. [161].

Ultraviolet Photoelectron Spectroscopy (UPS) was employed to obtain the valence band energy and electronic work function. It uses the same principles as XPS except for the fact that the ionizing radiation at energies of 10s of eV is much lower than it used in XPS where the typical photon energies are above 1 keV. Figure 3. 7 presents the data acquisition of different types of surface analysis in different materials. It shows that most core level photoemissions are not accessible using UPS due to the lower ionizing energy. In this sense, the spectral acquisition is limited to the valence band region. Consequently, UPS is usually implemented to perform the valence band acquisition and electronic work function ( $\Phi$ ) measurement. As shown in Figure 3. 8b, by measuring the difference from the onset of the secondary electrons up to the Fermi edge and subtracting it from the energy of the incident UV light ( $h\nu$ ), the  $\Phi$  is then given by

$$\Phi = h\nu - (cutoff - E_F) \quad \text{Equation 3. 2}$$

Note that UPS also exhibits greater surface sensitivity than XPS due to the difference in the short inelastic mean free path (IMFP, or  $\lambda$ ) of free electrons within a solid material.  $3\lambda$  from the surface (or information depth) where  $> 99\%$  of a photoemission signal originates is commonly regarded as the sensitivity of this technology.[161] Obviously, UPS has shallower information depth ( $<2-3$  nm) than XPS ( $<10$  nm) as demonstrated in Figure 3. 8a. UPS data in this work were acquired using an ESCALAB250Xi (Thermo Scientific, UK) under ultra-high vacuum (better than  $2 \times 10^{-9}$  mbar). The excitation energy during the UPS experiment was 21.2 eV (He I).

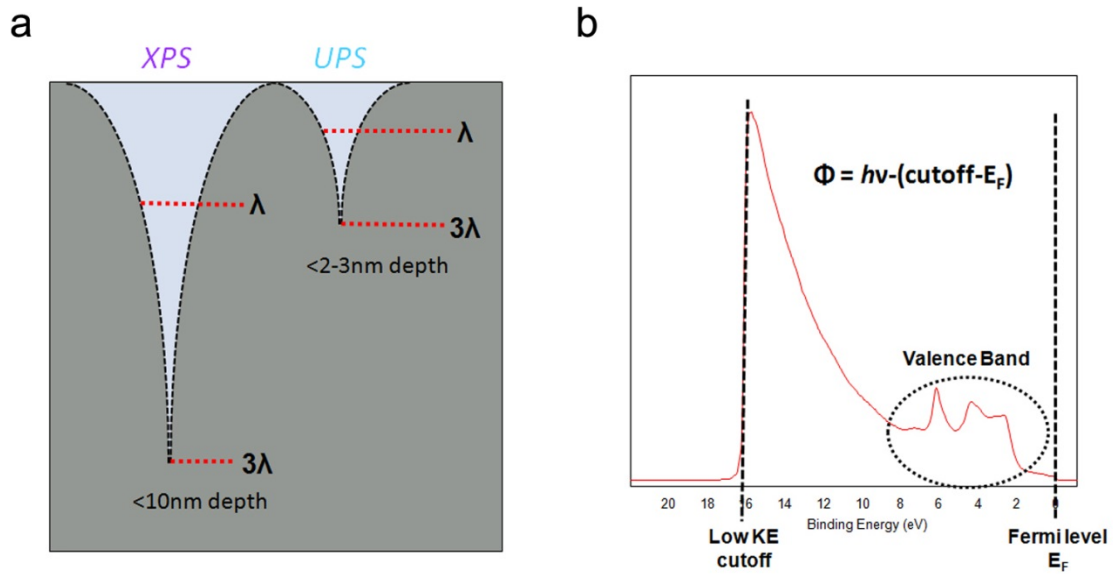


Figure 3. 8 a) Difference in information depth for XPS and UPS. b) Work function measurement using the UPS spectra. Adapted from [161].

The surface morphology of a material is critical to affecting its functionality in the application of solar cells. The optical and electrical properties of one layer or interface property between different layers are strongly related to the surface microstructure.[162, 163] In this work, the three-dimensional topography imaging of

the material surface will be measured by atomic force microscopy (AFM). The measurement are taken by scanning an AFM probe across a sample surface. AFM images in this work were obtained using Bruker Dimension Icon AFM system in the tapping mode.

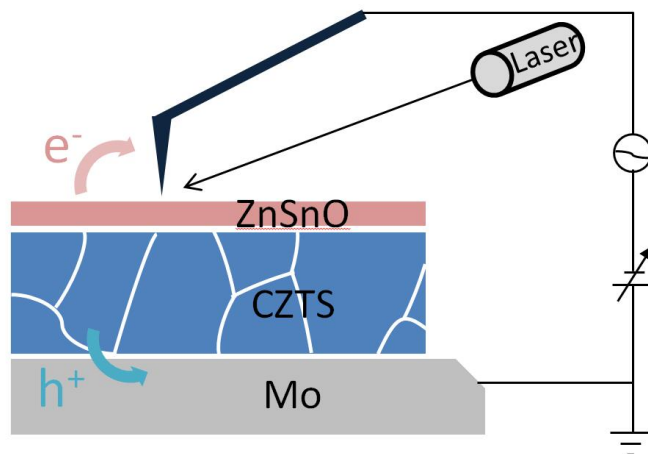


Figure 3. 9 KPFM set up under illumination for CZTS/ZnSnO on Mo-coated glass substrate.

Other than morphology information, Kelvin probe force microscopy (KPFM) was additionally used to determine images of the surface potential with nanometer resolution, providing the local electronic properties of the semiconductor surface.[164, 165] Therefore, KPFM is able to correlate electronic property with the structural property of the device. KPFM results indicate the surface potential differences between nanostructures, molecules or charge states. It is well suited to study the effects of grain boundary and surface defects on electronic properties of semiconductor films.[166-168] In this thesis, KPFM measurements were taken using an AFM (AIST-NT SmartSPM) in ambient. The KPFM set up under illumination is demonstrated in Figure 3. 9, which will be used to further examine the charge separation behavior in the heterojunction of the device. The data were collected by using a 6 nm radius of curvature

(HYDRA6R-100NG-10, APPNANO) with an AC voltage of -1 to +1 V. An external laser source with tunable wavelength and intensity was used to illuminate on the surface of the sample. Laser light with a wavelength of 1300 nm was used for beam deflection to avoid the absorption of the sample under test.

### **3.2.2.3 Structural and elemental properties**

X-ray diffraction (XRD) is an analytical method to quantify the crystalline nature of materials by measuring the diffraction of x-rays from the planes of atoms within the material. It is used to measure the crystalline content of materials, identify the crystalline phases present and to study preferential ordering and epitaxial growth of crystallites. However, XRD measurements of "thin" (<1000 nm) films using conventional  $\theta/2\theta$  scanning methods generally suffer from low peak intensity and a high signal originating from the substrate. Therefore, low-angle XRD techniques such as grazing incidence X-ray diffraction (GIXRD) have been developed to avoid intense signals from the substrate and get stronger signals from the thin film itself. The fixed angle is generally chosen to be slightly above the critical angle for the total reflection of the film material. The microstructures of the thin films were characterized by GIXRD using PANalytical Empyrean thin film X-ray diffractometer with Cu-K $\alpha$  radiation.

Raman spectroscopy is a nondestructive characterization technique that allows precise measurement of the vibrational modes of a material. This technique is based on inelastic scattering, or Raman scattering, of monochromatic laser light from the sample. Part of the scattered light has different energy (higher or lower) resulting from the interaction with phonons. Not all vibrational modes interact with light and those who do not are called "silent" modes. Raman can operate in resonant mode, when the excitation photon energy corresponds to an electronic transition in the material and non-resonant mode when the material is transparent to this light. The Renishaw inVia Raman spectroscopy with a 514nm excitation laser was used to analyze the phase of



the CZTS absorber. The resonant mode was carried out for characterization of ZnMgO samples by using 325 nm excitation laser.

Apart from the structural measurement, elemental characterization is essential to investigate the film property and its relationship with other fundamental properties. Inductively coupled plasma optical emission spectroscopy (ICP-OES) is an analytical technique used for the detection of chemical elements.[169] The metal element composition of the films was always obtained by ICP-OES using samples deposited on glass substrates. This technique is a destructively analyzing method and mainly determine the average composition of the sample instead of elemental distribution. To obtain the elemental depth compositional profiles of the sample, the analysis could be taken by time of flight secondary ion mass spectroscopy (ToF-SIMS). ToF-SIMS is a surface-sensitive analytical method that uses a focused, pulsed ion beam (typically Cs or Ga) to remove molecules from a material surface.[170] Secondary particles are removed from atomic monolayers on the surface and then accelerated into a "flight tube" and their mass is determined by measuring the exact time at which they reach the detector (i.e. time-of-flight).[171, 172] Thus, it is possible to determine a mass resolution of one part in a thousand of the mass of a proton. The used primary beam in this work was Bi ions at 15 KeV and the current was 1.33 pA (+/-0.03pA). The area of the analyzed area was  $101.5 \times 101.5 \mu\text{m}^2$  with a random raster mode. The utilized secondary sputtering beam was Cs ions at 2 KeV and the related current was approximately 86 nA (+/-5 nA). The area of the sputtered sample was kept to be  $400 \times 400 \mu\text{m}^2$ .

Scanning Electron Microscope (SEM) is a remarkably versatile technique to investigate the morphology and composition of a sample.[173] As the schematic shown in Figure 3. 10, the electrons in an SEM never form a real image of the sample like the light produces in a light microscope. The magnified images of a sample are created by using a focused beam of high energy electrons scanned across the surface of a specimen. The beam is generated by an electron gun and focused at the specimen after

processed by magnetic lenses. The electrons interact with atoms in the sample, producing various signals that can be detected and analyzed to extract information about the sample's surface topography and composition.[174] The types of signals produced by an SEM include secondary electrons (SE), back-scattered electrons (BSE), characteristic X-rays, light [cathodoluminescence (CL)], specimen current and transmitted electrons. The most common imaging mode detects the secondary electrons emitted by atoms excited by the electron beam. The morphology and structure of the samples in this work were obtained in a field emission scanning electron microscopy (FE-SEM, FEI Nova NanoSEM 450) at 5-15 kV.

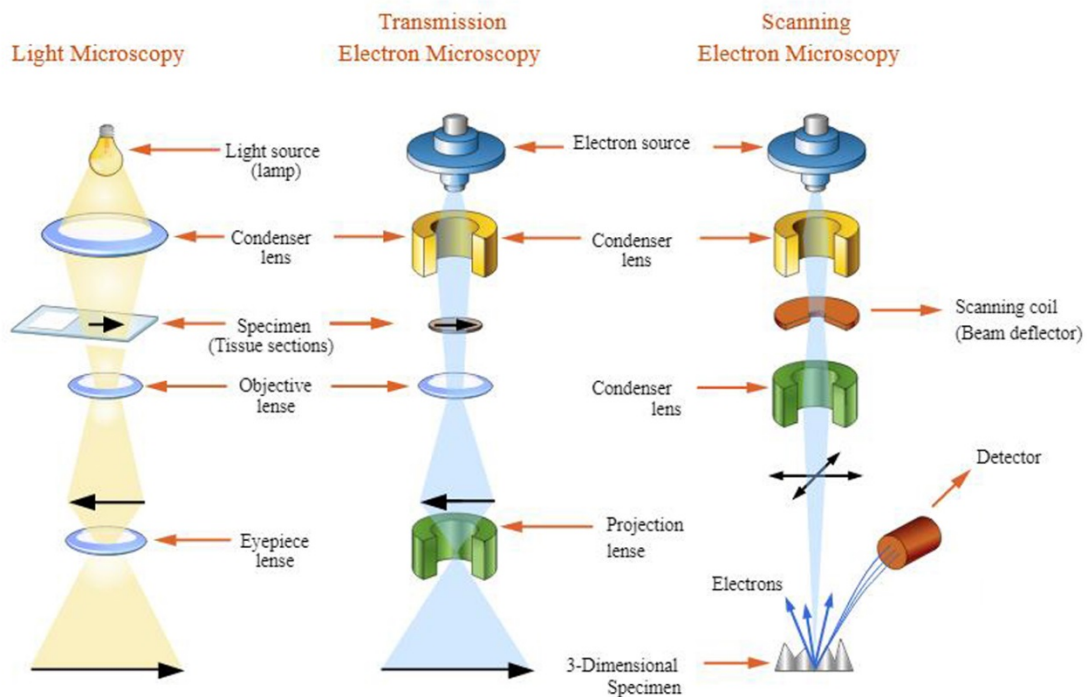


Figure 3. 10 Configuration of the electron microscopy compared with light microscopy. Adapted from Ref. [175].

Transmission electron microscopy (TEM) is a microscopy technique in which an electron beam is transmitted through an ultra-thin sample. An image is formed from the interaction of the electrons with the local electronic potential of the sample.[176] The

image is magnified and focused onto an imaging device, such as a fluorescent screen, a photographic film, or a CCD camera. TEMs are capable of imaging at a significantly higher resolution than light microscopes, owing to the small de Broglie wavelength of high-energy electrons (200 keV in our case). Energy dispersive spectroscopy EDS (or Energy Dispersive X-ray spectroscopy EDX) is a chemical microanalysis technique used in conjunction with Scanning Electron Microscopy and Transmission Electron Microscopy. The X-ray energy is characteristic of the chemical element from which it was emitted. The EDS detector measures the relative abundance of emitted x-rays versus their energy. The microstructure and compositional profiles were measured by JEOL JEM-ARM200F (200 kV) aberration-corrected scanning transmission electron microscope (STEM) equipped with energy-dispersive X-ray spectroscopy system (EDX).

Atom Probe Tomography (APT) is a powerful microscopy technique that generates a three-dimensional (3D) atom-by-atom reconstruction of a small volume within a material.[177] The technique is a complement to other microscopy techniques such as SIMS and TEM, providing the highest available spatial resolution for chemical analysis.[178] APT requires samples to be milled to a sharp point before using a pulsed laser to induce atom evaporation, and therefore sample preparation is extensive. In this thesis, APT measurements were performed on needle-shaped specimens with a tip diameter of less than 100 nm. These were prepared using a Zeiss Auriga FEG SEM, equipped with a focused ion beam (FIB). Due to extreme beam damage of the APT specimens, once the diameter of the needle was below 1  $\mu\text{m}$ , an accelerating voltage of less than 5 kV had to be used for imaging and milling in order to avoid any damage. The atom probe measurements were conducted on a Camera LEAP 4000XSi, at a temperature of  $\sim 50$  K, using a pulse frequency of 200 kHz, pulse energy of 50 pJ and a detection rate of 0.5%. All data sets were reconstructed in IVAS 3.6.18.

### 3.2.3 Device characterization

The current density-voltage ( $J$ - $V$ ) curve of a solar cell is the superposition of the  $I$ - $V$  curve of the solar cell diode in the dark with the light-generated current. The total current as a function of voltage under illumination is given by:

$$J_{\text{light}}(V) = J_0 \left( \exp\{q(V - J_{\text{light}}R_s)/AkT\} - 1 \right) + ((V - J_{\text{light}}R_s)G_{sh} + J_{sc}\eta(V))$$

Equation 3. 3

Here,  $J_0$  is the saturation current density for the recombination mechanism under illumination,  $\eta(V)$  is the external collection efficiency. The  $J$ - $V$  curves were measured using an AM 1.5G solar simulator from PV Measurements calibrated with a standard Si reference and a Keithley 2400 source meter.

Table 3. 3 List of device characterization methods used in this thesis.

Characterization method	Abbreviation	Purpose properties
Current density-voltage measurement	JV	Current density-voltage curves
External quantum efficiency	EQE	Spectral response
Capacitance-voltage measurement	C-V	Doping concentration and depletion width
Drive-level capacitance profiling measurement	DLCP	Bulk carrier density
Suns- $V_{OC}$ measurements	Suns-Voc	Extract $J_{01}$ and $J_{02}$
Photoluminescence	PL	Electrical bandgap, recombination property
Time-resolved photoluminescence	TR-PL	Minority carrier lifetime

The external quantum efficiency (EQE) quantifies the number of electron-hole

pairs generated per incident photon. Instead of the photon flux, the experimental setup measures the ratio between the current produced on the sample cell by monochromatic light and the current generated in a reference detector at the same wavelength. Since not all the incoming light reaches the active part of the solar cell (mainly due to the cell reflectance and to the parasitic absorbance of the window layers), the EQE is not the best parameter to evaluate the efficiency of the active part of the cell. The internal quantum efficiency (IQE) can be calculated from the EQE as  $\text{IQE} = \text{EQE}/(1-R)$  where  $R$  is the reflectance at the corresponding wavelength. EQE data in this work were collected by a QEX10 spectral response system (PV measurements, Inc.) calibrated by the National Institute of Standards and Technology (NIST)-certified reference Si and Ge photodiodes.

The capacitance-voltage ( $C$ - $V$ ) measurement is a simple technique to determine the junction properties such as the carrier density and the depletion width. The junction capacitance was obtained from the measured quadrature current response induced by an ac voltage perturbation. The variation in junction capacitance with dc bias is then determined. The charge density at the edge of the depletion region ( $N_w$ ) can then be given as:

$$N_w = \frac{C^3}{q\epsilon A^2 \left(\frac{dC}{dV}\right)} = -\frac{2}{q\epsilon A^2} \left[ \frac{d\left(\frac{1}{C^2}\right)}{dV} \right]^{-1}, \quad \text{Equation 3.4}$$

where  $W$  is the width of the depletion region,  $A$  is the area of the device, and  $q$  is the fundamental charge.[179] The capacitance-voltage ( $C$ - $V$ ) measurement was carried out using an impedance analyzer at a frequency of 100 kHz with a DC bias voltage sweeping from  $-1.5$  to  $0.5$  V.

Drive-level capacitance profiling (DLCP) is an alternate technique for measuring the energetic and spatial distribution of defects in the bandgap. The DLCP method examines the junction capacitance dependence over a range of ac voltage amplitudes in addition to a range of dc bias, to obtain more information about the film response than

is available from the aforementioned  $C-V$ . Generally, we obtain information about the free carriers, bulk and interface defects deduced from the  $C-V$  measurements, while we identify the response only from the free carrier and the bulk defects using the DLCP technique.[180, 181] DLCP measurement was performed with the a.c. amplitude varied from 10 mV to 110 mV and the d.c. bias from -1.6 V to 0.6 V.

Suns- $V_{OC}$  measurements were taken out to investigate the location of the recombination through extracting the recombination current density. The Suns- $V_{OC}$  measurements shown using a decaying light pulse with a full-width half maximum (FWHM) of about 2 ms from a xenon flash lamp, which enables the quasi-steady state photovoltage  $V_{OC}$  to be measured across the  $p-n$  junction in the open-circuit condition. The light intensity was monitored by a single-crystal silicon reference cell plotted against  $V_{OC}$ .

Photoluminescence (PL) is an important technique for measuring the purity and crystalline quality of semiconductors and for quantification of the amount of disorder present in a system. In fact, defects and impurities often introduce electronic states in the bandgap associated with radiative transitions. In a typical PL experiment, a semiconductor is excited with a light source that provides photons with energy larger than the bandgap energy. When electrons are excited high in the conduction band, the carrier temperature initially decreases quite fast via emission of optical phonons. This is quite efficient due to the comparatively large energy associated with optical phonons and their rather flat dispersion, allowing for a wide range of scattering processes under the conservation of energy and momentum. Once the carrier temperature decreases below the value corresponding to the optical phonon energy, acoustic phonons dominate the relaxation. Photoluminescence (PL) spectra were measured using a 1/4 m monochromator (Cornerstone 260) equipped with a silicon charge-coupled device (CCD) camera. A continuous-wave laser (405 nm, 50 mW) was used as the excitation source and the luminescence signal was detected by a CCD. Time-resolved photoluminescence (TRPL) measurements were performed using time-correlated

single-photon counting (TCSPC) technique with a Microtime-200 (Picoquant) system. This system was equipped with a 780–800 nm detector and a 470 nm solid-state laser excitation source tuned at a repetition rate of 10 MHz with an incident power of 0.18 W/cm<sup>2</sup>.

# Chapter 4 ZnSnO as Cd-free CZTS buffer layer<sup>1</sup>

Heterojunction interface management is of critical importance to tackle interface recombination. In this chapter, atomic layer deposition (ALD) was implemented to synthesize a wide range of  $\text{Zn}_{1-x}\text{Sn}_x\text{O}$  (ZTO,  $0 \leq x \leq 1$ ) films for application as a buffer layer in CZTS solar cells. A favorable band alignment is achieved using a 10 nm  $\text{Zn}_{0.77}\text{Sn}_{0.23}\text{O}$  buffer layer which enabled an impressive 10 % increase in the open-circuit voltage of the CZTS solar cell. The microstructure and chemical nature of the CZTS/ZTO interface are carefully studied and the presence of an ultra-thin Zn(S, O) tunnel layer is demonstrated. The decreased interfacial defects stemming from the minor lattice mismatch at the CZTS/Zn(S,O)/ZTO heterointerface in combination with the passivation provided by a higher sodium concentration throughout the CZTS/ZTO device explains the significant increase in open-circuit voltage. Finally, an efficiency of 9.3% was obtained for Cd-free pure sulfide CZTS solar cells with a structure of Mo/CZTS/ZnSnO/i-ZnO/ITO.

## 4.1 Introduction

As discussed in Section 1.2.1, the performance gap between CZTS solar cells and

---

<sup>1</sup> Part of this chapter has been published as: Cui, X.; Sun, K.; Huang, J.; Lee, C.-Y.; Yan, C.; Sun, H.; Zhang, Y.; Liu, F.; Hossain, M. A.; Zakaria, Y.; Wong, L. H.; Green, M.; Hoex, B.; Hao, X., Chem. Mater. 2018, 30, (21), 7860-7871.



its CIGS counterpart can mainly be attributed to the large  $V_{OC}$  deficit ( $E_g/q - V_{OC}$ ,  $E_g$  is the bandgap,  $q$  is the electron charge).[1] This  $V_{OC}$  deficit is typically attributed to a high density of bulk defects, band tailing in the CZTS films[64, 65] and recombination at interface defects.[1, 46, 182] Heterojunction interface management is of critical importance to tackle interface recombination, thus will be investigated in this chapter. Generally, the interface recombination is mainly originating from non-ideal band-alignment and a high defect density at the CZTS/CdS heterojunction interface. On the one hand, the conduction band offset (CBO) between CdS and pure sulfide CZTS has been identified as ‘cliff-like’, which could explain why CZTS has a relatively larger  $V_{OC}$  deficit compared to CZTSSe.[56, 57] On the other hand, the lattice mismatch of the CZTS and CdS interface is 7%,[183] thus introducing more interfacial defects. Additionally, the relatively low bandgap of CdS ( $E_g = 2.4\sim 2.5\text{eV}$ ) results in significant optical absorption losses and thus reduces the short-circuit current density of the solar cell. To overcome these issues, alternative buffer layers such as  $\text{In}_2\text{S}_3$ , [41]  $\text{Zn}(\text{O},\text{S})$ , [42]  $\text{Zn}_{1-x}\text{Cd}_x\text{S}$ , [59] and  $\text{Zn}_{1-x}\text{Sn}_x\text{O}$  [43, 44] have been proposed. Especially  $\text{ZnSnO}$  (ZTO) is an appealing alternative as it contains only non-toxic constituents and the most promising results have been obtained using atomic layer deposition (ALD). [43] ALD is an appealing deposition method as it is compatible with other vacuum-based processes used in the CZTS process flow. In addition, ALD enables precise control of ZTO stoichiometry, atomic level uniformity as well as a conformal coverage over large-scale areas, and has demonstrated usefulness in photovoltaic devices as surface passivation [81, 184] layer and buffer layer. [131, 134]

ALD ZTO buffer layers have been employed in chalcogenide solar cells including CIGS, [131] CZTSSe, [27] CZTS [43] which have shown comparable performance to devices with a standard CdS buffer layer. Previous research of ZTO buffer layers in CIGS devices revealed that the position of the conduction band, as well as the valence band, could be modified by changing the stoichiometry of the ZTO film. [105] Also, the position of the conduction band could be changed independently by changing the

substrate temperature during the ALD process due to quantum confinement effects in the resulting ZTO layer.[103, 104] Li *et al.* first reported the use of ZTO in a CZTSSe cell, claiming the achievement of an 8.6% efficient CZTSSe cell with the improved band alignment at CZTSSe/ZTO heterojunction by optimizing Sn-content of ZTO to be 0.167. This Sn-content of ZTO needs to be carefully tuned if applying to the pure sulfide CZTS solar cells to obtain a favorable band alignment at the pure sulfide CZTS/ZTO hetero-interface since CZTS has a higher conduction band minimum than that of CZTSSe.[54] Recently, Ericson *et al.* demonstrated a 9.0% efficient CZTS solar cell with an ALD  $\text{Zn}_{0.72}\text{Sn}_{0.28}\text{O}$  buffer layer which was synthesized at 145 °C, where they emphasized that the band alignment can be adjusted by varying substrate temperature and confirmed that part of the device improvement could be attributed to annealing during the ALD process. [43, 132] However, few studies have focused on the effect of the ZTO stoichiometry on pure-sulfide CZTS cell performance. In addition to band alignment, the interfacial trap states at the CZTS/ZTO heterojunction should be minimized to eradicate interface recombination. Therefore, the examination of nanoscale microstructure and chemistry at the CZTS/ZTO interface is needed to elucidate the interface property at an atomic level and its correlation with device performance.

## **4.2 Zn-based ternary oxides growth by thermal ALD**

### **4.2.1 Growth of binary metal oxide**

ZnO, SnO<sub>x</sub> and MgO films were deposited on native-Si and SLG substrate in the deposition temperature range of 100-200 °C using thermal ALD. Diethylzinc [ $\text{Zn}(\text{C}_2\text{H}_5)_2$  DEZ, Sigma-Aldrich], tetrakis(diethylamido)tin(IV) [ $\text{Sn}(\text{N}(\text{CH}_3)_2)_4$  or TDMASn, Strem Chemicals]) and bis(ethylcyclopentadienyl)magnesium ( $\text{Mg}(\text{CpEt})_2$ , Strem Chemicals) were used as Zn, Sn, Mg precursor, respectively. The DEZ precursor was kept at room temperature while the TDMASn precursor was heated to 75 °C and

the  $\text{Mg}(\text{CpEt})_2$  precursor was heated to 90 °C contained in a stainless steel cylinder, respectively. Water was held in a stainless steel cylinder at room temperature and used as the reactant in thermal ALD process. The standard ALD process contained a sequential cycle of precursor dose/purge/reactant dose/purge, which can be expressed as time sequence of  $t_1$ :  $t_2$ :  $t_3$ :  $t_4$  in seconds.

The growth properties of the metal oxides were monitored by *in situ* QCM and *in situ* SE. A QCM sensor housed in a holder was held in the reaction chamber. The crystal was maintained at the same temperature for several hours to achieve thermal equilibrium. The QCM signal can be converted to the film thickness if the mass density of the target film is known. The thickness and optical properties of the deposited films on native Si substrates were evaluated by *in situ* spectroscopic ellipsometry (M-2000 Spectroscopic Ellipsometer, J.A. Woollam Co.). Measurements were done in the wavelength range between 245 and 1000 nm at an angle of incidence of 70° with respect to the substrate. The SE measurements as a function of time were acquired at 0.5 s intervals. Modeling was carried out using the CompleteEASE software package.[156] The data from deposited film samples were modeled using a three-layer model, comprising Si, native  $\text{SiO}_2$  and metal oxides. A temperature-dependent Si layer model from the CompleteEASE software library was used to fit the parameter of Si depending on the process temperature. The ZnO film was modeled through an oscillator model, which including a polynomial spline function (the psemi-m0 oscillator) and a Tauc-Lorentz oscillator. The  $\text{SnO}_x$  and MgO layers were modeled using a Lorentz oscillator and Sellmeier oscillator, respectively. The optical constants of the films were fitted in a Kramers–Kronig consistent manner.

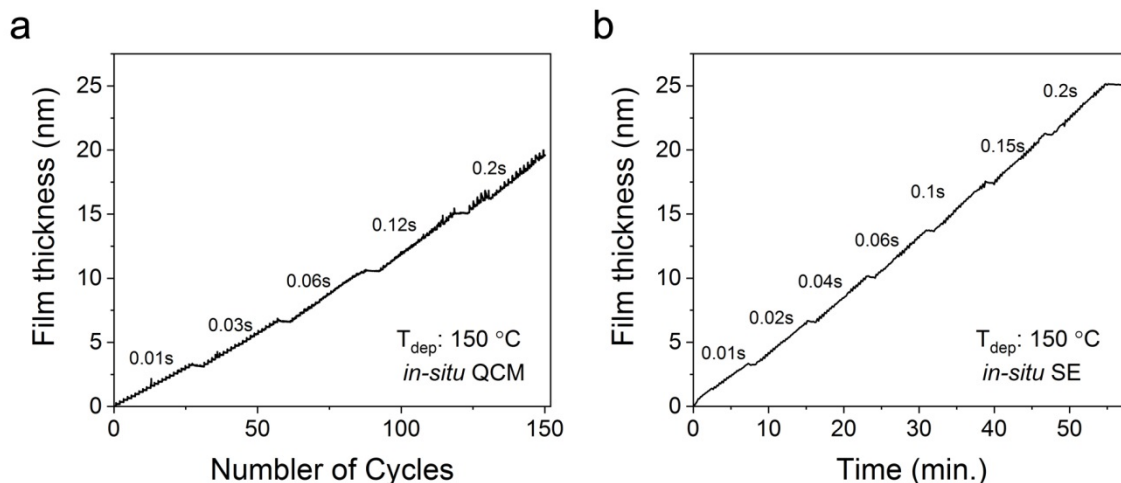
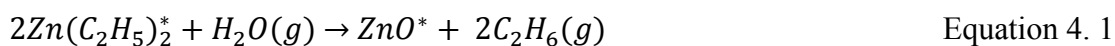


Figure 4. 1 a) *In situ* QCM and b) *in situ* SE measurements for ZnO deposition during thermal ALD cycles at 150 °C.

To examine the growth behavior, *in situ* measurements were performed to determine the conditions for the ALD growth of ZnO. Figure 4. 1 shows the pulse time tuning of ZnO deposited by thermal ALD acquired from *in situ* QCM and SE. The corresponding reaction mechanism of diethyl zinc (DEZ)[147, 148] reacting with co-reactant water (H<sub>2</sub>O) is[147]:



DEZ is a highly volatile precursor and is reactive towards H<sub>2</sub>O, thus ZnO can be easily deposited in the deposition temperature range of 100-200 °C.

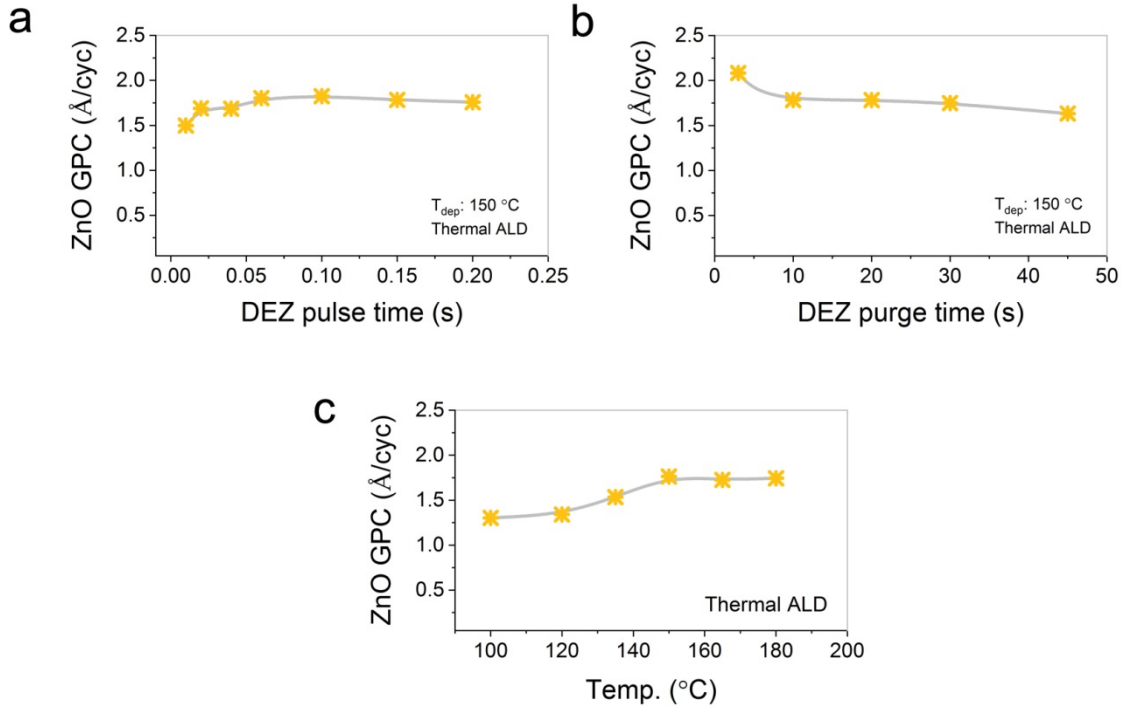


Figure 4. 2 Growth behavior of ZnO using thermal ALD, a self-limited reaction depending on a) DEZ pulse time, b) Ar purge time and c) temperature.

The DEZ precursor pulse time  $t_1$  was tuned from 0.01 to 0.2 s using time sequence:  $t_1$ : 10;  $t_3$ : 10 at 150  $^{\circ}\text{C}$ . Note  $\text{H}_2\text{O}$  pulse time  $t_3$  was kept constant as 0.06s which was sufficient as the oxygen source. To accelerate the tuning process while minimizing the material consumption, 20 repeating cycles were done for each parameter and the tuning could be finished within one ALD deposition. Figure 4. 1a reveals the linear growth of ZnO as a function of the time for each DEZ pulse time, indicating sustained layer-by-layer growth behavior. A similar growth behavior was found in Figure 4. 1b extracted from the SE data. Therefore, the growth per cycle (GPC) as a function of the DEZ pulse time can be evaluated and is shown in Figure 4. 2a. A typical self-limiting reaction was found where the growth rate of  $\sim 1.7\text{\AA}/\text{cycle}$  saturated with a precursor dose of 0.06 s at 150  $^{\circ}\text{C}$ . Therefore, the DEZ pulse time was fixed to 0.06 s to ensure saturation in subsequent experiments. The Ar purging time after the DEZ dose was also

investigated as shown in Figure 4. 2b. It also shows saturated growth characteristics when Ar purge time after DEZ pulse reaching 10s. Figure 4. 1c presents the GPC of ZnO as a function of deposition temperature ranging from 100 to 180 °C. The growth rate displays an increase from 100 to 150 °C with a slight plateau in the range of 150 to 180 °C. The growth rate varies from ~1.3 Å/cycle at 100 °C to ~1.7 Å/cycle at 150 °C, respectively.

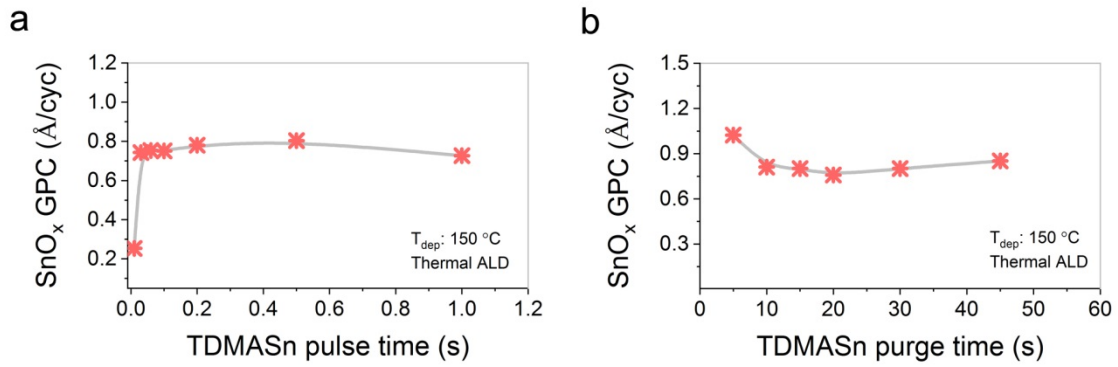
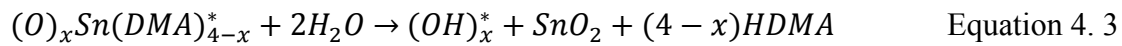
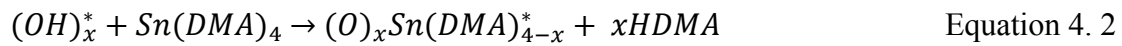


Figure 4. 3 Growth behavior of SnO<sub>x</sub> using thermal ALD, a self-limited reaction depending on a) TDMASn pulse time and b) Ar purge time.

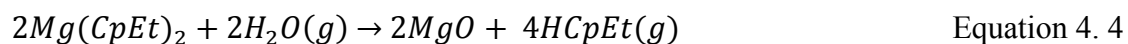
A similar recipe tuning method was also implemented in the case of SnO<sub>x</sub> deposition. Here, tetrakis (dimethylamino) tin (TDMASn) was used as Sn precursor and H<sub>2</sub>O as the oxygen source. The tin oxide (SnO<sub>2</sub>) deposited by TDMASn precursor with water as the co-reactant have reaction mechanism as following[185]:



DMA indicates the dimethylamino ligand, while HDMA is dimethylamine, \* representing the surface-bound species and  $x$  is the number of DMA ligands released during the TDMASn pulse. It has been suggested that the density of surface

hydroxylation is important for the initial adsorption of the precursor. The pulse time of TDMASn and the purge time after TDMASn exposure were investigated to determine the condition for saturated ALD of SnO<sub>x</sub> at 150 °C. The TDMASn precursor pulse time  $t_1$  was tuned from 0.01 to 1 s using time sequence:  $t_1$ : 10: 0.06: 10 at 150 °C. The saturated pulse time of Sn precursor was determined to be 0.15s as shown in Figure 4. 3a. The saturated growth rate for SnO<sub>x</sub> was found to be ~0.7 Å/cycle. The growth rate with increasing Ar purge time after TDMASn exposure was then studied by fixing TDMASn pulse time to be 0.15s, as shown in Figure 4. 3b. A time sequence of 0.15:  $t_2$ : 0.06: 10 was used and  $t_2$  was tuned from 5 to 45 s. Purging time was optimized to be 10 s for supporting saturated growth characteristics of SnO<sub>x</sub>.

In the case of MgO deposition, higher volatility of ethylcyclopentadienyl magnesium (Mg (CpEt)<sub>2</sub>) was used as Mg precursor and H<sub>2</sub>O as an oxygen source to deposit binary magnesium oxide (MgO) [150], following the proposed MgO ALD reaction:



The above depositions process were performed in the temperature range of 125-400 °C.

Figure 4. 4a shows that the growth rates of the MgO film were saturated at approximately 1.1 Å/cycle at Mg (CpEt)<sub>2</sub> pulse time of 0.5s. For the pulse time tuning, a time sequence:  $t_1$ : 10: 0.06: 10 was applied with  $t_1$  ranging from 0.01 to 1.5 s and deposition was performed at 150 °C. Figure 4. 4b shows the changes in the GPC as a function of the Ar purge time after Mg (CpEt)<sub>2</sub> exposure. The GPC of MgO film decreases gradually from 5 s to 20 s to a plateau over 20 s. The saturation growth should take place at 20 s although the change in GPC from 5 s to 20 s is not significant. Figure 4. 4c presents the growth rates of the MgO with respect to deposition temperature ranging from 100 to 180 °C. The growth rate displays a plateau from 100

to 150 °C with a slight increase from 150 to 180 °C. The growth rate varies from ~1.1 Å/cycle at 150 °C to ~1.2 Å/cycle at 180 °C, respectively.

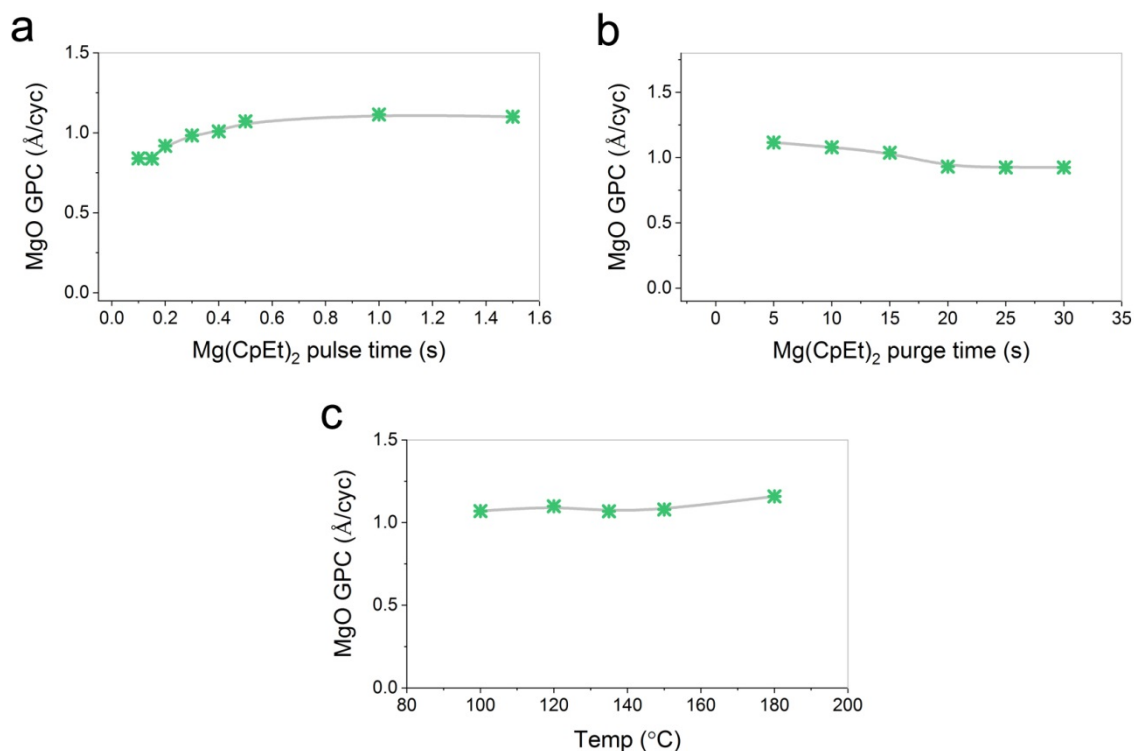


Figure 4. 4 Growth behavior of MgO using thermal ALD, a self-limited reaction depending on a) (Mg(CpEt)<sub>2</sub> pulse time, b) Ar purge time and c) temperature.

#### 4.2.2 Deposition and properties of ZnSnO

In this study, the synthesis of ternary oxides films was carried out using supercycle ALD, which consists of alternating subcycles of binary oxide depositions. ZTO thin films with different compositions were synthesized at a substrate temperature of 150 °C. The ALD process contained a Zn/ Sn: Ar: H<sub>2</sub>O: Ar cycle with pulse lengths of 0.06/0.15:10:0.06:10 s, respectively. A super-cycle scheme of ZTO consisted of ZnO and SnO<sub>x</sub> sub-cycles were employed to tune the composition of Sn/ (Zn + Sn). Four different Zn to Sn sub-cycles ratio of 5/1, 4/1, 3/1, 2/1 were investigated in this thesis, with nominal growth rate per cycle (GPC) were 1.3, 1.0, 0.7, 0.5 Å, respectively. The optical properties of the ZTO films were fitted through an oscillator model, which



including a polynomial spline function (the psemi-m0 oscillator) and a Tauc-Lorentz oscillator, to represent the optical constants of the films in a Kramers–Kronig consistent manner.

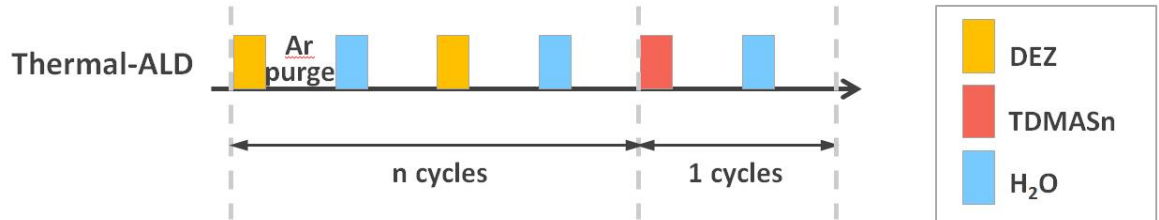


Figure 4. 5 Schematic of super-cycle method used for ternary ZnSnO deposition by thermal ALD.

Based on previous reports, a ZTO buffer layer with a Sn-content of 0.1~0.3 would provide a favorable band alignment with CZTS absorber. Thus, the composition of the ZTO films was varied by tuning the ratio of ZnO and SnO<sub>x</sub> sub-cycles in the 5:1 to 2:1 range. The pristine ZnO and SnO<sub>x</sub> binary metal oxides were also synthesized for comparison purposes. Silicon substrates were included in the ZTO deposition run to evaluate the thickness and optical properties by *in situ* spectroscopic ellipsometry (SE). It should be noted that the ALD process on c-Si could be different compared to that on CZTS, in particular for the initial growth cycles. The Sn content, defined as Sn/(Zn + Sn), was found to be 0.17-0.27 for the ZTO films depending on the sub-cycle ratio as listed in Table 4. 1.

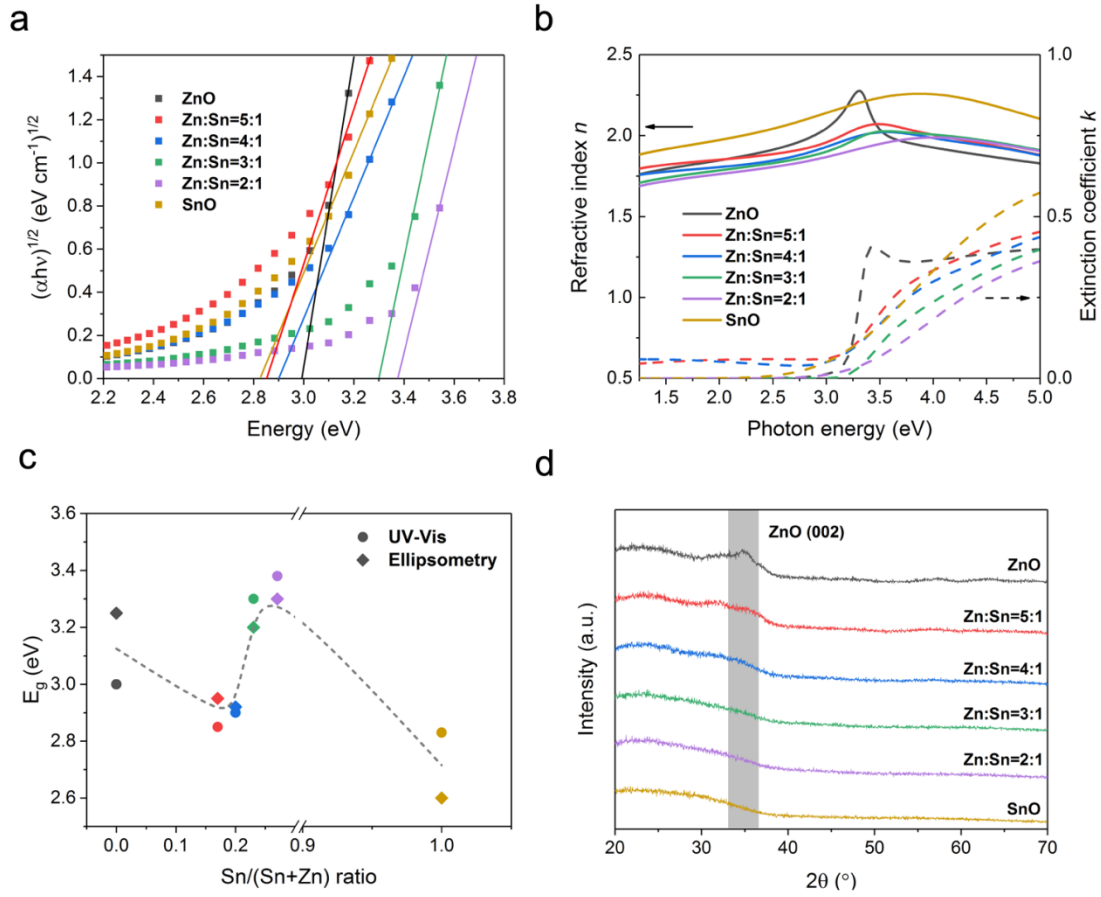


Figure 4. 6 a) Tauc plot and (b) refractive index and extinction coefficient as a function of the photon energy for the ZTO films grown using various Zn:Sn sub-cycle ratios. The absorption coefficient for the Tauc plot was determined from transmission-reflection while the optical properties were determined from spectroscopic ellipsometry measurements. The c)  $E_g$  extracted from the Tauc plot analysis and spectroscopic ellipsometry as a function of the relative Sn ratio. d) GIXRD pattern of the ZTO films as a function of Zn:Sn sub-cycle ratio.

The optical properties of the ZTO films with different atomic compositions on glass were characterized by transmission-reflection measurements and the results are shown in Figure 4. 6a. The bandgap was extracted from the Tauc plot using the following equation  $(\alpha h\nu)^n = A(h\nu - E_g)$ , where  $n = 0.5$  for amorphous films and  $n = 2$  for direct-gap crystalline films. Here  $n = 0.5$  was used for calculation as the ZTO films

were identified to be amorphous by grazing incidence X-ray diffraction (GIXRD) measurements which are shown in Figure 4. 6d. The absorption coefficient  $\alpha$  was derived from a simplified formula  $\alpha = d^{-1} \ln (T^{-1})$ , where  $d$  is the thickness of ZTO films and  $T$  is the transmittance from the transmission-reflection measurements. For comparison, the bandgap was also determined from the extinction coefficient related absorption coefficient by SE measurement. The absorption coefficient was calculated from the well-known relation  $\alpha = 4\pi k/\lambda$ , where  $k$  represents the imaginary part of the complex dielectric constant and  $\lambda$  is the light wavelength. Figure 4. 6c provides the bandgap extracted from transmission-reflection measurements with those determined by spectroscopic ellipsometry as a function of Sn content of ZTO films. With increasing Sn incorporation, the bandgap of ZTO films first drops from 3.2 eV for pure ZnO to 2.9 eV for  $\text{Zn}_{0.80}\text{Sn}_{0.20}\text{O}$ , then increases again to 3.3 eV for  $\text{Zn}_{0.77}\text{Sn}_{0.23}\text{O}$  and finally dropping to 2.7 eV for pure  $\text{SnO}_x$ .

Table 4. 1 Properties of ZnSnO thin films with different compositions compared to the pure ZnO and  $\text{SnO}_x$  films.

Sampl e	Zn/Sn ratio	Sn /( Sn +Zn) ratio	Sn /( Sn +Zn) by ICP	GPC ( Å/cycle)	Bandgap (eV)	Resistivity ( $\Omega\cdot\text{cm}$ )
ZnO	0	0	0	1.7	3.2	$6.53\times 10^{-2}$
ZTO	5:1	0.17	0.17	1.3	2.9	N/A
ZTO	4:1	0.2	0.2	1.0	2.9	N/A
ZTO	3:1	0.25	0.23	0.7	3.3	N/A
ZTO	2:1	0.33	0.27	0.5	3.4	N/A
SnO	1	1	1	0.7	2.7	N/A

The SE measurements were also used to extract the refractive index ( $n$ ) and extinction coefficient ( $k$ ) values of the ZTO films. Figure 4. 6b shows the  $n$  and  $k$

values as a function of the photon energy for different ZTO film compositions. The  $n$  (at 1.98 eV) of ZTO films decreased for higher Sn content. However, it increases significantly for pure  $\text{SnO}_x$  without Zn doping. For pure ZnO, a sharp absorption edge of the extinction coefficient was found at  $\sim 3.3$  eV, which agrees with the bandgap of intrinsic ZnO reported in the literature.[186] The presence of the excitonic peak observed at 3.4 eV indicates that the ZnO film was polycrystalline.[111, 187] This feature is consistent with the diffraction peaks of ZnO evaluated by GIXRD which exhibits a hexagonal wurtzite structure, as illustrated in Figure 4. 6d. Nevertheless, the intermediate ZTO and pure  $\text{SnO}_x$  films were believed to be amorphous or nano-crystals with broad diffraction peak at around  $34^\circ$ , similar to reported in the literature.[188-190] The amorphous nature of these films can be likely attributed to the different cation valences and crystal structures of each binary material.[191] This amorphous nature enables excellent stability and uniformity over large areas, and thus providing reproducible device performance.[188]

#### 4.2.3 Deposition and properties of ZnMgO

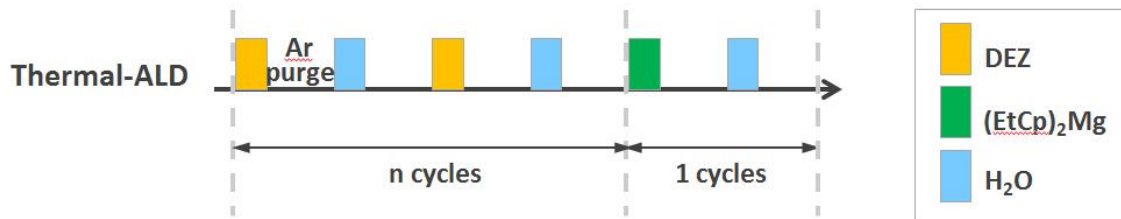


Figure 4. 7 Schematic of the super-cycle method used for ternary ZnMgO deposition by thermal ALD.

A supercycle ALD method was also used for the synthesis of ternary ZnMgO films. Thin films were deposited with different Mg content ( $\text{Mg} / \text{Mg} + \text{Zn}$ ) at a substrate temperature of  $150^\circ\text{C}$ . The substrates used were glass and silicon wafers with native

oxide (~1.5 nm thickness). The diethylzinc (DEZ, Sigma-Aldrich), bis(ethylcyclopentadienyl)magnesium [Mg(CpEt)<sub>2</sub>, Strem Chemicals] were used as Zn and Mg precursor, respectively. The DEZ precursor was kept at room temperature while the Mg(CpEt)<sub>2</sub> precursor was heated to 90 °C contained in a stainless steel cylinder. Deionized water (H<sub>2</sub>O) served as an oxidizing source in thermal-ALD. The ZnMgO ternary films were deposited by tuning the ZnO: MgO ratio with a super-cycle approach, as illustrated in Figure 4. 7. A typical super-cycle consisted of alternating *m* cycles of the ZnO process followed by one cycle of the MgO process. The desired thickness was achieved by looping of the ALD supercycles. For thermal-ALD deposition of ZnMgO, the ZnO cycle consisted of a processing sequence of 0.06 s DEZ pulse, 10 s Ar purge, 0.06 s deionized water pulse, 10 s Ar purge (0.06 s/10 s/0.06 s/10 s). The MgO cycle was performed at a time sequence of 0.5 s/10 s/0.06 s/10 s with longer Mg precursor time to reach the saturated ALD growth. Three different Zn to Mg sub-cycles ratio of 2/1, 4/1, 9/1 were investigated in the thesis, with nominal growth rate per cycle (GPC) were 1.4, 1.6, 1.7 Å/cycle, respectively. The optical properties of the ZMO films were fitted through an oscillator model, which including a polynomial spline function (the psemi-m0 oscillator) and a Tauc-Lorentz oscillator, to represent the optical constants of the films in a Kramers–Kronig consistent manner.

Table 4. 2 Growth properties of ZnMgO thin films with different compositions.

Sample	Zn/Mg Ratio	Mg/(Mg+Zn)	Mg/(Mg+Zn) by ICP	cycles	Thickness (nm)	GPC ( Å/cycle)
ZnO	0	0	0	200	34	1.7
ZMO	9:1	0.1	0.101	300	52	1.7
ZMO	4:1	0.2	0.201	300	48	1.6
ZMO	2:1	0.33	0.349	300	42	1.4
MgO	1	1	1	300	33	1.1

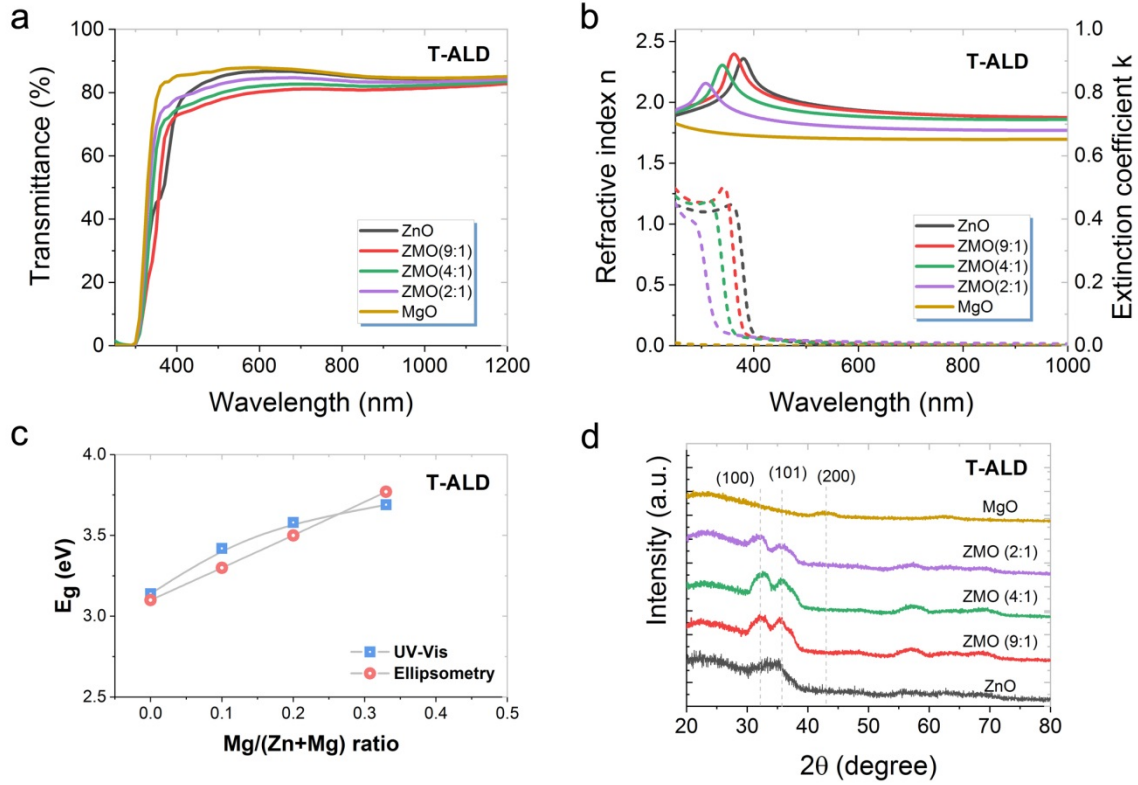


Figure 4. 8 a) Transmittance and (b) refractive index and extinction coefficient as a function of the wavelength for the ZMO films grown using various Zn:Mg sub-cycle ratios determined from spectroscopic ellipsometry measurements. The c)  $E_g$  extracted from the Tauc plot analysis and spectroscopic ellipsometry as a function of the relative Mg ratio. d) GIXRD spectra of the ZMO films as a function of Zn:Mg sub-cycle ratio.

The optical transmission of the ZMO films with different atomic compositions on glass was characterized by transmission-reflection measurements and the results are shown in Figure 4. 8a. The transparency exhibits large discrepancy in the visible light range between ZMO compounds and pure oxides, most likely due to the samples used with different thicknesses, where thinner films have higher transparency. Therefore, it is more reasonable to compare the band edge of different films by evaluating the absorption edge from the transmittance spectra. The near band-edge wavelength for pristine ZnO is around 375 nm, while it moves to the short wavelength as the Mg ratio increases, indicating that the addition of Mg increases the bandgap. This phenomenon

was further confirmed by the bandgap extracted from the ellipsometry measurement shown in Figure 4. 8b. For comparison purposes, Figure 4. 8c provides the bandgap extracted from transmission-reflection measurements with those determined by spectroscopic ellipsometry as a function of Mg content of ZMO films. With increasing Mg incorporation, the bandgap of ZMO increases almost linearly from ~3.2 eV to ~3.8 eV for  $\text{Zn}_{0.65}\text{Mg}_{0.35}\text{O}$ . Therefore, the bandgap of ZMO compounds can be easily tuned by varying the Mg content.

The SE measurements were also used to extract the refractive index ( $n$ ) and extinction coefficient ( $k$ ) values of the ZMO films shown in Figure 4. 8b. It reveals the refractive index and extinction coefficient as a function of the wavelength for the ZMO films grown using various Zn:Mg sub-cycle ratios. The  $n$  (at 632 nm) of ZnO and MgO is ~2.0 and ~1.7, respectively. The  $n$  values of the ZMO compounds were between the binary material and show decreasing trend with the Mg content. With increasing Mg content in ZMO films, the excitonic peak observed for the extinction coefficient seems to be broadened. This could be attributed to the alloy composition fluctuation in ternary materials, thereby making the absorption edges of ZMO alloys less distinct than ZnO.[192] The presence of the excitonic peak observed at 3.4 eV indicates that the ZnO film was polycrystalline.[111, 187] This feature is consistent with the diffraction peaks of ZnO evaluated by GIXRD which exhibits a hexagonal wurtzite structure, as illustrated in Figure 4. 8d. The MgO film was found to be overall amorphous with little nanocrystalline because of the presence of (200) peak in low intensity. Here, the low intensity of the signature peak of all the films could be the result of very thin (<50 nm) film used for GIXRD characterization. The intermediate ZMO films show the characteristic peak of (100) and (101), indicating  $\text{Zn}_{1-x}\text{Mg}_x\text{O}$  retains the ZnO wurtzite structure for Mg content up to  $x \approx 0.35$ .[193]

The carrier concentration ( $n$ ), Resistivity ( $\sigma$ ) and Hall mobility ( $\mu$ ) of ZnMgO thin films were measured by the van der Pauw method employing indium contacts at room temperature and the results are listed in Table 4. 3. With the Mg content increasing up

to 0.2, the resistivity was found to increase in the ZMO films while the carrier mobility was found to decrease. The decreases in both carrier concentration and the electron mobility contribute to the increase in resistivity. The decrease in carrier concentration has been variously attributed to both an increasing donor activation energy due to a larger effective mass[194] or change of band structure[195] and a lowering of the active donor concentration due to composition enrichment.[194] For the decrease in mobility, both an increased alloy scattering[196] and enhanced grain boundary scattering has been suggested. However, when the Mg content was larger than 0.2, the hall signal could hardly be detected based on the used measurement configuration due to the large resistivity of the thin films.

Table 4. 3 Optical and electrical properties of ZnMgO thin films with different compositions.

<b>Sampl e</b>	<b>Zn/Mg Ratio</b>	<b>Mg/(Mg+Zn) by ICP</b>	<b>Band gap (eV)</b>	<b>Carrier concentration (cm<sup>-3</sup>)</b>	<b>Resistivity (Ω·cm)</b>	<b>Hall mobility</b>
ZnO	<b>0</b>	0	3.14	$-9.10 \times 10^{18}$	$6.53 \times 10^{-2}$	6.44
ZMO	<b>9:1</b>	0.101	3.29	$-8.54 \times 10^{18}$	$1.11 \times 10^{-1}$	6.59
ZMO	<b>4:1</b>	0.201	3.48	$-5.45 \times 10^{16}$	$1.64 \times 10^1$	2.44
ZMO	<b>2:1</b>	0.349	3.76	N/A	N/A	N/A
MgO	<b>1</b>	1	7.30	N/A	N/A	N/A

### 4.3 Application of ZnSnO as buffer layer on CZTS solar cell

#### 4.3.1 Experiment

CZTS absorbers were deposited onto a Mo-coated soda-lime glass substrate from co-sputtered Cu/ZnS/SnS precursors by using a magnetron sputtering system (AJA International, Inc., Model ATC-2200). The composition of CZTS absorbers was



controlled to be Cu-poor ( $\text{Cu}/(\text{Zn}+\text{Sn}) = 0.88$ ) and Zn-rich ( $\text{Zn}/\text{Sn} = 1.18$ ) as described in Section 3.1.1. The films were then subjected to the sulfurization process in combined sulfur and SnS atmosphere at  $560\text{ }^{\circ}\text{C}$  with a heating rate of  $15\text{ }^{\circ}\text{C min}^{-1}$  for 3 min. Reference devices with 50 nm CdS buffers were fabricated using chemical bath deposition. For ZTO buffer devices, after sulfurization, the samples were stored in a nitrogen box or immediately transferred into the ALD reactor to deposit ZTO thin films. Different thickness and composition of ZTO buffer layers were applied to investigate their effects on the device performance. An i-ZnO/ITO (50 nm/210 nm) top contact was then deposited by radio frequency sputtering, followed by Al grids using evaporation. An antireflection coating of 110 nm  $\text{MgF}_2$  was deposited on the best performing devices by thermal evaporation and  $0.224\text{ cm}^2$  solar cells were finally defined by mechanical scribing.

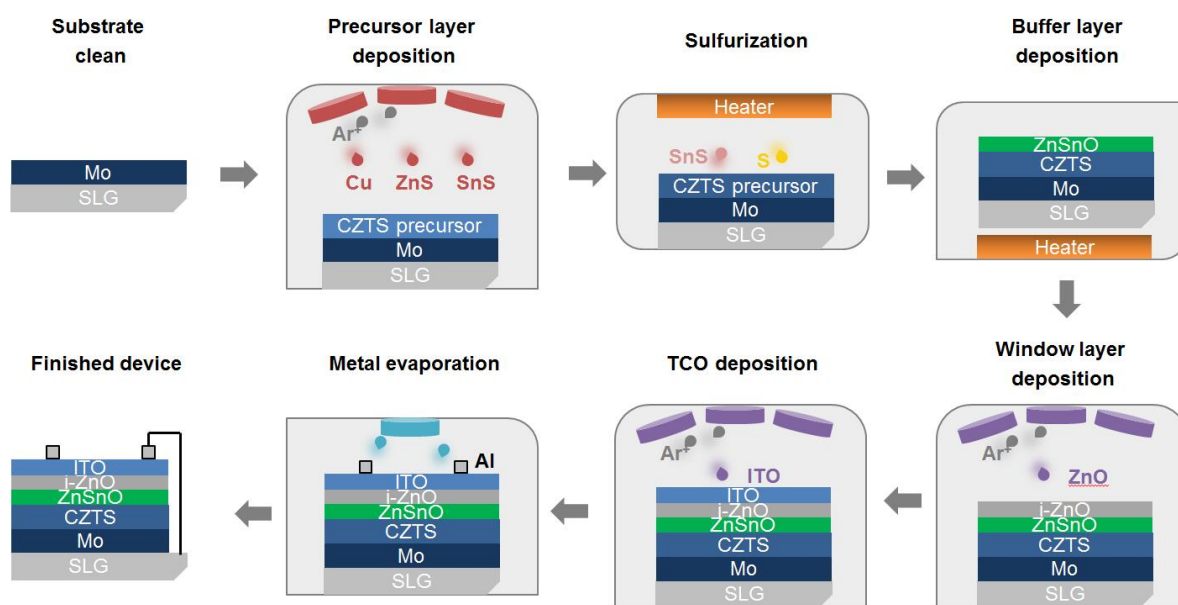


Figure 4. 9 Schematic of the fabrication of CZTS/ZnSnO thin film solar cell.

#### 4.3.2 Influence of ZnSnO thickness on the device properties

The effect of the buffer layer thickness on the CZTS/ZTO cell performance was examined and the results are shown in Figure 4. 10. A ZTO thickness in the 10 - 50 nm range was investigated by changing the number of ALD cycles while keeping the

Zn:Sn pulse ratio constant at 3:1. Representative  $J$ - $V$  and EQE curves are shown in Figure 4. 11 and corresponding one-Sun  $I$ - $V$  parameters are summarized in Table 4. 4. The results indicate that a thicker ZTO buffer layer does not necessarily result in a better performance. The general trends of  $V_{OC}$  and  $J_{sc}$  show no significant difference for ZTO buffers of 10, 20, 30 nm thickness from their statistical parameters. However, those parameters drop rapidly when the thickness of the ZTO layers was increased to 50 nm. The decline of  $J_{sc}$  for thicker ZTO buffer layers could be attributed to optical losses in the 400 - 450 nm range as is evident from the EQE measurements shown in Figure 4. 11b.

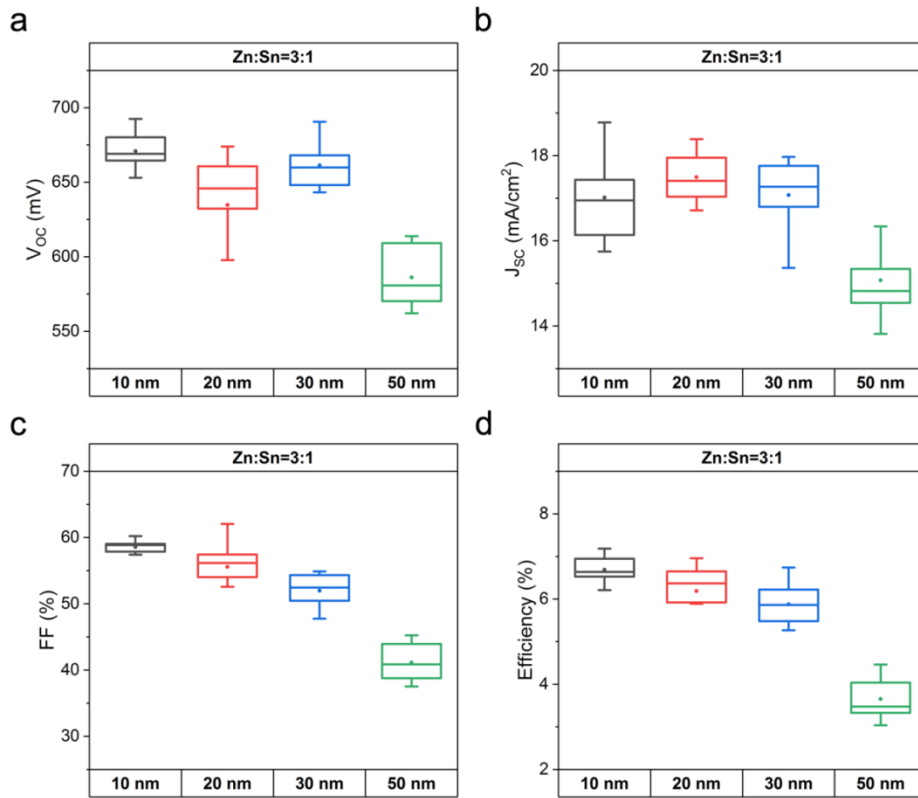


Figure 4. 10 a-d) Box-plots of performance parameters of CZTS cells for various ZTO buffer layer thickness. The Zn/Sn ratio was 3/1 during all ALD depositions. Box, horizontal bars, point symbols and indicate 25/75 percentile, min/max and mean values, respectively.

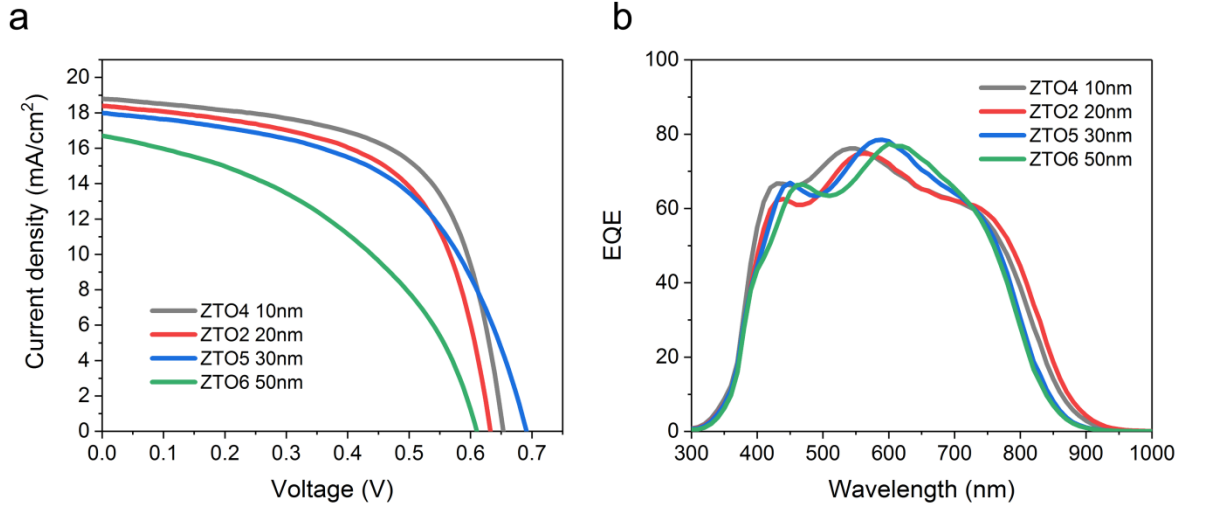


Figure 4. 11  $J$ - $V$  curves b) External quantum efficiency of the CZTS solar cells with different thickness of ZTO buffers.

Specifically, one can note that the  $FF$  value, as well as the PCE, decreases gradually as ZTO buffer layer thickness increases, likely due to the increased series resistance from the fitting parameter in Table 4. 4. J. Lindahl *et al.* reported similar trends for  $FF$  changes with thicker ZTO buffer applied on CIGS solar cells.[131] A part of the lower  $FF$  can be explained by the corresponding lower  $V_{OC}$  for the ZTO samples, as the effect of  $V_{OC}$  can be obtained by the following empirical relationship (ignoring the effect of series and shunt resistance):[197]

$$FF = \frac{v_{oc} - \ln(v_{oc} + 0.72)}{v_{oc} + 1} \quad \text{Equation 4. 5}$$

where  $v_{oc}$  is the normalized voltage defined as  $V_{OC} / (AkT/q)$ .  $A$  is the diode ideality factor and the parameter  $kT/q$  is approximately 26 mV at room temperature. Using this relationship one can calculate that the  $\sim 40$  mV lower  $V_{OC}$  for the CZTS/ZTO solar cell with the thickest ZTO buffer layer only accounts for a 1.4% absolute lower  $FF$ . Hence, the drop in  $V_{OC}$  is not the dominant reason for the dramatic loss of  $FF$ . For CZTS/ZTO

devices, no linear change in  $R_s$  and  $R_{sh}$  was observed when thicker ZTO buffer layers were employed probably due to the low accuracy in the extracted  $R_s$  and  $R_{sh}$  value in low-performance devices. The intrinsic factors of the shunt resistance change with thickness still need further structural and electrical characterization to be fully understood.

### 4.3.3 Influence of ZnSnO composition on the device properties

Next, a series of CZTS solar cells were fabricated to test the performance of the ALD-ZTO buffer layer at the solar cell device level and compare it to devices with the standard CdS buffer layer grown by CBD as a reference. For the solar cells with the ZTO buffer layers, the ratio of the ZnO and SnO<sub>x</sub> sub-cycle was tuned from 2:1 to 4:1 and the resulting solar cell parameters are shown in Figure 4. 12. The thickness of the ZTO layers was kept constant at 20 nm to exclude any thickness effect. In terms of  $V_{oc}$ , a clear benefit from ZTO buffer was observed for higher Sn contents (Zn: Sn = 2:1 and 3:1) as can be seen in Figure 2a. Table 1 summarizes the parameters of ALD-ZTO buffer layer and the one Sun device parameters obtained from the champion device in each group. A strong dependence of the  $V_{oc}$  on the buffer composition is observed. For the devices with Zn:Sn pulse ratio of 4:1, the  $V_{oc}$  was comparable to the CdS reference. With increasing incorporation of Sn, the  $V_{oc}$  started to increase. A champion  $V_{oc}$ , 50 mV higher than the CdS control device, was found for a Zn<sub>0.73</sub>Sn<sub>0.27</sub>O buffer layer which was grown using a Zn:Sn pulse ratio of 2:1 during the ALD process. This trend indicates that an effective band alignment might be introduced when the composition of ZTO is properly tuned.

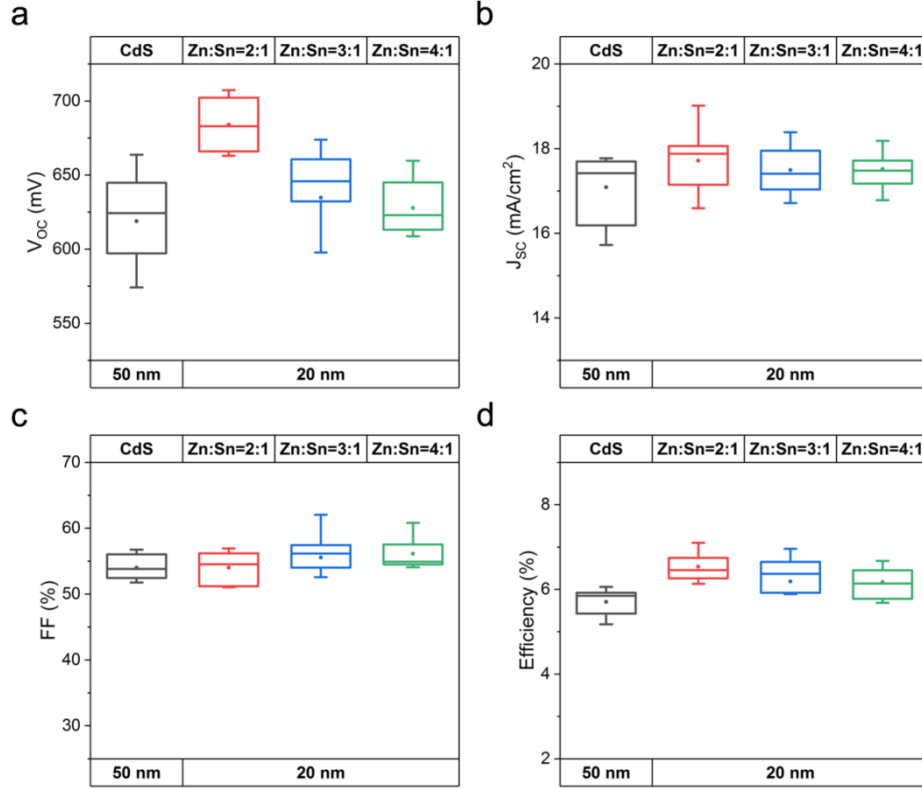


Figure 4. 12 Box-plot of the one-sun solar cell performance parameters of CZTS cells made with the various compositions of the ZTO buffer layer. 10 CZTS solar cells were fabricated per experimental condition. Box, horizontal bars, point symbols and indicate 25/75 percentile, min/max and mean values, respectively. Results obtained for a CZTS device with a CdS buffer layer are included as a reference as well.

The CZTS/ZTO devices typically yield a higher  $J_{sc}$  than the CZTS/CdS control device as shown in Figure 2b. This is mainly due to a higher absorption in the short wavelength range as can be seen in the external quantum efficiency (EQE) curves shown in Figure 4. 14b and can be attributed to a higher transparency of the ZTO ( $E_g=3.3$  eV) film compared to the reference CdS ( $E_g=2.4$  eV) buffer layer. Also, one can note the absorption loss for CZTS/ZTO in the wavelength range of 500 to 800 nm, which could be attributed to the interference of incident light. Despite that, the overall  $J_{sc}$  of the CZTS/ZTO devices still improves due to the gain in the short wavelength range. Besides, the  $J_{sc}$  improvement shows no significant variance among devices

with different compositions of ZTO buffers.

Table 4. 4 Corresponding maximum values of device parameters of CZTS/CdS cells and CZTS/ZTO cells with ZTO buffer in different composition and thickness

Sample	Thickness (nm)	Actual Sn content	Pulse ratio Zn:Sn	$V_{OC}$ (mV)	$J_{SC}$ (mA $\text{cm}^{-2}$ )	FF(%)	Eff (%)	$R_s$ ( $\Omega \text{ cm}^2$ )	$R_{sh}$ ( $\Omega \text{ cm}^2$ )
CdS	50	-	-	624	17.7	54.9	6.06	1.9	341
ZTO1	20	0.27	2:1	665	19.0	56.2	7.10	1.5	200
ZTO2	20	0.23	3:1	632	18.4	60.0	6.96	1.3	235
ZTO3	20	0.20	4:1	625	18.6	57.5	6.67	1.3	201
ZTO4	10	0.23	3:1	653	18.8	62.4	7.65	2.0	253
ZTO5	30	0.23	3:1	690	18.0	54.3	6.74	7.2	255
ZTO6	50	0.23	3:1	609	16.7	43.9	4.46	4.9	162

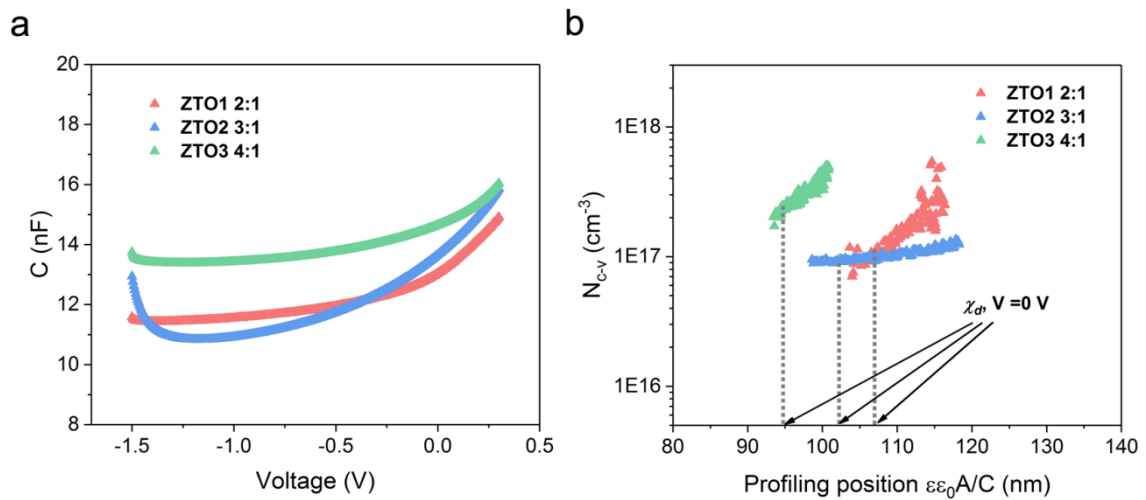


Figure 4. 13 a)  $C$ - $V$  curves of the CZTS devices with different composition of ZTO buffer. b) Free carrier density and depletion width derived from the  $C$ - $V$  curves.

To further investigate the  $p$ - $n$  junction quality of CZTS/ZTO devices, capacitance-frequency ( $C$ - $f$ ), capacitance-voltage ( $C$ - $V$ ) measurements were performed. Figure 4. 14c shows the measurements of the diode capacitance as a function of frequency at room temperature which was used to determine the densities and energy levels of trap states present in the depletion region. At high frequencies, the device capacitance spectra converge to a low capacitance value, namely the geometric capacitance of the cell ( $C_g$ ). In the geometric capacitance regime, the device behaves like an insulator along with the dielectric freeze-out effect occurring in the CZTS absorber layer, mainly because the electrical conductivity is too low and the charging and discharging of the defect can no longer follow the applied AC frequency.[198] At low frequencies, the capacitance plateau denoted as the depletion capacitance ( $C_d$ ) is found for the devices, which is relevant to the charging and discharging of the interface and bulk defect levels present in the depletion region.[199] It should be noted that the CZTS/ZTO device with increased Sn content ZTO buffer had a lower  $C_d$ . This suggests a significantly reduced interface recombination occurred at CZTS/ZTO heterojunction with higher Sn content ZTO buffer, contributing to the higher  $V_{OC}$  value.

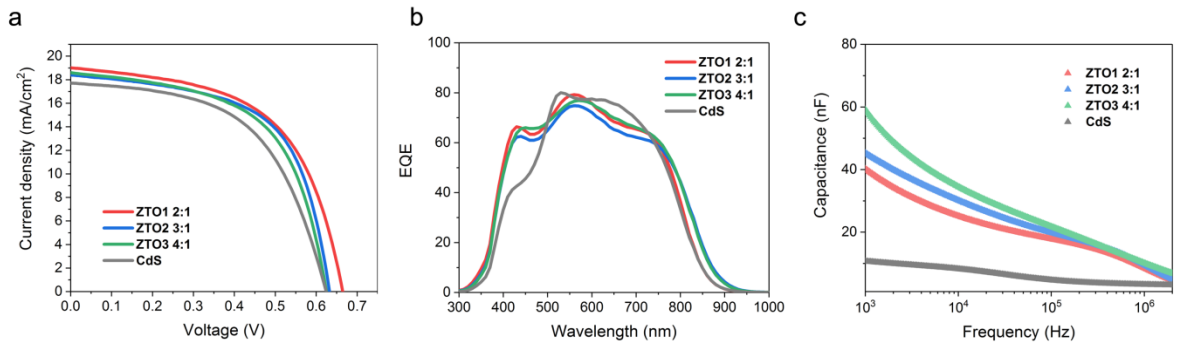


Figure 4. 14 a) The current density-voltage, b) External quantum efficiency, and c) Room-temperature capacitance-frequency characteristics of the CZTS solar cells with different compositions of ZTO buffer layer compared to corresponding CdS control device, measured with 0 V (DC) and 0.01 V (AC) bias in the dark.

More heterojunction information including carrier density and depletion width of CZTS devices with different ZTO buffer layer compositions was extracted from  $C$ - $V$  measurements performed with a -1.5 to 0.3 V bias voltage (see Figure 4. 13a, b). It is noted that the addition of Sn in the ZTO buffer increased the depletion width from 95 nm to 107 nm. Besides, a CZTS device with a  $\text{Zn}_{0.80}\text{Sn}_{0.20}\text{O}$  buffer layer was found to have a free carrier concentration of  $2.38 \times 10^{17} \text{ cm}^{-3}$ , while the value for solar cells with a  $\text{Zn}_{0.77}\text{Sn}_{0.23}\text{O}$  and  $\text{Zn}_{0.73}\text{Sn}_{0.27}\text{O}$  buffer layers was found to be slighter lower at  $0.91 \times 10^{17} \text{ cm}^{-3}$  and  $1.07 \times 10^{17} \text{ cm}^{-3}$ , respectively. Thus, the devices with a  $\text{Zn}_{0.77}\text{Sn}_{0.23}\text{O}$  and  $\text{Zn}_{0.73}\text{Sn}_{0.27}\text{O}$  buffer layer have a larger depletion width and lower free carrier concentration than the devices with a  $\text{Zn}_{0.80}\text{Sn}_{0.20}\text{O}$  buffer layer.

The series and shunt resistance,  $R_s$  and  $R_{sh}$  were extracted from the  $J$ - $V$  curves using a two-diode model[200] and the results are summarized in Table 4. 4. Note that a 20 nm ZTO buffer layer employed in this series induces a slight decrease of  $R_s$  and  $R_{sh}$  when compared to the 50 nm CdS buffer layer. Therefore, the  $FF$  for all the CZTS/ZTO samples was comparable to the control samples. Consequently, the overall power conversion efficiencies (PCEs) of all CZTS/ZTO cells was improved due to the contribution from a higher  $J_{sc}$  and  $V_{oc}$ . Devices using Zn:Sn ratio of 2:1 and 3:1 both demonstrate a higher performance than the control devices.

#### 4.3.4 Influence of heterojunction interface on the device properties

Figure 4. 15a shows the schematic of CZTS/CdS and CZTS/ZnSnO solar cell structures presented in this thesis. As aforementioned, the devices using an ALD ZTO buffer layer with the Zn:Sn ratio of 2:1 and 3:1 demonstrate comparable performance, which is higher than devices with a CdS buffer layer. With the same quality absorber layer that yielded a 6.9 % CZTS solar cell with a CdS buffer layer, I demonstrated the highest solar cell efficiency using a ZTO buffer layer which was grown using a Zn:Sn ratio of 3:1 and had a thickness of 10 nm. The  $J$ - $V$  characteristics of the champion solar cells with a ZTO and CdS (reference) buffer layers are shown in Figure 4. 15b. For



CZTS/ZTO device, it shows a total-area efficiency of 8.2% without an anti-reflection coating (ARC) and a 9.3% efficiency with evaporated 110 nm MgF<sub>2</sub> ARC. The  $J_{sc}$ ,  $V_{oc}$ , and  $FF$  of this device were measured to be 20.5 mA/cm<sup>2</sup>, 720 mV, and 63.5% respectively. The  $V_{oc}$  of CZTS/ZTO device without an ARC is significantly increased by 56 mV compared to the control CZTS/CdS reference, with a relative  $V_{oc}$  improvement of ~10%. This enhancement can be attributed to the more favorable ‘spike-like’ CBO at CZTS/ZTO interface as well as interface defect passivation, which correlated to the decreased ideality factor ( $A$ ) and saturation current density ( $J_0$ ) of the device as shown in Table 4. 5. The origin of this passivation and favorable band alignment effect will be discussed in the following part.

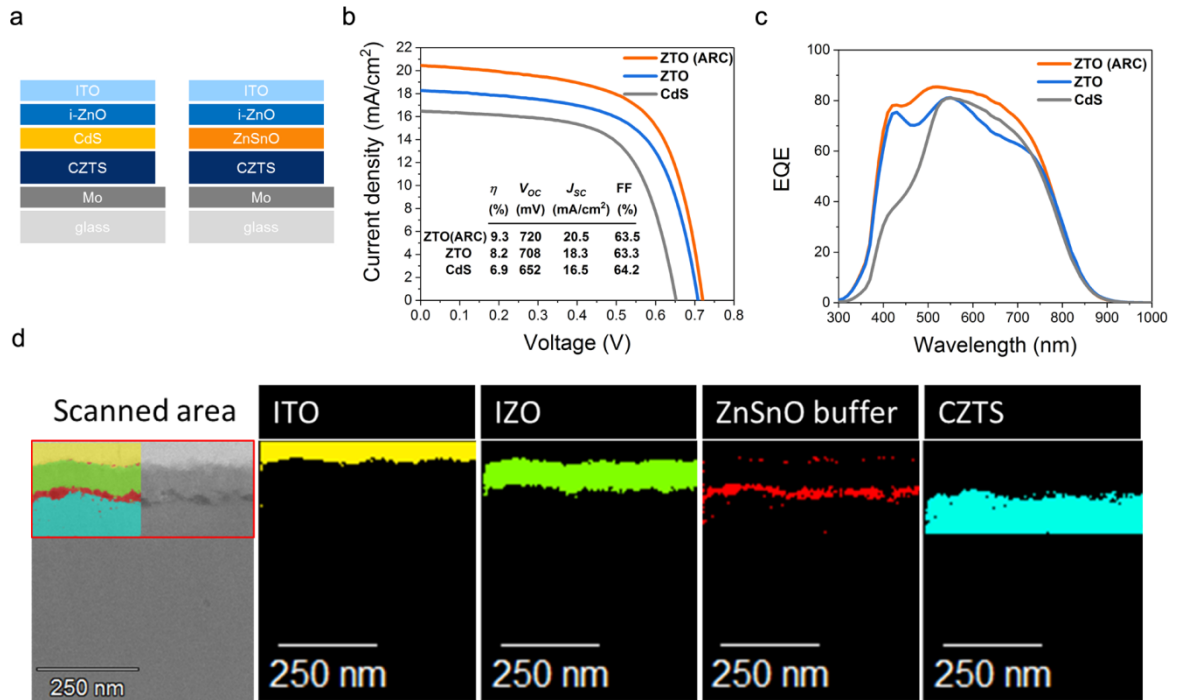


Figure 4. 15 a) The schematic of CZTS/CdS and CZTS/ZnSnO solar cell structures used in this work. b)  $J-V$  characteristics and c) EQE of the champion CZTS/ZnSnO solar cell with and without ARC compared with CZTS/CdS reference solar cell without ARC. d) High angle annular dark-field (HAADF) scanning TEM image of the enlarged CZTS/ZTO/i-ZnO/ITO stack (left) and corresponding estimated phase structure from the EDS mapping (right) of the best-performing CZTS/ZnSnO solar cell.

Table 4. 5 Corresponding values of photovoltaic parameters of the champion CZTS/ZTO solar cells compared to the champion CZTS/CdS reference.

Cell	$V_{oc}$ (mV)	$J_{sc}$ (mA cm <sup>-2</sup> )	$FF$ (%)	Eff (%)	$R_s$ ( $\Omega$ cm <sup>2</sup> )	$R_{sh}$ ( $\Omega$ cm <sup>2</sup> )	$A$	$J_0$ (mA cm <sup>-2</sup> )
<b>ZTO(ARC)</b>	720	20.4	63.5	9.34	0.40	669	2.58	$3.59 \times 10^{-4}$
<b>ZTO</b>	708	18.3	63.3	8.18	0.82	687	2.56	$3.68 \times 10^{-4}$
<b>Ref</b>	652	16.5	64.2	6.90	1.48	544	2.82	$1.38 \times 10^{-3}$

Apart from the  $V_{oc}$ , the  $J_{sc}$  was found to be increased from 16.5 mA/cm<sup>2</sup> to 18.3 mA/cm<sup>2</sup> for CZTS/ZTO sample as summarized in Table 4. 5. One can see a clear increase in the EQE shown in Figure 4. 15c particularly at ~360 nm for ZTO buffer, while a plateau at 400~450 nm was seen for CdS buffer. Therefore, the  $J_{sc}$  of CZTS/ZTO device has a significantly better blue response compared to the CZTS/CdS reference because of its wider bandgap of 3.3 eV versus 2.4 eV for CdS. However, a decrease in EQE in the 500 to 800 nm range can be observed for CZTS/ZTO solar cell, which was attributed to light interference. This interference could be eliminated after the application of the MgF<sub>2</sub> ARC as is shown in Figure 4. 15c. Finally, a photocurrent density of 20.35 mA/cm<sup>2</sup> was obtained by integrating the EQE over the solar spectrum which is in good agreement with the  $J_{sc}$  of 20.5 mA/cm<sup>2</sup> obtained from the  $J$ - $V$  measurement. Considering the similar absorption edge in the long wavelength, the absorber quality for both reference and CZTS/ZTO devices is expected to be identical since they were from the same batch, indicating that the significant increase in performance from the CZTS/ZTO devices can be attributed to the change in the buffer layer.

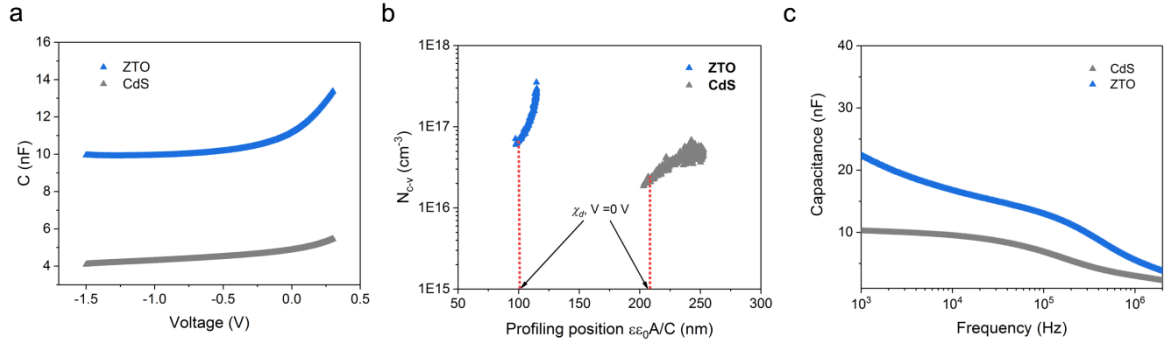


Figure 4. 16 a)  $C$ - $V$  curves of the CZTS devices with ZTO and CdS buffer. b) Free carrier density and depletion width derived from the  $C$ - $V$  curves. c) Room-temperature capacitance-frequency characteristics of the CZTS solar cells with ZTO and CdS buffer measured with 0V (DC) and 0.01 V (AC) bias under dark conditions.

The  $C$ - $V$  measurements were also performed with a -1.5 to 0.3 V bias to evaluate the heterojunction quality of the champion CZTS devices with ZTO and CdS buffer, as shown in Figure 4. 16a. The extraction of the carrier concentration and depletion width is taken at zero bias, as shown in Figure 4. 16b. On the one hand, it is clear that the depletion width of CZTS/ZTO device ( $\sim 100$  nm) is much smaller than the CZTS/CdS device ( $\sim 210$  nm). On the other hand, the device with a ZTO buffer layer has a carrier concentration of  $7.44 \times 10^{16} \text{ cm}^{-3}$ , whereas the carrier concentration for the device with a CdS buffer layer was found to be  $2.26 \times 10^{16} \text{ cm}^{-3}$ . A slightly lower  $FF$  was found for the CZTS/ZTO device compared to CZTS/CdS device, which could be attributed to the decreasing depletion width of ZnSnO buffered cell. The frequency-dependent capacitance is shown in Figure 4. 16c, the even higher capacitance at low frequencies for CZTS/ZTO is found compared to CZTS/CdS device, indicating a higher defect densities CZTS/ZTO heterojunction interface compared to the CZTS/CdS interface. Thus, the advantage of ZTO buffer layer cannot be readily explained by the  $C$ - $f$  measurements.

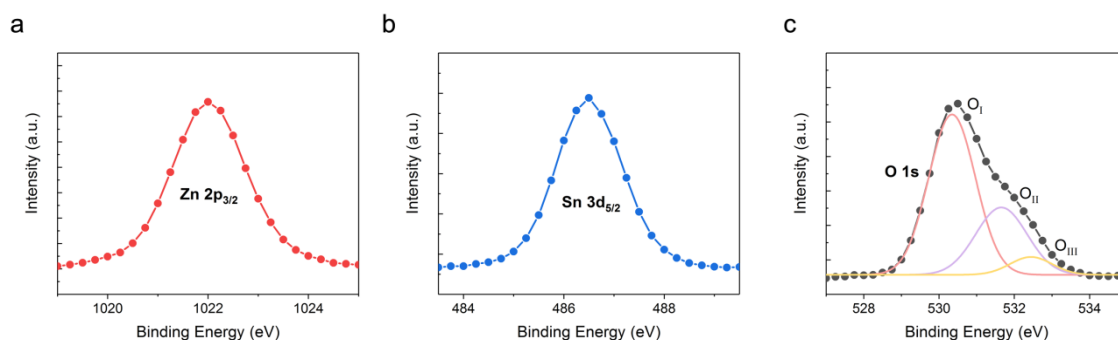


Figure 4. 17 Surface XPS spectra of a) Zn 2p<sub>3/2</sub>, b) Sn 3d<sub>5/2</sub>, c) O 1s peak of Zn<sub>0.77</sub>Sn<sub>0.23</sub>O film on CZTS solar cells

To unravel the mechanism of the improved device performance, detailed microscopy analysis was performed on the champion solar cell to understand what explains the enhancement in  $V_{OC}$ . A high angle annular dark-field (HAADF) scanning TEM image and corresponding estimated phase structure from the EDS mapping of the enlarged CZTS/ZTO/i-ZnO/ITO stack of the best-performing CZTS/ZTO device is shown in Figure 4. 15d. The layer structure of CZTS/ZTO/i-ZnO/ITO stack can be identified based on their contrast. Figure 4. 15d also shows the EDS mapping for the region denoted by a red rectangle in the corresponding TEM image. The EDS mapping data were processed by principle component analysis and phase analysis to determine the covariance of different elements, where different signals that vary in a similar fashion can be picked up as one single phase. The estimated phase profiles in Figure 4. 18b indicate an identical schematic with our CZTS/ZTO device structure shown in Figure 4. 15a. Noticeably, a thin layer estimated to be around 10~20 nm can be identified as the ZnSnO buffer layer, which exhibits a conformal coverage on the CZTS surface. Although the roughness undulations of CZTS were on the scale of 50 nm, a ~10 nm ZnSnO buffer could effectively cover the rough surface with a uniform thickness. CZTS/ZTO stacks measured by XPS with a 10 nm ZTO buffer layer (see Figure 4. 17) also confirmed the good coverage of ALD deposition process, where no peaks of Cu related to CZTS were observed in the surface XPS spectra.

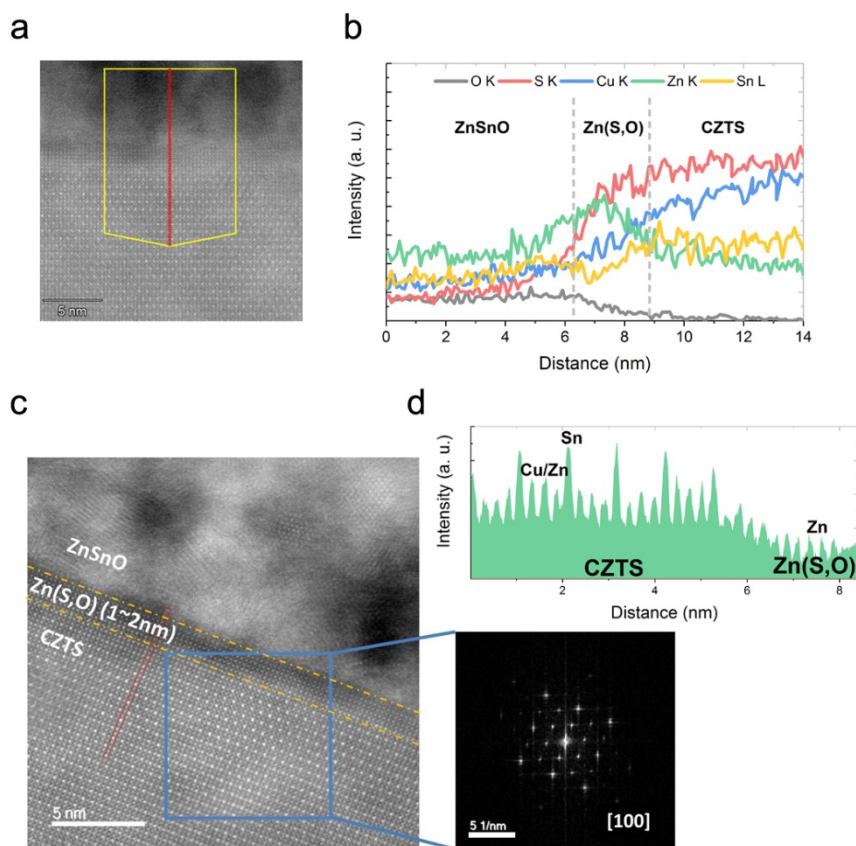


Figure 4. 18 a) HAADF scanning TEM image and b) corresponding EDS element line scan of the CZTS/ZTO interface of the champion solar cell. c) Atomic-resolution HAADF image and the FFT pattern of the corresponding area of the CZTS/ZTO interface. d) A representative intensity profile for a cations column at the interface marked by the red rectangular in Fig. 6c.

To visualize the detailed nanoscale microstructure and element distribution of the CZTS/ZTO interface, the author confined the regions of interest to higher magnifications. The HAADF scanning TEM image and corresponding energy dispersive spectroscopy (EDS) element line scan of the specific CZTS/ZTO interface area is shown in Figure 4. 18a and b. As expected, the atomic ratios were found to be constant in the CZTS and ZnSnO bulk regions. In the heterointerface transition region, however, the Zn concentration increases sharply while the Sn concentration slightly decreases. This Zn rich layer was also confirmed by EDS measurements performed in the same area shown in Figure 4. 19e. A Zn-rich and Sn-poor interfacial layer are

distinctly visible in the element mapping. The ultra-thin layer at the CZTS/ZTO interface is constituted by mainly Zn and S, with very low amount of O detected, which can be denoted as Zn(O,S). This layer is similar to ZnS in terms of crystalline structure with a similar lattice constant.

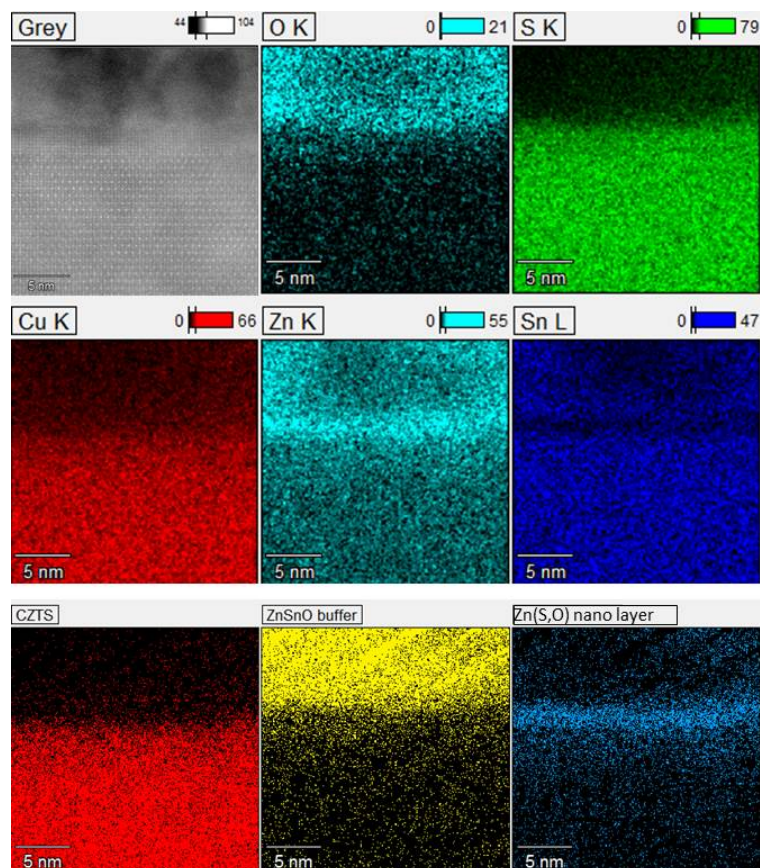


Figure 4. 19 Estimated phase structure from the EDS mapping of the CZTS/ZTO interface.



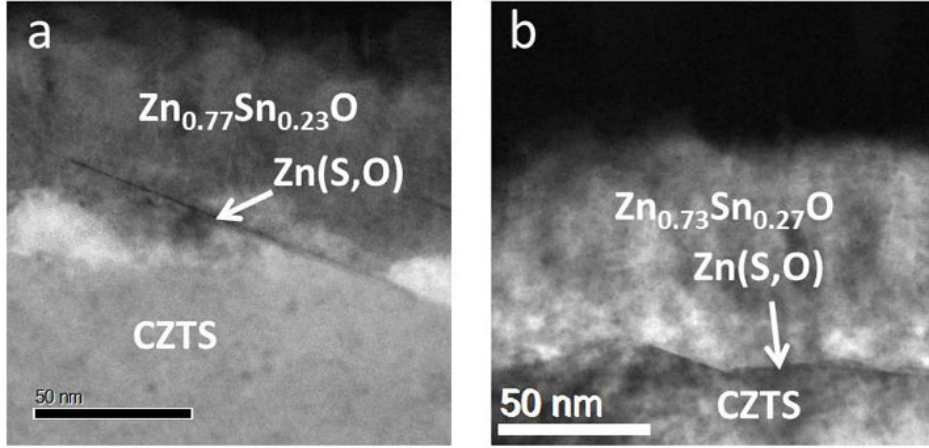


Figure 4. 20 High resolution transmission electron microscope (HRTEM) images of the CZTS/ZTO heterojunction region showing the microstructure for different ZTO buffers  
a)  $\text{Zn}_{0.77}\text{Sn}_{0.23}\text{O}$  b)  $\text{Zn}_{0.73}\text{Sn}_{0.27}\text{O}$

Figure 4. 18c shows the atomic-resolution HAADF image where atomic layers transit from CZTS to ZTO forming an abrupt interface. The HAADF image reveals the amorphous nature of the ZTO region with the presence of nano-crystalline domains. The fast Fourier transform (FFT) pattern of the corresponding area in the blue box highlights the good crystallinity of the CZTS layer near the interface. More importantly, a single-phase corresponding to the CZTS [100] zone-axis in FFT diffraction pattern indicated a high quality of epitaxial growth at the interface.[201] Furthermore, the intensity of an atomic column in the HAADF imaging is proportional to  $\sim Z^2$ , where  $Z$  denotes the atomic number.[202] Therefore, the line profile of the atomic columns can be used to differentiate Cu/Zn (with similar  $Z$ ) and Sn (with much larger  $Z$  compared to Cu/Zn) based on the intensity profile. As shown in Figure 4. 18d, as the scan goes through CZTS region, both Sn and Cu/Zn were observed as the alternating higher and lower column intensity presents. Interestingly, the Sn column diminished when scanning through the interlayer, indicating the Sn deficits in this area. Thus, one can safely conclude that this 1~2 nm ultra-thin layer could be ascribed to the ZnS phase, with little amount of O detected by EDS mapping and line-scan in Figure 4.

18b,e, which has a similar crystal structure and lattice parameters to that of CZTS.[203] Such a lattice-matched hetero-interface of CZTS/ZnS gives a better crystallinity interface with less crystalline defects, which is expected to lead to reduced interface recombination compared to that with large lattice mismatch.

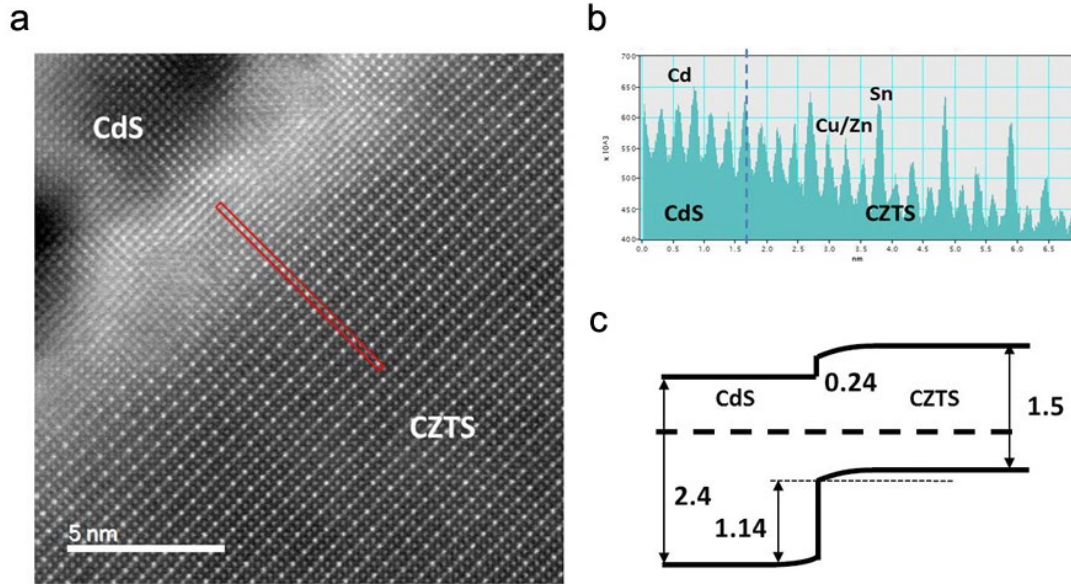


Figure 4. 21 a) Atomic-resolution HAADF image of the CZTS/CdS interface. b) A representative intensity profile for a cations column at the interface marked by the red rectangular in Fig. S6a. c) Schematic of the band alignment at CZTS/CdS interface extracted from our previous report.

The high-resolution transmission electron microscope (HRTEM) images of high-performance CZTS devices with a  $\text{Zn}_{0.77}\text{Sn}_{0.23}\text{O}$  and a  $\text{Zn}_{0.73}\text{Sn}_{0.27}\text{O}$  buffer layer were used to confirm the microstructure at the CZTS/ZTO heterojunction interface (see Figure 4. 20a,b). This analysis revealed the presence of an ultrathin interfacial layer in the transition region for both cases. Interestingly, a similar phenomenon has been recently reported, i.e. ZnS phase in between the CZTS and SILAR processed ZnCdS buffer, in our previous SILAR-ZnCdS buffered CZTS with a less Zn-rich content.[204] In contrast, in the conventional CdS buffered CZTS reference samples, there was no



such Zn(S,O) interlayer at the CZTS/CdS hetero-interface or on the surface of bare CZTS absorber. An atomic-resolution HAADF image of the CZTS/CdS interface was taken to confirm if there was only CdS formed at the heterojunction, where the pattern of intensity profile at the interface was observed to be different from the CZTS/ZTO structure as no Zn-rich thin layer was observed (see Figure 4. 21a,b). Notice that the common part of ALD-ZnSnO and SILAR-ZnCdS buffer is that Zn source was used to start the initial formation of the buffer on the CZTS surface. Therefore, this Zn-rich thin layer can be explained by the initial growth of ZnO during the first ALD cycles before the first SnO<sub>x</sub> sub-cycle.

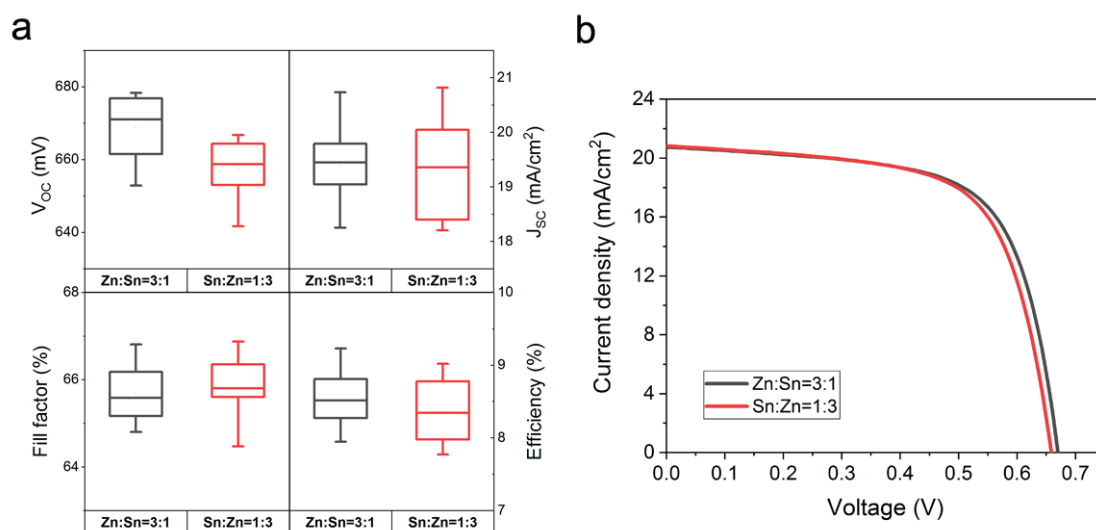


Figure 4. 22 a) Box-plots of performance parameters and b)  $J-V$  curves of the CZTS cells for ALD ZnSnO buffer layers with a different sequence of ZnO and SnO<sub>x</sub> sub-cycles.

To further understand the formation of this Zn-rich layer, the CZTS performance for ZTO buffers with a different sequence of ZnO and SnO<sub>x</sub> ALD sub-cycles were also compared. A Zn:Sn pulse ratio of ZTO was kept as 3:1 with one group start with ZnO sub-cycles (denoted as Zn:Sn=3:1) while the other started with SnO<sub>x</sub> sub-cycles (denoted as Sn:Zn=1:3) and the resulting solar cell parameters are shown in Figure 4. 22a. It shows that the overall efficiency of the CZTS solar cells grown using the ZnO

first sequence was higher compared to the  $\text{SnO}_x$  first sequence. The higher performance of the devices starting with ZnO sub-cycles was mainly due to a higher  $V_{oc}$  (see Figure 4. 22b), which might be attributed to the presence of a similar  $\text{Zn}(\text{S},\text{O})$  interface layer as shown in Figure 4. 19e. Besides that, the precipitate of  $\text{Zn}(\text{S},\text{O})$  could originate from the reaction between Zn precursor and the S bonded CZTS surface in the initial step of the ALD process. Ericson *et al.*[43] reported the improved CZTS/ZTO device performance benefited from Zn-treated surface and post-annealing in the 105 °C to 165 °C temperature range, which on the other hand demonstrate the benefits from Zn-rich layer and annealing effect though no such Zn-rich layer was revealed in their work.

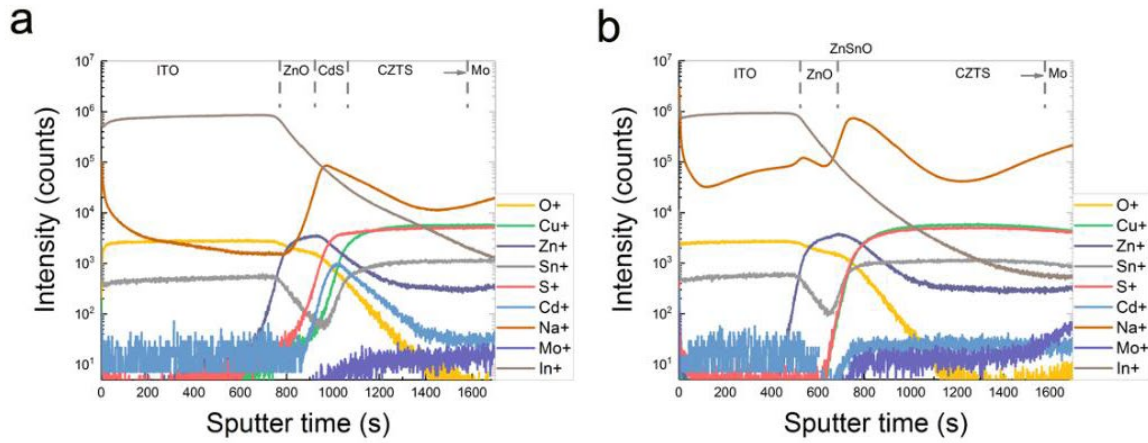


Figure 4. 23 a,b) TOF-SIMS elemental depth profiles from the TCO to the SLG substrate of CZTS solar cells with CdS and ZnSnO buffer.

Considering the possible impact on absorber by the different buffer deposition processes (CBD-CdS vs. ALD-ZTO) in terms of processing temperature and duration, time of flight secondary ion mass spectroscopy (TOF-SIMS) was also carried out in the CZTS/CdS control device and the champion CZTS/ZTO device to compare the compositional depth profiles, as shown in Figure 4. 23a,b. The different stack layers can be identified based on the depth profiles of its main elements in each device. It was clearly observed that Cu, Zn, Sn, and S had a similar intensity and approximately

homogeneous distribution in the CZTS layer for both cases. However, the Na intensity relative to Cu, Zn, Sn intensity (same level in two sample) throughout the CZTS/ZTO samples was an order of magnitude higher compared to the CZTS/CdS sample. Considering the different buffer layer synthesis processes for the two devices, the most likely cause of the different Na distribution is the difference in processing temperature. The higher temperature (ALD-150 °C vs. CBD-80 °C ) and longer processing duration (ALD-1 hour vs. CBD-8 min) during the ALD-ZnSnO process can effectively facilitate the diffusion of Na from the soda-lime glass (SLG) substrate into the device. Furthermore, the depth profiles of ITO layer of the CZTS/CdS device showed similar profiles to the CZTS/ZTO device, however, the intensities of the Na profiles were observed to be lower than the CZTS/ZTO device and decreased as a function of depth. The lower intensities of Na in ITO could be due to the presence of a thicker CdS which might act as a physical barrier layer or the Na dissolution loss in the chemical bath process. The incorporation of Na in CZTS device has been known to increase the carrier concentration and mobility of the bulk CZTS layer[205, 206] and reduce the concentration of deep-level recombination centers[207]. Furthermore, Na benefits device performance was shown mainly due to the enhancement of  $V_{OC}$  and FF, which are sensitive to defects and traps. [205] [207] Thus, the  $V_{OC}$  enhancement of our CZTS/ZTO device can be partially correlated with the larger concentration of Na distribution throughout the device which passivates the defects at the bulk and interface.

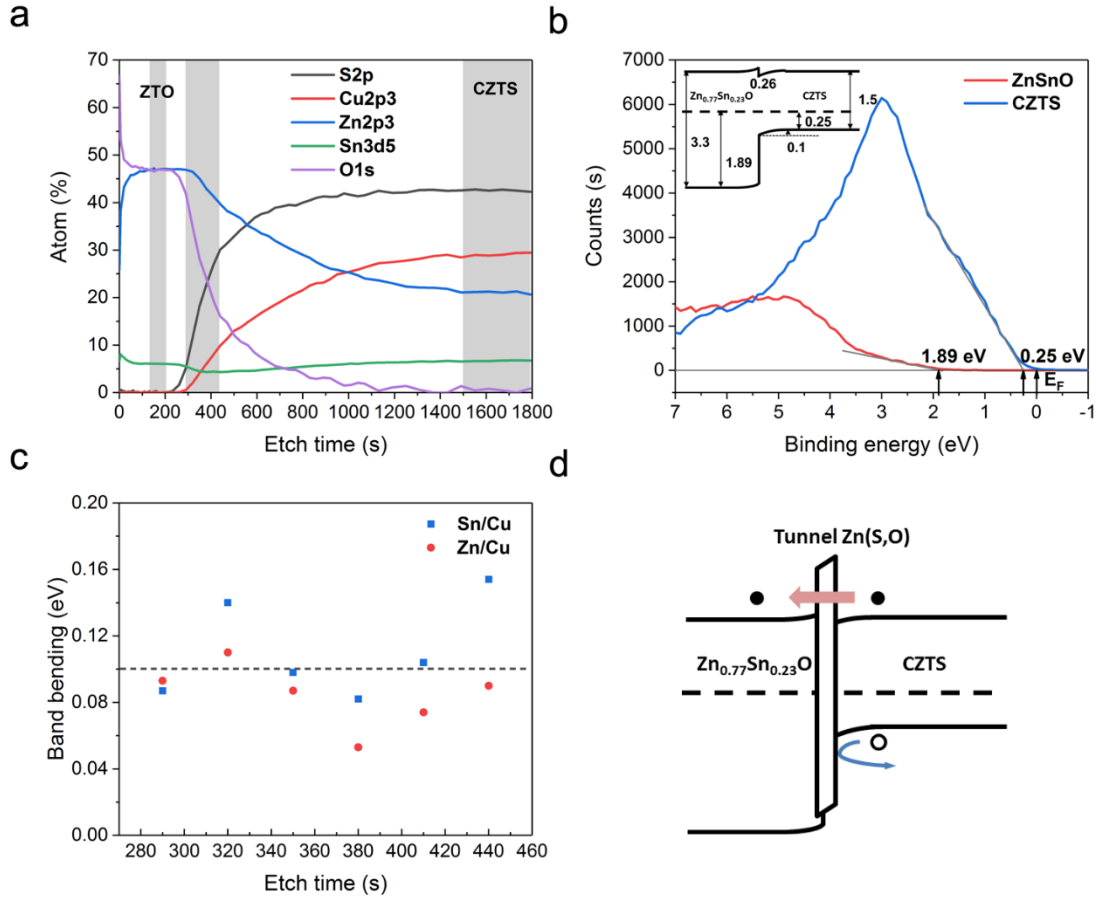


Figure 4. 24 a) The XPS composition profile for CZTS absorber with a Zn<sub>0.77</sub>Sn<sub>0.23</sub>O buffer layer. The depth profile was divided into three regions, namely the ZTO region, CZTS/ZTO interface region, and CZTS bulk region as a function of sputtering time according to the composition transformation. b) Normalized VB data of CZTS/Zn<sub>0.77</sub>Sn<sub>0.23</sub>O heterojunction measured by XPS. Binding energies were measured with respect to the Fermi energy (E<sub>F</sub>). c) Band bending of the CZTS/ Zn<sub>0.77</sub>Sn<sub>0.23</sub>O interface as a function of sputtering time. d) Schematic of the band alignment at CZTS/Zn<sub>0.77</sub>Sn<sub>0.23</sub>O interface with Zn(S, O) tunnel layer.

X-ray photoelectron spectroscopy (XPS) measurements were carried out on the 10 nm Zn<sub>0.77</sub>Sn<sub>0.23</sub>O film on CZTS absorber to investigate the chemical bonding state of ZTO films and the composition depth profile of CZTS/ZTO interface. To avoid preferential oxygen sputtering from the film surface, the composition depth profile and

corresponding core-level spectra for CZTS with ZTO buffer was achieved by mildly sputtering with argon ions at 1 keV. Figure S4 shows the XPS spectra of the Zn 2p<sub>3/2</sub>, Sn 3d<sub>5/2</sub>, O1s core levels for the Zn<sub>0.77</sub>Sn<sub>0.23</sub>O film on CZTS solar cells after sputtering the sample for 5 s. The peaks at 1021.9 and 486.5 eV indicates Zn 2p<sub>3/2</sub> and Sn 3d<sub>5/2</sub>, respectively, which correspond to the Zn<sup>2+</sup> and Sn<sup>4+</sup> oxidation states,[208] respectively. Meanwhile, the broad peak around 531 eV, corresponding to the O 1s core level, can be deconvoluted into three peaks by using the Gaussian curve approximation.[209] The three deconvoluted O 1s core-level features can be attributed to: (1) O<sub>I</sub>, metal oxide (M-O-M) lattice species at 530.3 eV, (2) O<sub>II</sub>, lattice oxygen in oxygen-deficient region at 531.6 eV, and (3) O<sub>III</sub>, weakly bond (M-OR) species such as H<sub>2</sub>O, -OH and -CO<sub>3</sub> at 532.4 eV, which might originate from O-H bonds or residual water absorbed on the sample surface. One should note that it is quite likely that the ZnSnO ALD process results in hydrogenation of the device when using ALD Al<sub>2</sub>O<sub>3</sub> as heterojunction interface layer in CZTS/CdS solar cells, [151] however, this is beyond the scope of this work. Figure 4. 24a depicts the measured composition depth profile of each element contained in both CZTS absorber and ZTO buffer. I then classify the depth profile into three regions, namely the ZTO region, CZTS/ZTO interface region and the CZTS bulk region according to the composition transformation. Despite the oxygen-rich feature at the sample surface before sputtering, the composition of Zn, Sn and O shows no significant variation in the ZTO region.

To further unravel the mechanism of the improved device performance, I investigated the band alignment at the CZTS/ZTO interface combined XPS core-level spectroscopy with XPS VB spectroscopy. An X-ray photo source was applied to characterize the Cu, Sn and Zn core levels with respect to the valence band maximum of CZTS and ZTO layers. As shown in Figure 4. 24c, the behavior of Cu2p3/Zn2p3/Sn3d5 core-level line shapes, intensity ratios and binding energy positions exhibit no changes after sputtering cycles, confirming that Ar<sup>+</sup> bombardment did not induce any surface modification. Thus, the CBO can be deduced from the

valence band offset (VBO) determined by XPS together with optical bandgap. By using an indirect method [57, 210], the VBO can be obtained by using the formula

$$\text{VBO} = E_{VB}^b - E_{VB}^a + V_{bb} \quad \text{Equation 4. 6}$$

where  $E_{VB}^b$  and  $E_{VB}^a$  represent the energy positions of the valence band edge of the bulk  $\text{Zn}_{0.77}\text{Sn}_{0.23}\text{O}$  and bulk CZTS while  $V_{bb}$  is the band bending. The valence band edges were determined by linear extrapolation of the valence edge to zero intensity as shown in Figure 4. 24b. An estimated value of -1.89 eV and -0.25 eV was found for  $\text{Zn}_{0.77}\text{Sn}_{0.23}\text{O}$  and CZTS, respectively. Additionally, the total average  $V_{bb}$  was calculated to be  $(-0.1 \pm 0.1)$  eV for six sets of band bending values at different depths of the CZTS/  $\text{Zn}_{0.77}\text{Sn}_{0.23}\text{O}$  interface. The VBO value obtained by the indirect method was then calculated to be -1.54 eV by Eq. (2). Accordingly, the CBO can be readily calculated according to the VBO value and bandgap values of  $\text{Zn}_{0.77}\text{Sn}_{0.23}\text{O}$  and CZTS, where bandgap values of 3.3 and 1.5 eV for  $\text{Zn}_{0.77}\text{Sn}_{0.23}\text{O}$  and CZTS were used in our case. Therefore, the CZTS/ $\text{Zn}_{0.77}\text{Sn}_{0.23}\text{O}$  interface yields a CBO of  $(0.26 \pm 0.1)$  eV, indicating a ‘spike-like’ CBO heterojunction interface which is favorable for the CZTS solar cell performance. For comparison purposes, I also include the schematic of band alignment at CZTS/CdS interface (Figure 4. 20c) extracted from our previous report, which shows ‘cliff-like’ CBO heterojunction of -0.26 eV.

A schematic of the band alignment at CZTS/  $\text{Zn}_{0.77}\text{Sn}_{0.23}\text{O}$  interface is illustrated in the inset of Figure 4. 24b. A ‘spike-like’ CBO within the range of 0–0.4 eV is believed to be the optimum conduction band alignment enabling high-performance heterojunction solar cell to facilitate electron-hole separation regardless of carrier lifetimes at the interface, according to simulation studies presented in the literature.[51] In the case of ‘spike-like’ CBO, it is the majority carrier electron concentration at the absorber surface which governs the occupation of interface defects. Thus the interface recombination is dominated by the concentration of free holes at the absorber surface.

For a positive CBO, the hole concentration is small both for zero bias and for forward bias leading to the decreased  $J_0$  (high  $V_{OC}$ ) and the increased photocurrent  $J_{sc}$ . [9] If we further take the Zn(S,O) interlayer into consideration, the band diagram of CZTS/ $Zn_{0.77}Sn_{0.23}O$  heterojunction with a Zn(S,O) tunnel layer under thermal equilibrium conditions is sketched and shown in Figure 4. 24d. The valence band maximum and conduction band minimum value of Zn(S,O) in the diagram was extracted from our previous work.[58] As can be seen from the structure, the *p*-type CZTS absorber was separated from the *n*-type ZTO buffer by an ultra-thin Zn(S,O) tunnel layer which reduced the interface recombination significantly. The tunnel layer does not hinder the efficient transport of the majority carriers from the absorber into the buffer, thus allows for excellent performance improvement of the device.

#### 4.3.5 SCAPS simulation of CZTS/ZnSnO baseline model

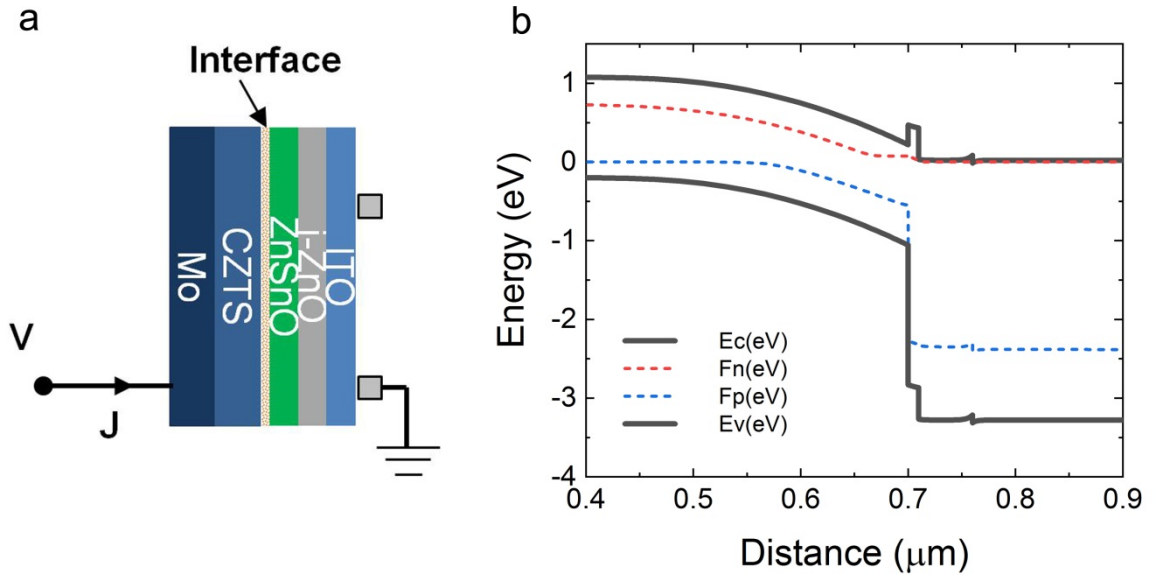


Figure 4. 25 a) Illustration of device structure used for CZTS/ZTO model. b) Schematic band diagrams under light at short circuit condition for CZTS/ZnSnO baseline model.

Numerical simulations by SCAPS 1D[211] were applied to describe the model of

CZTS/ $\text{Zn}_{0.77}\text{Sn}_{0.23}\text{O}$  devices shown in the experimental part (section 4.3.1). The device structure of the model built in SCAPS is shown in Figure 4. 25a. While Figure 4. 25b demonstrates the corresponding band diagram for the CZTS/ $\text{ZnSnO}$  baseline model with  $\text{Zn}_{0.77}\text{Sn}_{0.23}\text{O}$  as buffer layer. Most of the parameters were taken from the CZTS/CdS model from the literature[212] except for the  $\text{ZnSnO}$  layer and interface layer. Table 4. 6 summarizes the parameters used. Pu *et al.* have reported that both inferior heterojunction interface and bandgap fluctuation in the bulk contribute to the large  $V_{OC}$  deficit in CZTS devices. Therefore, the bandgap of CZTS absorber implemented in the model was set to 1.275 eV, which was determined from the effective electronic bandgap based on PL peaks rather than the optical bandgap extracted from the EQE curve. Here, a flat band approximation was used for the 1D simulation due to the bandgap fluctuation in the disordered CZTS triggered by the band tail states. The corresponding electron affinity ( $\chi$ ) of CZTS was assumed to be 4.2 eV according to the literature[213]. An interface layer at heterojunction was added to represent the surface recombination properties of the device. For ZTO layer, the measured optical bandgap of 3.3 eV was used in the model. The ZTO electron affinity of  $\sim 3.95$  eV was calculated using the CBO value at CZTS/ $\text{Zn}_{0.77}\text{Sn}_{0.23}\text{O}$  interface and the electron affinity of CZTS. Finally, the  $J$ - $V$  data was used to model additional series and shunt resistance and matched with the measured  $FF$ .

The  $J$ - $V$  plots of measured data and simulation results are shown in Figure 4. 26 and the resulting photovoltaic parameters are summarized in Table 4. 7. It can be seen that a good match was achieved between the measured data and simulation data. Therefore, a baseline model for CZTS/ZTO device was established. This baseline model ensures a credible basis for further optimization and investigation of the device performance.



Table 4. 6 Material parameters used for the simulation of CZTS/ZTO devices in SCAPS-1D.

Property	CZTS	CZTS/ZTO interface	ZTO	i-ZnO	ITO
Thickness (nm)	700		10	50	200
Effective Electronic bandgap (eV)	1.275		3.3 (2.9~3.5)	3.3	3.3
Electron affinity (eV)	4.2		3.95 (3.85~4.45)	4.35	4.45
Relative dielectric constant	7		10	10	10
Conduction band density of states (cm <sup>-3</sup> )	2.2*10 <sup>18</sup>		2.2*10 <sup>18</sup>	2.2*10 <sup>18</sup>	2.2*10 <sup>18</sup>
Valence band density of states (cm <sup>-3</sup> )	1.8*10 <sup>19</sup>		1.8*10 <sup>19</sup>	1.8*10 <sup>19</sup>	1.8*10 <sup>19</sup>
Electron mobility (cm <sup>2</sup> /V/s)	1.02		5	100	100
Hole mobility (cm <sup>2</sup> /V/s)	1		5	25	25
Free carrier concentration (cm <sup>-3</sup> )	1.0*10 <sup>16</sup>		1.0*10 <sup>17</sup>	1.0*10 <sup>18</sup>	1.0*10 <sup>18</sup>
Interface recombination velocity (cm/s)		10 <sup>5</sup>			

Table 4. 7 Corresponding values of photovoltaic parameters of the experimental CZTS/Zn<sub>0.77</sub>Sn<sub>0.23</sub>O solar cells compared to the simulation results.

	$J_{sc}$ (mA cm <sup>-2</sup> )	$V_{oc}$ (V)	FF (%)	PCE (%)
Measured	19.0	0.691	62.8	8.20
SCAPS	19.3	0.685	61.9	8.21

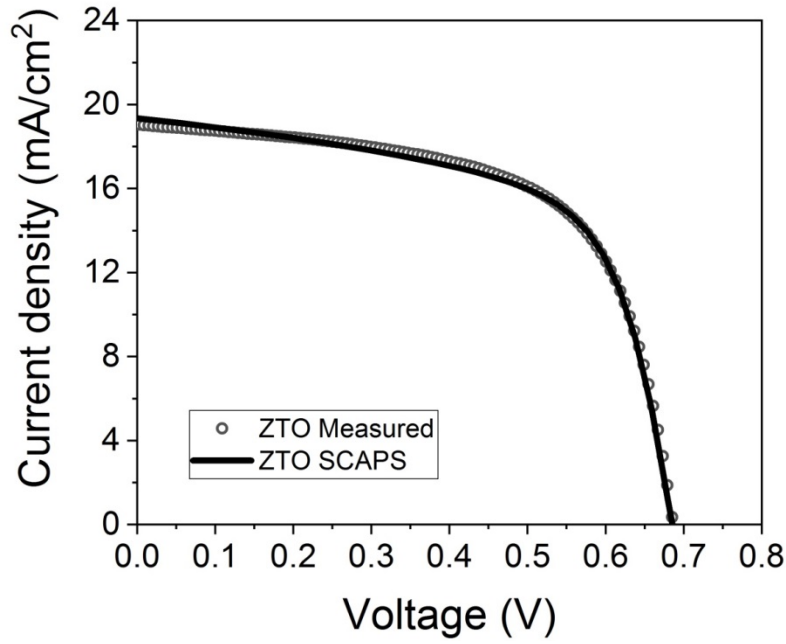


Figure 4. 26  $J$ - $V$  characteristics of measured data and simulation results for CZTS/ZTO baseline solar cell.

Based on the aforementioned model, the effects of ZnSnO bandgaps and electron affinities with respect to the absorber layer on the device performance were investigated. The electron affinity (or conduction band energy) offsets  $\Delta E_c$  at absorber/buffer layer interface was tuned from cliff-like to spike-like (i.e., negative to positive). Device characterization and simulation were all performed at 298 K. Figure 4. 27 shows the resulting device parameters with respect to the variation of  $E_{g,ZTO}$  and  $\Delta E_c$ . In terms of  $E_{g,ZTO}$ , the impact on device properties is not that significant within the range studied. The gain in  $J_{sc}$  is almost neglectable for  $E_{g,ZTO} > 2.9$  eV, this is

consistent with the experimental results where experimental  $J_{sc}$  value changes slightly by changing the composition of the ZTO buffer layer.

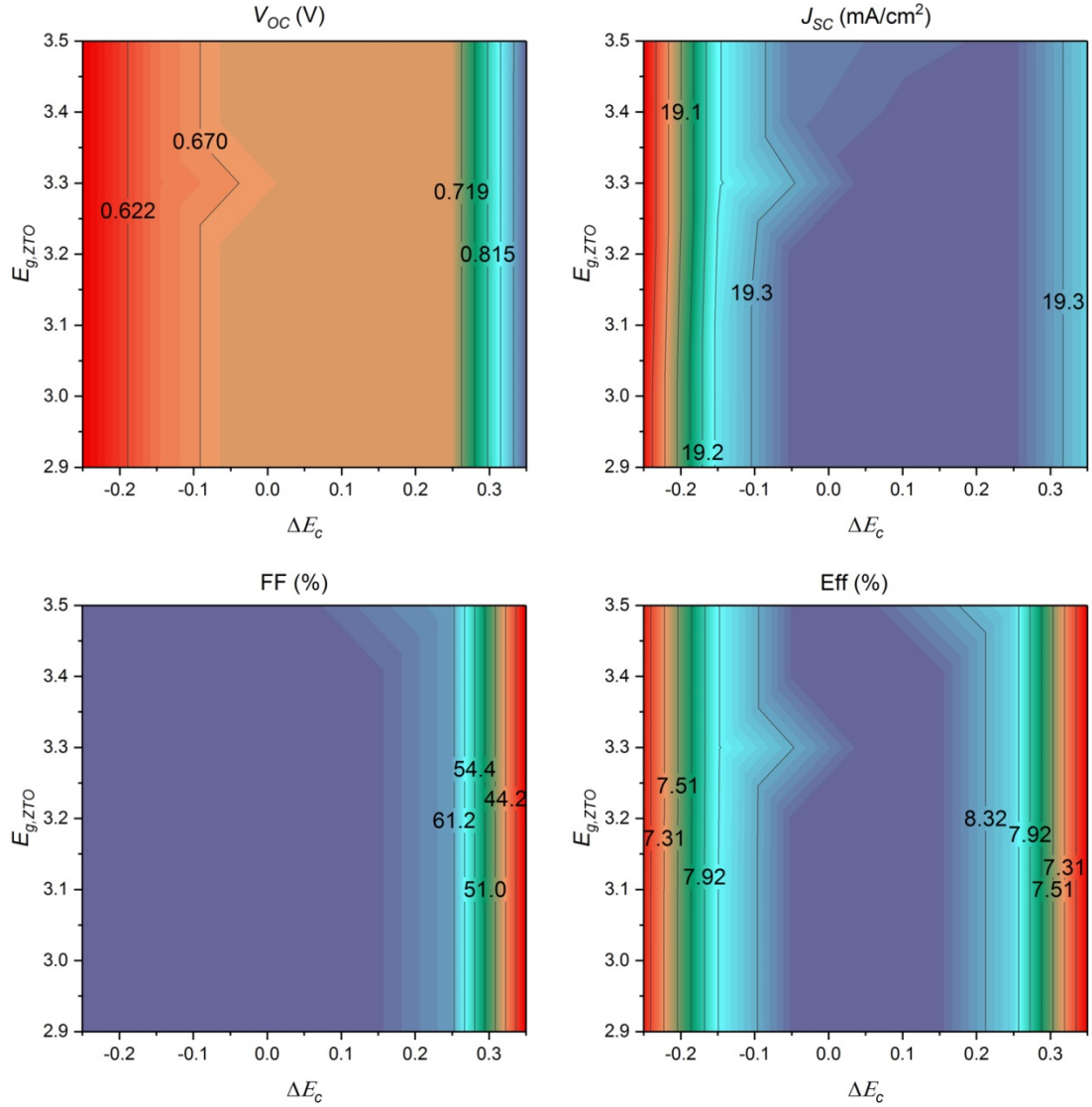


Figure 4. 27 Calculated contour plots of (a) open-circuit voltage, (b) short-circuit current, (c) fill-factor, and (d) efficiency for CZTS/ZnSnO devices with the variation of ZTO properties (left axis indicates bandgap  $E_{g,ZTO}$ , bottom axis indicates conduction band minimum offset at CZTS/ZTO  $\Delta E_c$ ).

For  $\Delta E_c$  ranging from -0.05 to 0.15, the best photovoltaic performances are achieved. When the  $\Delta E_c$  is higher than 0.15 eV (spike-like CBO), a slow decrease in PCE appears as a consequence of FF drop. As the  $\Delta E_c$  increases to 0.3 eV, the device

performance degrades due to the limitation in photo-current extraction which could be attributed to the large barrier for the forward current.[214] However, the  $V_{OC}$  keeps increasing with the advantageous spike-like  $\Delta E_c$ , which limits the number of holes available for recombination. On the opposite side, when  $\Delta E_c$  is smaller than 0 eV (cliff-like CBO),  $V_{OC}$  losses arise due to unfavorable reversed band bending which drives the electrons back and away from the buffer layer. As the cliff increases, the  $V_{OC}$  losses increase dramatically as the initial field strength under short circuit condition weakens.[215]

#### 4.4 General conclusions

This chapter reports on the synthesis of ZTO and ZMO ternary oxides films using the supercycle ALD method which consists of alternating subcycles of binary oxide depositions. ZTO thin films with different compositions were designed to obtain the desired buffer layer for application in a CZTS solar cell. Fundamental studies were carried out by *in-situ* and *ex-situ* methods to learn the growth property of thin films, as well as optical and electrical properties.

A significant improvement in the efficiency of Cd-free CZTS solar cells was achieved by applying the ALD-ZTO buffer with optimized stoichiometry and thickness. The key feature of the ALD-ZTO buffer layer was that we could take advantage of the composition tuning of ZTO to find the suitable band alignment at the heterojunction interface and reduce the optical losses in the buffer layer. A 10 nm ZTO buffer layer was confirmed to be sufficient to form a conformal coverage of the CZTS absorber and give the best device performance. The nanoscale microstructure and chemistry of the champion device were carefully studied and the presence of an ultra-thin Zn(S, O) tunnel layer at CZTS/ZTO interface was revealed. TOF-SIMS measurements confirmed an even larger Na concentration throughout the CZTS/ZTO device compared to the CZTS/CdS device, which facilitates defect passivation and the  $V_{OC}$  enhancement of the device. Furthermore, the band alignment of CZTS/ $\text{Zn}_{0.77}\text{Sn}_{0.23}\text{O}$

interface was investigated by XPS, confirming the formation of a favorable ‘spike-like’ CBO heterojunction interface. Benefits from both the favorable conduction band alignment of CZTS/ZTO and reduced interface defects stemming from the Zn(S, O) tunnel layer and Na-related passivation and thereby decreased interface recombination, I demonstrated an increase of  $V_{OC}$  by up to 10 %. An efficiency of 9.3% was obtained for Cd-free pure sulfide CZTS solar cells.

# Chapter 5 ZnMgO as window layer for CZTS solar cell

Window layer management is essential to minimize the optical loss as well as prevent shunt paths in CZTS thin-film solar cells. In this chapter, both thermal ALD and plasma-enhanced ALD were implemented to synthesize a wide range of  $\text{Zn}_{1-x}\text{Mg}_x\text{O}$  (ZMO,  $0 \leq x \leq 0.4$ ) films for application as a window layer in CZTS solar cells. *In-situ* ellipsometry measurement revealed the different growth behavior for ZMO films deposited by thermal ALD and PE-ALD and correlated them with the different fundamental properties of the films. The device with optimized thermal ALD deposited ZMO did not necessarily surpass the performance of the control device. However, the device with PE-ALD deposited ZMO exhibited an increased efficiency compared to the i-ZnO window layer. The wider bandgap of ZMO layers minimized the optical loss from the window layer and led to an enhanced  $J_{SC}$ . A more favorable conduction band alignment is believed to contribute to the improvement in  $V_{OC}$ . Finally, a champion 9.2% efficient Cd-free CZTS device with a structure of Mo/CZTS/ZnSnO/PE-ZMO/ITO was fabricated without anti-reflection coating, thanks to the significantly enhanced  $J_{SC}$  and  $V_{OC}$ .

## 5.1 Introduction

As discussed in Chapter 4, a Cd-free CZTS solar cell with a structure of Mo/CZTS/ZnSnO/i-ZnO/ITO demonstrated an efficiency of 9.3%. To further enhance

the device performance of Cd-free CZTS solar cell especially the short current density ( $J_{SC}$ ), additional optical losses beyond the buffer layer need to be avoided. Therefore, the traditional window layer i-ZnO should be replaced by a wider bandgap material. A sputtered intrinsic ZnO layer is commonly used as a window layer in CZTS or CIGS solar cells to increase the shunt resistance by blocking shunt pathways such as pinholes, cracks, and voids, thereby improving the  $FF$ . [216] Moreover, a highly resistive film could compensate for the inhomogeneity of high resistance owing to the high photoconductivity of CdS layer. The function of i-ZnO to preventing the shunting path was extremely useful when the absorber layer is coated with a chemical bath deposited CdS buffer layer. Generally, the CdS buffer layer deposited by chemical bath deposition has a relatively rough and uneven surface compared to the ZnSnO buffer layer deposited by atomic layer deposition. Therefore, i-ZnO might not be necessary in Cd-free CZTS solar cells with an ALD buffer layer. Another reason for using an alternative window layer to replace the i-ZnO window layer is tailoring the conduction band minimum (CBM) difference between the window layer and absorber layer. It has been reported that a favorable conduction band offset of the window layer/absorber layer interface plays a key role in reducing the carrier recombination at the interface, thereby essentially reduce the  $V_{OC}$  deficit in CIGS solar cell. As a consequence, a suitable window layer compromising all the above factors can probably help to boost the efficiency of Cd-free kesterite solar cells.

Mg-doped ZnO has a wider bandgap than intrinsic ZnO (i-ZnO), which could be able to replace the i-ZnO window layer. Chantana and his group have already implemented ZnMgO layers in CIGS solar cells. Their recent study demonstrates a 19.6% efficient CIGSSe solar cell with  $Zn_{1-x}Mg_xO$  window layer together with (Cd,Zn)S buffer layer. [141] They deposited  $Zn_{1-x}Mg_xO$  by co-sputtering and found an optimal value of 0.211 for  $x$ . A relative gain in  $J_{sc}$  of 5.7% and efficiency of 5.4% was achieved compared to the traditional CdS/ZnO counterpart. Such improvement shows the great potential of  $Zn_{1-x}Mg_xO$  as a window layer in CZTS, with the possibility to

boost the  $J_{sc}$  further. Solar Frontier used ALD to deposit ZnMgO to replace i-ZnO as a second buffer layer in high-efficient CIGS solar cells.[142] The high-performed device was achieved by using ZnMgO as the second buffer layer (or window layer) on top of the Zn(O,S,OH) buffer layer, with an efficiency of 22.8 %, even higher than the devices with Cd containing buffer.[126]

## 5.2 ZnMgO growth by thermal and plasma-enhanced ALD

The ZnMgO depositions were carried out in the Fiji G2 ALD system from Cambridge Nanotech. Both thermal ALD and plasma-enhanced ALD processes were implemented for the deposition. Thin films were deposited with different Mg content (Mg / Mg+ Zn) over a range of substrate temperatures (80~150 °C). The substrates used were glass and silicon wafers with native oxide (~1.5 nm thickness). Diethylzinc (DEZ, Sigma-Aldrich), bis(ethylcyclopentadienyl)magnesium (Mg(CpEt)<sub>2</sub>, Strem Chemicals) were used as Zn and Mg precursor, respectively. The DEZ precursor was kept at room temperature while the Mg(CpEt)<sub>2</sub> precursor was heated to 90 °C. Deionized water (H<sub>2</sub>O) served as an oxidizing source in thermal ALD and a remote O<sub>2</sub> plasma (inductively coupled, 13.56 MHz) as the oxidizing source in PE-ALD. All the O<sub>2</sub> plasma process involved a mixed O<sub>2</sub> and Ar flow rate of 30 and 80 sccm, respectively, with the plasma power kept at 300 W unless indicated otherwise.

The ZnMgO ternary films were deposited by tuning the ZnO: MgO ratio with a super-cycle approach, as the sequence of the two processes illustrated in Figure 5. 2. Here, thermal ALD is abbreviated to “T-ALD” and plasma-enhanced ALD is abbreviated to “PE-ALD”. A typical super-cycle consisted of alternating  $m$  cycles of the ZnO process followed by one cycle of the MgO process. The desired thickness was achieved by looping of the ALD supercycles. For the thermal ALD deposition of ZnMgO, the ZnO cycle consisted of a processing sequence of 0.06 s DEZ pulse, 10 s Ar purge, 0.06 s deionized water pulse, 10 s Ar purge (0.06 s/10 s/0.06 s/10 s). The MgO cycle was 0.5 s/10 s/0.06 s/10 s with longer Mg precursor time to reach the



saturated ALD growth. For PE-ALD deposition of ZnMgO, the Zn and Mg precursor pulse time was kept identical as in the T-ALD process whilst purge times of 5 s between each precursor and reactant exposure were utilized to remove residual species or byproducts from the reaction chamber. O<sub>2</sub> gas was introduced into the reaction chamber and mixed with Ar using O<sub>2</sub>/Ar = 0.18 flux ratio. This took place 5 s before the plasma turning on and maintained until the end of plasma. The plasma was turned on for 5 s during the oxidant pulse step using O<sub>2</sub>/Ar gas to allow for the adequate surface reaction.

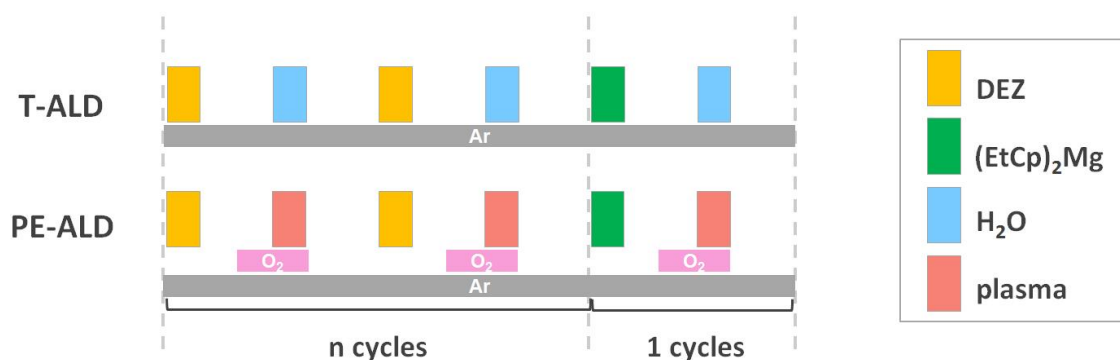


Figure 5. 1 Schematic of the super-cycle method used for ternary ZnMgO deposition by T-ALD and PE-ALD.

To observe the growth properties of ZnMgO films, *in situ* SE was performed during the film deposition on the substrate of Si with native oxide (denoted as native-Si). Here, *in situ* SE is a non-destructive optical diagnostic that has been widely used to monitor film growth by physical and chemical vapor deposition techniques.[217, 218] The ZnMgO thickness during ALD was extracted in real-time by fitting the SE spectra using a layered model of Si/native SiO<sub>2</sub>/ ZnMgO. Measurements were operated in the wavelength range between 245 and 1000 nm at an angle of incidence of 70° with respect to the substrate. The SE measurements as a function of time were acquired at 0.5 s intervals. Modeling of the SE measurements was carried out using the CompleteEASE software package. The data from deposited film samples

were modeled using a three-layer model, comprising Si, native SiO<sub>2</sub> and ZMO. A temperature-dependent Si layer model from the CompleteEASE software library was used to fit the parameter of Si changing with process temperature. The ZMO layers were modeled through an oscillator model, which including a polynomial spline function (the psemi-m0 oscillator) and a Tauc-Lorentz oscillator, to represent the optical constants of the films in a Kramers–Kronig consistent manner. It should be noted that the SE model parameters were kept constant while only the film thickness was fitted for different time slices. In this respect, it is noted that the trend in initial film thickness was found to be virtually independent of the model parameters employed, although the thickness values can (slightly) vary when adjusting the model parameters.

### **5.2.1 Comparison of ZnMgO growth property by in situ ellipsometry**

ZnMgO films with Zn:Mg pulse ratio of 4:1 deposited through both T-ALD and PE-ALD were used as an example to study the initial growth behavior, as shown in Figure 5. 2a. At first glance, the film growth via the T-ALD process is observed to have a distinct incubation period at the initial ~20 cycles and the growth started afterward. This nucleation behavior is consistent with previous reports, which shows that ZnO by thermal ALD exhibits an island-like growth on Si at the initial stage.[219] The process behind the island-like growth is probably due to the limited surface density of defect sites and hydroxyl groups on the surface of the native-Si. In comparison, a linear ALD growth behavior is observed without a distinct nucleation delay for PE-ALD process. The tremendous changes of the nucleation stage could be attributed to the more reactive sites provided by O<sub>2</sub>/Ar plasma, which result in higher growth per cycle (GPC) at the initial stage.

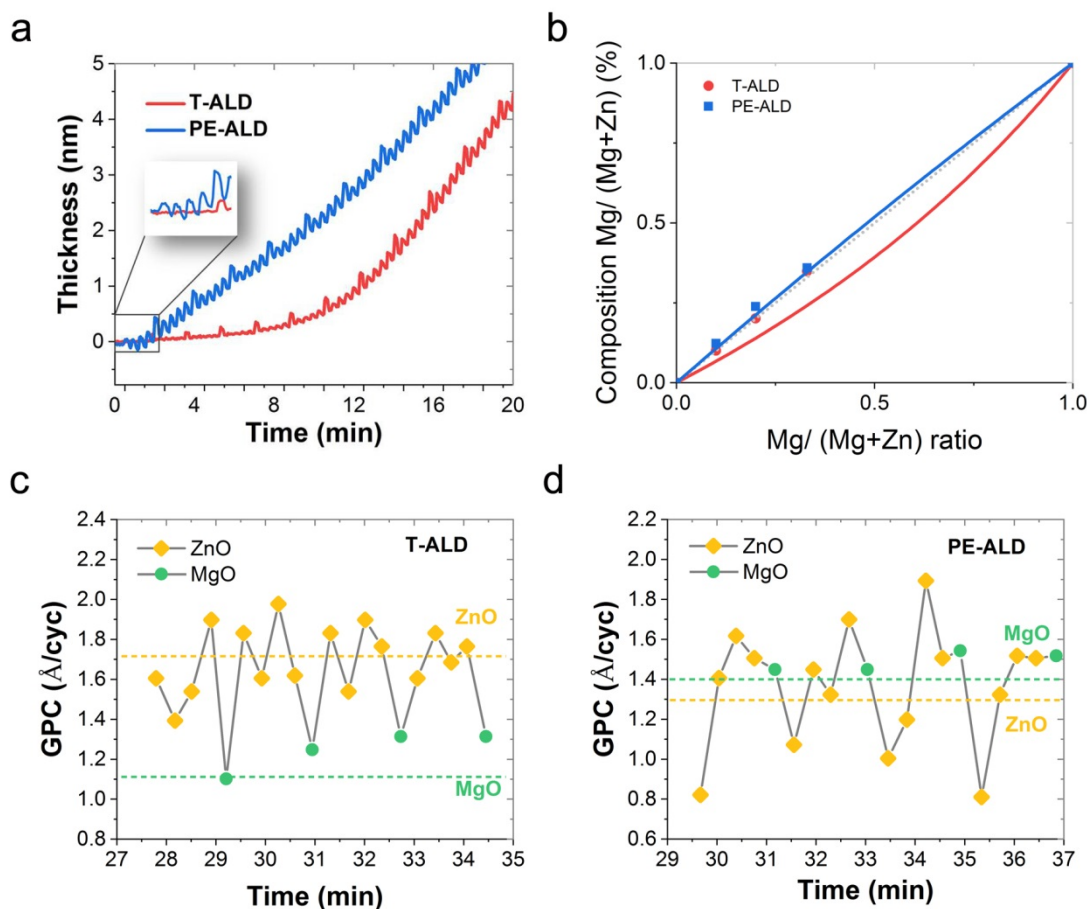


Figure 5. 2 a) The initial stage of ZnMgO film growth during T-ALD and PE-ALD at 150 °C on Si (111). b) Experimental composition (solid line) from ICP-OES of the thin films closely follows the expected composition (dash line) from the weighted average of the growth rates (rule of mixtures, ROM). Growth per cycle of consecutive ZnO and MgO sub-cycles using c) T-ALD and d) PE-ALD as measured by *in situ* ellipsometry. The dashed lines indicate the growth per cycle for pure ZnO and MgO.

On careful examination of the initial growth, the first few cycles' growths were given in the inset of Figure 5. 2a. For thermal ALD growth, no significant thickness changes at the first 4 cycles mean it is difficult for either DEZ or H<sub>2</sub>O absorption on the surface in the ZnO subcycles. After that, a clear thickness gain was witnessed when the Mg(CpEt)<sub>2</sub> precursor was introduced to the deposition, indicating the surface absorption of Mg precursor. As following is the decrease of the nominal thickness,

corresponding to the removal of surface methyl ( $-\text{CH}_3$ ) group through a reaction with pulsed  $\text{H}_2\text{O}$ . The net thickness changes during this  $\text{MgO}$  sub-cycle gives the growth per cycle (GPC). The reaction behavior of  $\text{O}_2/\text{Ar}$  plasma with  $\text{Zn}$  precursor at the initial stage seems quite different from the thermal one. One can even observe a decreased growth for the first two cycles, whereas slight accelerated  $\text{Al}_2\text{O}_3$  growth by PE-ALD is observed for the first few cycles in previous reports.[220] This abnormal phenomenon was further investigated using  $\text{O}_2/\text{Ar}$  plasma exposure test on bare native-Si to exclude the influence from the  $\text{Zn}$  precursor. It shows that the thickness of native-Si decreased once the substrate exposure to  $\text{O}_2/\text{Ar}$  plasma, with a decreased thickness similar to that in  $\text{ZnMgO}$  PE-ALD process. This test suggests the negative GPC is from the interplay of plasma with substrates, rather than from the PE-ALD of  $\text{ZnO}$  cycle itself. The reduced GPC could either come from the  $\text{O}^-$  plasma clean of the organic residue on the native-Si or the  $\text{Ar}^+$  plasma damage on the loose native oxides. Note that the initial film thicknesses were fitted by keeping the SE model parameters constant, without taking the plasma damaged surface with porous or roughness into consideration. After the initial stage, the plasma effects became weak on the surface, thus the growth via PE-ALD went to constant region as expected for ALD growth.

In a super-cycle scheme of  $\text{ZnMgO}$ , the growth behavior of each sub-cycle could differ from pure  $\text{ZnO}$  and  $\text{MgO}$ , therefore the values of GPC at the steady growth stage were also investigated from in situ SE data. The GPCs for pure  $\text{ZnO}$  (yellow dash line) and  $\text{MgO}$  (green dash line) were also included to compare with that in the super-cycle via T-ALD and PE-ALD, as can be seen from Figure 5. 2c and Figure 5. 2d. An approximately constant GPC was observed for both  $\text{ZnO}$  and  $\text{MgO}$  sub-cycles in T-ALD, without too much variation of the GPC of pure oxides. Note that  $\text{MgO}$  yields a higher GPC than its binary compound. In the case of PE-ALD, however, a nucleation delay was found for the first cycle of  $\text{ZnO}$  after one cycle of  $\text{MgO}$ . Notably, such growth delay has been reported in the case of  $\text{ZnAlO}$ , [221]  $\text{ZnSnO}$ , [190]  $\text{ZnMgO}$ , [133] where less density and/or fewer reactive sites on the surface may retard the growth of

ZnO during the sub-cycle transition. This effect is also possible to play a role in the PE-ALD ZnMgO, however, the surface chemistry needs to be further investigated to provide deep insight into this behavior.

Table 5. 1 Growth properties of ZnMgO thin films with different compositions synthesized by T-ALD and PE-ALD.

Zn/Mg Ratio	cycles	T-ALD			PE-ALD		
		Mg/(Mg+ Zn) content	Thickness (nm)	GPC ( Å/cycle)	Mg/(Mg+ Zn) content	Thickness (nm)	GPC ( Å/cycle)
0	200	0	34	1.7	0	27	0.9
9:1	300	0.101	52	1.7	0.123	39.8	1.3
4:1	300	0.201	48	1.6	0.238	40.2	1.3
2:1	300	0.349	42	1.4	0.359	40.9	1.4
1	300	1	33	1.1	1	27	0.9

The thickness and GPC values of ZnMgO thin films with different compositions synthesized by T-ALD and PE-ALD are summarized in Table 5. 1. Figure 5. 2b displays the relative Mg concentration (Mg to (Zn+Mg) composition ratio) as a function of Mg: (Zn+Mg) cycle ratio for this set of ZnMgO nanolaminates determined by ICP-OES, films with a thickness of  $40 \pm 3$  nm were deposited as monitored by *in situ* SE. The ZnMgO films were deposited as nanolaminates by employing different ratios between ZnO and MgO sub-cycles which were tuned to be 9:1, 4:1, 2:1. As different oxides have different GPC, the expected Mg concentration of ZnMgO can be expressed using the rule of mixtures (ROM) formula:[221]

$$\text{Mg}_{\text{ROM}} = \frac{r_{\text{Mg}} f_{\text{Mg}}}{r_{\text{Mg}} f_{\text{Mg}} + r_{\text{Zn}} (1 - f_{\text{Mg}})} \quad \text{Equation 5. 1}$$

Where  $r_x$ ,  $f_x$  refer to the growth rate and the fraction of the cycle of metal oxide  $x$ , respectively. The growth rate for binary materials was measured using ellipsometry under the same ALD condition. As the reduced GPC of ZnO after MgO cycles, the composition of the ternary films should have higher Mg concentration with respect to the estimated composition from the binary films. The solid line in Figure 5. 2b indicates the expected composition of Mg atom concentration in metal ions without including oxygen from the ROM formula. The fractional Mg compositions were also obtained experimentally by ICP-OES for comparison purposes. It shows that the experimental results yield higher Mg content value than the fitting value for the film deposited by T-ALD, which could be attributed to the higher MgO GPC compared to its binary compound. In contrast, the experimental values and expected values are in good agreement in the case of ZMO films deposited by PE-ALD despite the fluctuation of the ZnO sub-cycle growth.

### 5.2.2 Comparison of ZnMgO on morphology and structural property

The structural properties of the deposited ZMO films formed by T-ALD and PE-ALD process were then analyzed by GIXRD patterns, as illustrated in Figure 5. 3. All the patterns demonstrate overall amorphous features while containing broadened characteristic peaks. These broaden peaks indicate the formation of nanocrystalline in the films which typically take place when the measured films are very thin. For pure ZnO and MgO, the two processes yield similar crystal structural where ZnO dominated by (101) orientation and MgO featured by (200) orientation. However, the XRD peaks for the ZMO films deposited by thermal and PE-ALD are quite different. From Figure 5. 3a, one can learn that the (100) and (101) orientations are clearly observed for T-ALD grown ZMOs. Whereas for PE-ALD grown ZMO films, the XRD peaks were

found to be mainly in the (101) orientation. This discrepancy might be attributed to the preferential crystal growth using different oxygen co-reactant as oxygen radicals are significantly more reactive. The difference in the crystal structure might lead to the different surface morphology of the deposited films.

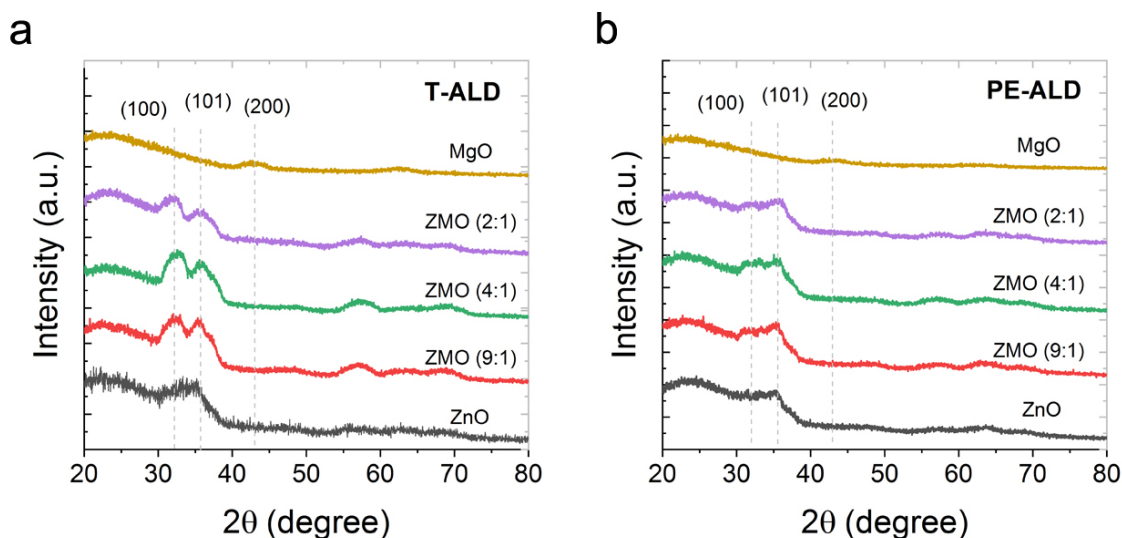


Figure 5. 3 GIXRD patterns for ZMO thin films deposited on SLG substrates through a) T-ALD and b) PE-ALD.

Apart from this, Raman measurements were also performed to check the properties of the ZMO nanocrystalline layers grown from T-ALD and PE-ALD. Here, the Raman measurements were performed in resonant excitation condition by using a 325 nm excitation wavelength ( $\sim 3.8$  eV), which is close to an electronic transition in the material as the energy bandgap in the case of semiconductors. This resonant Raman strategy allows for the assessment of extremely thin nanometric layers with high sensitivity due to the enhancement of the intensity of Raman peaks especially corresponding to LO modes.[222] Figure 5. 4 shows the Raman scattering spectra measured on ZMO thin films with different Mg content deposited through T-ALD and PE-ALD process. The peaks around 600, 1200 and 1800  $\text{cm}^{-1}$  can be identified as the first, second and third-order of the LO vibrational mode from the ZMO compounds, respectively. The main LO peaks were featured by broadened asymmetric shape with a

low-frequency tail with increasing the Mg content in ZMOs. Generally, it could be attributed to the alloy potential fluctuation due to the Mg alloy.[223] For both T-ALD and PE-ALD processed ZMOs, a monotonous increase of the frequency of the LO main peaks with Mg alloying can be observed. This is related to the increase of the lattice constant of ZMO film with increasing Mg doping, which indicates the successful incorporation of Mg into the ZnO wurtzite structure.

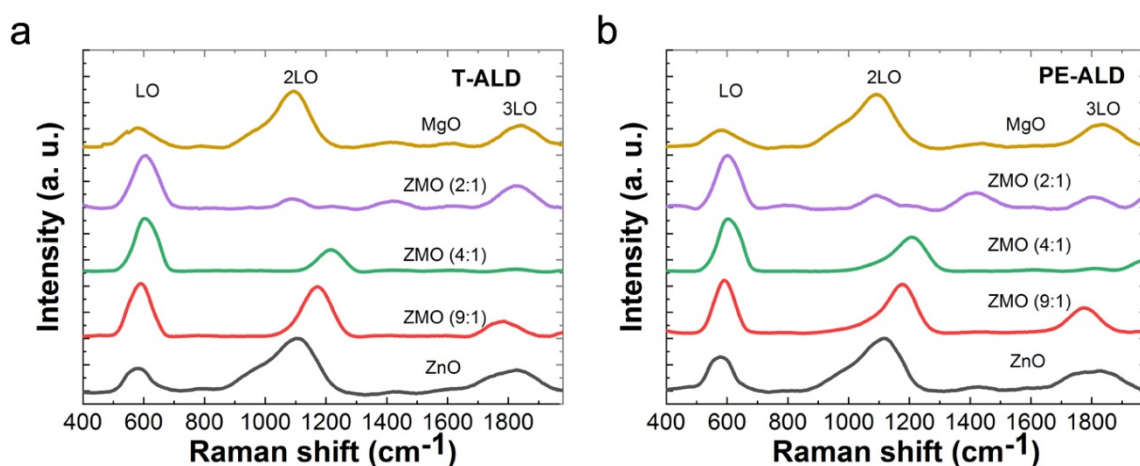


Figure 5. 4 Raman scattering spectra for ZMO thin films deposited through a) T-ALD and b) PE-ALD. An excitation wavelength of 325 nm was used for the measurements.

The surface morphology and roughness of ZMO thin films were then investigated by atomic force microscope (AFM) measurements. Figure 5. 5 presents AFM images of ZMO films deposited through different methods with various compositions on soda-lime glass (SLG) substrates. At first glance, the ZMO deposited through T-ALD exhibits superior smoothness and less rough surface than those of PE-ALD. This roughness difference is commonly observed between T-ALD and PE-ALD due to the surface recombination loss of plasma radicals in PE-ALD.[224, 225] The T-ALD ZMO films display root mean square (rms) surface roughness of 4.0, 2.5 and 2.1 nm for ZMO with Zn;Mg pulse ratio of 9:1, 4:1 and 2:1, respectively. A smoother surface was obtained for ZMO films with a higher Mg concentration. It was suggested that variation of surface roughness was correlated with the crystallinity and crystal size of



the films, where larger crystals grow as a result of lower nucleation rate or smaller surface diffusion rate of the atoms.[226] It was found that the roughness of ALD ZnO films decreased with increasing Al doping, probably due to the prohibited ZnO crystal growth induced by  $\text{Al}^{3+}$  ions substituting surface  $\text{Zn}^{2+}$  ions.[226, 227]

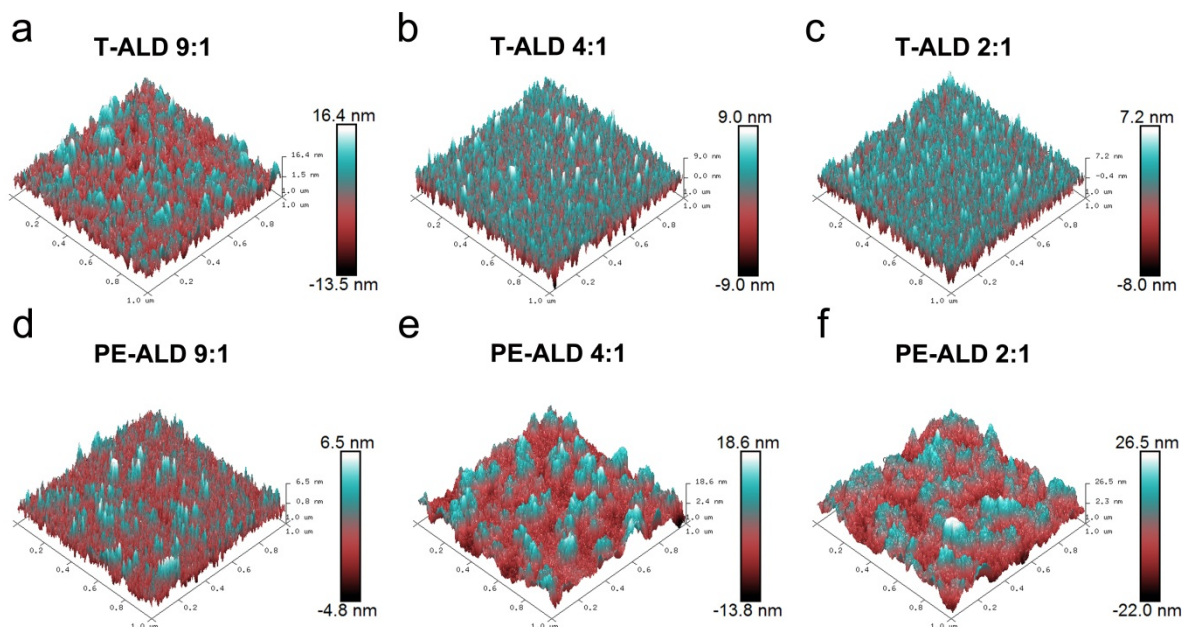


Figure 5. 5 AFM morphology of ZMO thin films deposited through a-c) T-ALD and d-f) PE-ALD.

This decreased ZnO crystal growth could also happen in the case of T-ALD ZnO films doped with Mg. The crystallinity of ZnO could become poorer with increasing Mg incorporation which has been shown in the XRD results of ZMO. However, this roughness variation shows the opposite trend for ZMO grown using PE-ALD. Specifically, a rms of 1.5, 5.1 and 7.0 nm were found for ZMO with Zn;Mg pulse ratio of 9:1, 4:1 and 2:1, respectively. Ola Nilsen *et al.* have thoroughly investigated the growth dynamics of polycrystalline films in ALD and correlated the surface morphology and crystal growth direction with an initial structure of nano-crystal.[228] ZMO deposited by T-ALD and PE-ALD should exhibit different crystal structures as shown in Figure 5. 3. The (100) and (101) orientations are observed for T-ALD grown

ZMOs, whilst the dominant (101) orientation is distinguished for PE-ALD grown ZMOs. For low Mg-doped ZnO films (9:1) where ZnO crystal dominates, PE-ALD process shows a faster grain growth due to the energy introduced into the films from the more active plasma source, which increases the surface diffusion rate and results in a smoother surface. When Mg content increases, the dominant (101) orientation grows even faster and thus the crystal size becomes larger. This will lead to the significant “texturing” of the film surface and a large roughness of the deposited film. The discrepancy of the ZMO roughness might affect the other properties of the films, thus result in various functions as a window layer in the solar cells.

### **5.2.3 Comparison of ZnMgO on optical and electrical property**

To test the optical transparency of the ZMOs deposited on SLG, UV-vis transmission measurements were performed and results are shown in Figure 5. 6. The transparency exhibits a large discrepancy in the visible light range between ZMO compounds and pure oxides, where pure oxides have higher transmittance than ZMOs. For ZMO compounds, the transmittance increases as the doping of Mg. Similar variation in the curves is observed for both T-ALD and PE-ALD process. The curves were then compared from the band edge of different films by evaluating the absorption edge from the transmittance spectra. The near band-edge wavelength for pristine ZnO is around 375 nm, while it moves to the short wavelength range as the Mg ratio increases. It means with increasing Mg doping, the bandgap of the ZMO film increases and is larger than the ZnO film. This phenomenon was further confirmed by the bandgap extracted from the ellipsometry measurement shown in Figure 5. 8a, b.

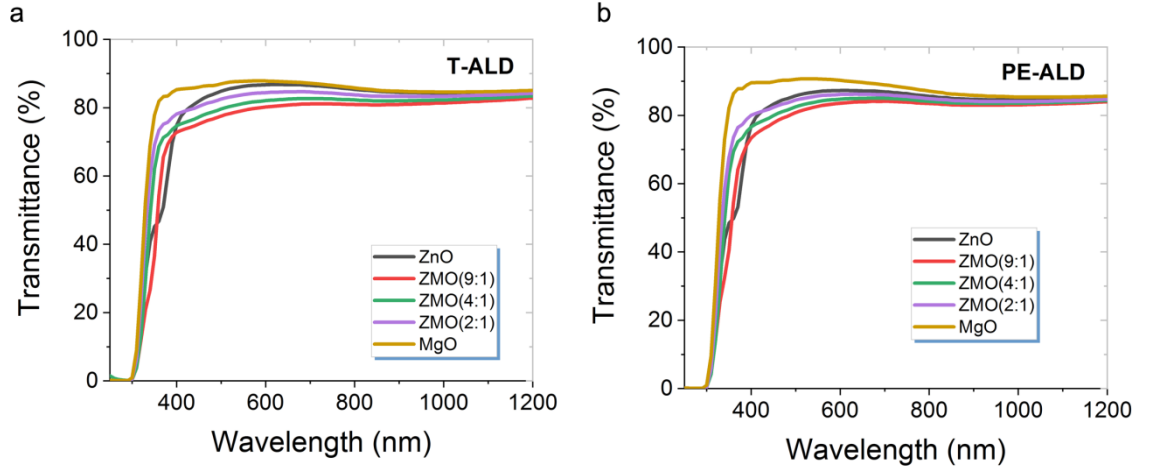


Figure 5. 6 Transmittance as a function of the wavelength for the ZMO films grown using various Zn:Mg sub-cycle ratios through a) T-ALD and b) PE-ALD.

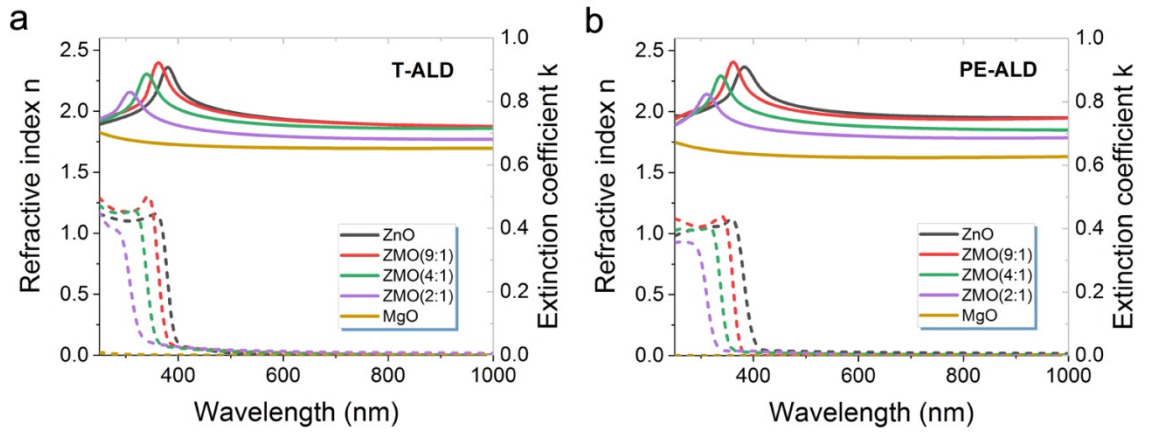


Figure 5. 7 Refractive index and extinction coefficient as a function of the wavelength for the ZMO films grown using various Zn: Mg sub-cycle ratios through a) T-ALD and b) PE-ALD determined from spectroscopic ellipsometry measurements.

The SE measurements were also used to extract the refractive index ( $n$ ) and extinction coefficient ( $k$ ) values of the ZTO films. Figure 5. 7a, b shows the  $n$  and  $k$  values as a function of the photon energy for different ZTO film compositions. The  $n$  (at 1.98 eV) of ZMO films decreased with more Mg-doped down to the pure MgO. The absorption coefficient was calculated from the well-known relation  $\alpha = 4\pi k/\lambda$ , where  $k$

represents the imaginary part of the complex dielectric constant and  $\lambda$  is the light wavelength. Figure 5. 8c provides the bandgap determined by spectroscopic ellipsometry as a function of Mg content of ZMO films deposited through T-ALD and PE-ALD. It seems that the bandgap is independent of the deposition method. The bandgap of ZMO increases almost linearly from  $\sim 3.2$  eV to  $\sim 3.8$  eV as function of Mg content in the range of  $0 \leq \text{Mg}/(\text{Mg}+\text{Zn}) \leq 0.36$ , taking account of ZMOs deposited from both T-ALD and PE-ALD. Therefore, the bandgap of ZMO compounds can be easily tuned by varying the Mg content, in good agreement with previously published results.[141, 229]

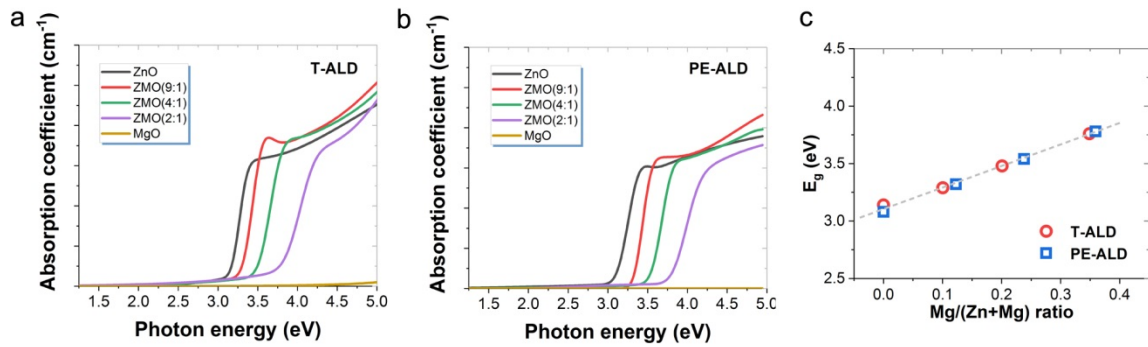


Figure 5. 8 a, b) Absorption coefficient as a function of the photon energy for the ZMO films grown using various Zn:Mg sub-cycle ratios through T-ALD and PE-ALD. c)  $E_g$  extracted from spectroscopic ellipsometry as a function of the relative Mg ratio in ZMO.

The electrical properties of ZMO films were obtained from Hall measurements. The carrier concentration ( $n$ ) and resistivity ( $\sigma$ ) of ZnMgO thin films were measured by the van der Pauw method employing indium contacts at room temperature and the results are listed in Table 5. 2. For T-ALD processed ZMO films, the resistivity was found to increase with the Mg content increasing up to 0.2 while the carrier mobility was found to decrease. The decreases in carrier concentration have contributed to an increase in resistivity. The decrease in carrier concentration has been previously attributed to both an increasing donor activation energy due to a larger effective

mass[194] or change of band structure[195] and a lowering of the active donor concentration due to composition enrichment.[194] However, when then Mg content becomes larger than 0.2, the Hall signal can be hardly detected based on the used measurement configuration due to the large resistivity of the thin films. In addition, all the PE-ALD processed ZMO films demonstrated high resistivity which was not able to be acquired through the hall measurement.

Table 5. 2 Optical and electrical properties of ZnMgO thin films changing along with Mg content synthesized from T-ALD and PE-ALD.

		T-ALD			PE-ALD		
Zn/Mg	cycles	Carrier			Carrier		
Ratio		Bandgap	concentrat	Resistivity	Bandgap	concentrat	Resistivity
		(eV)	ion	( $\Omega\cdot\text{cm}$ )	(eV)	ion	( $\Omega\cdot\text{cm}$ )
			( $\text{cm}^{-3}$ )			( $\text{cm}^{-3}$ )	
0	200	3.14	$-9.10\times 10^{18}$	$6.53\times 10^{-2}$	3.08	N/A	N/A
9:1	300	3.29	$-8.54\times 10^{18}$	$1.11\times 10^{-1}$	3.32	N/A	N/A
4:1	300	3.48	$-5.45\times 10^{16}$	$1.64\times 10^1$	3.54	N/A	N/A
2:1	300	3.76	N/A	N/A	3.78	N/A	N/A
1	300	7.30	N/A	N/A	7.30	N/A	N/A

### 5.3 Application of ZnMgO as window layer on CZTS solar cell

#### 5.3.1 SCAPS simulation of ZnMgO as the window layer for CZTS solar cell

Before performing the experimental work of ZnMgO window layer on CZTS, numerical simulations were performed using a Solar Cell Capacitance Simulator (SCAPS 1D)[211] to describe the model of CZTS device with ZnMgO as the window layer. The device structure of the CZTS/ZnSnO/ZnMgO used SCAPS is shown in

Figure 5. 9a and Figure 5. 9b demonstrates the corresponding band diagram for the CZTS/ZTO/ZMO model. Most of the parameters were taken from the CZTS/ZTO baseline model in Section 4.3.5, except for the ZnMgO window layer.

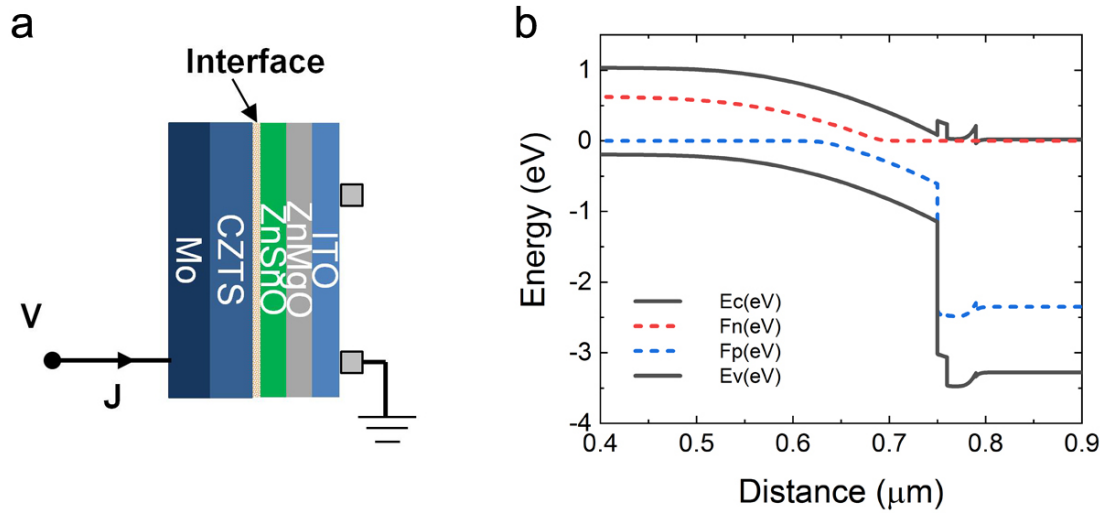


Figure 5. 9 a) Illustration of device structure used for CZTS/ZTO/ZMO model. b) Schematic band diagrams under light at short circuit conditions for CZTS/ZTO/ZMO baseline model.

Table 5. 3 summarizes the parameters inputted into each layer. A systematic study focusses on the impact of window layer electron affinities ( $\chi_{\text{ZMO}}$ ) and carrier concentration on the device performance. Since the bandgap is large enough ( $>3.3$  eV) to not be a critical parameter, it was fixed at 3.5 eV in the following ZMO window layer study. The change in electron affinity, however, matters a lot as it alters the recombination rate at interface thus the  $V_{OC}$ ,  $FF$ , and PCE. The electron affinity values of ZMO were reported to be 4.0 to 4.7 eV corresponding to different compositions of  $\text{Zn}_{1-x}\text{Mg}_x\text{O}$  ( $x$  from 0 to 0.35) based on the parameters in the literature.[215] Here, the electron affinity values of ZMO were tuned from 3.9 to 4.6 eV as the input parameter in simulation. As the experimental studies of the ALD-ZMO (in Chapter 4.2.3) demonstrates, the doping density level varies as a function of the Mg content, and higher Mg incorporation leads to lower doping density. Therefore, carrier

Table 5. 3 Material parameters used for the simulation of CZTS/ZTO/ZMO devices in SCAPS-1D.

Property	CZTS	CZTS/ZTO interface	ZTO	ZnMgO	ITO
Thickness (nm)	700		10	10	200
Effective Electronic bandgap (eV)	1.275		3.3	3.3~3.8	3.3
Electron affinity (eV)	4.2		3.95	3.9~4.6	4.45
Relative dielectric constant	7		10	10	10
Conduction band density of states (cm <sup>-3</sup> )	2.2*10 <sup>18</sup>		2.2*10 <sup>18</sup>	2.2*10 <sup>18</sup>	2.2*10 <sup>18</sup>
Valence band density of states (cm <sup>-3</sup> )	1.8*10 <sup>19</sup>		1.8*10 <sup>19</sup>	1.8*10 <sup>19</sup>	1.8*10 <sup>19</sup>
Electron mobility (cm <sup>2</sup> /V/s)	1.02		5	100	100
Hole mobility (cm <sup>2</sup> /V/s)	1		5	25	25
Free carrier concentration (cm <sup>-3</sup> )	1.0*10 <sup>16</sup>		1.0*10 <sup>17</sup>	1.0*10 <sup>16</sup> ~ 1.0*10 <sup>19</sup>	1.0*10 <sup>18</sup>
Interface recombination velocity (cm/s)		10 <sup>5</sup>			

concentration values from  $1 \times 10^{16}$  to  $1 \times 10^{19} \text{ cm}^{-3}$  were used for ZMO in the simulations.

The thickness of ZMOs was set to be 10 nm in the simulation to minimize the absorption loss. Assuming ZMOs are as resistive as i-ZnO window layer, the series and shunt resistance was fixed to be 0.2 and 1000  $\Omega\cdot\text{cm}^2$ , respectively.

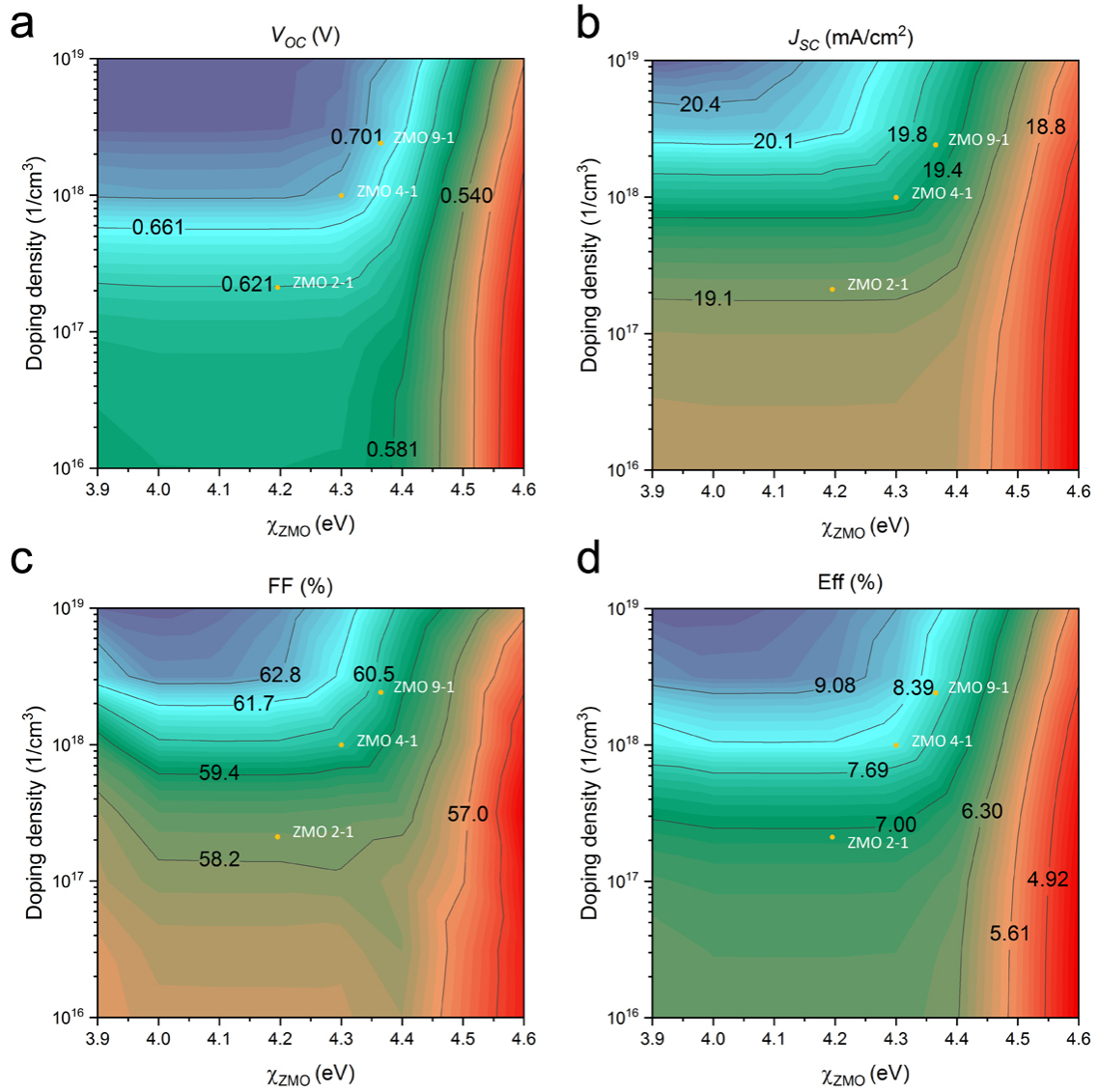


Figure 5. 10 Calculated contour plots of a) open-circuit voltage, b) short-circuit current, c) fill-factor, and d) efficiency for CZTS/ZnSnO/ZnMgO devices with the variation of ZMO properties (left axis indicates doping density, bottom axis indicates electron affinity  $\chi_{\text{ZMO}}$  ).



The resulting device parameters were then summarized in Figure 5. 10. It can be observed that the highest efficiency was achieved in the region with lower ZMO electron affinity and higher ZMO doping density. When  $3.9 < \chi_{\text{ZMO}} < 4.2$  eV, the efficiency decreased slightly with decreased carrier concentration in ZMO mainly due to the  $V_{\text{OC}}$  change. This is because the increased free carrier density will flatten the bands in the buffer/window layer and thus result in increased band bending in the absorber. Therefore, the dependence of  $V_{\text{OC}}$  on carrier density of the buffer/window layer is severe. It should be noted that  $V_{\text{OC}}$  changes independent with ZMO electron affinity, which means the recombination rate does not increase due to the quasi-Fermi level for electrons at the CZTS surface lay sufficiently below trap position. When  $\chi_{\text{ZMO}} > 4.45$  eV, the efficiency dropped drastically, primarily attributed to the decrease in  $FF$  and  $V_{\text{OC}}$ . The  $J_{\text{sc}}$  variation is much smaller because the recombination of the photo-generated carriers is minimized due to the presence of the electrical field in the space charge region. On the other hand, when  $4.2 < \chi_{\text{ZMO}} < 4.45$  eV, the efficiency was maintained at an intermediate level as a result of the compromise between electron affinity and doping density of the window layer. Consequently, it was suggested that the highly performed CZTS/ZTO/ZMO device could be achieved with  $\chi_{\text{ZMO}}$  below 4.45 eV and reasonably high carrier density without considering the resistivity effect of the window layer. Therefore, the experimental work of varied ZMO composition was carried out and presented in the next section.

### **5.3.2 CZTS device made from ZnMgO window layer via thermal ALD and PE-ALD**

The CZTS solar cells with ZnSnO buffer and ZnMgO window layers were fabricated following the process described in Figure 5. 11. CZTS absorbers were deposited onto a Mo-coated soda-lime glass substrate from co-sputtered Cu/ZnS/SnS precursors by using a magnetron sputtering system (AJA International, Inc., Model

ATC-2200). The composition of CZTS absorbers was controlled to be Cu-poor ( $\text{Cu}/(\text{Zn}+\text{Sn}) = 0.88$ ) and Zn-rich ( $\text{Zn}/\text{Sn} = 1.18$ ) as described in our previous work.<sup>27</sup> The films were then subjected to the sulfurization process in combined sulfur and SnS atmosphere at 560 °C with a heating rate of 15 °C min<sup>-1</sup> for 3 min. After sulfurization, the samples were stored in a nitrogen box or immediately transferred into the ALD reactor to deposit ZTO buffer layer. Reference devices with 50 nm i-ZnO were fabricated in each batch. For experimental devices, different composition of 10-nm-thick ZMO window layers was applied to investigate their effects on the device performance. An ITO (210 nm) top contact was then deposited by radio frequency sputtering, followed by Al grids using evaporation.

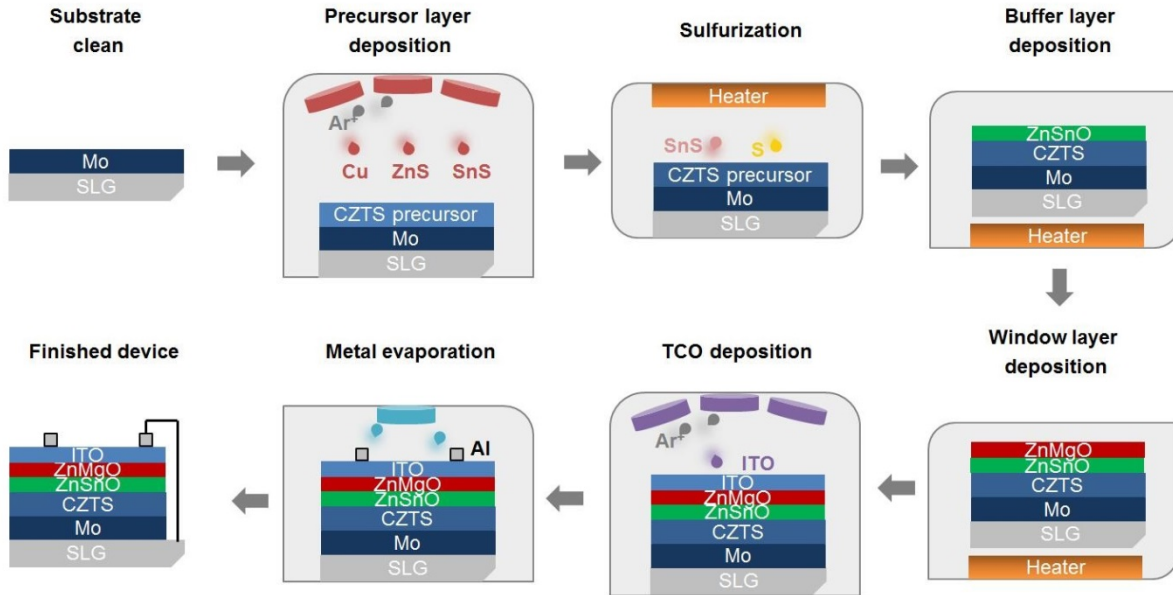


Figure 5. 11 Schematic of the fabrication of CZTS/ZnSnO/ZnMgO thin-film solar cell.

### 5.3.3 Influence of ZnMgO composition on the device properties

A series of CZTS solar cells were fabricated with T-ALD processed ZMO as a window layer by changing the composition of ZMO. The device with a sputtered i-ZnO window layer (50-nm-thick) was used as a reference. The ratio of the ZnO and MgO sub-cycle was tuned to be 2:1, 4:1 and 9:1 and the corresponding solar cells were

named ZMO 2-1, ZMO 4-1 and ZMO 9-1, respectively. The thickness of the ZMO layers was kept constant at 10 nm to exclude the effect of the film thickness. The resulting performance parameters are shown in Figure 5. 12. Note that very low-efficiency cells due to shunt problems were excluded in the box-plots. The ZMO 9-1 sample had only three devices presented because of significant shunting problems caused by the low resistive ZMO layer. Therefore, it had an extremely low yield using a low Mg content ZMO window layer. The experimental devices reach the highest efficiency with a ZMO 4-1 window layer, although slightly lower than the control device.

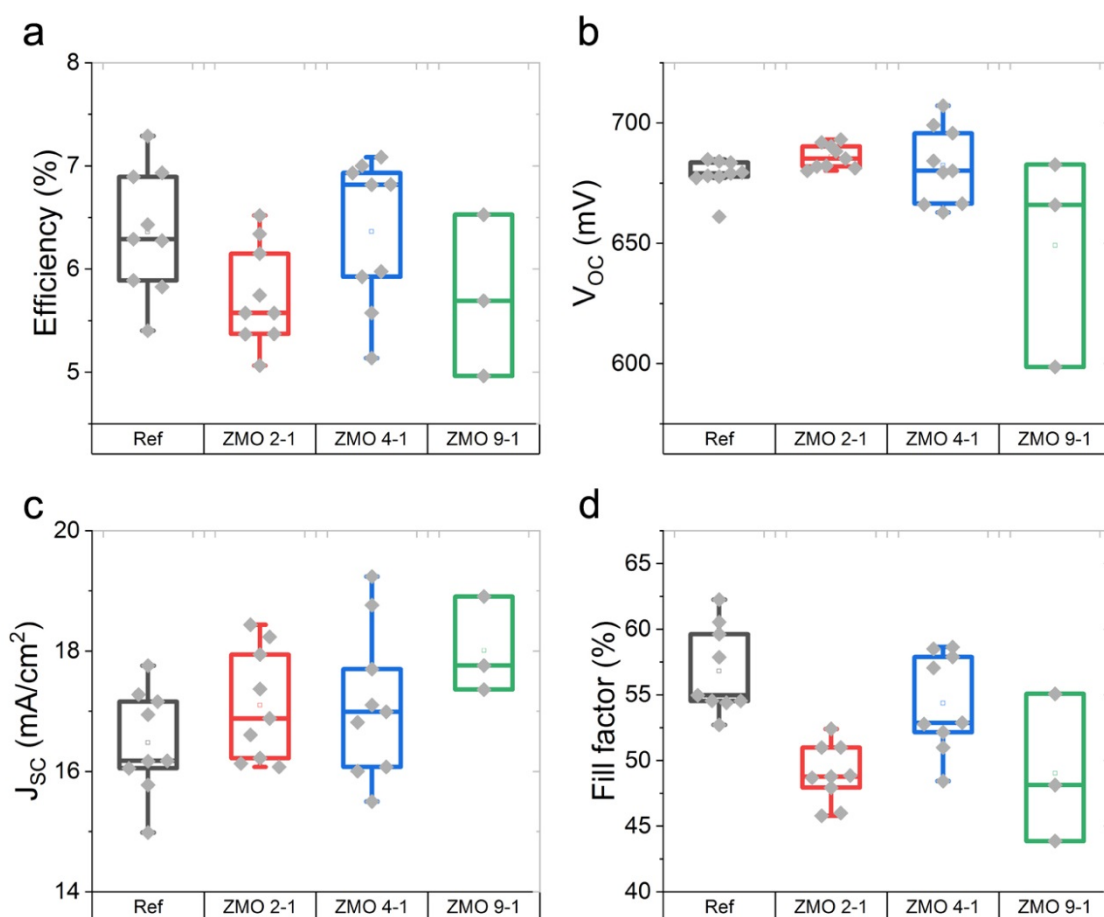


Figure 5. 12 a-d) Box-plots of performance parameters of CZTS cells with a variable composition of ZMO window layer compared to the corresponding i-ZnO control device. 10 CZTS solar cells were fabricated per experimental condition.

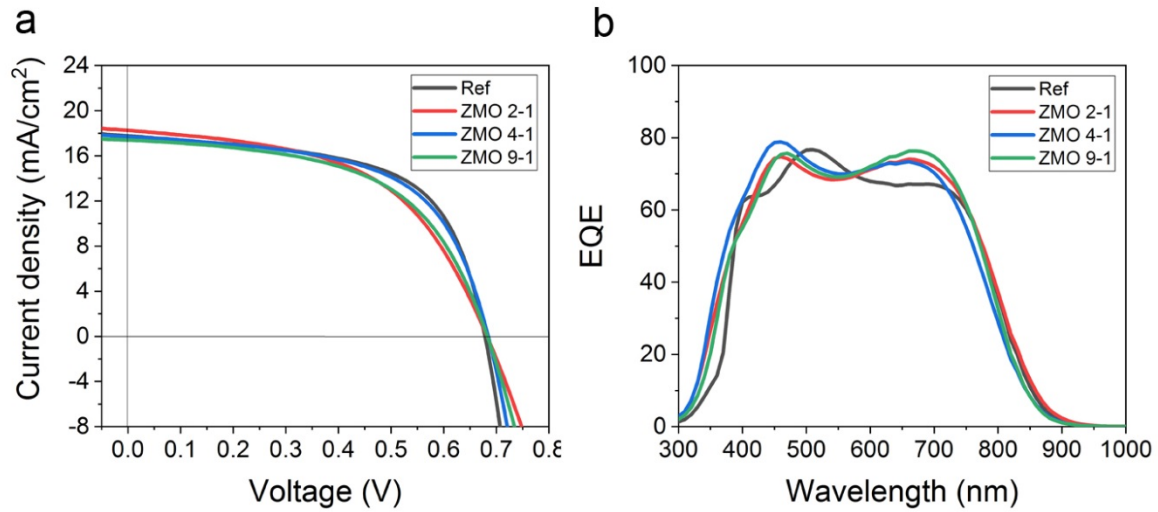


Figure 5. 13 a) The current density-voltage curves b) External quantum efficiency of the CZTS solar cells with different compositions of ZMO buffer layer compared to a corresponding i-ZnO control device.

In terms of  $V_{OC}$ , the ZMO 4-1 device with  $Mg/(Mg+Zn)$  content of  $\sim 0.2$  was observed to have the highest  $V_{OC}$ . A strong dependence of the  $V_{OC}$  on the ZMO composition is observed probably attributed to the conduction band alignment between the window layer and absorber/buffer layer. As can be learned from the numerical simulation in Section 5.3.1, the  $V_{OC}$  improved with decreased  $\chi_{ZMO}$  using ZMO with  $Mg/(Mg+Zn)$  content ranging from 0 to 0.35. In addition, the carrier density of ZMO layer played a critical role in affecting the  $V_{OC}$  value. Therefore, ZMO 2-1 device with even higher Mg content did not necessarily yield higher  $V_{OC}$  than ZMO 4-1 device, probably due to the much lower carrier density of ZMO. The ZMO devices typically yield a higher  $J_{SC}$  than i-ZnO control device as shown in Figure 5. 12. This is mainly due to higher absorption in the short wavelength range as can be seen in the external quantum efficiency (EQE) curves shown in Figure 5. 13b. This phenomenon could be attributed to higher transparency of the ZMO ( $E_g > 3.3$  eV) film compared to the reference i-ZnO ( $E_g=3.3$  eV) window layer, but most likely because of the much thinner ALD ZMO applied in the solar cell. It was also noticed the quantum efficiency

differed in the wavelength range of 450 to 750 nm, which could be attributed to the interference of incident light. Despite that, the overall  $J_{sc}$  of the ZMO devices still improves due to the gain in the short wavelength range. Nevertheless, the efficiency variation seems to be mainly dominated by the  $FF$ . Higher  $\chi_{ZMO}$  (ZMO 9-1) tends to yield negative conduction band offset between window and absorber layer, thereby deteriorates  $FF$ . A lower doping density (ZMO 2-1) also decreases  $FF$  due to the poor quality of ZMO with Mg content over 0.3, as presented in Section 5.3.1. Therefore, ZMO 4-1 device with Mg/(Mg+Zn) content of  $\sim 0.2$  was found to be the optimized composition although the  $FF$  still needs improvement.

### 5.3.1 Influence of ZnMgO deposition method on the device properties

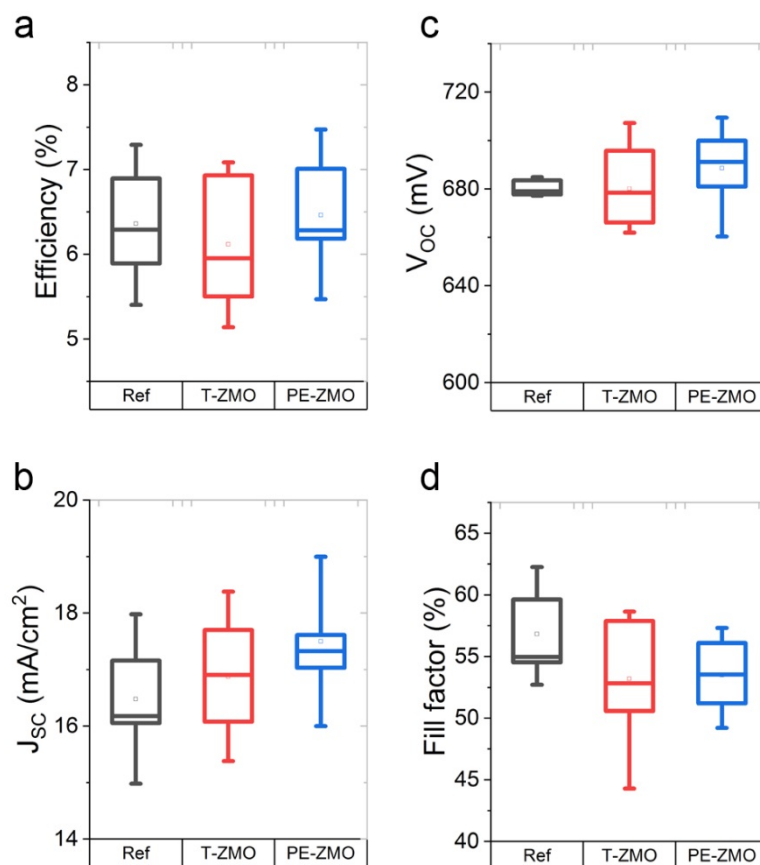


Figure 5. 14 a-d) Box-plots of performance parameters of CZTS cells with ZMO window layer deposited from T-ALD and PE-ALD compared to a corresponding i-ZnO

control device.

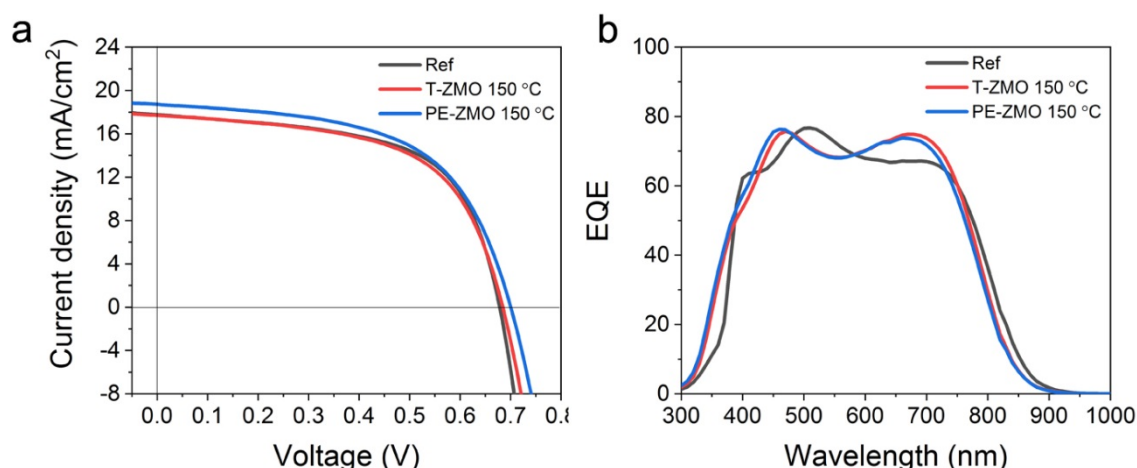


Figure 5. 15 a) The current density-voltage and b) external quantum efficiency of the CZTS solar cells with ZMO window layer deposited from T-ALD and PE-ALD compared to a corresponding i-ZnO control device.

Driven by the fact that T-ALD processed ZMO window layers were not able to enhance the CZTS efficiency, PE-ALD processed ZMO as an alternative window layer was then studied. A series of CZTS solar cells were fabricated with a 10-nm-thick ZMO window layer grown using both T-ALD (denoted as T-ZMO) and PE-ALD (denoted as PE-ZMO). The device with a sputtered i-ZnO window layer (50-nm-thick) was used as a reference. The Zn:Mg pulse ratio of ZTO was kept as identical as 4:1 and the resulting solar cell parameters are shown in Figure 5. 14. It shows that the overall efficiency of the CZTS solar cells grown using the PE-ZMO was higher than the T-ZMO even outperforming the i-ZnO reference. The higher performance of the PE-ZMO devices could mainly be attributed to a higher  $V_{OC}$  and  $J_{sc}$ , which might be attributed to the better quality of PE-ZMO and more favorable band structure. The increased  $J_{sc}$  can be attributed to higher absorption in the short wavelength range between 350 nm ~ 450 nm, as seen from EQE curves in Figure 5. 15b. This can be probably explained by the larger bandgap of PE-ZMO (3.54 eV) than the T-ZMO (3.48 eV), thus allows for enhanced absorption in the above region. However, the  $FF$  the

PE-ZMO devices dropped significantly compared to reference and T-ZMO devices, probably due to the large roughness of the film which led to poor coverage of the underlying layers.

As the absorber quality for those devices is expected to be identical since they were from the same batch, the significant increase in performance from the PE-ZMO devices can be attributed to the change in the window layer. The effect of deposition method on the chemical state and compositional mixing in the ZMO ternary oxides was then investigated by high-resolution XPS measurements. The core-level peak of Zn 2p<sub>3/2</sub>, Mg 1s, and O 1s are shown in Figure 5. 16. Meanwhile, the O 1s core level can be deconvoluted into two peaks by using the Gaussian curve approximation.[209] The deconvoluted O 1s features can be attributed to (1) O<sub>I</sub>, metal oxide (M-O-M) lattice species at 530.3 eV, (2) O<sub>II</sub>, lattice oxygen in the oxygen-deficient region at 531.6 eV. Figure 5. 17 demonstrates the chemical composition from the XPS spectra. One can notice that there were more or less C in the two samples, indicating the presence of bulk C incorporation during both T-ALD and PE-ALD. The atomic ratios of O/Zn+Mg in the ZMO films were determined to be 0.97 and 0.99 by evaluating the O 1s, Zn 2p<sub>3/2</sub>, and Mg 1s peak areas. This confirms the formation of more stoichiometric films when the O<sub>2</sub> plasma used as the co-reactant. Another noticeable phenomenon was the discrepancy in O<sub>I</sub>/ O<sub>II</sub> ratio which represents the ratio of M-O-M species to lattice oxygen. The ratio value for PE-ZMO was found to be 1.36 whilst T-ZMO to be 1.25, hence PE-ZMO possessed higher metal oxide lattice species and lower density of oxygen deficiency. Oxygen vacancies were generally regarded to be associated with the *n*-type conductivity in ZnO and therefore may play a similar role in the ZMO films.[230, 231] Thus, the PE-ALD processed ZMO films possessed enhanced resistivity due to the less oxygen deficiency, which is well correlated with the previous investigation on the electrical properties of the ZMO films in Section 5.2.3.

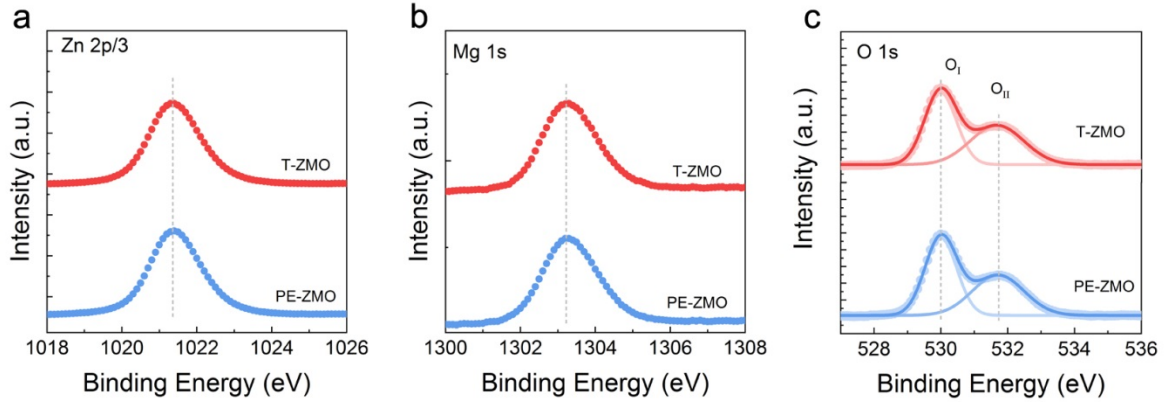


Figure 5. 16 a-c) XPS peak of Zn 2p<sub>3</sub>, Mg 1s, O 1p, respectively, obtained from the surface of ZMO thin films deposited through T-ALD and PE-ALD.

Ultraviolet photoelectron spectroscopy (UPS) measurements were done to investigate the band alignments between absorber, buffer layer and ZMO window layers. Figure 5. 17b shows an overlay of the UPS spectra for the T-ZMO and PE-ZMO where the valence band maximum (VBM) relative to the Fermi energy level ( $E_F$ ) can be determined from the well-established method of extrapolating the valence density of states to zero density. The VBM estimated from the valence band spectra for T-ZMO and PE-ZMO sample was  $2.94 \pm 0.1$  eV and  $2.69 \pm 0.1$  eV below the  $E_F$ , respectively. Once the VBM was determined, the conduction band minimum (CBM) of ZMOs can be obtained by adding the bandgaps of T-ZMO (3.48 eV) and PE-ZMO (3.54 eV) determined from the optical measurements in Chapter 5.2.3. Herein, the band diagrams at the heterojunction for CZTS/ZTO/ZMO are depicted in Figure 5. 17c. Clearly, the PE-ZMO demonstrated a higher VBM compared to the T-ZMO. The resulting conduction band offsets at ZTO/ZMO were found to be  $-0.25 \pm 0.1$  eV and  $-0.45 \pm 0.1$  eV for PE-ZMO and T-ZMO, respectively. Therefore, PE-ZMO demonstrated a reduced cliff-like CBO which was beneficial for the  $V_{OC}$  of CZTS/ZTO/PE-ZMO devices. However, PE-ALD produced the higher resistive PE-ZMO, therefore deteriorate the  $FF$  of the device. This band structure could well explain the  $I$ - $V$  performance of the CZTS/ZTO/ZMO devices.



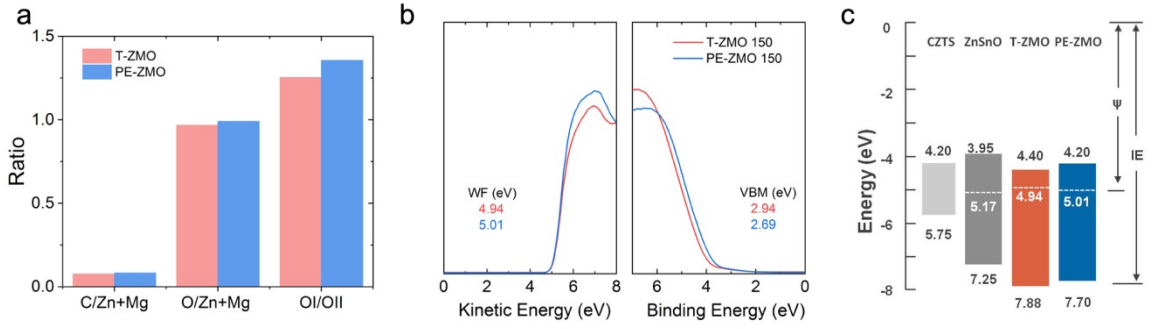


Figure 5. 17 a) Atomic composition, b) UPS spectra and c) band diagram of the CZTS solar cells with ZMO window layer deposited from T-ALD and PE-ALD.

With a better quality of the CZTS absorber layer, the enhanced photovoltaic performance of the CZTS/ZTO/PE-ZMO device could be achieved. The  $J-V$  characteristic of the champion solar cell with a PE-ZMO window layer is shown in Figure 5. 18a. In contrast to the champion 9.3% efficient CZTS/ZTO solar cell, the champion 9.2% efficient PE-ZMO presented here was fabricated without 110 nm  $\text{MgF}_2$  ARC. The  $J_{sc}$  of this champion device was measured to be  $21.1 \text{ mA/cm}^2$  which was even higher than the  $20.5 \text{ mA/cm}^2$  of CZTS/ZTO with ARC. This enhancement indicates the better light-harvesting of the PE-ZMO device by using window layer with larger bandgap and thinner thickness. The  $V_{oc}$  of PE-ZMO device was slightly increased from 720 mV to 727 mV that potentially can be explained by reduced cliff-like CBO between buffer and window layer. Unfortunately, the  $FF$  of the PE-ZMO device dropped dramatically from 63.5% to 59.8%, which is a critical issue for further enhancing device performance. The poor  $FF$  could be assigned to the poor coverage of the underneath layer when using a relatively rough ultrathin PE-ZMO layer, consequently produce a shunt path in the device. It is expected that higher  $FF$  can be gained with a smooth and resistive ZMO layer while maintaining the Mg content of  $\sim 0.2$ . In this sense, ZMO deposited by PE-ALD in low temperatures could probably yield high resistivity and smoother surface, therefore benefit the overall efficiency.

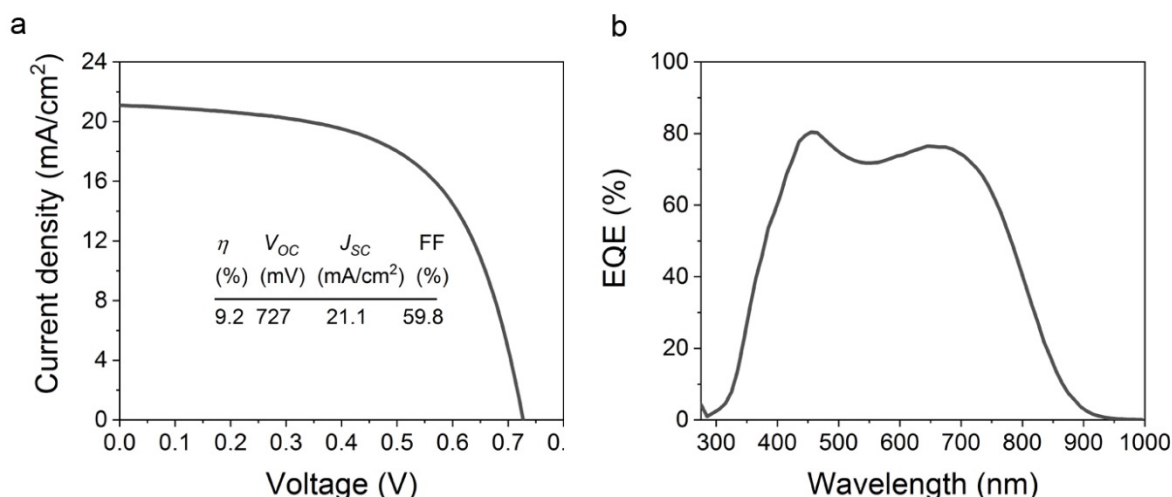


Figure 5. 18 a)  $J$ - $V$  characteristics and b) EQE of the champion CZTS/ZTO/PE-ZMO solar cell without anti-reflection coating.

## 5.4 General conclusions

In this chapter, ZMO ternary oxides films with various compositions were deposited by using both thermal ALD and plasma-enhanced ALD. The growth property, morphology, and structural property, optical and electrical property of the ZMO films as a function of the Mg content were systematically investigated. *In-situ* ellipsometry measurement revealed the different growth behavior for ZMOs deposited by T-ALD and PE-ALD due to different reactivity of the oxidant. Consequently, the resulted thin films exhibited quite different crystalline structures and surface morphology. Generally, the ZMO deposited through T-ALD exhibits superior smoothness and less rough surface than those of PE-ALD. The bandgap of ZMO was found to increase linearly as a function of Mg content in the range of  $0 \leq \text{Mg}/(\text{Mg}+\text{Zn}) \leq 0.36$ , for both T-ALD and PE-ALD processed films. In addition, PE-ALD processed ZMO films demonstrated much higher resistivity than the T-ALD deposited films.

The numerical simulation of the effects of ZnMgO window layer on CZTS device performance was then performed. It was suggested that a high-performance CZTS/ZTO/ZMO device could be achieved with  $\chi_{ZMO}$  below 4.45 eV and reasonably high carrier density. The device with  $\text{Zn}_{0.8}\text{Mg}_{0.2}\text{O}$  layer showed a relatively higher

efficiency although the  $FF$  still needs improvement. Further study was carried out by using PE-ALD processed ZMO as an alternative window layer due to its higher quality and more suitable band alignment. The CZTS solar cells with a PE-ZMO devices window layer showed a higher efficiency, mainly due to a higher  $V_{OC}$  and  $J_{sc}$ . The reduced cliff-like CBO between absorber and window layer was believed to be beneficial for the  $V_{OC}$  of CZTS/ZTO/PE-ZMO devices. However, the relatively higher roughness of PE-ZMO could deteriorate the  $FF$  of the device. Finally, a champion 9.2% efficient PE-ZMO device was fabricated without anti-reflection coating thanks to the significantly enhanced  $J_{sc}$ , primarily because of the less optical loss in the thinner window layer with large bandgap.

## Chapter 6 $\text{Al}_2\text{O}_3$ as interface passivation layer for CZTS<sup>2</sup>

In this chapter, a Cd-free CZTS solar cell that exhibits an energy conversion efficiency of 10.2 % is presented resulting from the application of an aluminum oxide ( $\text{Al}_2\text{O}_3$ ) passivation layer prepared by atomic layer deposition (ALD). It was demonstrated that the application of full ALD cycles as well as trimethylaluminum (TMA) exposures resulted in a significant increase in  $V_{OC}$  and relate this to the properties of the CZTS interface. Both processes facilitate the formation of a thicker Cu-deficient nanolayer with a higher concentration of Na and O, forming a homogeneous passivation layer across the CZTS surface. This nanolayer reduces the local potential fluctuation of band edges and leads to the widened electrical bandgap and suppressed defects recombination at the heterojunction interface, thus an improvement in  $V_{OC}$  and device performance. The ability of nanolayers to alter the atomic composition in the near-surface region of compound semiconductors might be beneficial for a wider range of semiconductor devices.

---

<sup>2</sup> Part of this chapter has been published as: Cui, X., K. Sun, J. Huang, J. Yun, C.-Y. Lee, C. Yan, H. Sun, Y. Zhang, C. Xue, M. K. Eder, L. Yang, J.M. Cairney, J. Seidel, N.J. Ekins-Daukes, M. Green, B. Hoex and X. Hao, Energy & Environmental Science, 2019, 12(9): 2751-2764.

## 6.1 Introduction

A conformal coating by atomic layer deposition (ALD) can provide precise modification and passivation at the interface due to the intrinsic self-terminating nature of the process. Aluminum oxide ( $\text{Al}_2\text{O}_3$ ) nanolayers deposited by ALD have shown to be an effective way to passivate *p*- and *n*-type silicon surfaces through chemical and field-effect passivation[184, 232]. Generally, chemical passivation is achieved by hydrogen passivation[233] or an interfacial silicon oxide layer[220] whereas the field-effect passivation is associated with the high density of negative fixed charges located within the first nanometers of the  $\text{Al}_2\text{O}_3$  layer[234, 235]. The origin of negative fixed charges may arise from excess oxygen during the initial growth of nonstoichiometric  $\text{Al}_2\text{O}_3$ [236] or a gradient in coordination through the negative charges of the tetrahedral coordination[232]. ALD- $\text{Al}_2\text{O}_3$  has also been employed in chalcogenide thin-film solar cells such as  $\text{Cu}(\text{In}, \text{Ga})\text{Se}_2$ [237],  $\text{CdTe}$ [144], and  $\text{CZTSe}$ [79, 81] solar cells, demonstrating good interface passivation. With the introduction of ALD- $\text{Al}_2\text{O}_3$  before the  $\text{CdS}$  buffer, Lee *et al.* demonstrated effective surface passivation as well as improved short-circuit current density ( $J_{SC}$ ) and fill factor ( $FF$ ), leading to an enhancement of 15% in the relative efficiency for CZTSSe devices.[81] The applicability of ALD- $\text{Al}_2\text{O}_3$  was also extended to CZTS solar cells with  $\text{CdS}$  buffer in the work of Park *et al.*, where hydrogen was proposed to account for the passivation effect at the surface.[82] Despite the seminal studies demonstrating the benefits of  $\text{Al}_2\text{O}_3$  in CZTS(Se) devices with  $\text{CdS}$  buffer, the application of  $\text{Al}_2\text{O}_3$  in CZTS device with Cd-free buffer has not been investigated to date. Furthermore, the factors governing the underlying passivation mechanisms have only partly been uncovered, especially on the evolution of the chemical and electronic properties of CZTS surface when it is subjected to the ALD treatment. Hence, a detailed investigation is required on the interaction of CZTS with ALD precursors and co-reactants during the deposition of  $\text{Al}_2\text{O}_3$  on the CZTS surface. As it was shown in the

Section 4.3, a CZTS/ZnSnO solar cell exhibited quite different bulk and heterojunction properties compared to a CZTS/CdS cell, where a larger Na concentration was found throughout the CZTS/ZnSnO device.[122] Therefore, it is quite likely that the impact of the application of an ALD  $\text{Al}_2\text{O}_3$  film will be significantly different in these devices as well.

This chapter elucidates for the first time how an ALD- $\text{Al}_2\text{O}_3$  coating can effectively passivate the interface defects in a Cd-free CZTS device with ZnSnO buffer layer. It is demonstrated that ultrathin  $\text{Al}_2\text{O}_3$  films deposited by ALD can effectively improve the performance of Cd-free CZTS devices (with a structure of Mo/CZTS/ZnSnO/i-ZnO/ITO) through heterojunction modification. With a significant gain of  $V_{OC}$  and  $FF$ , a device efficiency of 10.2 % was obtained. To understand the mechanism governing the passivation and performance improvement in CZTS device with  $\text{Al}_2\text{O}_3$ , the effects of trimethylaluminum (TMA) precursor,  $\text{H}_2\text{O}$  precursor, and heating effects were all carefully investigated independently as well. The resulting photovoltaic performance demonstrated that the TMA exposure step plays a key role in the passivation of CZTS/ZnSnO heterojunction. Optoelectronic characterization confirmed that the improvements could mainly be attributed to the passivation of defects at the heterojunction interface. The improvement in  $V_{OC}$  after the various processes was found to correlate well with the Na concentration variation at the CZTS surface as identified through surface chemical and electronic analysis. Furthermore, the excess oxygen originating from the initial growth of ALD- $\text{Al}_2\text{O}_3$  might explain the segregation of Na from the bulk to the interface. Finally, a plausible mechanism for the passivation induced by ALD- $\text{Al}_2\text{O}_3$  is proposed. ALD- $\text{Al}_2\text{O}_3$  facilitates the formation of a thicker Cu-deficiency nano-layer with a higher concentration of Na and O, forming a homogeneous passivation layer across the CZTS surface. This nano-layer reduces the local potential fluctuation of the band edges and locally widens the bandgap and promotes downward band bending, hence the improvement in  $V_{OC}$  and device performance.

## 6.2 Passivation of CZTS/ZnSnO heterojunction interface by $\text{Al}_2\text{O}_3$

### 6.2.1 Experiment

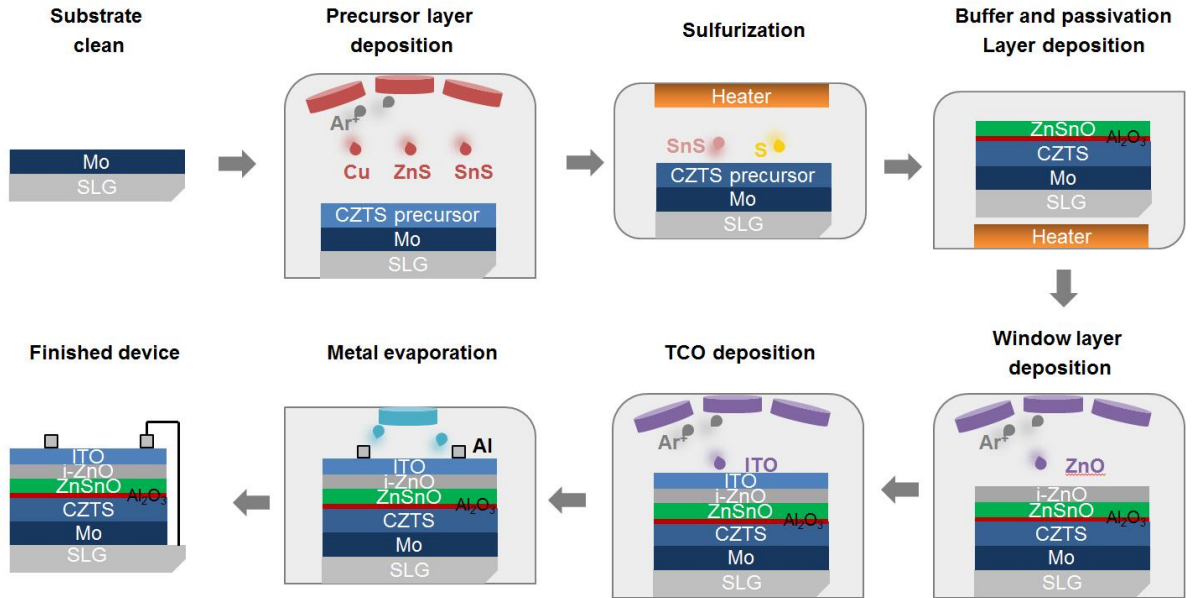


Figure 6. 1 Schematic of the fabrication of CZTS/ $\text{Al}_2\text{O}_3$ /ZnSnO thin-film solar cell.

The CZTS absorbers were prepared by co-sputtering on Mo-coated soda-lime glass substrates with a size of  $2.5 \times 2.5 \text{ cm}^2$ . The co-sputtering of the CZTS absorber was done from Cu/ZnS/SnS precursors using a magnetron sputtering system (AJA International, Inc., Model ATC-2200) as described in the previous work.[122] ICP-OES confirmed that the composition of CZTS absorbers was Cu-poor ( $\text{Cu}/(\text{Zn}+\text{Sn}) = 0.88$ ) and Zn-rich ( $\text{Zn}/\text{Sn} = 1.18$ ). The films were then loaded into a closed graphite box with combined elemental sulfur and SnS. Our baseline annealing process was performed at  $560^\circ\text{C}$  with a heating rate of  $10^\circ\text{C min}^{-1}$  for 3 min. After sulfurization, the samples were either stored in a nitrogen box or immediately transferred into the ALD reactor for subsequent treatments. The ALD processes were done in a Fiji G2 ALD system (Cambridge Nanotech) at a substrate temperature of  $150^\circ\text{C}$ .  $\text{Al}_2\text{O}_3$  was

directly deposited on the CZTS absorber by using TMA and deionized water as precursors, with argon (Ar) as the carrier gas. Both water and the TMA precursor were kept at room temperature. The ALD process contained an Al: Ar: H<sub>2</sub>O: Ar cycle with pulse lengths of 0.06:10:0.06:10 s, repeated to obtain the desired thickness. TMA (H<sub>2</sub>O) treatment was conducted using TMA (H<sub>2</sub>O) half-cycles while leaving other conditions the same as the Al<sub>2</sub>O<sub>3</sub> deposition. A control sample (“Heat”) was subjected to the identical deposition temperature and reactor ambient with no ALD process running. The parameter details of different ALD processes are listed in Table 6. 1.

Table 6. 1 List of key parameters used for different ALD processes

<b>Sample</b>	<b>TMA pulse (s)</b>	<b>Ar purge (s)</b>	<b>H<sub>2</sub>O pulse (s)</b>	<b>Ar purge (s)</b>	<b>Cycles</b>	<b>Heat Temp. (°C)</b>
<b>Ref</b>	-	-	-	-	-	RT
<b>Al<sub>2</sub>O<sub>3</sub></b>	0.06	10	0.06	10	5	150
<b>TMA</b>	0.06	10	-	-	5	150
<b>H<sub>2</sub>O</b>	-	-	0.06	10	5	150
<b>Heat</b>	-	-	-	-	-	150

For ZTO buffer devices, after sulfurization, the samples were stored in a nitrogen box or immediately transferred into the ALD reactor to deposit ZTO thin films. After the sulfurization process ALD-ZnSnO layers were synthesized using diethylzinc [Zn(C<sub>2</sub>H<sub>5</sub>)<sub>2</sub> DEZ, Sigma-Aldrich], tetrakis(diethylamido)tin(IV) [Sn(N(CH<sub>3</sub>)<sub>2</sub>)<sub>4</sub> or TDMASn, Strem Chemicals] as Zn, Sn precursor, and water as an oxidant. The Zn to Sn sub-cycles with a 3:1 ratio was employed and the substrate temperature was kept at 150 °C. Such conditions contribute to the best performing Cd-free CZTS solar cell based on our previous study.[122] A transparent front contact of i-ZnO/ITO (50 nm/210 nm) bi-layer was then deposited by radio frequency sputtering before Al grids



were deposited using evaporation. For the best performing devices, an antireflection coating of 100 nm  $\text{MgF}_2$  was deposited by thermal evaporation and  $0.224 \text{ cm}^2$  solar cells were finally defined by mechanical scribing.

### 6.2.2 Influence of $\text{Al}_2\text{O}_3$ thickness on the device properties

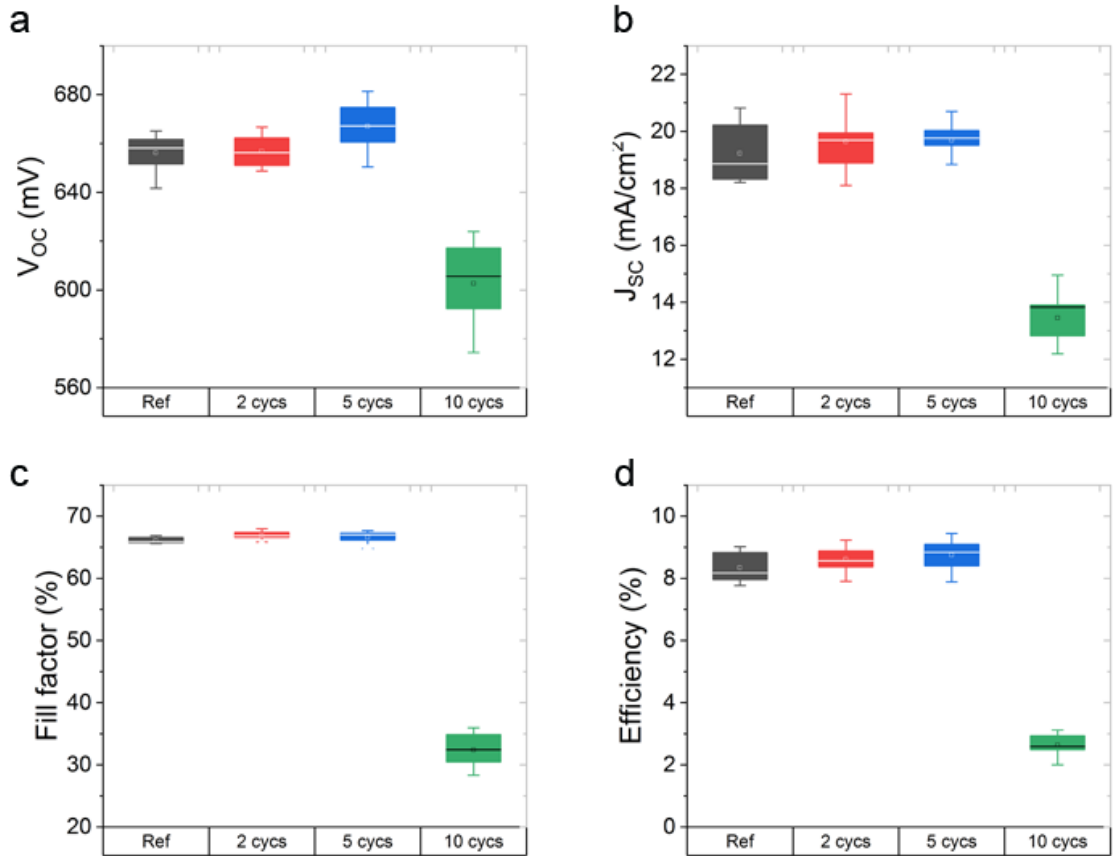


Figure 6. 2. a-d) Box-plot diagram of the one-sun solar cell parameters of CZTS cells as a function of the number of ALD cycles used for the  $\text{Al}_2\text{O}_3$  passivation layer. 10 CZTS solar cells were fabricated per experimental condition. The box, horizontal bars, and point symbols indicate the 25/75 percentile, min/max and mean values, respectively.

In this work, an ultrathin ALD- $\text{Al}_2\text{O}_3$  layer was inserted between the CZTS/ $\text{ZnSnO}$  heterojunction based on the previously proposed structure ( $\text{Mo}/\text{CZTS}/\text{ZnSnO}/i\text{-ZnO}/\text{ITO}$ ) as shown in the schematic process in Figure 6. 1. The

optimization of ALD- $\text{Al}_2\text{O}_3$  layer thickness was done by fabricating a series of CZTS solar cells with a different number of ALD cycles ranging from 2 to 10, which was equal to 0.2~1 nm in thickness. The box-plot diagram of the PV performance parameters of CZTS cells incorporating various ALD cycles can be found in Figure 6. 2. For 2 cycles of ALD- $\text{Al}_2\text{O}_3$ , no significant effect on the CZTS device performance can be seen, probably due to the incomplete coverage of the CZTS absorber. When the number of the cycles reached 10 (1 nm thickness), both  $J_{SC}$  and  $FF$  decreased significantly, most likely due to impaired carrier transport through the thick  $\text{Al}_2\text{O}_3$  layer. 5  $\text{Al}_2\text{O}_3$  ALD-cycles were found to be the optimum parameter in terms of the efficiency of the CZTS device.

### 6.2.3 Influence of ALD sub-steps on the device properties

To understand the mechanism governing the passivation and performance improvement in CZTS devices with ALD  $\text{Al}_2\text{O}_3$ , the independent effects from the TMA precursor,  $\text{H}_2\text{O}$  and heating effects were investigated separately. A schematic illustration of the investigated absorbers treated with different ALD process is presented in Figure 6. 3a. The procedure of sample preparation with different ALD treatment is described in Section 6.2.1. All the samples were then processed into full devices in order to study each effect on solar cell performance, as shown in Figure 6. 3b. While all the treatments had little influence on the  $J_{SC}$ , they mainly affected the  $V_{OC}$  and  $FF$  in most cases except for the heat treatment. Devices with TMA treatment show a similar improvement in  $V_{OC}$  with respect to  $\text{Al}_2\text{O}_3$  treatment, which was significantly higher than the  $\text{H}_2\text{O}$  treatment. The  $FF$ , however, does not show a strong variation but still follows a similar trend with the  $V_{OC}$ . Therefore, the combination of all the trends results in the highest efficient devices with  $\text{Al}_2\text{O}_3$  and TMA treatment followed by the devices with the  $\text{H}_2\text{O}$  treatment. These results demonstrate that TMA plays a key role in the passivation scheme, which might help to understand the underlying mechanism of  $\text{Al}_2\text{O}_3$  passivation. The  $V_{OC}$  becomes our main focus in evaluating the mechanism

from ALD treatments, as it presents the most pronounced variation in the device with different treatments.

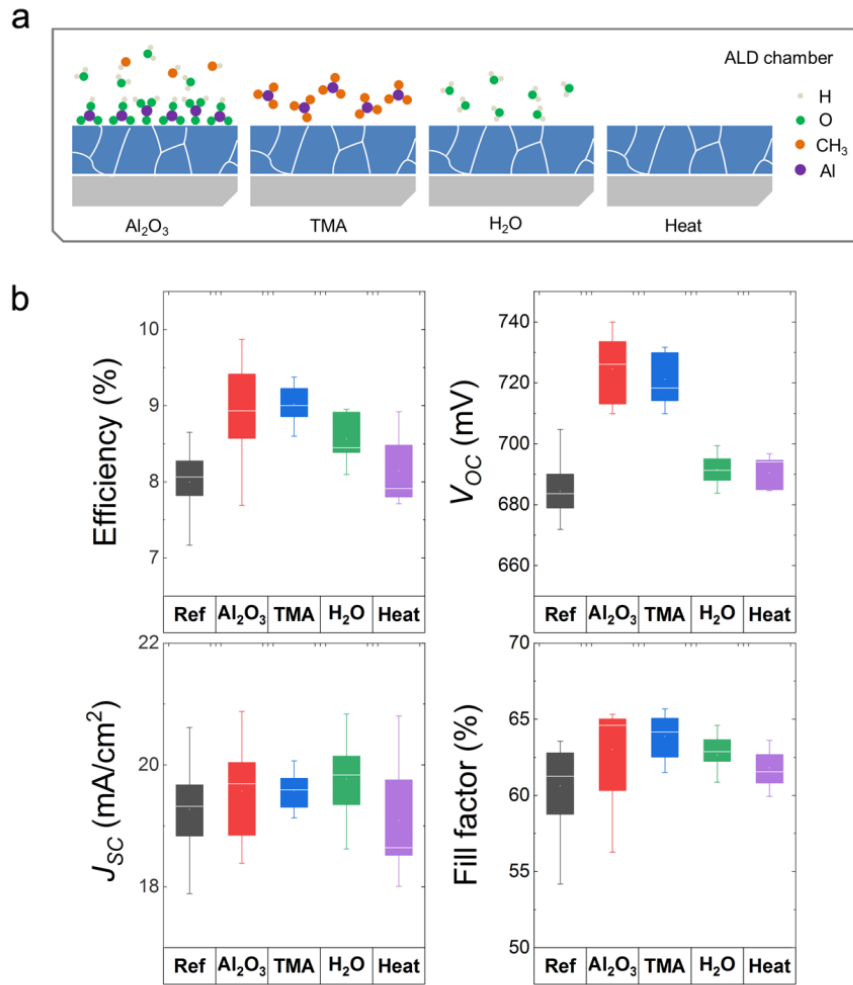


Figure 6. 3 a) Schematic view of the processes investigated in this section to elucidate the impact of the various components of the Al<sub>2</sub>O<sub>3</sub> ALD process. In addition to the full Al<sub>2</sub>O<sub>3</sub> ALD process shown to the left, also the TMA and H<sub>2</sub>O half-reaction were investigated in isolation as well as exposing the sample solely to the process temperature used during the ALD process. b) Box-plot diagram of the one-sun  $J$ - $V$  performance parameters of CZTS cells made with no treatment (Ref), Al<sub>2</sub>O<sub>3</sub> treatment, TMA treatment, H<sub>2</sub>O treatment and heat treatment within the ALD chamber. 10 CZTS solar cells were fabricated per experimental condition. Box, horizontal bars, point symbols and indicate 25/75 percentile, min/max and mean values, respectively.

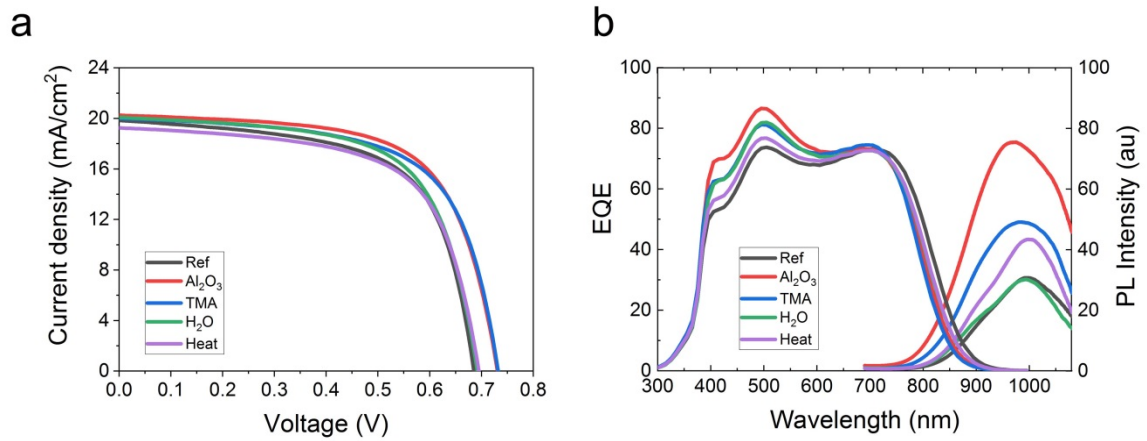


Figure 6. 4 a)  $J$ - $V$  curves and b) EQE spectra and PL spectra of the CZTS devices with various treatment: no treatment (Ref), Al<sub>2</sub>O<sub>3</sub> treatment, TMA treatment, H<sub>2</sub>O treatment and heat treatment within the ALD chamber.

Optoelectronic measurements were performed on the champion devices with different ALD treatment, to study the origin of the performance improvement. The EQE spectra of the champion devices are shown in Figure 6. 4b. One can observe an enhanced blue response in the curves of devices with ALD treatment. These improvements were consistent with the trend of PCE improvement, where TMA shows better blue response than the other effects. On the other hand, the ALD treatment leads to a blue shift of the band edge which is observable between 750 and 850 nm in the EQE spectrum, corresponding to an increased optical bandgap of the CZTS. Several studies showed that the post-annealing treatments could affect the bulk bandgap of CZTS by changing the bandgap fluctuation induced by the Cu-Zn order in CZTS.[40, 238, 239] Therefore, the widened bandgap after all the ALD treatments with annealing effects involved can be partly explained by the reduced bandgap fluctuation.[40] It is interesting to see that both the Al<sub>2</sub>O<sub>3</sub> and TMA treatment present a larger shift in optical bandgap than the other effects compared to the control device. In this case, more effects from Al<sub>2</sub>O<sub>3</sub> and TMA treatment should exist other than annealing effects. Furthermore, this bandgap value change agrees with the PL peak positions determined

from the photoluminescence (PL) measurement shown in Figure 6. 4b, which demonstrate a blue shift for the ALD- treated device in Figure 6. 5a. Note that an excitation laser with a wavelength of 405 nm was used in the PL measurement, thus the luminescence mainly came from the near surface region of the CZTS layer. Hence, the improvement in  $V_{OC}$  might be correlated with the enhanced bandgap of CZTS surface after the ALD treatment. In terms of the PL peak intensity, it has been reported that the photoluminescence intensity increased after the CZTS subject to  $Al_2O_3$  coating.[81] It is also observed an increase in photoluminescence intensity for our devices with ALD treatment, which means the non-radiative recombination has been suppressed. A TMA exposure was again found to passivate the CZTS better compared to an  $H_2O$  or heat treatment as evidenced by the fact that the PL intensity was found to be significantly higher.

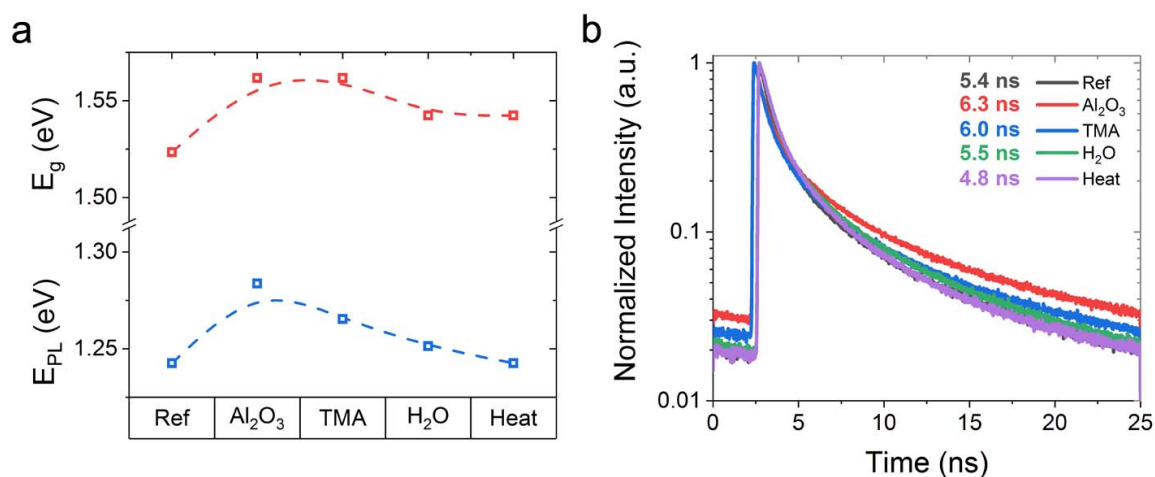


Figure 6. 5 a) Bandgap values extracted from the EQE measurements and PL peak position for devices with various ALD treatment. The inflection point of the EQE was used to determine the bandgap ( $E_g$ ), dash lines are plotted for guiding purpose. b) Time-resolved photoluminescence (TRPL) obtained at an excitation wavelength of 470 nm for the corresponding devices.

## 6.3 Mechanism of heterojunction passivation by Al<sub>2</sub>O<sub>3</sub>

### 6.3.1 Interface properties of the device

Another important issue that needs to be addressed is whether the recombination was mainly suppressed in the bulk or just within the heterojunction region. For this reason, time-resolved photoluminescence (TRPL) and Suns-  $V_{OC}$  measurements were done to identify the location of the passivated defects. Time-resolved photoluminescence (TRPL) was used to qualitatively compare the effects of different ALD treatment on the minority charge carrier lifetime of the device. The measurement was done using an excitation wavelength of 470 nm, which has a penetration length of 256 nm and consequently is mainly sensitive to the surface of CZTS absorber. As shown in Figure 6. 5b, the normalized PL decay curves could be fitted by a two-exponential function and the decay time were extracted to be 5.4, 6.3, 6.0, 5.5, 4.8 ns for devices with no treatment (Ref), Al<sub>2</sub>O<sub>3</sub>, TMA, H<sub>2</sub>O and heat treatment, respectively. A prolonged carrier lifetime for the Al<sub>2</sub>O<sub>3</sub> and TMA sample indicates that the defects being passivated after those treatments could mainly stem from the heterojunction region. This conclusion can be further confirmed from the Suns-  $V_{OC}$  measurements, where the  $V_{OC}$  was measured as a function of incident light intensity. The saturation current  $J_{01}$  and  $J_{02}$  were extracted by using a two-diode model fit to identify the origin of the passivation effects. Note that the recombination in the bulk of the solar cell is usually represented by  $J_{01}$ , while recombination at the space charge region is attributed to  $J_{02}$ . It can be understood from Figure 6. 6a that the  $J_{01}$  values were approximately identical for all the treated devices, whereas  $J_{02}$  was significantly lower after the TMA and Al<sub>2</sub>O<sub>3</sub> treatment compared to the H<sub>2</sub>O and heat treatment. Again, TMA and Al<sub>2</sub>O<sub>3</sub> treatment helped to suppress defects recombination at the space charge region (SCR) more efficiently than those of H<sub>2</sub>O and heat treatment.

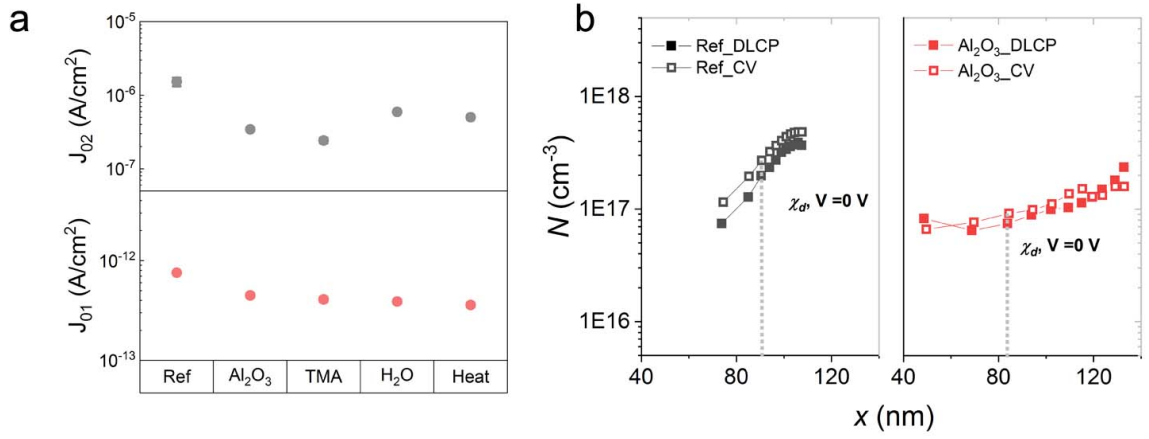


Figure 6. 6 a) Saturation current density of different CZTS devices obtained by fitting their Suns- $V_{OC}$  curves using a two-diode model. b)  $C$ - $V$  and DLCP profiling for the CZTS devices with no treatment (Ref) and Al<sub>2</sub>O<sub>3</sub> treatment.

Furthermore, the capacitance-voltage ( $C$ - $V$ ) measurements and drive-level capacitance profiling (DLCP) were used to distinguish the defects between bulk and interface. Generally, one can obtain information about the free carriers, bulk and interface defects deduced from the  $C$ - $V$  measurements, while identifying the response only from the free carrier and the bulk defects using the DLCP technique.[180, 181] Thus, the defects density at CZTS/ZnSnO interface can be determined by subtracting the DLCP defect density ( $N_{DLCP}$ ) from the  $C$ - $V$  defect density ( $N_{CV}$ )[240], as shown in Figure 6. 6b. The near overlap of the  $C$ - $V$  and DLCP profile in the case of the Al<sub>2</sub>O<sub>3</sub>-treated sample means the interface defects were mostly passivated. Quantitatively, the relative value between  $N_{DLCP}$  and  $N_{CV}$  at  $V_{dc} = 0$  were chosen to quantify the defect density (in Figure 6. 7), where the Ref device possessed a larger interface state response ( $7.3 \times 10^{16} \text{ cm}^{-3}$ ) than the Al<sub>2</sub>O<sub>3</sub>-treated one ( $1.7 \times 10^{16} \text{ cm}^{-3}$ ), suggesting a lower density of interface defects in the device with an Al<sub>2</sub>O<sub>3</sub> passivation layer. With this strong device-level evidence of interface passivation triggered by Al<sub>2</sub>O<sub>3</sub> and TMA, it is interesting to understand the chemical origin of this performance improvement.

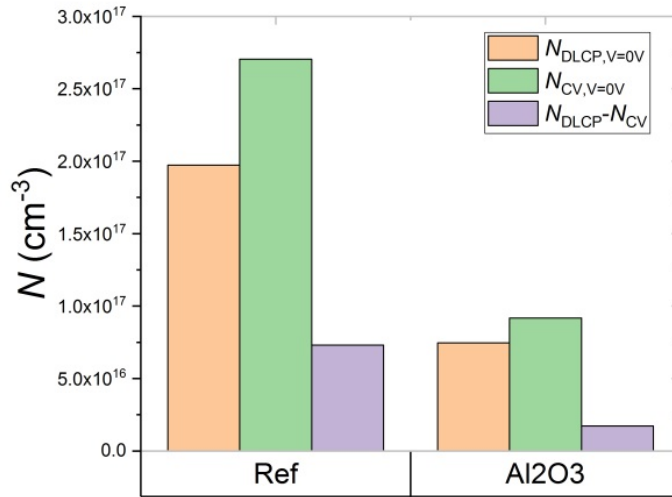


Figure 6. 7 Defect density  $N_{DLCP}$  and  $N_{CV}$  at  $V_{dc} = 0$  derived from  $C-V$  and DLCP measurements of devices with different ALD treatment, respectively.

### 6.3.2 Surface chemical analysis

Firstly, the structural properties of CZTS were examined after ALD treatment using Raman spectroscopy, and the results are shown in Figure 6. 8. The measurements were taken on bare CZTS absorbers and CZTS/ZnSnO with different ALD treatment recorded with a 514 nm excitation wavelength. No significant changes in the CZTS phases can be seen either from the intensity or the peak position of the characteristic peaks. Hence, the focus was turned to the chemical modifications of the CZTS surface after each ALD treatment. XPS analysis was then carried out on a bare CZTS surface (Ref) as well as CZTS surface after Al<sub>2</sub>O<sub>3</sub> treatment, TMA treatment or H<sub>2</sub>O treatment. The exposure time of the samples (within 15 min) to the ambient atmosphere was kept similar to that in the fabrication process of the CZTS device to minimize the chemical difference between samples and devices. In order to determine the surface composition and the chemical state of Al, O, Na and Cu after each treatment, curve fitting was performed on the Cu3s/Al 2s, O 1s, Na 1s, and Cu 2p3 peaks, as shown in Figure 6. 10a-d.



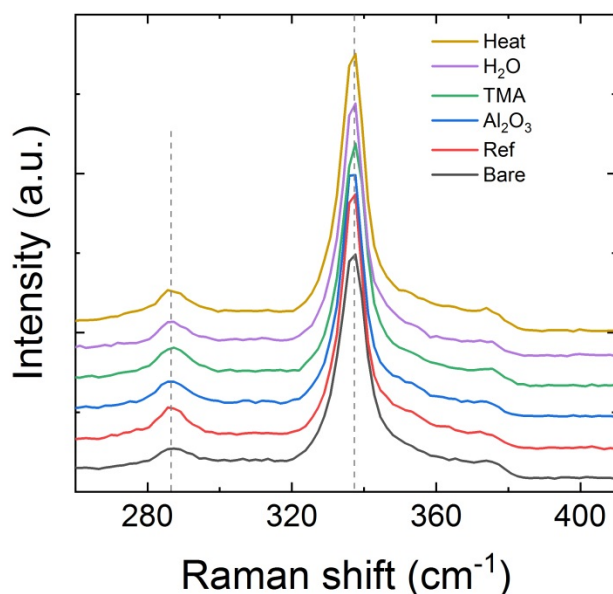


Figure 6. 8 Raman spectra for bare CZTS absorbers and CZTS/ZnSnO after different ALD treatment. An excitation wavelength of 514 nm was used for the measurements.

It has been reported that surface oxides and Na-containing compounds may exist on the surface of CZTS absorber with air exposure [83, 241]. This was also found in our case, where the characteristic O 1s peak (531.2 eV) and Na 1s peak (1071.6 eV) were identified in the bare CZTS surface. Besides, the binding energy peak at 532.8 eV which is representative of the hydroxyl (-OH) species presents in the CZTS surface without treatment and with H<sub>2</sub>O treatment. In the Al 2s region, the component 118.7 eV assigned to oxidized Al species was found in the CZTS after Al<sub>2</sub>O<sub>3</sub> and TMA treatment, indicating the presence of Al<sub>2</sub>O<sub>3</sub> after either treatment.[242] This was corroborated by the complementary decrease in the -OH bonds in the case of Al<sub>2</sub>O<sub>3</sub> and TMA treated sample, as was determined by the decreased intensity of -OH peak at 532.8 eV. It is interesting to note that TMA consumed the hydroxyl groups on CZTS surface even when no H<sub>2</sub>O cycle was used in the experiment. Residual water from the wall of the ALD chamber might also react with the deposited TMA to form a higher aluminum oxidation state, as evidenced by the increasing Al-O peak at 531.2 eV.[243]

The O 1s (Al-O contribution) and Al 2s peak areas were then used to estimate O and Al atomic percentages. For the Al<sub>2</sub>O<sub>3</sub> and TMA sample, the Al-O contribution was roughly evaluated by subtracting the contribution of metal-O of the Ref sample from the entire O 1s area. Thus, the O/Al ratio after Al<sub>2</sub>O<sub>3</sub> and TMA treatment is found to be 8.0 and 7.0, much higher than the stoichiometric ratio 1.5. The resulting excess oxygen at the interface was suggested to contribute as oxygen interstitial (O<sub>i</sub>) defects as has been earlier reported for ALD Al<sub>2</sub>O<sub>3</sub> on top of Si, which is believed to contribute to the negative charge at the interface.[244, 245] This might be indicative of similar growth behavior of ALD-Al<sub>2</sub>O<sub>3</sub> based on –OH terminated surface, either on Si or CZTS.

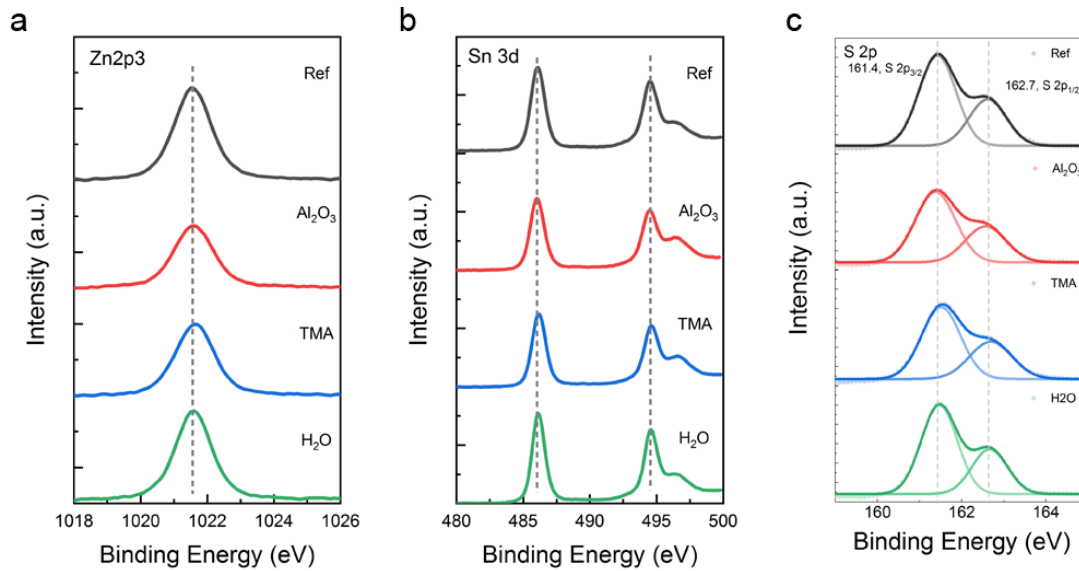


Figure 6. 9 a-c) XPS peak of Zn 2p<sub>3</sub>, Sn 3d, S 2p, respectively, obtained from the surface of CZTS absorbers with no treatment (Ref), Al<sub>2</sub>O<sub>3</sub>, TMA , and H<sub>2</sub>O treatment.

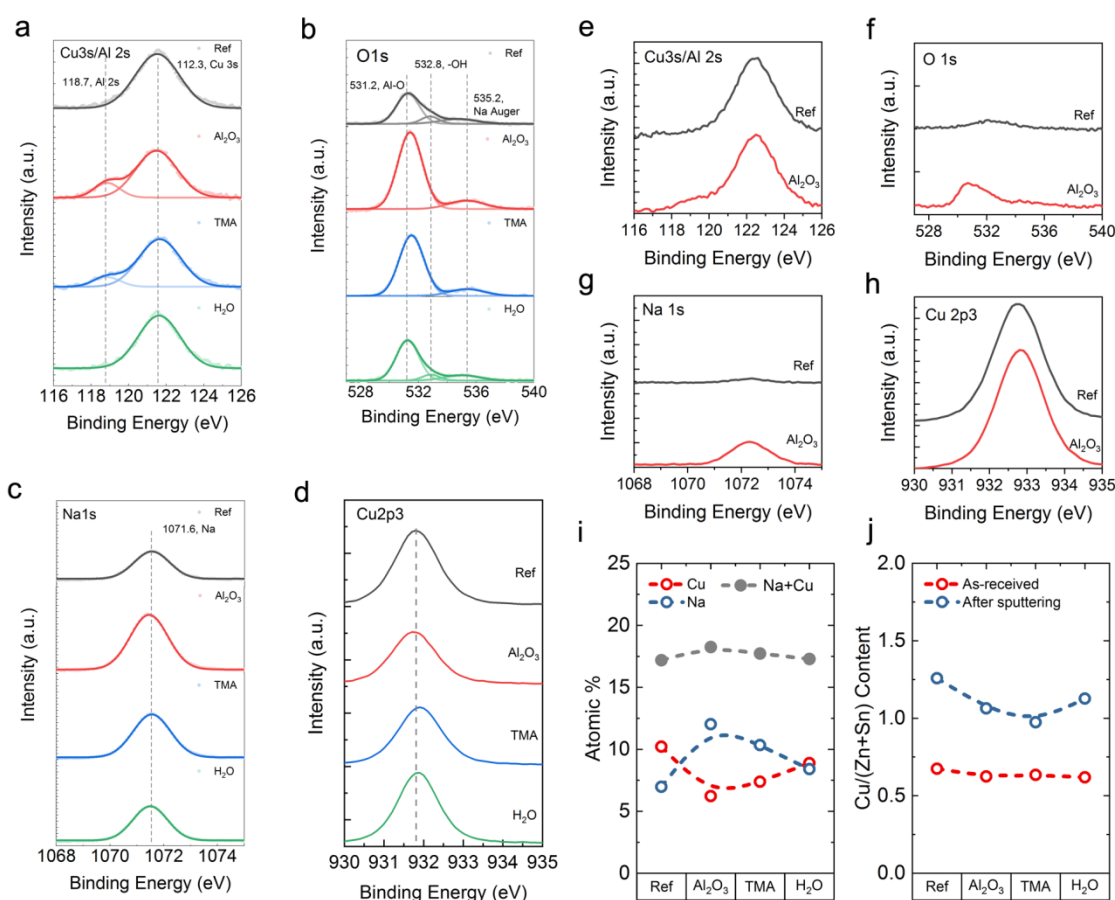


Figure 6. 10 Surface chemical analysis. a-d) XPS peak of Al 2s, O 1s, Na 1s, Cu 2p3, respectively, obtained from the surface of CZTS absorbers with no treatment (Ref), Al<sub>2</sub>O<sub>3</sub> treatment, TMA treatment, and H<sub>2</sub>O treatment. e-h) XPS peak of Al 2s, O 1s, Na 1s, Cu 2p3, respectively, at the surface of CZTS absorbers with no treatment (Ref) and Al<sub>2</sub>O<sub>3</sub> treatment after the sputtering with approximately 0.5 nm. i) Na and Cu atomic percentages measured at the surface of as-received absorbers with different treatments. j) Cu/(Zn+Sn) atomic percentage ratio of the surface of absorbers with different treatments before and after sputtering in a depth of 0.5 nm. Dash lines in i) and j) are plotted for guiding purposes.

Besides the O-rich Al<sub>2</sub>O<sub>3</sub> layer formed after Al<sub>2</sub>O<sub>3</sub> and TMA treatment, one can also notice the significant increase of [Na] accompanied by the decrease of [Cu], [Zn], [Sn] and [S] (See Figure 6. 9). This observation indicates the formation of surface

oxides with an even larger amount of Na after either  $\text{Al}_2\text{O}_3$  or TMA treatment. The variation in the atomic concentration of Na and Cu as a function of treatment is presented in Figure 6. 10i. Notice that a clear increase of Na accompanied by a decrease of the Cu after ALD treatment, while the overall quantity maintains relatively constant. The variation of the Na amount agrees well with the change tendency in the  $V_{OC}$  along with different ALD treatment. It seems that heat treatment prompted the transportation of Na to the CZTS surface, while  $\text{Al}_2\text{O}_3$  and TMA treatment make the amount of Na segregation to the surface even larger. These measurements suggest that the increased Na composition along with Cu deficit at the CZTS surface induced by the ALD treatment might contribute to the  $V_{OC}$  improvement.

To investigate the near-surface region of the CZTS before and after ALD- $\text{Al}_2\text{O}_3$  treatment, XPS measurements were also carried out after sputtering to remove approximately 0.5 nm of material, as illustrated in Figure 6. 10e-h. The characteristic Al 2s peak almost completely disappeared for the  $\text{Al}_2\text{O}_3$  treated sample after sputtering, confirming the removal of  $\text{Al}_2\text{O}_3$ . Meanwhile, the O and Na were almost completely removed for the Ref sample after sputtering indicating those surface oxides and Na-containing compounds are limited to a thickness around 0.5 nm. However, there were still oxides accompanied by Na present at CZTS/ $\text{Al}_2\text{O}_3$  interface in the  $\text{Al}_2\text{O}_3$  sample, likely due to a larger amount of Na segregation in the presence of the  $\text{Al}_2\text{O}_3$  coating. This phenomenon was also confirmed from the near atomic-scale chemical analysis by atom probe tomography (APT). Figure 6. 11a shows the 3-D distribution of the atoms at the CZTS/ $\text{Al}_2\text{O}_3$ /ZnSnO interfaces of the 10.2% efficient CZTS device. Only the Na ions (green) and Cu ions (orange) are shown in this reconstruction. The concentration profile of Cu, Zn, Sn, S, O and Na atoms along the cylinder positioned across the interface (see Figure 6. 11) is illustrated in Figure 6. 11b. A bin size of 1 nm was chosen and all species present were decomposed into their constituent elements, as several molecular ions were present in the mass spectrum. The concentration changes in Figure 6. 11b show that Na segregated between CZTS and ZnSnO, together with Al.

If only the [Na], [O], and [Al] is plotted it can be seen that the Al accumulation is also accompanied by an oxygen peak right between the CZTS absorber and ZnSnO buffer layer, hence confirms the excess O induced from the Al<sub>2</sub>O<sub>3</sub>. Together with the more O-rich surface layer of the passivated sample that was confirmed by the XPS results, the author hypothesizes that the excess oxygen, originating from the initial growth of ALD Al<sub>2</sub>O<sub>3</sub>, could form negative charged interstitial O<sub>i</sub><sup>-</sup>, and therefore attract interstitial Na<sub>i</sub><sup>+</sup> from bulk to the interface. The role of Na has been found to act as a surfactant and suppressor of non-radiative recombination at the interface of CZTS solar cells.[86]

Furthermore, after sputtering the Cu related peaks increased drastically compared with the as-received samples. In Figure 6. 10j, a further check of the Cu/(Zn+Sn) ratio before and after sputtering demonstrate that the Cu concentration increased considerably after sputtering, revealing a depletion of Cu at the near-surface region of the CZTS. Al<sub>2</sub>O<sub>3</sub> and TMA treatment lead to a stronger reduction of the Cu/(Zn+Sn) ratio compared to the Ref treatment, thus leading to more depletion of Cu near the surface. The Cu depletion has also been observed at CIGS surfaces, however, caused by different mechanisms. Some reports suggested that the oxygenation-induced redistribution and increased Fermi energy at the surface should contribute to the liberation of Cu from surface to bulk.[246, 247] From the complementary relationship between Na and Cu, the increased concentration of Na seems to induce enhanced Cu depletion, probably attributed to ion exchange itself or the promotion of oxygenation. It is also interesting to note that the Al<sub>2</sub>O<sub>3</sub> and TMA lead to a modification of the chemical composition at the CZTS surface (Na-rich, Cu-depletion) thus could induce the enlargement of the bandgap at the near-surface. The Al<sub>2</sub>O<sub>3</sub>/TMA induced bandgap widening at the CZTS surface suppressing the defects recombination between absorber and buffer layer might also be the reason for the improved solar cell performance.[74]

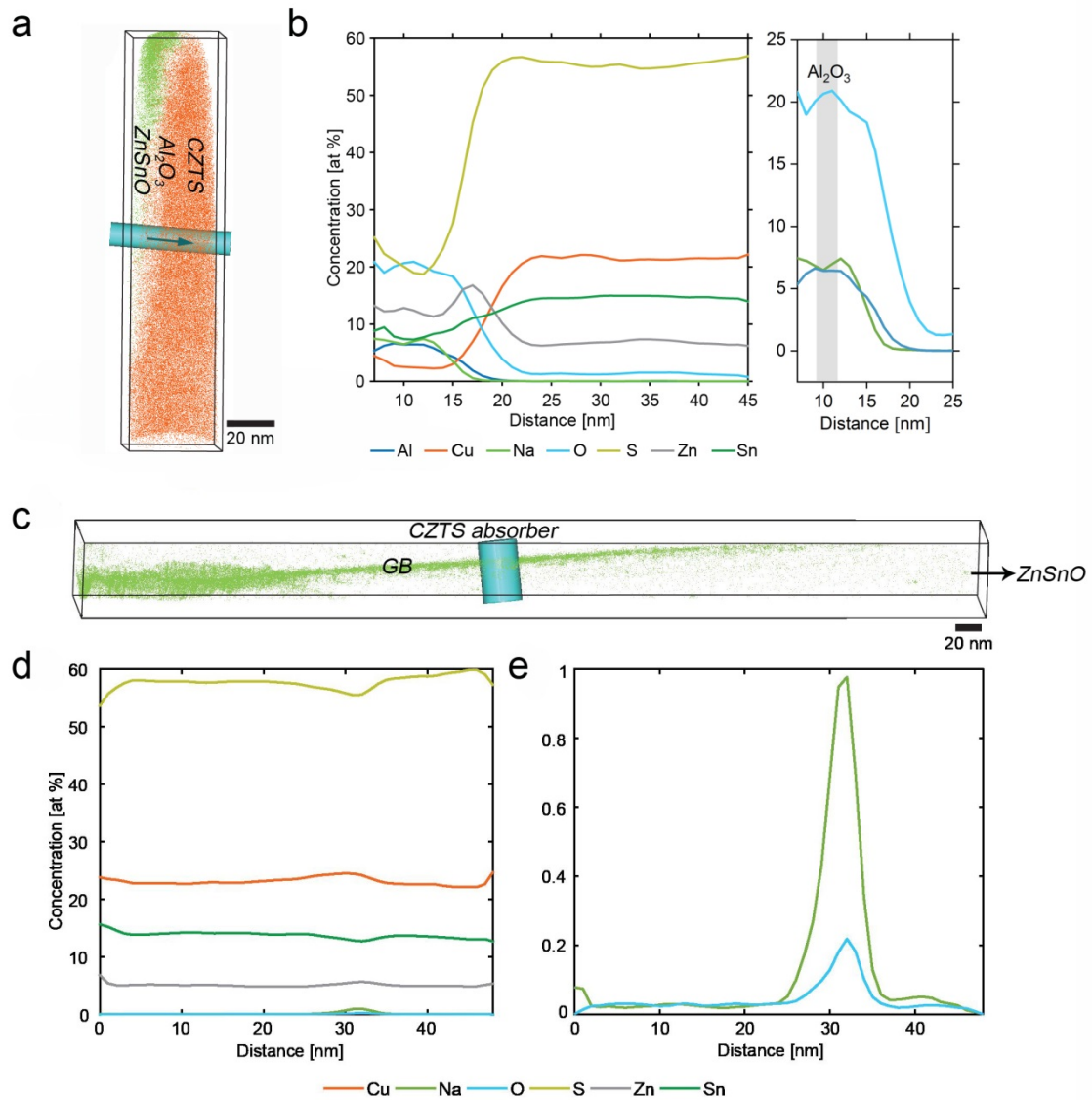


Figure 6. 11 Atom Probe Tomography of the 10.2% efficient CZTS device. a) Atom probe reconstruction of the ZnSnO/Al<sub>2</sub>O<sub>3</sub>/ CZTS interface area. Only the Na<sup>+</sup> ions are displayed in light green, Cu<sup>+</sup> ions in orange. A cylinder was positioned across the interface to determine concentration changes along the direction of the arrow, and the results are shown in the concentration profile b) A bin size of 1 nm was chosen and all species were decomposed into their constituent elements. c) Partial atom probe reconstructions of the CZTS absorber layer where Na segregation along a grain boundary. Na<sup>+</sup> ions are displayed in green. Na-rich areas are displayed by using an isoconcentration surface with a Na value of 0.9 at.%. A cylinder was positioned

perpendicular across the grain boundary, to produce a one-dimensional cross-section measure of the concentration changes. The results are shown in the concentration profile d) and e). A bin size of 1 nm was chosen and all species were decomposed into their constituent elements.

### 6.3.3 Surface electronic analysis

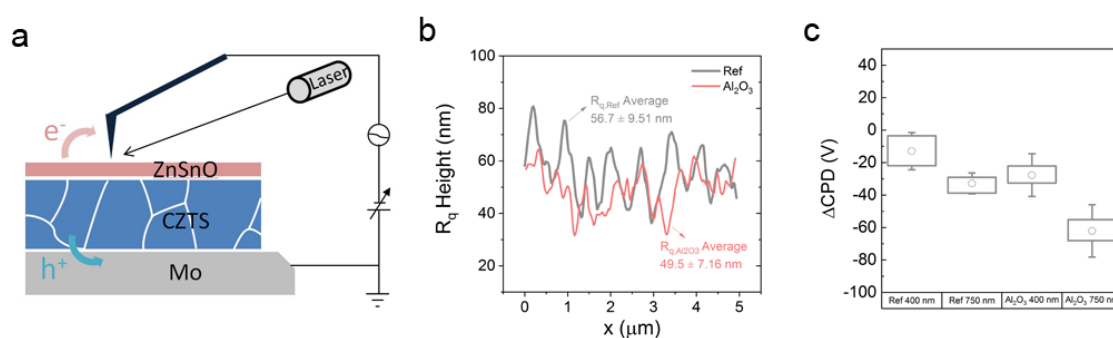


Figure 6. 12 a) KPFM set up under illumination. b) Root-mean-square (RMS) roughness ( $R_q$ ) distribution profile across the captured images in Figure 5a,e. c) Average CPD values difference between dark and light at illumination intensities of  $894 \text{ mW/cm}^2$  (400 nm) and  $12000 \text{ mW/cm}^2$  (750 nm) for the reference and  $Al_2O_3$  treatment samples. Measurements were taken at a wavelength of 400 nm and 750 nm.

Kelvin probe force microscopy (KPFM) was performed to study the effects of the  $Al_2O_3$  treatment at the CZTS/ZnSnO heterojunction by detecting the local surface potential, providing the morphology and local electronic properties of the CZTS films upon passivation treatment. A schematic of the KPFM measurement setup is shown in Figure 6. 12a. The topography of the Ref and  $Al_2O_3$  samples are shown in Figure 6. 13a,e, no clear difference in the surface morphology and grain size due to the  $Al_2O_3$  treatment could be seen. Figure 6. 12b depicts the Root-mean-square (RMS) roughness ( $R_q$ ) distribution of the CZTS/ZnSnO heterojunction films with and without  $Al_2O_3$  treatment, where the Ref (56.7 nm) sample shows a similar roughness compared to the  $Al_2O_3$  sample (49.5 nm). To compare the electronic surface properties of the samples,

the simultaneously recorded contact potential difference (CPD) spatial maps were captured in dark conditions for Ref and the  $\text{Al}_2\text{O}_3$  samples, as shown in Figure 6. 13b,f. Due to the absence of photoinduced charge carriers, the CPD results collected in dark conditions merely represent the properties of the as-prepared surface. It is visibly distinguishable that CPDs at the grain boundaries (GBs) are lower than grain interiors (GIs); a similar surface potential was also observed in the CZTS film without any treatment when measured in the dark in our previous research.[151] This lower GB potential formed due to the built-in electrical field arising from the passivation effects through Na segregation at the GBs.[70] According to previous first-principle calculations, an interstitial  $\text{Na}_i^+$  atom around the GB region could create a dip in the energy band diagram of CZTSe, which assists electron flow towards the GB and simultaneously repel holes.[248] Figure 6. 13i shows the distribution histogram of the CPD values measured in dark where a narrower distribution of CPD is observed in the sample with  $\text{Al}_2\text{O}_3$  treatment, suggesting enhanced homogeneous chemical and/or electronic characteristics.

Also, the overall CPD is shifted to a higher value for the  $\text{Al}_2\text{O}_3$  sample which indicates higher band bending with respect to the tip and implies that the surface electronic and chemical states are different from the reference sample. Combining with the above chemical analysis results, one can suspect that change of the surface chemistry, rich in Na and O concentration, increases the overall CPD, thus, results in more band bending with respect to the tip. The author then checks the CPD values at the GBs and GIs for corresponding samples in Figure 6. 13k. It shows that average CPD value increased by 5.6% (7.0%) at the GIs compared to 9.0% (11.2%) at the GBs after treatment at a wavelength of 400 nm (750 nm), which infers that the increase of the overall CPD is mainly attributed to the CPD value increase at the GBs. Assuming that the electron affinity is nearly uniform over the CZTS surface, the potential distribution profile can be considered as a profile of the conduction band edge of the CZTS materials without regard to their raw numerical values.[249] The schematic



bandgap fluctuation for CZTS with and without  $\text{Al}_2\text{O}_3$  treatment is shown in Figure 6. 16a. Generally, the CZTS bandgap exhibits large local potential fluctuations triggered by a random distribution of charged point defects and Cu-Zn disorder.[65, 239] When the CZTS treated with  $\text{Al}_2\text{O}_3$ , the charged point defects can be passivated thus resulting in fewer local potential fluctuations, thus a large  $V_{OC}$  improvement is expected.

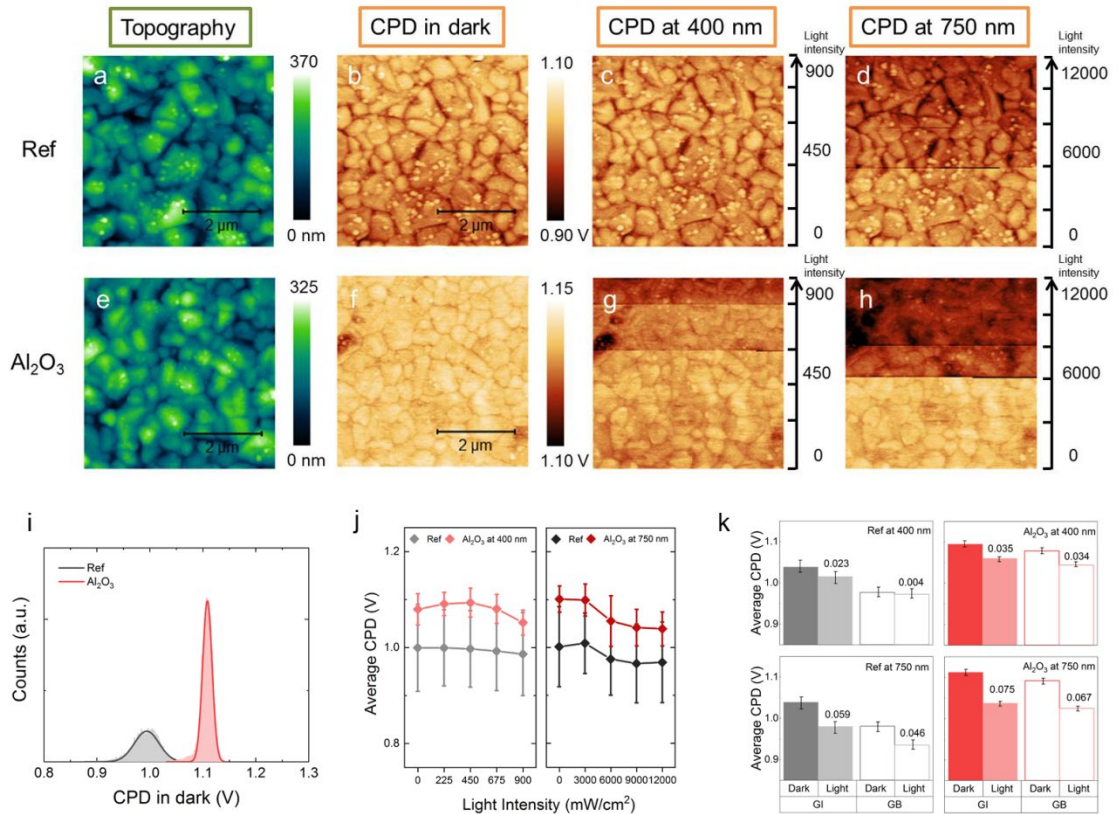


Figure 6. 13 Topography and light-induced surface potential measurements of the CZTS/ZnSnO heterojunction films with and without  $\text{Al}_2\text{O}_3$  treatment. KPFM measurements of the two samples showing a, e) Topography and b, f) simultaneously recorded CPD spatial maps in the dark c, g) CPD spatial maps under various laser illumination intensities at a wavelength of 400 nm d, h) CPD spatial maps under various laser illumination intensities at a wavelength of 750 nm of CZTS/ZnSnO and CZTS/ $\text{Al}_2\text{O}_3$ /ZnSnO, respectively. i) CPD distribution obtained in dark conditions for the two investigated samples. j) Average CPD values for the reference and  $\text{Al}_2\text{O}_3$

treatment samples as a function of illumination intensity at a wavelength of 400 nm and 750 nm. k) Average CPD values and CPD values difference between dark and light with illumination intensities of 894 mW/cm<sup>2</sup> (400 nm) and 12000 mW/cm<sup>2</sup> (750 nm) at GBs and GIs for corresponding samples. The scanning scales were 5  $\mu\text{m}$   $\times$  5  $\mu\text{m}$ .

To further examine the charge separation behavior in CZTS heterojunction before and after Al<sub>2</sub>O<sub>3</sub> treatment, KPFM measurements under the illumination were performed using an excitation wavelength of 400 nm and 750 nm, respectively. Note that, a laser excitation wavelength of 400 nm is expected to induce the photo-generated carriers near to the surface of CZTS, whereas 750nm excitation produces a more uniform photogeneration within the bulk of CZTS. For each excitation wavelength, the illumination was switched on about every 1  $\mu\text{m}$  during continuous scanning with increased illumination intensity from 0 to 894 mW/cm<sup>2</sup> for 400 nm and 0 to 12000 mW/cm<sup>2</sup> for 750 nm (scan-axis is from bottom-to-top), as shown in Figure 6. 13c, d and Figure 6. 13g, h for Ref and Al<sub>2</sub>O<sub>3</sub> sample, respectively. One can notice the two samples depict clearly different CPD contrast changing with the light intensity, as well as quite different responses to the illumination of different excitation wavelengths. Figure 6. 13j shows the average CPD values for the corresponding samples as a function of illumination intensity. The average CPD decreases as the light intensity increasing suggest that the photo-generated free electrons are accumulated at the front surface separated by the CZTS/ZnSnO heterojunction. The CPD drops from dark to highest intensity of illumination for Al<sub>2</sub>O<sub>3</sub> sample is almost 2.3 times (1.8 times) larger than the Ref sample at a wavelength of 400 nm (750 nm) (shown in Figure 6. 12c), indicating the more effective charge-separation capability induced by the passivation layer. Especially at an excitation wavelength of 400 nm, the passivated sample shows an even larger CPD drop than the reference sample, likely due to the more efficient carrier separation at the surface of CZTS. Therefore, the Al<sub>2</sub>O<sub>3</sub> sample passivates defects at the surface which promotes photo-generated charges carrier collection at

short wavelength, thereby explaining the enhanced blue response from EQE in the  $\text{Al}_2\text{O}_3$  device (Figure 6. 4b).

The CPD values difference between dark and light, also known as surface photovoltage (SPV), were calculated at GBs and GIs for corresponding samples, as shown in Figure 6. 13k. For the Ref sample,  $\text{SPV}_{\text{GI}}$  was 23 mV whereas  $\text{SPV}_{\text{GB}}$  was almost zero which indicated that there is no charge separation at the GB. On the other hand, the  $\text{SPV}_{\text{GB}}$  becomes 34 mV when passivated and  $\text{SPV}_{\text{GI}}$  becomes slightly higher compared to the Ref sample indicates that charge separation is much more enhanced at the GBs compare to GIs. The author suspect that more Na will accumulate at GBs during the negative charged interstitial  $\text{O}_i^-$  at the CZTS surface which attracts the interstitial  $\text{Na}_i^+$  from bulk to the interface. The partial atom probe reconstructions of the CZTS absorber layer shown in Figure 6. 11c was used to examine the elemental concentrations in the vicinity of GBs. It is observed that significant amounts of Na segregated towards the CZTS grain boundary, whereas hardly any Na was detected in the grain interior. A cylinder was positioned perpendicular across the grain boundary to determine the concentration changes as illustrated in Figure 6. 11d. Please note that a common problem with APT is that ion identification and range widths within the mass spectrum have an extensive effect on chemical composition.[250] Since a large number of molecular peaks were detected in the mass spectrum of this dataset, there is a chance that some of them might have been identified incorrectly, which would lead to errors in the concentration profile. Furthermore, there are several peak overlaps between some of the major peaks, e.g. Zn and  $\text{S}_2$  at 32 Da. The concentration values should, therefore, be regarded as qualitative, rather than quantitative. After careful analysis, the author found Cu and Zn enrichments, and Sn, S depletion at GBs compared to the GIs. Additionally, segregation of O accompanied by Na was also detected at GBs as shown in Figure 6. 11e. Our result suggests that the presence of Na in combination with O contributed to the passivation of the point defects at the CZTS grain boundary. Similar results have been reported in CIGS and CZTSSe films, where the formation of oxide at

the GBs also played an important role in defect passivation. Furthermore, an oxygen-substituted layer at the grain boundary resulted in lowered CBM of the CZTS grain boundary, thus formed hole barriers in the vicinity of the GBs.[84, 86]

### 6.3.4 Mechanism of $\text{Al}_2\text{O}_3$ passivation on CZTS

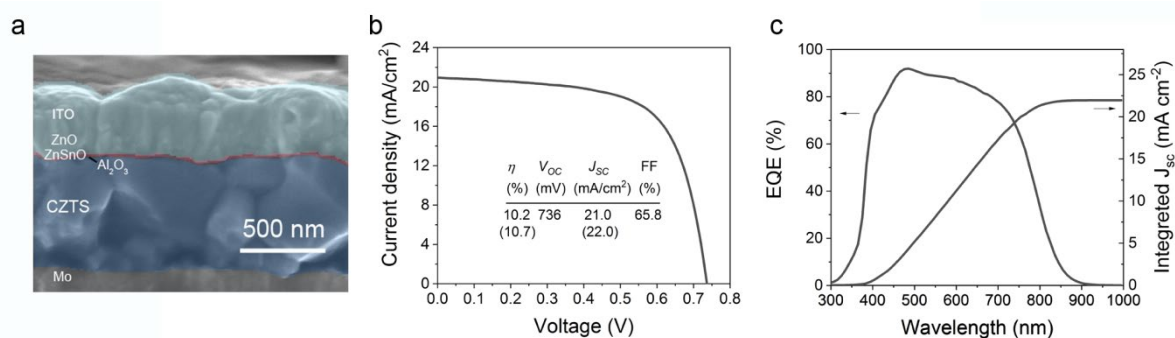


Figure 6. 14 a) SEM cross-sectional image of Cd-free CZTS solar cell with an  $\text{Al}_2\text{O}_3$  passivation layer inserted between CZTS and ZnSnO. b) Current density-voltage ( $J$ - $V$ ) characteristics and c) external quantum efficiency (EQE) of CZTS/ZnSnO record devices with  $\text{Al}_2\text{O}_3$  interlayer under 1 Sun illumination (AM 1.5G spectrum). The integrated photocurrent density is included on the right Y-axis.

As a direct demonstration of the benefits of ALD- $\text{Al}_2\text{O}_3$  passivation layer, the photocurrent density-voltage ( $J$ - $V$ ) characteristic of the champion Cd-free CZTS cell is shown in Figure 6. 14b. This ALD-treated device was obtained by depositing 5 cycles of  $\text{Al}_2\text{O}_3$  before the ZnSnO buffer layer, leading to a  $J_{SC}$  of 21.0  $\text{mA}/\text{cm}^2$ ,  $V_{OC}$  of 736 mV, FF of 65.8% and PCE of 10.2%, enabling an increase of 10% relative in efficiency compared to previous record device without  $\text{Al}_2\text{O}_3$ , as shown in Table 6. 2. Figure 6. 14c presents the external quantum efficiency (EQE) of the champion device with  $\text{Al}_2\text{O}_3$ . The EQE-derived  $J_{SC}$  under 1 Sun illumination at 1000  $\text{W}/\text{m}^2$  was measured to be 22.0  $\text{mA}/\text{cm}^2$  for the  $\text{Al}_2\text{O}_3$  device, which was higher than the  $J_{SC}$  obtained from the  $J$ - $V$  measurement. This is reasonable as the small spot measurement used in EQE avoids the optical loss from the metal grid shading that was present in the  $J$ - $V$  measurement.

Therefore, an active area efficiency of 10.7% was obtained for the record solar cell. Another noticeable improvement for the device with ALD treatment was the higher  $V_{OC}$  and  $FF$ , pointing to the improved electronic quality of the CZTS/ZnSnO interface, especially considering that both devices were fabricated using otherwise identical experimental conditions.

Table 6. 2 Corresponding values of photovoltaic parameters of the champion CZTS/ $Al_2O_3$ /ZnSnO solar cells compared to the previous champion CZTS/ZnSnO reference without  $Al_2O_3$  passivation. Values based on the active area are reported in parentheses.

Cell	$V_{OC}$ (mV)	$J_{SC}$ (mA $cm^{-2}$ )	$FF$ (%)	Eff (%)	$R_s$ ( $\Omega$ $cm^2$ )	$R_{sh}$ ( $\Omega$ $cm^2$ )	$A$	$J_0$ (mA $cm^{-2}$ )
CZTS/ZnSnO	720	20.5	63.5	9.3	0.40	669	2.58	$3.59 \times 10^{-4}$
CZTS/ $Al_2O_3$ /ZnSnO	736	21.0 (22.0)	65.8	10.2 (10.7)	0.30	418	2.46	$1.78 \times 10^{-4}$

The energy level of the CZTS surface before and after ALD treatment was characterized using ultraviolet photoelectron spectroscopy (UPS) measurements (Figure 6. 15). The valence band maximum (VBM) estimated from the valence band spectra for Ref sample was  $0.53 \pm 0.1$  eV below the Fermi energy level ( $E_F$ ). This value seems unchanged for the  $H_2O$  treated sample while it improved for the TMA and  $Al_2O_3$  treated samples. It was found that the valence band maximum shifted by about  $0.12 \pm 0.1$  eV away from the Fermi energy level after  $Al_2O_3$  treatment. Subsequently, the conduction band minimum (CBM) of CZTS surface can be obtained by adding the bandgap determined from the EQE band edge at long wavelength. Herein, the band diagrams illustrating the band alignment at the heterojunction for CZTS with and

without  $\text{Al}_2\text{O}_3$  treatment are depicted in Figure 6. 16**b, c**. Clearly, the  $\text{Al}_2\text{O}_3$  passivated sample demonstrated a lowered VBM at the surface, as well as slightly lowered CBM, compared to the reference. Consequently, the additional downward band bending induced by  $\text{Al}_2\text{O}_3$  treatment is expected to decrease the interface recombination. This modified band alignment can be attributed to the Cu-depleted compound with a higher concentration of O and Na (see the XPS analysis) formed at the near-surface region of CZTS/  $\text{Al}_2\text{O}_3$ . Density function theory (DFT) calculations on  $\text{Cu}_2\text{ZnSnSe}_4$  and oxidized  $\text{Cu}_2\text{ZnSnSe}_3\text{O}_1$  have shown that O substitution for Se can suppress the VBM and lead to an increase in bandgap.[84] This O substitution for S might also take place at the surface of CZTS and demonstrate a similar change in the electronic band structure of  $\text{Cu}_2\text{ZnSn}(\text{S}, \text{O})_4$ . The downward band bending also suggests the net negative charge originated from interstitial  $\text{O}_i^-$  at the surface has been mostly compensated, due to a large amount of Na segregation.

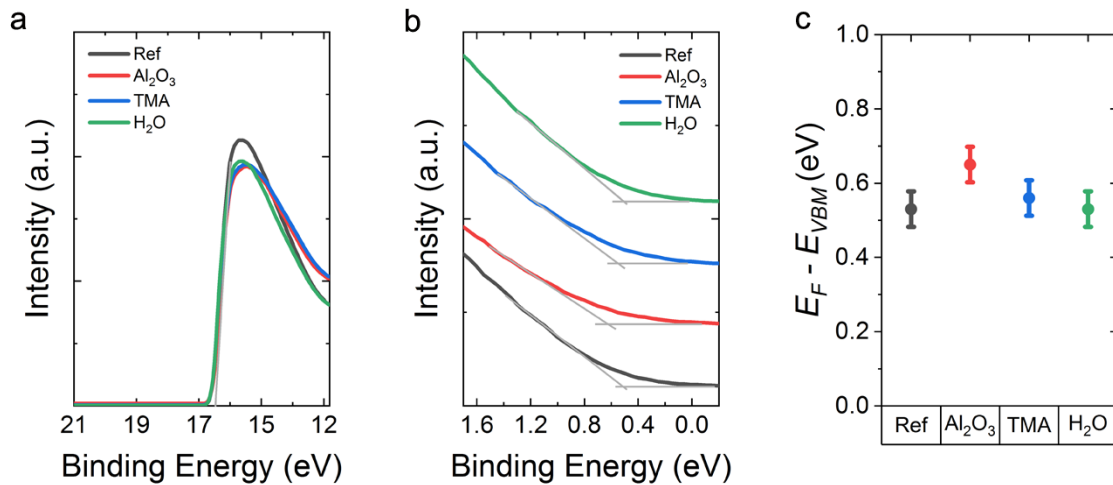


Figure 6. 15 a, b) UPS spectra of the CZTS absorbers with different ALD treatment. c) Energy band positions for CZTS absorbers of valence band maximum with respect to Fermi level energy,  $E_F$ .

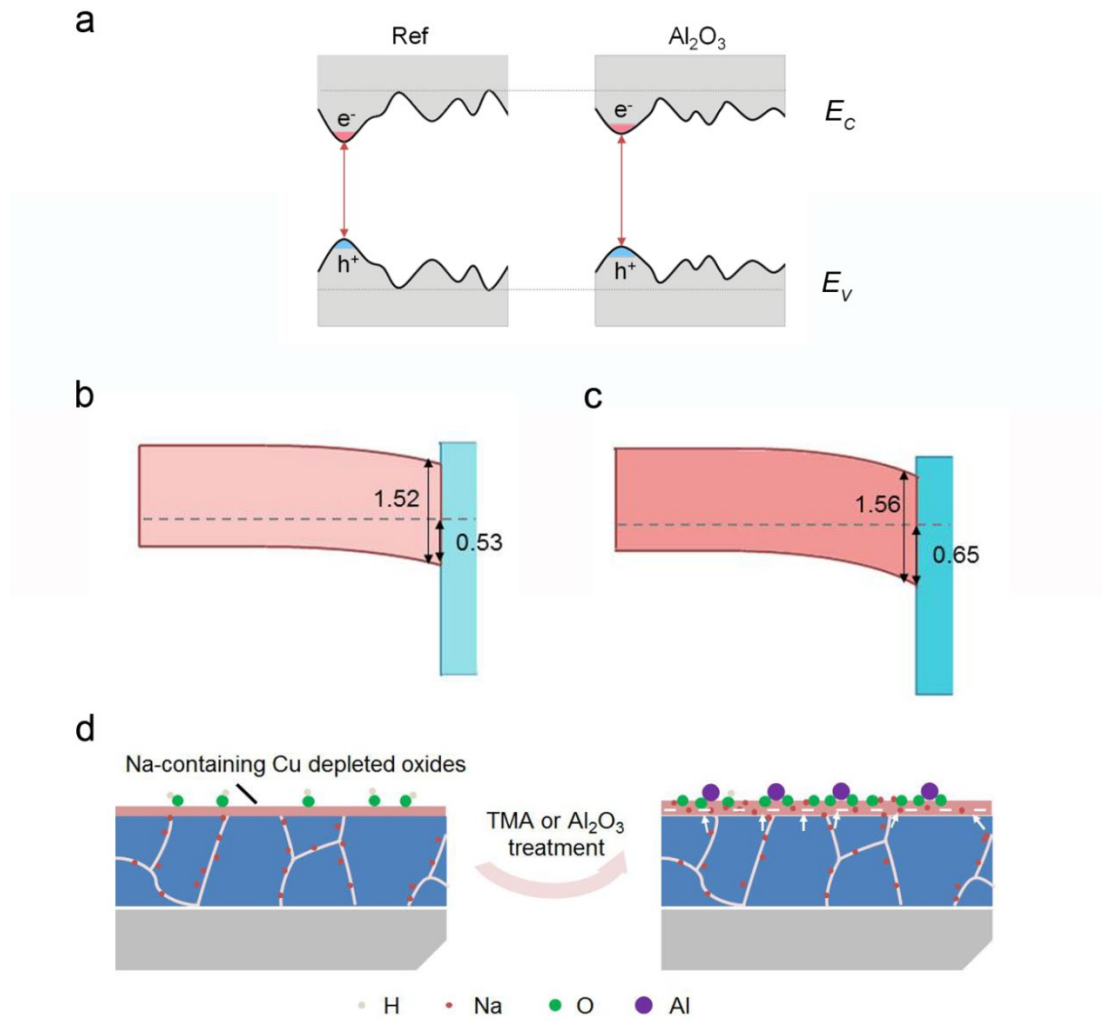


Figure 6. 16 a) Schematic bandgap fluctuation in the electronic structures of CZTS with and without  $\text{Al}_2\text{O}_3$  treatment. Band diagrams illustrating the band alignment structure for b) CZTS/ZnSnO and c) CZTS/ $\text{Al}_2\text{O}_3$ /ZnSnO. d) Mechanism illustration of the CZTS absorber surface modification when exposed to ALD- $\text{Al}_2\text{O}_3$  treatment.

The author then proposes a potential mechanism of the CZTS absorber surface modification when exposed to the ALD- $\text{Al}_2\text{O}_3$  treatment in Figure 6. 16d. The pristine CZTS absorber after sulfurization had a Na-containing nano-layer when exposed to an ambient atmosphere, accompanied by  $-\text{OH}$  groups on the surface. This nano-layer was Cu-poor, Zn- and Sn-rich compared to the bulk composition, which might be attributed to the oxygenation-induced redistribution of Cu or Na substitution for Cu. When the

absorber was subjected to a TMA or  $\text{Al}_2\text{O}_3$  treatment,  $\text{Al}_2\text{O}_3$  clusters featured by a higher O/Al ratio than the stoichiometric value will form at the initial growth of the ALD process. The resulting excess of oxygen at the interface is speculated to be at least partly present negative charged interstitial  $\text{O}_i^-$ , therefore, attracting interstitial  $\text{Na}_i^+$  from bulk to the interface. Thus, the  $\text{Al}_2\text{O}_3$  treated CZTS surface had a thicker Cu-deficiency nano-layer with an even higher concentration of Na and O. The additional Na and O then acted as surfactant and suppressor of non-radiative recombination at the interface of CZTS solar cells, hence reduces the local potential fluctuation of band edges and leads to the widened electrical bandgap, hence the improvement in  $V_{OC}$  and device performance.

## 6.4 General conclusions

In this chapter, it was demonstrated that the ALD-  $\text{Al}_2\text{O}_3$  as a passivation layer can greatly enhance the performance of CZTS solar cells by promoting downward band bending, reduced the bandgap fluctuation and suppressed defect recombination at the heterojunction interface. Specifically, TMA plays a key role rather than other ALD sub-steps in the passivation of CZTS/ZnSnO heterojunction. This prompted us to identify the origin of the chemical modification of the CZTS surface through different sub-steps of the ALD process. The improvement in  $V_{OC}$  resulting from the different ALD treatments was found to be well correlated with the Na variation at the CZTS surface. It was then speculated that the excess oxygen originating from the initial growth of ALD alumina might explain the enhanced segregation of Na at the CZTS/ $\text{Al}_2\text{O}_3$  interface. Finally, a plausible mechanism for the passivation induced by ALD- $\text{Al}_2\text{O}_3$  was proposed. ALD- $\text{Al}_2\text{O}_3$  facilitates the formation of a thicker Cu-deficient nano-layer with a higher concentration of Na and O, forming a homogeneous passivation layer across the CZTS surface. This nano-layer reduces the local potential fluctuation of band edges and leads to the widened electrical bandgap, hence the improvement in  $V_{OC}$  and device performance.



# Chapter 7 Summary

## 7.1 Conclusions

Kesterite  $\text{Cu}_2\text{ZnSnS}_4$  solar cell, which only consists of earth-abundant non-toxic elements, is regarded as one of the most promising candidates for sustainable large-scale PV deployment. The demand for more efficient photovoltaic devices has motivated the design and materials at the nanoscale which can be easily achieved by atomic layer deposition technique.

To deal with the  $V_{OC}$  deficit issue, I first presented the study of Cd-free buffer layers deposited by thermal ALD and their application on CZTS devices. In this part, the recipes for deposition of ZnO,  $\text{SnO}_x$  and MgO films by thermal ALD were developed with the help of *in-situ* diagnosis. The synthesis of a wide range of  $\text{Zn}_{1-x}\text{Sn}_x\text{O}$  ( $0 \leq x \leq 0.3$ ) films was then carried out. By carefully optimizing the thickness and composition of ZTO, a Cd-free CZTS solar cell with an efficiency of 9.3 % was achieved. The decreased interfacial crystalline defects stemming from the minor lattice mismatch at the CZTS/ $\text{Zn}(\text{S},\text{O})/\text{ZTO}$  hetero-interface in combination with the favorable band alignment of CZTS/ZTO explained the significant increase in open-circuit voltage. A SCAPS model was established to describe the characteristics of CZTS/ $\text{Zn}_{0.77}\text{Sn}_{0.23}\text{O}$  devices as the baseline model.

Secondly, I reported about the development of an alternative window layer, which is essential to minimize the optical loss as well as prevent shunt paths in CZTS thin-film solar cells. I proposed the use of a high bandgap window layer  $\text{Zn}_{1-x}\text{Mg}_x\text{O}$

and investigated its impact on device performance. A wide range of  $\text{Zn}_{1-x}\text{Mg}_x\text{O}$  ( $0 \leq x \leq 0.4$ ) films were synthesized through thermal and plasma-enhanced ALD. The optical and structural properties of ZMO thin films with different stoichiometry grown from both different ALD techniques were systematically investigated. The optimized solar cell with thermal ALD processed ZMO window layer demonstrates the expected improvement in both  $J_{sc}$  and  $V_{OC}$  but not the  $FF$  and efficiency. In contrast, ZMO films fabricated by plasma-enhanced ALD showed the expected increase in  $J_{sc}$ ,  $V_{OC}$  and efficiency although the  $FF$  was still relatively low. A 9.2% efficient Cd-free CZTS device with a structure of Mo/CZTS/ZnSnO/PE-ZMO/ITO was fabricated. The explanation of the difference was given in terms of the material properties, band alignment coupled with numerical device simulation.

Finally, I demonstrated the application of ALD  $\text{Al}_2\text{O}_3$  as heterojunction passivation layer and discerned the mechanism behind the effective passivation effects. This part presents a world-record efficiency of 10.2 % for Cd-free CZTS device resulting from the application of an  $\text{Al}_2\text{O}_3$  passivation layer prepared by ALD. The ALD  $\text{Al}_2\text{O}_3$  as a passivation layer can greatly enhance the performance of CZTS solar cells by promoting downward band bending, reduced bandgap fluctuation and suppressed defect recombination at the heterojunction interface. Specifically, it shows that TMA plays a key role rather than other ALD sub-steps in the passivation of CZTS/ZnSnO heterojunction. The improvement in  $V_{OC}$  resulted from the different ALD treatments was found to be well correlated with the Na variation at the CZTS surface. In addition, the excess oxygen originating from the initial growth of ALD alumina might explain the enhanced segregation of Na at the CZTS/  $\text{Al}_2\text{O}_3$  interface. Finally, a plausible mechanism for the passivation induced by ALD- $\text{Al}_2\text{O}_3$  was proposed. ALD- $\text{Al}_2\text{O}_3$  facilitates the formation of a thicker Cu-deficient nano-layer with a higher concentration of Na and O, forming a homogeneous passivation layer across the CZTS surface. This nano-layer reduces the local potential fluctuation of band edges and leads to the widened electrical bandgap, hence the improvement in  $V_{OC}$  and device

performance.

## 7.2 Original contributions

The original contributions arising from this thesis are listed below:

- The deposition and characterization of Zn-based ternary compounds by the supercycle ALD process was established. The implementation of *in situ* measurements accelerated the development of various functional materials with tunable compositions and properties.
- The ZnSnO films fabricated by thermal ALD were applied as a buffer layer in CZTS solar cells to test their performance at the device level. The high conversion efficiency of 9.3 % and an impressive 10 % increase in open-circuit voltage were achieved by carefully optimizing the thickness and composition of ZnSnO, demonstrating the great potential of ZnSnO buffer layer for Cd-free CZTS application. This was a world-record efficiency for a Cd-free CZTS solar cell at that time.
- An ultra-thin Zn(S,O) tunnel layer was firstly confirmed by characterizing the microstructure and chemical nature of the CZTS/ZnSnO interface, which contributes to the decreased interfacial defects at the heterointerface. This finding in combination with the passivation provided by a higher sodium concentration throughout the CZTS/ZTO device could explain the significant increase in open-circuit voltage.
- The synthesis of ZnMgO films was performed using both thermal ALD and plasma-enhanced ALD techniques. *In-situ* ellipsometry measurement revealed the different growth behavior for ZMO films deposited by thermal ALD and PE-ALD and correlated them with the different fundamental properties of the films.
- ZnMgO films were employed as a window layer to minimize the optical loss as well as prevent shunt path in CZTS thin-film solar cells. The device with

PE-ALD deposited ZnMgO exhibited better performance than thermal ALD deposited ZnMgO. A 9.2% efficient Cd-free CZTS device was fabricated with a novel structure of Mo/CZTS/ZnSnO/PE-ZnMgO/ITO without anti-reflection coating, thanks to the significantly enhanced  $J_{sc}$  and  $V_{oc}$ .

- Efficiency greater than 10 % for Cd-free CZTS cell was achieved for the first time, resulting from the application of an ALD- $\text{Al}_2\text{O}_3$  passivation layer at the CZTS/ZTO heterojunction interface. The ALD- $\text{Al}_2\text{O}_3$  as a passivation layer can greatly enhance the performance of CZTS solar cells by promoting downward band bending, reduced bandgap fluctuation and suppressed defect recombination at the heterojunction interface.
- The mechanism of  $\text{Al}_2\text{O}_3$  passivation effect on CZTS solar cells was systematically investigated by optoelectronic characterization, surface chemical and electronic analysis. A plausible mechanism for the passivation induced by ALD- $\text{Al}_2\text{O}_3$  was proposed: ALD- $\text{Al}_2\text{O}_3$  facilitates the formation of a thicker Cu-deficiency nano-layer with a higher concentration of Na and O, forming a homogeneous passivation layer across the CZTS surface. The ability of nanolayers to alter the atomic composition in the near surface region of compound semiconductors might be beneficial for a wider range of semiconductor devices.

### 7.3 Perspectives

Although impressive improvement has been made in this work regarding CZTS solar cells by employing ALD thin films, there are still opportunities to push it even further. Motivated by the studies in this thesis, alternative buffer layers, interface passivation layers and transparent conductive oxide layer or different ALD process could be explored for CZTS solar cells.

### **7.3.1 Alternative dopants for Zn-based buffer layers**

To avoid the utilization of the CdS buffer layer, a potentially interesting research topic is the exploration of Zn-based thin films by ALD for application as a buffer layer. In addition to ZnSnO studied in this thesis, there are still other alternatives such as Zn(O,S)[42], ZnMgO which have shown great achievements in CIGS solar cells. By carefully tuning the composition and deposition condition of those materials, more favorable band alignment and microstructure property could probably be achieved. Therefore, high-performance solar cells could be achieved due to the enhanced quality of the absorber/buffer heterojunction.

### **7.3.2 Alternative oxides for interface layers**

From the lessons we learned from the Al<sub>2</sub>O<sub>3</sub> passivation effect on CZTS, the metal precursor played a critical role in passivating the interface defects. Therefore, for interface modification of heterojunction, current research can still be further expanded by using different metal precursors in ALD process. An example of alternative Al precursor is the non-pyrophoric aluminum isopropoxide which has shown effective passivation effects on c-Si wafer.[220] Potential research could focus on the development of alternative precursors for the deposition of ultra-thin Al<sub>2</sub>O<sub>3</sub> passivation layer in high-efficiency CZTS concepts.

For back contact interface, application of high work function materials such as WO<sub>3</sub>/MoO<sub>3</sub> on CZTS devices could create an electrostatic field in the back contact to decrease the recombination of holes and electrons, thus have great potential to enhance the device properties.[96, 251] WO<sub>3</sub> and MoO<sub>3</sub> thin films by ALD offer numerous merits including atomic-scale thickness control at low deposition temperatures thus have the potential to improve the quality of the back contact interface.[252, 253]

### 7.3.3 Alternative ALD process for window layers

Triggered by the record efficiency of CIGS solar cell with ZnMgO as a window layer, opportunities still exist to boost the CZTS performance by optimizing the ZnMgO characteristics with alternative ALD process.[142] Besides, other functional materials including ZnMgO:Al[254, 255], ZnMgO:B[256], InZrO[257] have demonstrated their application on CIGS or c-Si solar cells as a window or TCO layer. Those materials are accessible by ALD with adjustable properties, which can also be effective in CZTS devices to minimize the band alignment mismatch, parasitic absorptions and interference effects. Together with the electrical and optical design of the buffer/window layers, optimized ALD thin films can be easily achieved to fulfill the requirement of CZTS solar cells.

# List of Publications

## Journal Publications:

1. **Cui, X.**, K. Sun, J. Huang, J. Yun, C.-Y. Lee, C. Yan, H. Sun, Y. Zhang, C. Xue, M. K. Eder, L. Yang, J.M. Cairney, J. Seidel, N.J. Ekins-Daukes, M. Green, B. Hoex and X. Hao. Cd-free Cu<sub>2</sub>ZnSnS<sub>4</sub> solar cell with an efficiency greater than 10 % enabled by Al<sub>2</sub>O<sub>3</sub> passivation layers [J]. **Energy & Environmental Science**, 2019, 12(9): 2751-2764.
2. **Cui, X.**, K. Sun, J. Huang, C.-Y. Lee, C. Yan, H. Sun, Y. Zhang, F. Liu, M. A. Hossain, Y. Zakaria, L. H. Wong, M. Green, B. Hoex and X. Hao. Enhanced Heterojunction Interface Quality To Achieve 9.3% Efficient Cd-Free Cu<sub>2</sub>ZnSnS<sub>4</sub> Solar Cells Using Atomic Layer Deposition ZnSnO Buffer Layer[J]. **Chemistry of Materials**, 2018, 30(21): 7860-7871.
3. Hossain, M. A., K. T. Khoo, **X. Cui**, G. K. Poduval, T. Zhang, X. Li, W. M. Li and B. Hoex. Atomic layer deposition enabling higher efficiency solar cells: A review [J]. **Nano Materials Science**, 2019.
4. Sun, K., C. Yan, J. Huang, F. Liu, J. Li, H. Sun, Y. Zhang, **X. Cui**, A. Wang, Z. Fang, J. Cong, Y. Lai, M. A. Green and X. Hao, Beyond 10% efficiency Cu<sub>2</sub>ZnSnS<sub>4</sub> solar cells enabled by modifying the heterojunction interface chemistry. **Journal of Materials Chemistry A**, 2019.
5. Zhang, Y., J. Huang, C. Yan, K. Sun, **X. Cui**, F. Liu, Z. Liu, X. Zhang, X. Liu, J. A. Stride, M. Green and X. Hao. High open-circuit voltage CuSbS<sub>2</sub> solar cells

achieved through the formation of epitaxial growth of CdS/CuSbS<sub>2</sub> hetero-interface by post-annealing treatment. **Progress in Photovoltaics: Research and Applications**, 2019, 27(1): 37-43.

6. Lee, C.-Y., S. Deng, T. Zhang, **X. Cui**, K. Khoo, K. Kim and B. Hoex. Evaluating the impact of thermal annealing on c-Si/Al<sub>2</sub>O<sub>3</sub> interface: Correlating electronic properties to infrared absorption [J]. **AIP Advances**, 2018, 8(7): 075204.
7. Lee, C. Y., S. Wang, **X. Cui**, T. Zhang, R. Deng, K. T. Khoo and B. Hoex. Improving the Silicon Surface Passivation by Aluminum Oxide Grown Using a Non-Pyrophoric Aluminum Precursor [J]. **physica status solidi (RRL)–Rapid Research Letters**, 2018, 12(7): 1800156.

#### **Conference Publications:**

1. **Cui, X.**, K. Sun, J. Huang, C.-Y. Lee, C. Yan, H. Sun, Y. Zhang, M. Green, B. Hoex and X. Hao. High-efficient Cd-free CZTS solar cells achieved by nanoscale atomic layer deposited aluminium oxide, **2019 IEEE 46th Photovoltaic Specialists Conference (PVSC)**, Chicago, USA, (2019). To be published.
2. **Cui, X.**, K. Sun, C.-Y. Lee, J. Huang, C. Yan, H. Sun, Y. Zhang, M. Green, B. Hoex and X. Hao. ALD ZnSnO buffer layer for enhancing heterojunction interface quality of CZTS solar cells[C], **2018 IEEE 7th World Conference on Photovoltaic Energy Conversion**, Hawaii, USA, (2018): 1166-1171.
3. Lee C Y, **Cui X**, Zhang T, Lee, R. Deng, K. T. Khoo and B. Hoex. Evaluating the Impact of Thermal Annealing on Al<sub>2</sub>O<sub>3</sub>/c-Si Interface Properties by Non-Destructive Measurements[C], **2018 IEEE 7th World Conference on Photovoltaic Energy Conversion**, Hawaii, USA, (2018): 2788-2791.



### Oral presentations:

1. **Cui, X.**, K. Sun, J. Huang, C.-Y. Lee, C. Yan, H. Sun, Y. Zhang, M. Green, B. Hoex and X. Hao. Heterojunction passivation by nanoscale ALD-alumina for beyond 10 % efficiency Cd-free CZTS solar cells, **29th International Conference on Photovoltaic Science and Engineering**, Xi'an, China (2019). Oral
2. **Cui, X.**, K. Sun, J. Huang, C.-Y. Lee, C. Yan, H. Sun, Y. Zhang, M. Green, B. Hoex and X. Hao. Defect and heterojunction engineering in CZTS solar cells by nanoscale atomic layer deposited aluminium oxide, **2018 ASIA-PACIFIC SOLAR RESEARCH CONFERENCE**, Sydney, Australia (2018). Oral
3. **Cui, X.**, K. Sun, C.-Y. Lee, J. Huang, C. Yan, H. Sun, M. Green, B. Hoex and X. Hao. Improvement of CZTS solar cell performance by ALD WO<sub>x</sub> interfacial layer, **2017 ASIA-PACIFIC SOLAR RESEARCH CONFERENCE**, Melbourne, Australia (2017). Oral



## Reference

- [1] A. Polman, M. Knight, E. C. Garnett, B. Ehrler, and W. C. Sinke, "Photovoltaic materials: Present efficiencies and future challenges," *Science*, vol. 352, no. 6283, p. aad4424, Apr 15 2016.
- [2] M. A. Green and S. P. Bremner, "Energy conversion approaches and materials for high-efficiency photovoltaics," *Nat Mater*, vol. 16, no. 1, pp. 23-34, Dec 20 2016.
- [3] K. Yoshikawa *et al.*, "Silicon heterojunction solar cell with interdigitated back contacts for a photoconversion efficiency over 26%," *Nature Energy*, vol. 2, no. 5, p. 17032, 2017.
- [4] IEA-PVPS, "IEA-PVPS Annual Report 2018," [http://www.iea-pvps.org/fileadmin/dam/public/report/FINAL\\_Annual\\_Report\\_2018-web\\_2019-05-24.pdf](http://www.iea-pvps.org/fileadmin/dam/public/report/FINAL_Annual_Report_2018-web_2019-05-24.pdf), May 2019.
- [5] G. Kavlak, J. McNerney, and J. E. Trancik, "Evaluating the causes of cost reduction in photovoltaic modules," *Energy Policy*, vol. 123, pp. 700-710, 2018.
- [6] F. I. f. S. Energy and Systems, "Photovoltaics Report," <https://www.ise.fraunhofer.de/content/dam/ise/de/documents/publications/studies/Photovoltaics-Report.pdf>, March 2019.
- [7] I. 2018, "International Technology Roadmap for Photovoltaic (ITRPV) Tenth Edition," vol. <https://itrpv.vdma.org/>, March 2019.
- [8] S. Siebentritt, "Chalcopyrite compound semiconductors for thin film solar cells," *Current Opinion in Green and Sustainable Chemistry*, vol. 4, pp. 1-7, 2017.
- [9] R. Scheer and H.-W. Schock, *Chalcogenide photovoltaics: physics, technologies, and thin film devices*. John Wiley & Sons, 2011.
- [10] T. Feurer *et al.*, "Progress in thin film CIGS photovoltaics - Research and development, manufacturing, and applications," *Progress in Photovoltaics: Research and Applications*, 2016.
- [11] Z. Yu, M. Leilaieoun, and Z. Holman, "Selecting tandem partners for silicon solar cells," *Nature Energy*, vol. 1, no. 11, 2016.
- [12] R. Kondrotas, C. Chen, and J. Tang, "Sb2S3 Solar Cells," *Joule*, vol. 2, no. 5, pp. 857-878, 2018.

- [13] M. A. Green, "Commercial progress and challenges for photovoltaics," *Nature Energy*, vol. 1, no. 1, 2016.
- [14] "First Solar achieves yet another cell conversion efficiency world record," *First Solar Press Release.*, 24 February 2016.
- [15] S. Frontier, "Solar Frontier Achieves World Record Thin-Film Solar Cell Efficiency of 23.35%," [http://www.solar-frontier.com/eng/news/2019/0117\\_press.html](http://www.solar-frontier.com/eng/news/2019/0117_press.html), 17 Jan 2019.
- [16] NREL, "Best Research-Cell Efficiency Chart," vol. <https://www.nrel.gov/pv/cell-efficiency.html>, 2019.
- [17] S. Giraldo, Z. Jehl, M. Placidi, V. Izquierdo-Roca, A. Perez-Rodriguez, and E. Saucedo, "Progress and Perspectives of Thin Film Kesterite Photovoltaic Technology: A Critical Review," *Adv Mater*, vol. 31, no. 16, p. e1806692, Apr 2019.
- [18] H. Azimi, Y. Hou, and C. J. Brabec, "Towards low-cost, environmentally friendly printed chalcopyrite and kesterite solar cells," *Energy Environ. Sci.*, vol. 7, no. 6, pp. 1829-1849, 2014.
- [19] A. Polizzotti, I. L. Repins, R. Noufi, S.-H. Wei, and D. B. Mitzi, "The state and future prospects of kesterite photovoltaics," *Energy & Environmental Science*, vol. 6, no. 11, p. 3171, 2013.
- [20] S. Delbos, "Kesterite thin films for photovoltaics : a review," *EPJ Photovoltaics*, vol. 3, p. 35004, 2012.
- [21] X. Liu *et al.*, "The current status and future prospects of kesterite solar cells: a brief review," *Progress in Photovoltaics: Research and Applications*, vol. 24, no. 6, pp. 879-898, 2016.
- [22] W. Shockley and H. J. Queisser, "Detailed Balance Limit of Efficiency of p - n Junction Solar Cells," *Journal of Applied Physics*, vol. 32, no. 3, pp. 510-519, 1961.
- [23] S. Siebentritt and S. Schorr, "Kesterites-a challenging material for solar cells," *Progress in Photovoltaics: Research and Applications*, vol. 20, no. 5, pp. 512-519, 2012.
- [24] D. B. Mitzi, O. Gunawan, T. K. Todorov, K. Wang, and S. Guha, "The path towards a high-performance solution-processed kesterite solar cell," *Solar Energy Materials and Solar Cells*, vol. 95, no. 6, pp. 1421-1436, 2011.
- [25] P. C. K. Vesborg and T. F. Jaramillo, "Addressing the terawatt challenge: scalability in the supply of chemical elements for renewable energy," *RSC Advances*, vol. 2, no. 21, 2012.
- [26] J. K. Larsen *et al.*, "Cadmium free Cu<sub>2</sub>ZnSnS<sub>4</sub> solar cells with 9.7% efficiency," *Advanced Energy Materials*, p. 1900439, 2019.
- [27] X. Li, Z. Su, S. Venkataraj, S. K. Batabyal, and L. H. Wong, "8.6% Efficiency CZTSSe solar cell with atomic layer deposited Zn-Sn-O buffer layer," *Solar Energy Materials and Solar Cells*, vol. 157, pp. 101-107, 2016.
- [28] M. Nakamura, K. Yamaguchi, Y. Kimoto, Y. Yasaki, T. Kato, and H. Sugimoto,

- "Cd-Free Cu(In,Ga)(Se,S)<sub>2</sub> Thin-Film Solar Cell With Record Efficiency of 23.35%," *IEEE Journal of Photovoltaics*, pp. 1-5, 2019.
- [29] D.-H. Son *et al.*, "Effect of solid-H<sub>2</sub>S gas reactions on CZTSSe thin film growth and photovoltaic properties of a 12.62% efficiency device," *Journal of Materials Chemistry A*, 2019.
- [30] P. K. Nayak, S. Mahesh, H. J. Snaith, and D. Cahen, "Photovoltaic solar cell technologies: analysing the state of the art," *Nature Reviews Materials*, vol. 4, no. 4, pp. 269-285, 2019.
- [31] M. Kumar, A. Dubey, N. Adhikari, S. Venkatesan, and Q. Qiao, "Strategic review of secondary phases, defects and defect-complexes in kesterite CZTS–Se solar cells," *Energy Environ. Sci.*, vol. 8, no. 11, pp. 3134-3159, 2015.
- [32] C. J. Hages *et al.*, "Identifying the Real Minority Carrier Lifetime in Nonideal Semiconductors: A Case Study of Kesterite Materials," *Advanced Energy Materials*, vol. 7, no. 18, 2017.
- [33] T. K. Todorov, K. B. Reuter, and D. B. Mitzi, "High-efficiency solar cell with Earth-abundant liquid-processed absorber," *Adv Mater*, vol. 22, no. 20, pp. E156-9, May 25 2010.
- [34] A. Redinger, D. M. Berg, P. J. Dale, and S. Siebentritt, "The consequences of kesterite equilibria for efficient solar cells," *J Am Chem Soc*, vol. 133, no. 10, pp. 3320-3, Mar 16 2011.
- [35] J. J. Scragg, T. Ericson, T. Kubart, M. Edoff, and C. Platzer-Björkman, "Chemical Insights into the Instability of Cu<sub>2</sub>ZnSnS<sub>4</sub> Films during Annealing," *Chemistry of Materials*, vol. 23, no. 20, pp. 4625-4633, 2011.
- [36] K. Kaur, N. Kumar, and M. Kumar, "Strategic review of interface carrier recombination in earth abundant Cu–Zn–Sn–S–Se solar cells: current challenges and future prospects," *J. Mater. Chem. A*, vol. 5, no. 7, pp. 3069-3090, 2017.
- [37] W. Wang *et al.*, "Device Characteristics of CZTSSe Thin-Film Solar Cells with 12.6% Efficiency," *Advanced Energy Materials*, vol. 4, no. 7, p. 1301465, 2014.
- [38] C. Yan *et al.*, "Cu<sub>2</sub>ZnSnS<sub>4</sub> solar cells with over 10% power conversion efficiency enabled by heterojunction heat treatment," *Nature Energy*, vol. 3, no. 9, pp. 764-772, 2018.
- [39] T. Taskesen *et al.*, "Device Characteristics of an 11.4% CZTSe Solar Cell Fabricated from Sputtered Precursors," *Advanced Energy Materials*, 2018.
- [40] J. K. Larsen *et al.*, "Cadmium Free Cu<sub>2</sub>ZnSnS<sub>4</sub> Solar Cells with 9.7% Efficiency," *Advanced Energy Materials*, 2019.
- [41] D. A. R. Barkhouse, R. Haight, N. Sakai, H. Hiroi, H. Sugimoto, and D. B. Mitzi, "Cd-free buffer layer materials on Cu<sub>2</sub>ZnSn(S<sub>x</sub>Se<sub>1-x</sub>)<sub>4</sub>: Band alignments with ZnO, ZnS, and In<sub>2</sub>S<sub>3</sub>," *Applied Physics Letters*, vol. 100, no. 19, p. 193904, 2012.
- [42] T. Ericson *et al.*, "Zn(O, S) Buffer Layers and Thickness Variations of CdS

- Buffer for Cu<sub>2</sub>ZnSnS<sub>4</sub> Solar Cells," *IEEE Journal of Photovoltaics*, vol. 4, no. 1, pp. 465-469, 2014.
- [43] T. Ericson *et al.*, "Zinc-Tin-Oxide Buffer Layer and Low Temperature Post Annealing Resulting in a 9.0% Efficient Cd-free Cu<sub>2</sub>ZnSnS<sub>4</sub> Solar Cell," *Solar RRL*, p. 1700001, 2017.
- [44] S. Tajima, M. Umehara, and T. Mise, "Photovoltaic properties of Cu<sub>2</sub>ZnSnS<sub>4</sub> cells fabricated using ZnSnO and ZnSnO/CdS buffer layers," *Japanese Journal of Applied Physics*, vol. 55, no. 11, p. 112302, 2016.
- [45] S. Bourdais *et al.*, "Is the Cu/Zn Disorder the Main Culprit for the Voltage Deficit in Kesterite Solar Cells?," *Advanced Energy Materials*, vol. 6, no. 12, 2016.
- [46] L. Yin, G. Cheng, Y. Feng, Z. Li, C. Yang, and X. Xiao, "Limitation factors for the performance of kesterite Cu<sub>2</sub>ZnSnS<sub>4</sub> thin film solar cells studied by defect characterization," *RSC Adv.*, vol. 5, no. 50, pp. 40369-40374, 2015.
- [47] M. E. Erkan, V. Chawla, and M. A. Scarpulla, "Reduced defect density at the CZTSSe/CdS interface by atomic layer deposition of Al<sub>2</sub>O<sub>3</sub>," *Journal of Applied Physics*, vol. 119, no. 19, 2016.
- [48] A. Walsh, S. Chen, X. G. Gong, S.-H. Wei, J. Ihm, and H. Cheong, "Crystal structure and defect reactions in the kesterite solar cell absorber Cu<sub>2</sub>ZnSnS<sub>4</sub>(CZTS): Theoretical insights," pp. 63-64, 2011.
- [49] O. Gunawan, T. K. Todorov, and D. B. Mitzi, "Loss mechanisms in hydrazine-processed Cu<sub>2</sub>ZnSn(S<sub>x</sub>Se<sub>1-x</sub>)<sub>4</sub> solar cells," *Applied Physics Letters*, vol. 97, no. 23, p. 233506, 2010.
- [50] T. Negami, T. Minemoto, and Y. Hashimoto, "CIGS solar cells using a novel window Zn/sub 1-x/Mg/sub x/O film," in *Photovoltaic Specialists Conference, 2000. Conference Record of the Twenty-Eighth IEEE*, 2000, pp. 634-637: IEEE.
- [51] T. Minemoto *et al.*, "Theoretical analysis of the effect of conduction band offset of window/CIS layers on performance of CIS solar cells using device simulation," *Solar Energy Materials and Solar Cells*, vol. 67, no. 1, pp. 83-88, 2001.
- [52] C. Yan *et al.*, "Beyond 11% Efficient Sulfide Kesterite Cu<sub>2</sub>Zn<sub>x</sub>Cd<sub>1-x</sub>SnS<sub>4</sub> Solar Cell: Effects of Cadmium Alloying," *ACS Energy Letters*, vol. 2, no. 4, pp. 930-936, 2017.
- [53] Y. S. Lee *et al.*, "Cu<sub>2</sub>ZnSnSe<sub>4</sub> Thin-Film Solar Cells by Thermal Co-evaporation with 11.6% Efficiency and Improved Minority Carrier Diffusion Length," *Advanced Energy Materials*, vol. 5, no. 7, p. 1401372, 2015.
- [54] S. Chen *et al.*, "Compositional dependence of structural and electronic properties of Cu<sub>2</sub>ZnSn(S<sub>x</sub>Se<sub>1-x</sub>)<sub>4</sub> alloys for thin film solar cells," *Physical Review B*, vol. 83, no. 12, 2011.
- [55] R. Haight *et al.*, "Band alignment at the Cu<sub>2</sub>ZnSn(S<sub>x</sub>Se<sub>1-x</sub>)<sub>4</sub>/CdS interface," *Applied Physics Letters*, vol. 98, no. 25, p. 253502, 2011.

- [56] M. Bär *et al.*, "Cliff-like conduction band offset and KCN-induced recombination barrier enhancement at the CdS/Cu<sub>2</sub>ZnSnS<sub>4</sub> thin-film solar cell heterojunction," *Applied Physics Letters*, vol. 99, no. 22, p. 222105, 2011.
- [57] A. Santoni, F. Biccari, C. Malerba, M. Valentini, R. Chierchia, and A. Mittiga, "Valence band offset at the CdS/Cu<sub>2</sub>ZnSnS<sub>4</sub> interface probed by x-ray photoelectron spectroscopy," *Journal of Physics D: Applied Physics*, vol. 46, no. 17, p. 175101, 2013.
- [58] C. Yan *et al.*, "Band alignments of different buffer layers (CdS, Zn(O,S), and In<sub>2</sub>S<sub>3</sub>) on Cu<sub>2</sub>ZnSnS<sub>4</sub>," *Applied Physics Letters*, vol. 104, no. 17, p. 173901, 2014.
- [59] K. Sun *et al.*, "Over 9% Efficient Kesterite Cu<sub>2</sub>ZnSnS<sub>4</sub> Solar Cell Fabricated by Using Zn<sub>1-x</sub>Cd<sub>x</sub>S Buffer Layer," *Advanced Energy Materials*, vol. 6, no. 12, p. 1600046, 2016.
- [60] F. Jiang *et al.*, "Effect of Indium Doping on Surface Optoelectrical Properties of Cu<sub>2</sub>ZnSnS<sub>4</sub> Photoabsorber and Interfacial/Photovoltaic Performance of Cadmium Free In<sub>2</sub>S<sub>3</sub>/Cu<sub>2</sub>ZnSnS<sub>4</sub> Heterojunction Thin Film Solar Cell," *Chemistry of Materials*, vol. 28, no. 10, pp. 3283-3291, 2016.
- [61] H. Hiroi, N. Sakai, T. Kato, and H. Sugimoto, "High voltage Cu<sub>2</sub>ZnSnS<sub>4</sub> submodules by hybrid buffer layer," in *Photovoltaic Specialists Conference (PVSC), 2013 IEEE 39th*, 2013, pp. 0863-0866: IEEE.
- [62] W. Bao and M. Ichimura, "First-Principles Study on Influences of Crystal Structure and Orientation on Band Offsets at the CdS/Cu<sub>2</sub>ZnSnS<sub>4</sub> Interface," *International Journal of Photoenergy*, vol. 2012, pp. 1-5, 2012.
- [63] M. Murata, J. Chantana, N. Ashida, D. Hironiwa, and T. Minemoto, "Influence of conduction band minimum difference between transparent conductive oxide and absorber on photovoltaic performance of thin-film solar cell," *Japanese Journal of Applied Physics*, vol. 54, no. 3, 2015.
- [64] S. Chen, J.-H. Yang, X.-G. Gong, A. Walsh, and S.-H. Wei, "Intrinsic point defects and complexes in the quaternary kesterite semiconductor Cu<sub>2</sub>ZnSnS<sub>4</sub>," *Physical Review B*, vol. 81, no. 24, p. 245204, 2010.
- [65] T. Gokmen, O. Gunawan, T. K. Todorov, and D. B. Mitzi, "Band tailing and efficiency limitation in kesterite solar cells," *Applied Physics Letters*, vol. 103, no. 10, p. 103506, 2013.
- [66] S. López-Marino *et al.*, "Alkali doping strategies for flexible and light-weight Cu<sub>2</sub>ZnSnSe<sub>4</sub> solar cells," *Journal of Materials Chemistry A*, vol. 4, no. 5, pp. 1895-1907, 2016.
- [67] Y.-T. Hsieh *et al.*, "Efficiency Enhancement of Cu<sub>2</sub>ZnSn(S,Se)<sub>4</sub> Solar Cells via Alkali Metals Doping," *Advanced Energy Materials*, vol. 6, no. 7, p. 1502386, 2016.
- [68] S. G. Haass *et al.*, "Complex Interplay between Absorber Composition and Alkali Doping in High-Efficiency Kesterite Solar Cells," *Advanced Energy Materials*, vol. 8, no. 4, 2018.

- [69] S. G. Haass *et al.*, "Effects of potassium on kesterite solar cells: Similarities, differences and synergies with sodium," *AIP Advances*, vol. 8, no. 1, 2018.
- [70] C.-Y. Liu, Z.-M. Li, H.-Y. Gu, S.-Y. Chen, H. Xiang, and X.-G. Gong, "Sodium Passivation of the Grain Boundaries in CuInSe<sub>2</sub> and Cu<sub>2</sub>ZnSnS<sub>4</sub> for High-Efficiency Solar Cells," *Advanced Energy Materials*, vol. 7, no. 8, 2017.
- [71] T. Gershon, C. Hamann, M. Hopstaken, Y. S. Lee, B. Shin, and R. Haight, "Chemical Consequences of Alkali Inhomogeneity in Cu<sub>2</sub>ZnSnS<sub>4</sub>Thin-Film Solar Cells," *Advanced Energy Materials*, vol. 5, no. 19, p. 1500922, 2015.
- [72] C. P. Muzzillo, "Review of grain interior, grain boundary, and interface effects of K in CIGS solar cells: Mechanisms for performance enhancement," *Solar Energy Materials and Solar Cells*, vol. 172, pp. 18-24, 2017.
- [73] T. Kodalle *et al.*, "Elucidating the Mechanism of an RbF Post Deposition Treatment in CIGS Thin Film Solar Cells," *Solar RRL*, vol. 2, no. 9, 2018.
- [74] E. Handick *et al.*, "Potassium Postdeposition Treatment-Induced Band Gap Widening at Cu(In,Ga)Se(2) Surfaces--Reason for Performance Leap?," *ACS Appl Mater Interfaces*, vol. 7, no. 49, pp. 27414-20, Dec 16 2015.
- [75] D. Hauschild *et al.*, "Impact of a RbF Postdeposition Treatment on the Electronic Structure of the CdS/Cu(In,Ga)Se<sub>2</sub> Heterojunction in High-Efficiency Thin-Film Solar Cells," *ACS Energy Letters*, vol. 2, no. 10, pp. 2383-2387, 2017.
- [76] H. Xin *et al.*, "Lithium-doping inverts the nanoscale electric field at the grain boundaries in Cu<sub>2</sub>ZnSn(S,Se)<sub>4</sub> and increases photovoltaic efficiency," *Phys Chem Chem Phys*, vol. 17, no. 37, pp. 23859-66, Oct 07 2015.
- [77] Y. Yang, X. Kang, L. Huang, and D. Pan, "Tuning the Band Gap of Cu(2)ZnSn(S,Se)(4) Thin Films via Lithium Alloying," *ACS Appl Mater Interfaces*, vol. 8, no. 8, pp. 5308-13, Mar 02 2016.
- [78] B. Hoex, J. Schmidt, P. Pohl, M. C. M. van de Sanden, and W. M. M. Kessels, "Silicon surface passivation by atomic layer deposited Al<sub>2</sub>O<sub>3</sub>," *Journal of Applied Physics*, vol. 104, no. 4, p. 044903, 2008.
- [79] J. Kim, S. Park, S. Ryu, J. Oh, and B. Shin, "Improving the open-circuit voltage of Cu<sub>2</sub>ZnSnSe<sub>4</sub> thin film solar cells via interface passivation," *Progress in Photovoltaics: Research and Applications*, 2017.
- [80] W. Wu *et al.*, "Characterization of CZTSSe photovoltaic device with an atomic layer-deposited passivation layer," *Applied Physics Letters*, vol. 105, no. 4, p. 042108, 2014.
- [81] Y. S. Lee *et al.*, "Atomic Layer Deposited Aluminum Oxide for Interface Passivation of Cu<sub>2</sub>ZnSn(S,Se)<sub>4</sub>Thin-Film Solar Cells," *Advanced Energy Materials*, vol. 6, no. 12, p. 1600198, 2016.
- [82] J. Park *et al.*, "The Role of Hydrogen from ALD-Al<sub>2</sub>O<sub>3</sub> in Kesterite Cu<sub>2</sub>ZnSnS<sub>4</sub> Solar Cells: Grain Surface Passivation," *Advanced Energy Materials*, vol. 8, no. 23, p. 1701940, 2018.
- [83] Y. Ren, J. J. Scragg, M. Edoff, J. K. Larsen, and C. Platzer-Bjorkman,



- "Evolution of Na-S(-O) Compounds on the Cu<sub>2</sub>ZnSnS<sub>4</sub> Absorber Surface and Their Effects on CdS Thin Film Growth," *ACS Appl Mater Interfaces*, vol. 8, no. 28, pp. 18600-7, Jul 20 2016.
- [84] J. H. Kim *et al.*, "Atomic-Scale Observation of Oxygen Substitution and Its Correlation with Hole-Transport Barriers in Cu<sub>2</sub>ZnSnSe<sub>4</sub>Thin-Film Solar Cells," *Advanced Energy Materials*, vol. 6, no. 6, p. 1501902, 2016.
- [85] H. Tampo, S. Kim, T. Nagai, H. Shibata, and S. Niki, "Improving the Open Circuit Voltage through Surface Oxygen Plasma Treatment and 11.7% Efficient Cu<sub>2</sub>ZnSnSe<sub>4</sub> Solar Cell," *ACS Appl Mater Interfaces*, vol. 11, no. 14, pp. 13319-13325, Apr 10 2019.
- [86] T. Gershon, B. Shin, N. Bojarczuk, M. Hopstaken, D. B. Mitzi, and S. Guha, "The Role of Sodium as a Surfactant and Suppressor of Non-Radiative Recombination at Internal Surfaces in Cu<sub>2</sub>ZnSnS<sub>4</sub>," *Advanced Energy Materials*, vol. 5, no. 2, 2015.
- [87] R. Haight, X. Shao, W. Wang, and D. B. Mitzi, "Electronic and elemental properties of the Cu<sub>2</sub>ZnSn(S,Se)<sub>4</sub> surface and grain boundaries," *Applied Physics Letters*, vol. 104, no. 3, p. 033902, 2014.
- [88] J. J. Scragg, J. T. Watjen, M. Edoff, T. Ericson, T. Kubart, and C. Platzer-Bjorkman, "A detrimental reaction at the molybdenum back contact in Cu<sub>2</sub>ZnSn(S,Se)<sub>4</sub> thin-film solar cells," *J Am Chem Soc*, vol. 134, no. 47, pp. 19330-3, Nov 28 2012.
- [89] L. Assmann, J. C. Bernède, A. Drici, C. Amory, E. Halgand, and M. Morsli, "Study of the Mo thin films and Mo/CIGS interface properties," *Applied Surface Science*, vol. 246, no. 1-3, pp. 159-166, 2005.
- [90] K.-J. Yang *et al.*, "Effects of Na and MoS<sub>2</sub>on Cu<sub>2</sub>ZnSnS<sub>4</sub>thin-film solar cell," *Progress in Photovoltaics: Research and Applications*, vol. 23, no. 7, pp. 862-873, 2015.
- [91] B. Shin, Y. Zhu, N. A. Bojarczuk, S. Jay Chey, and S. Guha, "Control of an interfacial MoSe<sub>2</sub> layer in Cu<sub>2</sub>ZnSnSe<sub>4</sub> thin film solar cells: 8.9% power conversion efficiency with a TiN diffusion barrier," *Applied Physics Letters*, vol. 101, no. 5, p. 053903, 2012.
- [92] X. Liu *et al.*, "Improving Cu<sub>2</sub>ZnSnS<sub>4</sub>(CZTS) solar cell performance by an ultrathin ZnO intermediate layer between CZTS absorber and Mo back contact," *physica status solidi (RRL) - Rapid Research Letters*, vol. 8, no. 12, pp. 966-970, 2014.
- [93] S. López-Marino *et al.*, "Inhibiting the absorber/Mo-back contact decomposition reaction in Cu<sub>2</sub>ZnSnSe<sub>4</sub> solar cells: the role of a ZnO intermediate nanolayer," *Journal of Materials Chemistry A*, vol. 1, no. 29, p. 8338, 2013.
- [94] F. Liu *et al.*, "Enhancing the Cu<sub>2</sub>ZnSnS<sub>4</sub> solar cell efficiency by back contact modification: Inserting a thin TiB<sub>2</sub> intermediate layer at Cu<sub>2</sub>ZnSnS<sub>4</sub>/Mo interface," *Applied Physics Letters*, vol. 104, no. 5, p. 051105, 2014.

- [95] S. Ranjbar *et al.*, "P–N Junction Passivation in Kesterite Solar Cells by Use of Solution-Processed TiO<sub>2</sub> Layer," *IEEE Journal of Photovoltaics*, vol. 7, no. 4, pp. 1130-1135, 2017.
- [96] P. D. Antunez *et al.*, "Back Contact Engineering for Increased Performance in Kesterite Solar Cells," *Advanced Energy Materials*, p. 1602585, 2017.
- [97] M. T. Winkler, W. Wang, O. Gunawan, H. J. Hovel, T. K. Todorov, and D. B. Mitzi, "Optical designs that improve the efficiency of Cu<sub>2</sub>ZnSn(S,Se)<sub>4</sub> solar cells," *Energy Environ. Sci.*, vol. 7, no. 3, pp. 1029-1036, 2014.
- [98] T. Suntola, "Atomic layer epitaxy," *Materials Science Reports*, vol. 4, no. 5, pp. 261-312, 1989.
- [99] A. F. Palmstrom, P. K. Santra, and S. F. Bent, "Atomic layer deposition in nanostructured photovoltaics: tuning optical, electronic and surface properties," *Nanoscale*, vol. 7, no. 29, pp. 12266-83, Aug 07 2015.
- [100] W. Niu *et al.*, "Applications of atomic layer deposition in solar cells," *Nanotechnology*, vol. 26, no. 6, p. 064001, Feb 13 2015.
- [101] J. R. Bakke, K. L. Pickrahn, T. P. Brennan, and S. F. Bent, "Nanoengineering and interfacial engineering of photovoltaics by atomic layer deposition," *Nanoscale*, vol. 3, no. 9, pp. 3482-508, Sep 01 2011.
- [102] J. A. van Delft, D. Garcia-Alonso, and W. M. M. Kessels, "Atomic layer deposition for photovoltaics: applications and prospects for solar cell manufacturing," *Semiconductor Science and Technology*, vol. 27, no. 7, p. 074002, 2012.
- [103] J. Lindahl, J. Keller, O. Donzel-Gargand, P. Szaniawski, M. Edoff, and T. Törndahl, "Deposition temperature induced conduction band changes in zinc tin oxide buffer layers for Cu(In,Ga)Se<sub>2</sub> solar cells," *Solar Energy Materials and Solar Cells*, vol. 144, pp. 684-690, 2016.
- [104] J. Lindahl, C. Hägglund, J. T. Wätjen, M. Edoff, and T. Törndahl, "The effect of substrate temperature on atomic layer deposited zinc tin oxide," *Thin Solid Films*, vol. 586, pp. 82-87, 2015.
- [105] M. Kapilashrami *et al.*, "Soft X-ray characterization of Zn(1-x)Sn(x)O(y) electronic structure for thin film photovoltaics," *Phys Chem Chem Phys*, vol. 14, no. 29, pp. 10154-9, Aug 07 2012.
- [106] D. Hironiwa, J. Chantana, N. Sakai, T. Kato, H. Sugimoto, and T. Minemoto, "Application of multi-buffer layer of (Zn,Mg)O/CdS in Cu<sub>2</sub>ZnSn(S,Se)<sub>4</sub> solar cells," *Current Applied Physics*, vol. 15, no. 3, pp. 383-388, 2015.
- [107] S. Kim, C. S. Lee, S. Kim, R. B. Chalapathy, E. A. Al-Ammar, and B. T. Ahn, "Understanding the light soaking effect of ZnMgO buffer in CIGS solar cells," *Phys Chem Chem Phys*, vol. 17, no. 29, pp. 19222-9, Jul 15 2015.
- [108] Z.-H. Li, E.-S. Cho, and S. J. Kwon, "Mg-doped ZnO thin films deposited by the atomic layer chemical vapor deposition for the buffer layer of CIGS solar cell," *Applied Surface Science*, vol. 314, pp. 97-103, 2014.
- [109] P. Poodt, A. Lankhorst, F. Roozeboom, K. Spee, D. Maas, and A. Vermeer,

- "High-speed spatial atomic-layer deposition of aluminum oxide layers for solar cell passivation," *Adv Mater*; vol. 22, no. 32, pp. 3564-7, Aug 24 2010.
- [110] R. L. Z. Hoyer *et al.*, "Research Update: Atmospheric pressure spatial atomic layer deposition of ZnO thin films: Reactors, doping, and devices," *APL Materials*, vol. 3, no. 4, p. 040701, 2015.
- [111] N. Nandakumar *et al.*, "Resistive Intrinsic ZnO Films Deposited by Ultrafast Spatial ALD for PV Applications," *IEEE Journal of Photovoltaics*, vol. 5, no. 5, pp. 1462-1469, 2015.
- [112] D. H. Kim *et al.*, "Highly reproducible planar Sb(2)S(3)-sensitized solar cells based on atomic layer deposition," *Nanoscale*, vol. 6, no. 23, pp. 14549-54, Nov 6 2014.
- [113] S. C. Riha, A. A. Koegel, J. D. Emery, M. J. Pellin, and A. B. Martinson, "Low-Temperature Atomic Layer Deposition of CuSbS<sub>2</sub> for Thin-Film Photovoltaics," *ACS Appl Mater Interfaces*, vol. 9, no. 5, pp. 4667-4673, Feb 08 2017.
- [114] E. Thimsen, S. C. Riha, S. V. Baryshev, A. B. F. Martinson, J. W. Elam, and M. J. Pellin, "Atomic Layer Deposition of the Quaternary Chalcogenide Cu<sub>2</sub>ZnSnS<sub>4</sub>," *Chemistry of Materials*, vol. 24, no. 16, pp. 3188-3196, 2012.
- [115] L. Reijnen, B. Meester, A. Goossens, and J. Schoonman, "Nanoporous TiO<sub>2</sub>/Cu<sub>1.8</sub>S heterojunctions for solar energy conversion," *Materials Science and Engineering: C*, vol. 19, no. 1-2, pp. 311-314, 2002.
- [116] J. Johansson, J. Kostamo, M. Karppinen, and L. Niinistö, "Growth of conductive copper sulfide thin films by atomic layer deposition," *Journal of Materials Chemistry*, vol. 12, no. 4, pp. 1022-1026, 2002.
- [117] M. Nanu, J. Schoonman, and A. Goossens, "Solar-Energy Conversion in TiO<sub>2</sub>/CuInS<sub>2</sub> Nanocomposites," *Advanced Functional Materials*, vol. 15, no. 1, pp. 95-100, 2005.
- [118] M. Nanu, F. Boulch, J. Schoonman, and A. Goossens, "Deep-level transient spectroscopy of TiO<sub>2</sub> / CuInS<sub>2</sub> heterojunctions," *Applied Physics Letters*, vol. 87, no. 24, p. 242103, 2005.
- [119] M. Nanu, J. Schoonman, and A. Goossens, "Inorganic Nanocomposites of n - and p - Type Semiconductors: A New Type of Three - Dimensional Solar Cell," *Advanced Materials*, vol. 16, no. 5, pp. 453-456, 2004.
- [120] J. Perrenoud, S. Buecheler, L. Kranz, C. Fella, J. Scharp, and A. Tiwari, "Application of ZnO 1- x S<sub>x</sub> as window layer in cadmium telluride solar cells," in *2010 35th IEEE Photovoltaic Specialists Conference*, 2010, pp. 000995-001000: IEEE.
- [121] J. Lindahl *et al.*, "Inline Cu(In,Ga)Se<sub>2</sub> Co-evaporation for High-Efficiency Solar Cells and Modules," *IEEE Journal of Photovoltaics*, vol. 3, no. 3, pp. 1100-1105, 2013.
- [122] X. Cui *et al.*, "Enhanced Heterojunction Interface Quality To Achieve 9.3% Efficient Cd-Free Cu<sub>2</sub>ZnSnS<sub>4</sub> Solar Cells Using Atomic Layer Deposition

- ZnSnO Buffer Layer," *Chemistry of Materials*, 2018.
- [123] S. W. Lee *et al.*, "Improved Cu<sub>2</sub>O - based solar cells using atomic layer deposition to control the Cu oxidation state at the p - n junction," *Advanced Energy Materials*, vol. 4, no. 11, p. 1301916, 2014.
  - [124] F. H. Teherani *et al.*, "Growth and characterization of ZnO-based buffer layers for CIGS solar cells," vol. 7603, p. 76030D, 2010.
  - [125] T. Kobayashi, Z. Jehl Li Kao, T. Kato, H. Sugimoto, and T. Nakada, "A comparative study of Cd- and Zn-compound buffer layers on Cu(In<sub>1-x</sub>Ga<sub>x</sub>)(S<sub>y</sub>Se<sub>1-y</sub>)<sub>2</sub> thin film solar cells," *Progress in Photovoltaics: Research and Applications*, vol. 24, no. 3, pp. 389-396, 2016.
  - [126] R. Kamada *et al.*, "New world record Cu(In, Ga)(Se, S)<sub>2</sub> thin film solar cell efficiency beyond 22%," in *2016 IEEE 43rd Photovoltaic Specialists Conference (PVSC)*, 2016, pp. 1287-1291.
  - [127] S. Hwang *et al.*, "Wet Pretreatment-Induced Modification of Cu(In,Ga)Se<sub>2</sub>/Cd-Free ZnTiO Buffer Interface," *ACS Appl Mater Interfaces*, vol. 10, no. 24, pp. 20920-20928, Jun 20 2018.
  - [128] S. Chaisitsak, T. Sugiyama, A. Yamada, and M. Konagai, "Cu (InGa) Se<sub>2</sub> thin-film solar cells with high resistivity ZnO buffer layers deposited by atomic layer deposition," *Japanese journal of applied physics*, vol. 38, no. 9R, p. 4989, 1999.
  - [129] C. Platzer-Björkman, J. Lu, J. Kessler, and L. Stolt, "Interface study of CuInSe<sub>2</sub>/ZnO and Cu (In, Ga) Se<sub>2</sub>/ZnO devices using ALD ZnO buffer layers," *Thin Solid Films*, vol. 431, pp. 321-325, 2003.
  - [130] M. Igalson and C. Platzer-Björkman, "The influence of buffer layer on the transient behavior of thin film chalcopyrite devices," *Solar Energy Materials and Solar Cells*, vol. 84, no. 1-4, pp. 93-103, 2004.
  - [131] J. Lindahl, J. T. Wätjen, A. Hultqvist, T. Ericson, M. Edoff, and T. Törndahl, "The effect of Zn<sub>1-x</sub>Sn<sub>x</sub>O<sub>y</sub> buffer layer thickness in 18.0% efficient Cd-free Cu(In,Ga)Se<sub>2</sub> solar cells," *Progress in Photovoltaics: Research and Applications*, vol. 21, no. 8, pp. 1588-1597, 2013.
  - [132] C. Platzer-Björkman *et al.*, "Reduced interface recombination in Cu<sub>2</sub>ZnSnS<sub>4</sub> solar cells with atomic layer deposition Zn<sub>1-x</sub>Sn<sub>x</sub>O<sub>y</sub> buffer layers," *Applied Physics Letters*, vol. 107, no. 24, p. 243904, 2015.
  - [133] T. Törndahl, C. Platzer-Björkman, J. Kessler, and M. Edoff, "Atomic layer deposition of Zn<sub>1-x</sub>Mg<sub>x</sub>O buffer layers for Cu(In,Ga)Se<sub>2</sub> solar cells," *Progress in Photovoltaics: Research and Applications*, vol. 15, no. 3, pp. 225-235, 2007.
  - [134] C. Platzer-Björkman, T. Törndahl, A. Hultqvist, J. Kessler, and M. Edoff, "Optimization of ALD-(Zn,Mg)O buffer layers and (Zn,Mg)O/Cu(In,Ga)Se<sub>2</sub> interfaces for thin film solar cells," *Thin Solid Films*, vol. 515, no. 15, pp. 6024-6027, 2007.
  - [135] J. Pettersson, C. Platzer-Björkman, and M. Edoff, "Temperature-dependent

- current-voltage and lightsoaking measurements on Cu(In,Ga)Se<sub>2</sub> solar cells with ALD-Zn<sub>1-x</sub>MgxO buffer layers," *Progress in Photovoltaics: Research and Applications*, vol. 17, no. 7, pp. 460-469, 2009.
- [136] J. Pettersson, C. Platzer-Björkman, U. Zimmermann, and M. Edoff, "Baseline model of graded-absorber Cu(In,Ga)Se<sub>2</sub> solar cells applied to cells with Zn<sub>1-x</sub>MgxO buffer layers," *Thin Solid Films*, vol. 519, no. 21, pp. 7476-7480, 2011.
- [137] C. Persson, C. Platzer-Bjorkman, J. Malmstrom, T. Torndahl, and M. Edoff, "Strong valence-band offset bowing of ZnO<sub>1-x</sub>S<sub>x</sub> enhances p-type nitrogen doping of ZnO-like alloys," *Phys Rev Lett*, vol. 97, no. 14, p. 146403, Oct 6 2006.
- [138] C. Platzer-Björkman, T. Törndahl, D. Abou-Ras, J. Malmström, J. Kessler, and L. Stolt, "Zn(O,S) buffer layers by atomic layer deposition in Cu(In,Ga)Se<sub>2</sub> based thin film solar cells: Band alignment and sulfur gradient," *Journal of Applied Physics*, vol. 100, no. 4, 2006.
- [139] H. K. Hong *et al.*, "Atomic layer deposited zinc oxysulfide n-type buffer layers for Cu<sub>2</sub>ZnSn(S,Se)<sub>4</sub> thin film solar cells," *Solar Energy Materials and Solar Cells*, vol. 155, pp. 43-50, 2016.
- [140] H. K. Hong, G. Y. Song, H. J. Shim, J. H. Kim, and J. Heo, "Recovery of rectifying behavior in Cu<sub>2</sub>ZnSn(S,Se)<sub>4</sub>/Zn(O,S) thin-film solar cells by in-situ nitrogen doping of buffer layers," *Solar Energy*, vol. 145, pp. 20-26, 2017.
- [141] J. Chantana, T. Kato, H. Sugimoto, and T. Minemoto, "Thin-film Cu(In,Ga)(Se,S)<sub>2</sub>-based solar cell with (Cd,Zn)S buffer layer and Zn<sub>1-x</sub>MgxO window layer," *Progress in Photovoltaics: Research and Applications*, 2017.
- [142] T. Kato, "Cu(In,Ga)(Se,S)<sub>2</sub> solar cell research in Solar Frontier: Progress and current status," *Japanese Journal of Applied Physics*, vol. 56, no. 4S, 2017.
- [143] J. Lockinger *et al.*, "ALD-Zn xTi yO as Window Layer in Cu(In,Ga)Se<sub>2</sub> Solar Cells," *ACS Appl Mater Interfaces*, vol. 10, no. 50, pp. 43603-43609, Dec 19 2018.
- [144] J. Liang *et al.*, "Rectification and tunneling effects enabled by Al<sub>2</sub>O<sub>3</sub> atomic layer deposited on back contact of CdTe solar cells," *Applied Physics Letters*, vol. 107, no. 1, 2015.
- [145] G. Zeng, X. Hao, S. Ren, L. Feng, and Q. Wang, "Application of ALD-Al<sub>2</sub>O<sub>3</sub> in CdS/CdTe Thin-Film Solar Cells," *Energies*, vol. 12, no. 6, 2019.
- [146] J. Keller, F. Gustavsson, L. Stolt, M. Edoff, and T. Törndahl, "On the beneficial effect of Al<sub>2</sub>O<sub>3</sub> front contact passivation in Cu(In,Ga)Se<sub>2</sub> solar cells," *Solar Energy Materials and Solar Cells*, vol. 159, pp. 189-196, 2017.
- [147] T. Tynell and M. Karppinen, "Atomic layer deposition of ZnO: a review," *Semiconductor Science and Technology*, vol. 29, no. 4, p. 043001, 2014.
- [148] C. R. Ellinger and S. F. Nelson, "Selective Area Spatial Atomic Layer Deposition of ZnO, Al<sub>2</sub>O<sub>3</sub>, and Aluminum-Doped ZnO Using Poly(vinyl pyrrolidone)," *Chemistry of Materials*, vol. 26, no. 4, pp. 1514-1522, 2014.

- [149] J. W. Elam, D. A. Baker, A. J. Hryn, A. B. F. Martinson, M. J. Pellin, and J. T. Hupp, "Atomic layer deposition of tin oxide films using tetrakis(dimethylamino) tin," *Journal of Vacuum Science & Technology A: Vacuum, Surfaces, and Films*, vol. 26, no. 2, pp. 244-252, 2008.
- [150] B. Burton, D. Goldstein, and S. George, "Atomic layer deposition of MgO using bis (ethylcyclopentadienyl) magnesium and H<sub>2</sub>O," *The Journal of Physical Chemistry C*, vol. 113, no. 5, pp. 1939-1946, 2009.
- [151] J. Park *et al.*, "The Role of Hydrogen from ALD-Al<sub>2</sub>O<sub>3</sub> in Kesterite Cu<sub>2</sub>ZnSnS<sub>4</sub> Solar Cells: Grain Surface Passivation," *Advanced Energy Materials*, 2018.
- [152] X. Du, Y. Du, and S. M. George, "In situ examination of tin oxide atomic layer deposition using quartz crystal microbalance and Fourier transform infrared techniques," *Journal of Vacuum Science & Technology A: Vacuum, Surfaces, and Films*, vol. 23, no. 4, pp. 581-588, 2005.
- [153] T. Muneshwar and K. Cadien, "Probing initial-stages of ALD growth with dynamic in situ spectroscopic ellipsometry," *Applied Surface Science*, vol. 328, pp. 344-348, 2015.
- [154] A. Y. Kovalgin *et al.*, "Hot-Wire Assisted ALD: A Study Powered by In Situ Spectroscopic Ellipsometry," *Advanced Materials Interfaces*, vol. 4, no. 18, 2017.
- [155] E. Langereis, S. B. S. Heil, H. C. M. Knoop, W. Keuning, M. C. M. van de Sanden, and W. M. M. Kessels, "In situ spectroscopic ellipsometry as a versatile tool for studying atomic layer deposition," *Journal of Physics D: Applied Physics*, vol. 42, no. 7, p. 073001, 2009.
- [156] J. A. W. C. Inc, "CompleteEASE TM Data Analysis Manual," pp. 1-207, 2011.
- [157] L. M. Hanssen and K. A. Snail, "Integrating spheres for mid-and near-infrared reflection spectroscopy," *Handbook of Vibrational Spectroscopy*, vol. 2, pp. 1175-1192, 2002.
- [158] M. B. Heaney, "Electrical conductivity and resistivity," *The measurement, instrumentation and sensors handbook*, pp. 1332-1345, 2000.
- [159] O. Philips' Gloeilampenfabrieken, "A method of measuring specific resistivity and Hall effect of discs of arbitrary shape," *Philips Res. Rep.*, vol. 13, no. 1, pp. 1-9, 1958.
- [160] "Microanalysis techniques arranged according to their spatial resolutions and sensitivities," <https://myscope.training/legacy/analysis/introduction/>, Sep 2019.
- [161] "Data acquisition of different types of surface analysis in different material," <https://xpssimplified.com/UPS.php>, Sep 2019.
- [162] J. Fritsche *et al.*, "Surface analysis of CdTe thin film solar cells," *Thin Solid Films*, vol. 387, no. 1-2, pp. 161-164, 2001.
- [163] T. Shyju, S. Anandhi, R. Suriakarthick, R. Gopalakrishnan, and P. Kuppusami, "Mechanosynthesis, deposition and characterization of CZTS and CZTSe materials for solar cell applications," *Journal of Solid State Chemistry*, vol. 227, pp. 1-10, 2019.

- pp. 165-177, 2015.
- [164] S. Sadewasser, "Surface potential of chalcopyrite films measured by KPFM," *physica status solidi (a)*, vol. 203, no. 11, pp. 2571-2580, 2006.
  - [165] W. Melitz, J. Shen, A. C. Kummel, and S. Lee, "Kelvin probe force microscopy and its application," *Surface Science Reports*, vol. 66, no. 1, pp. 1-27, 2011.
  - [166] Y. Rosenwaks, R. Shikler, T. Glatzel, and S. Sadewasser, "Kelvin probe force microscopy of semiconductor surface defects," *Physical Review B*, vol. 70, no. 8, 2004.
  - [167] S. Sadewasser, T. Glatzel, S. Schuler, S. Nishiwaki, R. Kaigawa, and M. C. Lux-Steiner, "Kelvin probe force microscopy for the nano scale characterization of chalcopyrite solar cell materials and devices," *Thin Solid Films*, vol. 431-432, pp. 257-261, 2003.
  - [168] N. Nicoara, T. Lepetit, L. Arzel, S. Harel, N. Barreau, and S. Sadewasser, "Effect of the KF post-deposition treatment on grain boundary properties in Cu(In, Ga)Se<sub>2</sub> thin films," *Sci Rep*, vol. 7, p. 41361, Jan 27 2017.
  - [169] R. H. Scott, V. A. Fassel, R. N. Kniseley, and D. E. Nixon, "Inductively coupled plasma-optical emission analytical spectrometry," *Analytical Chemistry*, vol. 46, no. 1, pp. 75-80, 1974.
  - [170] A. Benninghoven, "Chemical analysis of inorganic and organic surfaces and thin films by static time - of - flight secondary ion mass spectrometry (TOF - SIMS)," *Angewandte Chemie International Edition in English*, vol. 33, no. 10, pp. 1023-1043, 1994.
  - [171] L. Van Vaeck, A. Adriaens, and R. Gijbels, "Static secondary ion mass spectrometry (S - SIMS) Part 1: methodology and structural interpretation," *Mass Spectrometry Reviews*, vol. 18, no. 1, pp. 1-47, 1999.
  - [172] A. Adriaens, L. Van Vaeck, and F. Adams, "Static secondary ion mass spectrometry (S - SIMS) Part 2: material science applications," *Mass Spectrometry Reviews*, vol. 18, no. 1, pp. 48-81, 1999.
  - [173] D. McMullan, "Von Ardenne and the scanning electron microscope," *SPIE MILESTONE SERIES MS*, vol. 94, pp. 171-171, 1994.
  - [174] D. McMullan, "Scanning electron microscopy 1928–1965," *Scanning*, vol. 17, no. 3, pp. 175-185, 1995.
  - [175] "Configuration of the electron microscopy compared with light microscopy," [https://myscope.training/#/M10Ilevel\\_1\\_9](https://myscope.training/#/M10Ilevel_1_9), Sep 2019.
  - [176] B. Fultz and J. M. Howe, *Transmission electron microscopy and diffractometry of materials*. Springer Science & Business Media, 2012.
  - [177] M. Miller, "Atom probe tomography for studying phase transformations in steels," in *Phase Transformations in Steels*: Elsevier, 2012, pp. 532-556.
  - [178] S. Lozano-Perez, "Characterization techniques for assessing irradiated and ageing materials in nuclear power plant systems, structures and components (SSC)," in *Understanding and Mitigating Ageing in Nuclear Power Plants*: Elsevier, 2010, pp. 389-416.

- [179] G. Miller, "A feedback method for investigating carrier distributions in semiconductors," *IEEE Transactions on Electron Devices*, vol. 19, no. 10, pp. 1103-1108, 1972.
- [180] H.-S. Duan, W. Yang, B. Bob, C.-J. Hsu, B. Lei, and Y. Yang, "The Role of Sulfur in Solution-Processed  $\text{Cu}_2\text{ZnSn}(\text{S},\text{Se})_4$  and its Effect on Defect Properties," *Advanced Functional Materials*, vol. 23, no. 11, pp. 1466-1471, 2013.
- [181] J. T. Heath, J. D. Cohen, and W. N. Shafarman, "Bulk and metastable defects in  $\text{CuIn}_{1-x}\text{Ga}_x\text{Se}_2$  thin films using drive-level capacitance profiling," *Journal of Applied Physics*, vol. 95, no. 3, pp. 1000-1010, 2004.
- [182] S. Siebentritt, "Why are kesterite solar cells not 20% efficient?," *Thin Solid Films*, vol. 535, pp. 1-4, 2013.
- [183] A. Nagoya, R. Asahi, and G. Kresse, "First-principles study of  $\text{Cu}_2\text{ZnSnS}_4$  and the related band offsets for photovoltaic applications," *J Phys Condens Matter*, vol. 23, no. 40, p. 404203, Oct 12 2011.
- [184] B. Hoex, S. Heil, E. Langereis, M. Van de Sanden, and W. Kessels, "Ultralow surface recombination of c-Si substrates passivated by plasma-assisted atomic layer deposited  $\text{Al}_2\text{O}_3$ ," *Applied Physics Letters*, vol. 89, no. 4, p. 042112, 2006.
- [185] M. N. Mullings, C. Hägglund, and S. F. Bent, "Tin oxide atomic layer deposition from tetrakis(dimethylamino)tin and water," *Journal of Vacuum Science & Technology A: Vacuum, Surfaces, and Films*, vol. 31, no. 6, p. 061503, 2013.
- [186] V. Srikant and D. R. Clarke, "On the optical band gap of zinc oxide," *Journal of Applied Physics*, vol. 83, no. 10, pp. 5447-5451, 1998.
- [187] J. Muth, R. Kolbas, A. Sharma, S. Oktyabrsky, and J. Narayan, "Excitonic structure and absorption coefficient measurements of ZnO single crystal epitaxial films deposited by pulsed laser deposition," *Journal of Applied Physics*, vol. 85, no. 11, pp. 7884-7887, 1999.
- [188] J. Heo, S. Bok Kim, and R. G. Gordon, "Atomic layer deposited zinc tin oxide channel for amorphous oxide thin film transistors," *Applied Physics Letters*, vol. 101, no. 11, p. 113507, 2012.
- [189] H. Chiang, J. Wager, R. Hoffman, J. Jeong, and D. A. Keszler, "High mobility transparent thin-film transistors with amorphous zinc tin oxide channel layer," *Applied Physics Letters*, vol. 86, no. 1, p. 013503, 2005.
- [190] M. N. Mullings, C. Hägglund, J. T. Tanskanen, Y. Yee, S. Geyer, and S. F. Bent, "Thin film characterization of zinc tin oxide deposited by thermal atomic layer deposition," *Thin Solid Films*, vol. 556, pp. 186-194, 2014.
- [191] J.-Y. Kwon, D.-J. Lee, and K.-B. Kim, "Transparent amorphous oxide semiconductor thin film transistor," *Electronic Materials Letters*, vol. 7, no. 1, pp. 1-11, 2011.
- [192] C. Teng *et al.*, "Refractive indices and absorption coefficients of  $\text{Mg}_x\text{Zn}_{1-x}$



- O alloys," *Applied Physics Letters*, vol. 76, no. 8, pp. 979-981, 2000.
- [193] Y. Ke *et al.*, "Enhanced Electron Mobility Due to Dopant-Defect Pairing in Conductive ZnMgO," *Advanced Functional Materials*, vol. 24, no. 19, pp. 2875-2882, 2014.
- [194] K. Matsubara *et al.*, "Band-gap modified Al-doped Zn 1– x Mg x O transparent conducting films deposited by pulsed laser deposition," *Applied physics letters*, vol. 85, no. 8, pp. 1374-1376, 2004.
- [195] K. Fleischer, E. Arca, C. Smith, and I. Shvets, "Aluminium doped Zn 1– x Mg x O—A transparent conducting oxide with tunable optical and electrical properties," *Applied Physics Letters*, vol. 101, no. 12, p. 121918, 2012.
- [196] D. Cohen, K. Ruthe, and S. A. Barnett, "Transparent conducting Zn 1– x Mg x O:(Al, In) thin films," *Journal of Applied Physics*, vol. 96, no. 1, pp. 459-467, 2004.
- [197] M. A. Green, "Solar cell fill factors: General graph and empirical expressions," *Solid-State Electronics*, vol. 24, no. 8, pp. 788-789, 1981.
- [198] J. Lee, J. D. Cohen, and W. N. Shafarman, "The determination of carrier mobilities in CIGS photovoltaic devices using high-frequency admittance measurements," *Thin Solid Films*, vol. 480-481, pp. 336-340, 2005.
- [199] T. Eisenbarth, T. Unold, R. Caballero, C. A. Kaufmann, and H.-W. Schock, "Interpretation of admittance, capacitance-voltage, and current-voltage signatures in Cu (In, Ga) Se 2 thin film solar cells," *Journal of Applied Physics*, vol. 107, no. 3, p. 034509, 2010.
- [200] D. S. Chan and J. C. Phang, "Analytical methods for the extraction of solar-cell single-and double-diode model parameters from IV characteristics," *IEEE Transactions on Electron devices*, vol. 34, no. 2, pp. 286-293, 1987.
- [201] F. Liu *et al.*, "Nanoscale Microstructure and Chemistry of Cu<sub>2</sub>ZnSnS<sub>4</sub>/CdS Interface in Kesterite Cu<sub>2</sub>ZnSnS<sub>4</sub>Solar Cells," *Advanced Energy Materials*, vol. 6, no. 15, p. 1600706, 2016.
- [202] S. Pennycook and L. Boatner, "Chemically sensitive structure-imaging with a scanning transmission electron microscope," *Nature*, vol. 336, no. 6199, p. 565, 1988.
- [203] B. G. Mendis, M. C. J. Goodman, J. D. Major, A. A. Taylor, K. Durose, and D. P. Halliday, "The role of secondary phase precipitation on grain boundary electrical activity in Cu<sub>2</sub>ZnSnS<sub>4</sub> (CZTS) photovoltaic absorber layer material," *Journal of Applied Physics*, vol. 112, no. 12, 2012.
- [204] K. Sun *et al.*, "Self-assembled nanometer-scale ZnS structure at the CZTS/ZnCdS hetero-interface for high efficiency wide bandgap Cu<sub>2</sub>ZnSnS<sub>4</sub> solar cells," *Chemistry of Materials*, 2018.
- [205] H. Zhou *et al.*, "Rational Defect Passivation of Cu<sub>2</sub>ZnSn(S,Se)<sub>4</sub> Photovoltaics with Solution-Processed Cu<sub>2</sub>ZnSnS<sub>4</sub>:Na Nanocrystals," *Journal of the American Chemical Society*, vol. 135, no. 43, pp. 15998-16001, 2013/10/30 2013.

- [206] A. Nagaoka *et al.*, "Effects of sodium on electrical properties in Cu<sub>2</sub>ZnSnS<sub>4</sub> single crystal," *Applied Physics Letters*, vol. 104, no. 15, 2014.
- [207] J. V. Li, D. Kuciauskas, M. R. Young, and I. L. Repins, "Effects of sodium incorporation in Co-evaporated Cu<sub>2</sub>ZnSnSe<sub>4</sub> thin-film solar cells," *Applied Physics Letters*, vol. 102, no. 16, p. 163905, 2013.
- [208] J. H. Han *et al.*, "Growth of amorphous zinc tin oxide films using plasma-enhanced atomic layer deposition from bis(1-dimethylamino-2-methyl-2-propoxy)tin, diethylzinc, and oxygen plasma," *Applied Surface Science*, vol. 357, pp. 672-677, 2015.
- [209] Q. J. Jiang *et al.*, "Solvent sensors based on amorphous ZnSnO thin-film transistors," *RSC Advances*, vol. 5, no. 36, pp. 28242-28246, 2015.
- [210] J. R. Waldrop, R. W. Grant, S. P. Kowalczyk, and E. A. Kraut, "Measurement of semiconductor heterojunction band discontinuities by x - ray photoemission spectroscopy," *Journal of Vacuum Science & Technology A: Vacuum, Surfaces, and Films*, vol. 3, no. 3, pp. 835-841, 1985.
- [211] M. Burgelman, K. Decock, S. Khelifi, and A. Abass, "Advanced electrical simulation of thin film solar cells," *Thin Solid Films*, vol. 535, pp. 296-301, 2013.
- [212] A. Pu *et al.*, "Sentaurus modelling of 6.9% Cu<sub>2</sub>ZnSnS<sub>4</sub> device based on comprehensive electrical & optical characterization," *Solar Energy Materials and Solar Cells*, vol. 160, pp. 372-381, 2017.
- [213] I. Repins *et al.*, "Kesterites and Chalcopyrites: A Comparison of Close Cousins," *MRS Proceedings*, vol. 1324, 2011.
- [214] B. S. Sengar *et al.*, "Band alignment of Cd-free (Zn, Mg)O layer with Cu<sub>2</sub>ZnSn(S,Se)<sub>4</sub> and its effect on the photovoltaic properties," *Optical Materials*, vol. 84, pp. 748-756, 2018.
- [215] A. Bauer, S. Sharbati, and M. Powalla, "Systematic survey of suitable buffer and high resistive window layer materials in CuIn<sub>1-x</sub>Ga<sub>x</sub>Se<sub>2</sub> solar cells by numerical simulations," *Solar Energy Materials and Solar Cells*, vol. 165, pp. 119-127, 2017.
- [216] S. Ishizuka *et al.*, "Fabrication of wide-gap Cu(In<sub>1-x</sub>Ga<sub>x</sub>)Se<sub>2</sub> thin film solar cells: a study on the correlation of cell performance with highly resistive i-ZnO layer thickness," *Solar Energy Materials and Solar Cells*, vol. 87, no. 1-4, pp. 541-548, 2005.
- [217] S. B. S. Heil, J. L. van Hemmen, M. C. M. van de Sanden, and W. M. M. Kessels, "Reaction mechanisms during plasma-assisted atomic layer deposition of metal oxides: A case study for Al<sub>2</sub>O<sub>3</sub>," *Journal of Applied Physics*, vol. 103, no. 10, p. 103302, 2008.
- [218] E. Langereis, S. B. S. Heil, M. C. M. van de Sanden, and W. M. M. Kessels, "In situ spectroscopic ellipsometry study on the growth of ultrathin TiN films by plasma-assisted atomic layer deposition," *Journal of Applied Physics*, vol. 100, no. 2, 2006.

- [219] Z. Baji *et al.*, "Nucleation and Growth Modes of ALD ZnO," *Crystal Growth & Design*, vol. 12, no. 11, pp. 5615-5620, 2012.
- [220] C.-Y. Lee *et al.*, "Improving the Silicon Surface Passivation by Aluminum Oxide Grown Using a Non-Pyrophoric Aluminum Precursor," *physica status solidi (RRL) - Rapid Research Letters*, vol. 12, no. 7, 2018.
- [221] J. W. Elam and S. M. George, "Growth of ZnO/Al<sub>2</sub>O<sub>3</sub> Alloy Films Using Atomic Layer Deposition Techniques," *Chemistry of Materials*, vol. 15, no. 4, pp. 1020-1028, 2003/02/01 2003.
- [222] M. Guc *et al.*, "Resonant Raman scattering based approaches for the quantitative assessment of nanometric ZnMgO layers in high efficiency chalcogenide solar cells," *Sci Rep*, vol. 7, no. 1, p. 1144, Apr 25 2017.
- [223] J. D. Ye *et al.*, "Effects of alloying and localized electronic states on the resonant Raman spectra of Zn<sub>1-x</sub>Mg<sub>x</sub>O nanocrystals," *Applied Physics Letters*, vol. 91, no. 9, 2007.
- [224] H. Knoops, E. Langereis, M. Van De Sanden, and W. Kessels, "Conformality of plasma-assisted ALD: physical processes and modeling," *Journal of The Electrochemical Society*, vol. 157, no. 12, pp. G241-G249, 2010.
- [225] H. Profijt, S. Potts, M. Van de Sanden, and W. Kessels, "Plasma-assisted atomic layer deposition: basics, opportunities, and challenges," *Journal of Vacuum Science & Technology A: Vacuum, Surfaces, and Films*, vol. 29, no. 5, p. 050801, 2011.
- [226] J. Elam, Z. Sechrist, and S. George, "ZnO/Al<sub>2</sub>O<sub>3</sub> nanolaminates fabricated by atomic layer deposition: growth and surface roughness measurements," *Thin Solid Films*, vol. 414, no. 1, pp. 43-55, 2002.
- [227] P. Banerjee, W.-J. Lee, K.-R. Bae, S. B. Lee, and G. W. Rubloff, "Structural, electrical, and optical properties of atomic layer deposition Al-doped ZnO films," *Journal of Applied Physics*, vol. 108, no. 4, 2010.
- [228] O. Nilsen, O. B. Karlsen, A. Kjekshus, and H. Fjellvåg, "Simulation of growth dynamics in atomic layer deposition. Part III. Polycrystalline films from tetragonal crystallites," *Thin Solid Films*, vol. 515, no. 11, pp. 4550-4558, 2007.
- [229] T. Minemoto, T. Negami, S. Nishiwaki, H. Takakura, and Y. Hamakawa, "Preparation of Zn<sub>1-x</sub>Mg<sub>x</sub>O films by radio frequency magnetron sputtering," *Thin solid films*, vol. 372, no. 1-2, pp. 173-176, 2000.
- [230] M. Godlewski *et al.*, "Vertically stacked non-volatile memory devices—material considerations," *Microelectronic Engineering*, vol. 85, no. 12, pp. 2434-2438, 2008.
- [231] M. A. Thomas and J. B. Cui, "Highly tunable electrical properties in undoped ZnO grown by plasma enhanced thermal-atomic layer deposition," *ACS Appl Mater Interfaces*, vol. 4, no. 6, pp. 3122-8, Jun 27 2012.
- [232] B. Hoex, J. J. H. Gielis, M. C. M. van de Sanden, and W. M. M. Kessels, "On the c-Si surface passivation mechanism by the negative-charge-dielectric Al<sub>2</sub>O<sub>3</sub>," *Journal of Applied Physics*, vol. 104, no. 11, 2008.

- [233] G. Dingemans, W. Beyer, M. C. M. van de Sanden, and W. M. M. Kessels, "Hydrogen induced passivation of Si interfaces by Al<sub>2</sub>O<sub>3</sub> films and SiO<sub>2</sub>/Al<sub>2</sub>O<sub>3</sub> stacks," *Applied Physics Letters*, vol. 97, no. 15, 2010.
- [234] F. Werner *et al.*, "Electronic and chemical properties of the c-Si/Al<sub>2</sub>O<sub>3</sub> interface," *Journal of Applied Physics*, vol. 109, no. 11, 2011.
- [235] N. M. Terlinden, G. Dingemans, M. C. M. van de Sanden, and W. M. M. Kessels, "Role of field-effect on c-Si surface passivation by ultrathin (2–20 nm) atomic layer deposited Al<sub>2</sub>O<sub>3</sub>," *Applied Physics Letters*, vol. 96, no. 11, 2010.
- [236] B. Hoex, M. Bosman, N. Nandakumar, and W. M. M. Kessels, "Silicon surface passivation by aluminium oxide studied with electron energy loss spectroscopy," *physica status solidi (RRL) - Rapid Research Letters*, vol. 7, no. 11, pp. 937-941, 2013.
- [237] W. W. Hsu *et al.*, "Surface passivation of Cu(In,Ga)Se<sub>2</sub> using atomic layer deposited Al<sub>2</sub>O<sub>3</sub>," *Applied Physics Letters*, vol. 100, no. 2, p. 023508, 2012.
- [238] Y. Ren, N. Ross, J. K. Larsen, K. Rudisch, J. J. S. Scragg, and C. Platzer-Björkman, "Evolution of Cu<sub>2</sub>ZnSnS<sub>4</sub> during Non-Equilibrium Annealing with Quasi-in Situ Monitoring of Sulfur Partial Pressure," *Chemistry of Materials*, vol. 29, no. 8, pp. 3713-3722, 2017.
- [239] J. J. S. Scragg *et al.*, "Cu-Zn disorder and band gap fluctuations in Cu<sub>2</sub>ZnSn(S,Se)<sub>4</sub>: Theoretical and experimental investigations," *physica status solidi (b)*, vol. 253, no. 2, pp. 247-254, 2016.
- [240] J. T. Heath, J. D. Cohen, and W. N. Shafarman, "Distinguishing metastable changes in bulk CIGS defect densities from interface effects," *Thin Solid Films*, vol. 431-432, pp. 426-430, 2003.
- [241] M. Bär *et al.*, "Native oxidation and Cu-poor surface structure of thin film Cu<sub>2</sub>ZnSnS<sub>4</sub> solar cell absorbers," *Applied Physics Letters*, vol. 99, no. 11, 2011.
- [242] A. Gharachorlou *et al.*, "Trimethylaluminum and Oxygen Atomic Layer Deposition on Hydroxyl-Free Cu(111)," *ACS Appl Mater Interfaces*, vol. 7, no. 30, pp. 16428-39, Aug 5 2015.
- [243] M. D. Detwiler *et al.*, "Reaction of Trimethylaluminum with Water on Pt(111) and Pd(111) from 10–5 to 10–1 Millibar," *The Journal of Physical Chemistry C*, 2015.
- [244] D. K. Simon, P. M. Jordan, T. Mikolajick, and I. Dirnstorfer, "On the Control of the Fixed Charge Densities in Al<sub>2</sub>O<sub>3</sub>-Based Silicon Surface Passivation Schemes," *ACS Appl Mater Interfaces*, vol. 7, no. 51, pp. 28215-22, Dec 30 2015.
- [245] V. Naumann, M. Otto, R. B. Wehrspohn, and C. Hagendorf, "Chemical and structural study of electrically passivating Al<sub>2</sub>O<sub>3</sub>/Si interfaces prepared by atomic layer deposition," *Journal of Vacuum Science & Technology A: Vacuum, Surfaces, and Films*, vol. 30, no. 4, 2012.
- [246] U. Rau *et al.*, "Oxygenation and air-annealing effects on the electronic

- properties of Cu (In, Ga) Se<sub>2</sub> films and devices," *Journal of Applied Physics*, vol. 86, no. 1, pp. 497-505, 1999.
- [247] A. Klein, J. Fritsche, W. Jaegermann, J. Schön, C. Kloc, and E. Bucher, "Fermi level-dependent defect formation at Cu (In, Ga) Se<sub>2</sub> interfaces," *Applied surface science*, vol. 166, no. 1-4, pp. 508-512, 2000.
- [248] W.-J. Yin, Y. Wu, S.-H. Wei, R. Noufi, M. M. Al-Jassim, and Y. Yan, "Engineering Grain Boundaries in Cu<sub>2</sub>ZnSnSe<sub>4</sub> for Better Cell Performance: A First-Principle Study," *Advanced Energy Materials*, vol. 4, no. 1, 2014.
- [249] M. Takihara, T. Minemoto, Y. Wakisaka, and T. Takahashi, "An investigation of band profile around the grain boundary of Cu(InGa)Se<sub>2</sub> solar cell material by scanning probe microscopy," *Progress in Photovoltaics: Research and Applications*, pp. n/a-n/a, 2011.
- [250] S. Pedrazzini *et al.*, "Nanoscale stoichiometric analysis of a high-temperature superconductor by atom probe tomography," *Microscopy and Microanalysis*, vol. 23, no. 2, pp. 414-424, 2017.
- [251] K. Sardashti *et al.*, "Nanoscale Characterization of Back Surfaces and Interfaces in Thin-Film Kesterite Solar Cells," *ACS Appl Mater Interfaces*, vol. 9, no. 20, pp. 17024-17033, May 24 2017.
- [252] M. F. J. Vos, B. Macco, N. F. W. Thissen, A. A. Bol, and W. M. M. Kessels, "Atomic layer deposition of molybdenum oxide from (NtBu)<sub>2</sub>(NMe<sub>2</sub>)<sub>2</sub>Mo and O<sub>2</sub> plasma," *Journal of Vacuum Science & Technology A: Vacuum, Surfaces, and Films*, vol. 34, no. 1, p. 01A103, 2016.
- [253] S. Balasubramanyam, A. Sharma, V. Vandalon, H. C. M. Knoop, W. M. M. Kessels, and A. A. Bol, "Plasma-enhanced atomic layer deposition of tungsten oxide thin films using (tBuN)<sub>2</sub>(Me<sub>2</sub>N)<sub>2</sub>W and O<sub>2</sub> plasma," *Journal of Vacuum Science & Technology A: Vacuum, Surfaces, and Films*, vol. 36, no. 1, 2018.
- [254] J. Chantana, Y. Kawano, T. Nishimura, T. Kato, H. Sugimoto, and T. Minemoto, "Characterization of Cd-Free Zn<sub>1-x</sub>Mg<sub>x</sub>O:Al/Zn<sub>1-x</sub>Mg<sub>x</sub>O/Cu(In,Ga)(S,Se)<sub>2</sub> Solar Cells Fabricated by an All Dry Process Using Ultraviolet Light Excited Time-Resolved Photoluminescence," *ACS Appl Mater Interfaces*, vol. 11, no. 7, pp. 7539-7545, Feb 20 2019.
- [255] J. Chantana, T. Kato, H. Sugimoto, and T. Minemoto, "20%-Efficient Zn<sub>0.9</sub>Mg<sub>0.1</sub>O:Al/Zn<sub>0.8</sub>Mg<sub>0.2</sub>O/Cu(In,Ga)(S,Se)<sub>2</sub> Solar Cell Prepared by All Dry Process through Combination of Heat-Light Soaking and Light Soaking Process," *ACS Appl Mater Interfaces*, Mar 13 2018.
- [256] J. Chantana, Y. Kawano, T. Nishimura, T. Kato, H. Sugimoto, and T. Minemoto, "Characteristics of Zn<sub>1-x</sub>Mg<sub>x</sub>O:B and its application as transparent conductive oxide layer in Cu(In,Ga)(S,Se)<sub>2</sub> solar cells with and without CdS buffer layer," *Solar Energy*, vol. 184, pp. 553-560, 2019.
- [257] M. Morales-Masis *et al.*, "Highly Conductive and Broadband Transparent Zr-Doped In<sub>2</sub>O<sub>3</sub> as Front Electrode for Solar Cells," *IEEE Journal of Photovoltaics*, vol. 8, no. 5, pp. 1202-1207, 2018.